Coherence and Decoherence in High-mass Matter-wave Interferometry

Genehmigte Dissertation der Fakultät für Physik der Universität Duisburg-Essen

vorgelegt von

Kai Walter
aus Kyoto, Japan

zur Erlangung des akademischen Grades eines
Doktors der Naturwissenshaften (Dr. rer. nat.)

Duisburg, den 30.09.2016

Tag der mündlichen Prüfung: 04. Nov. 2016
Erstgutachter: Prof. Dr. Klaus Hornberger, Universität Duisburg-Essen
Zweitgutachter: Prof. Dr. Markus Arndt, Universität Wien

COHERENCE AND DECOHERENCE IN HIGH-MASS MATTER-WAVE INTERFEROMETRY

KAI WALTER

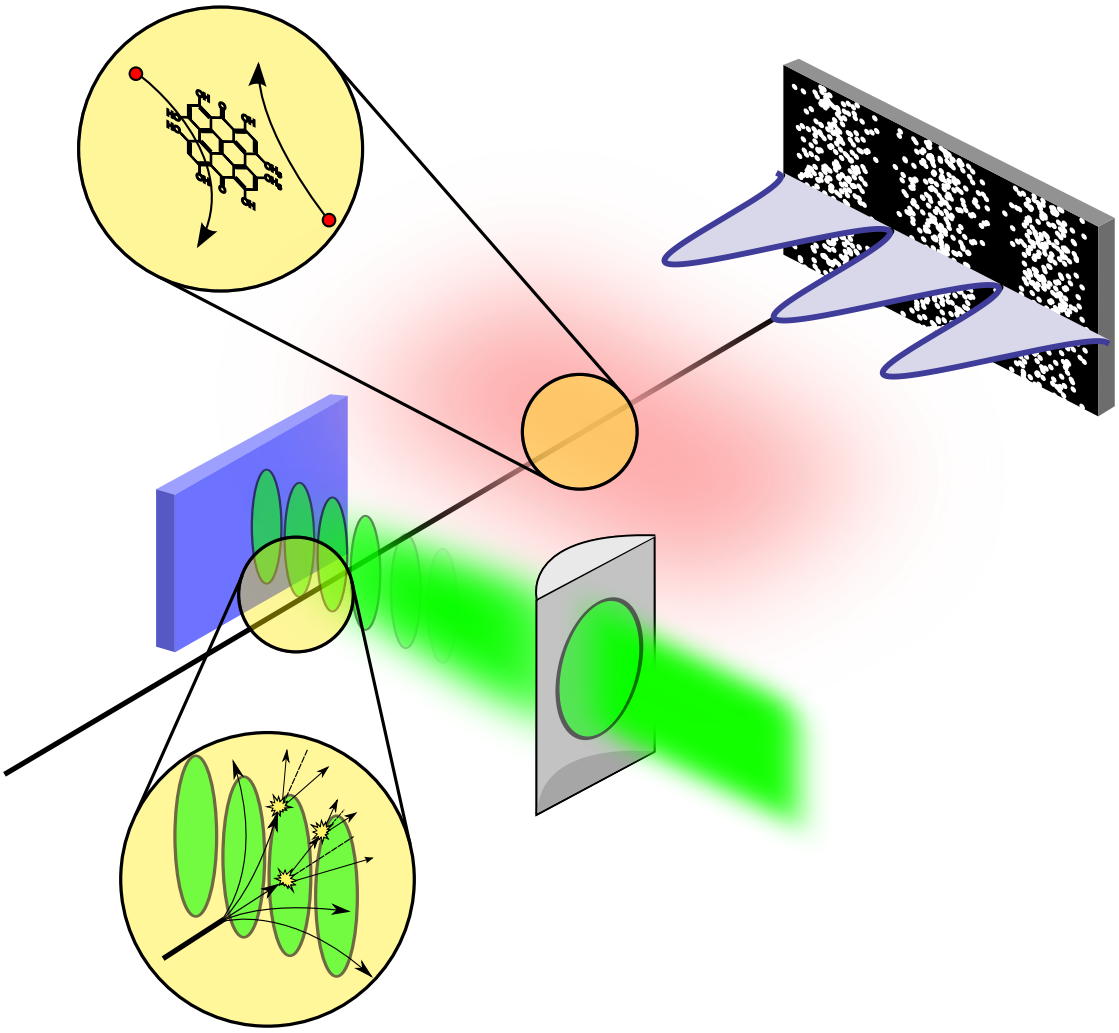

ABSTRACT

The present thesis deals with two main topics. First, I study in detail the interaction of a delocalized molecular matter-wave with a standing-wave laser grating. Due to absorption of photons in an optical grating, molecules can get excited and numerous internal photophysical processes are induced. For the theoretical description of the molecule-light interaction I take three relevant internal molecular processes into account: intersystem crossing, fluorescence and internal conversion. Furthermore, the fact that molecules can change their optical properties because of the photoexcitation is shown to have a measurable effect on matter-wave interferometry. The second topic of this thesis is about collisions between a polar molecule and non-polar environmental gas atoms, and their effects on the coherence of the center-of-mass state. Because the scattering potential depends on the molecular orientation the molecular rotational state must also be considered. Assuming a slow rotation of the molecule compared to the scattering time and that the molecular mass fairly exceeds the mass of a gas atom, I present a master equation of collisional decoherence, which depends on the molecular orientation. Its predictions for matter-wave interferometry are discussed both in the near and far field.

ZUSAMMENFASSUNG

Die vorliegende Arbeit behandelt zwei Hauptthemen. Das erste ist die Wechselwirkung zwischen der delokalisierten Materiewelle eines Moleküls und einer stehenden Laser-Welle. Aufgrund der Photonabsorptionen in dem optischen Gitter kann das Molekül elektronisch angeregt werden, was zahlreiche photophysikalische Prozesse zur Folge hat. Die hier entwickelte Beschreibung der Molekül-Licht-Wechselwirkung umfasst drei relevante interne molekulare Prozesse: intersystem crossing, interne Konversion und Fluoreszenz. Zudem können die optischen Eigenschaften eines Moleküls durch Photoanregung beeinflusst werden. Es wird in dieser Arbeit gezeigt, dass solche Änderungen eine große Auswirkung auf die Materiewellen-Interferometrie haben können. Das zweite Thema dieser Arbeit ist die Beschreibung von Kollisionen zwischen einem polaren Molekül und unpolaren Gasatomen und deren Auswirkung auf die Kohärenz des molekularen Schwerpunktszustandes. Da das Wechselwirkungspotential von der Orientierung des Moleküls abhängt, muss die Beschreibung eines Stoßvorgangs auch den Rotationszustand des Moleküls berücksichtigen. Die Mastergleichung für die Quanten-Dynamik des Moleküls aufgrund der Gasumgebung wird mit der Annahme hergeleitet, dass das Molekül im Vergleich zur Stoßzeit langsam rotiert und dass das Molekül gegenüber den Gasatomen sehr massiv ist. Schließlich illustriere und diskutiere ich ihre Konsequenzen anhand konkreter Materiewellen-Interferometer im Nah- und Fernfeld.

PUBLICATIONS

- J. P. Cotter, S. Eibenberger, L. Mairhofer, X. Cheng, P. Asenbaum, M. Arndt, **K. Walter**, S. Nimmrichter, K. Hornberger, *Coherence in the presence of absorption and heating in a molecule interferometer*, Nat. Commun. **6**, 7336 (2015)

- **K. Walter**, B. A. Stickler, K. Hornberger, *Collisional decoherence of polar molecules*, Phys. Rev. A **93** 063612 (2016)

- **K. Walter**, S. Nimmrichter, K. Hornberger, *Multiphoton absorption in optical gratings for matter waves*, Phys. Rev. A **94**, 043637 (2016)

CONTENTS

1 INTRODUCTION

Quantum theory has been verified by numerous experiments since its birth in 1900 when Max Planck introduced an energy quantum $\varepsilon = h\nu$ to explain the black body radiation [1]. One of the earlier successes of quantum mechanics is the description of the hydrogen spectrum. Classical electrodynamics predicts an unstable electron orbit in an atom because an electron would lose its energy by emitting Bremsstrahlung and it would fall into the nucleus within a short time of $\sim 10^{-11}$ sec [2]. Quantum theory, in contrast, predicts orbits with discrete radii due to the quantization of the electron's energy. Today, quantum electrodynamics (the quantized theory of electrodynamics) is one of the most accurate theories in physics, whose prediction (e.g. of the fine-structure constant α) agrees with experiment within an astonishingly small relative uncertainty of $\sim 10^{-6}$ % [3, 4].

Accompanied with its successes, quantum theory brings some curious conceptional and interpretative difficulties, which cannot be explained in the framework of classical theories. One of the most astonishing consequence is the *wave-particle duality*. This phenomenon is well illustrated by a double-slit experiment, analogous to *Young experiment* providing the wave nature of light. On the one hand, each measurement of a particle creates a point on the detection screen. On the other hand, the particles build up an interference fringe pattern, as becomes visible for large number of detected particles, see Fig. 1 from left to right. That is, each particle interferes with itself, passing the two slits simultaneously, just like a wave does. This experiment demonstrates impressively the particle-wave duality and is counted as the most beautiful experiment in physics [5]. Richard Feynman even went so far to say that this experiment contains the only mystery of quantum mechanics [6].

If one believes in the predictions of quantum mechanics, at least one of the most essential premises of classical physics must be renounced: *Locality*, meaning that no physical influence travels faster than the speed of light, or *realism*, i.e. physical objects

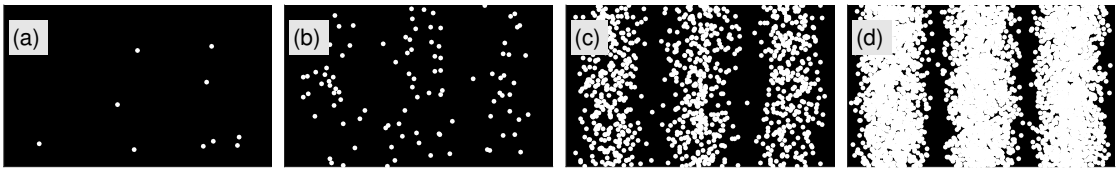

Figure 1: Schematic illustration of an interferogram of the Young experiment with matter-waves. Panel (a) - (d) show the interference pattern for different numbers of measured particles, 10, 100, 1000 and 5000, respectively.

have definite properties independent of measurement [7]. In the example of a double-slit experiment, a particle, which passes through two slits simultaneously, does not have a definite position before it gets measured on the screen. If the assumption of realism is abandoned, the measured and unmeasured particle in this example are simply *different objects* [7]. One may still take the view that a microscopic system (electron, photon, proton etc.) is governed by different physical laws than a macroscopic system: An electron, for example, is so far away form our everyday perception, it may seem plausibel that our common sense cannot be applied to it. But what is about a macroscopic object like a cat in Schrödinger's famous gedanken experiment, where quantum mechanics predicts a superposition of the cat in "dead" and "alive" state [8]?

Decoherence theory delivers a quantum mechanical description of the emergence of classical dynamics [9–11]. This theory is based on the concept of *open quantum dynamics*, that is, a considered quantum system is in permanent contact with an environment. In the example of Schrödinger's paradox, the cat interacts with environmental gas particles, emits thermal radiation etc. These couplings to the environment leads to a rapid loss of coherence, i.e. *decoherence*, of this macroscopic object and restore the classical dynamics. However, this theory still assumes the unitary dynamics of the total quantum system. That means that a considered system follows the law of quantum mechanics if it is perfectly isolated from the environment. One can argue that a macroscopic object is never perfectly isolated. But what is for example about a dust particle or even a comet floating perfectly isolated in the Universe? Could they exist in a quantum superposition? Is our assumption of macro-realism simply wrong?

Some theories predict a spontaneous localization of a wave function (*collapse of the wave function*) beyond a certain mass scale so that the macro-realism is recovered. One of these collapse theories, the *Schrödinger-Newton equation*, modifies the Schrödinger equation to include self-gravity [12–14]. The gravitational self-interaction creates an additional nonlinear term in the Schrödinger equation, which becomes noticeable for a large mass. A numerical evaluation of this equation shows that the effect of this additional term becomes observable, if for example a particle of mass 10^{10} amu is in a superposition of positions separated by about $2\,\mu m$ [15]. However, this model implies conceptional problems like superluminal communication [16] and its validity is still controversially discussed. Another prominent collapse theory is the *CSL (continuous spontaneous localization)* model. This model is based on the modification of the Schrödinger equation with an additional non-linear stochastic term [17]. The strength of the spontaneous collapse of the wave function is predicted to be directly proportional to the mass squared [18].

A matter-wave interferometer with a high-mass interfering particle provides a possibility for a direct verification of the particle's wave nature. Beginning with the demonstration of far-field interference of C_{60} [19], the quantum nature of molecules with increasing masses tested both in far-field [20] and in near-field interferometers [21–25]. The currently most massive interfering molecule has a mass exceeding $10,000$ amu, and consists of 810 atoms in total [26]. In the future, high-mass interferometers could

give the answer to the question, whether there is a boundary between a quantum and macroscopic world, or not [27].

The theoretical groundwork for high-mass matter-wave interferometry, as developed in [21, 28–33], involves the interaction of a delocalized particle with material gratings as well as with optical gratings. So far, the theoretical description between a light and a delocalized molecule was based on two phenomenological parameters, the molecular polarizability and the photon absorption cross section, and this description was verified by several experiments [19, 23, 25, 32, 34]. However, a strong laser field will lead to the population of the molecular triplet excited state, which can exhibit different optical internal properties, and can trigger fluorescence [35, 36]. These internal molecular photophysical processes are expected to affect significantly the matter-wave interference, which serves as a motivation to consider the first topic of the present thesis:

- **Interaction between a delocalized molecular matter-wave with an optical grating.** Here I present a transformation of the molecular center-of-mass state by an optical grating including several relevant internal photophysical processes. The optical properties of the molecular triplet state are shown to have a significant effect on matter-wave interference if the laser power of the optical grating is sufficiently high. This result can be used for a measurement of vacuum optical properties of a triplet excited molecule.

Decoherence due to environmental influences plays an essential role in matter-wave interferometry. It explains the emergence of classical dynamics and can predict the possible limit of interference in a matter-wave interferometer. The description of decoherence due to the thermal radiation of a hot molecule and collisional decoherence with environmental gas particles are presented in [37, 38] and [28, 39, 40], respectively. Especially, collisions with environmental gas particles are omnipresent and are the most significant source of decoherence. In general, the quantum dynamics of a particle in a gaseous environment follows *the quantum linear Boltzmann equation* [41, 42]. The description so far, however, is restricted to a spherical scattering potential. Because large organic molecules are predominantly polar and the scattering potential is thus non-spherical, it is intriguing to ask how the polarity affects the collisional decoherence. This motivates the second topic of this thesis:

- **Collisional decoherence of a polar molecule due to scattering with environmental gas atoms.** The collisional decoherence is described in terms of the total and the differential scattering cross section, which are a function of the molecular orientation in the case of nonspherical scattering potential. The polarity of a molecule is shown to have significant effect on scattering. That is, the permanent dipole moment of the molecule can be measured, in principle, by examining the total and differential cross section as shown in Chapter 5. I present an approximate analytical expression of the *decoherence function*, which describes decoherence due to a single scattering event. The result is compared with the numerical calculation, which shows a good agreement.

The results relating to these two main subjects are published in [43–45]. The present thesis is structured as follows.

In **Chapter 2**, I discuss the quantum motion of the molecular center of mass in two types of interferometers: A far-field interferometer and near-field Talbot-Lau interferometer. Here, the *Wigner function* is introduced for the description of the phase-space dynamics of a molecule, which provides us with an intuitive picture of the quantum motion [46]. In the framework of the Wigner representation, the essential concepts of *spatial* and *longitudinal coherence* of a quantum state are discussed, which represent a measure of the interference capability of a particle [47]. This chapter serves as a recapitulation of the molecular center-of-mass dynamic in interferometers, as developed previously in Ref. [28, 29, 31, 33, 47]. It contains no new material but is required as a reference for the rest of the thesis.

Chapter 3 deals with the interaction between a complex molecule and light. The theoretical description involves two essential phenomena: The dipole interaction and photon absorption. Unlike an atom, complex molecules can absorb many photons without subsequent re-emission, which leads to the stepwise increase of its internal temperature. It is an intriguing question whether a molecule is capable to interfere after absorption of photons, or whether "which way" information is revealed by absorptions. It is shown with the help of interferometers that molecules can still interfere even after many absorptions of laser photons. The absorption of photons ignites numerous photophysical processes in molecules, e.g. photo-excitation, fluorescence, phosphoresce etc. I discuss in this chapter especially the effect of the excitation of a molecule to the long-lived triplet state [35], which can change internal molecular properties. The theoretical developments reported in this chapter found an agreement with a matter-wave experiment with C_{70} [44], published also in Ref. [45].

The effect of fluorescence is examined in **Chapter 4**. Here, one expects decoherence, i.e. a reduction of the molecular spatial coherence, to occur because an emission of a fluorescence photon implies the transfer of momentum. In other words, the fluorescence photon reveals "which way" information about the molecule. Today, fluorescence finds wide applications in physics, chemistry and biology, e.g. in a STED microscope [48], which was awarded with the Nobel prise in 2014, or the detection of single molecules [49]. However, the effect of fluorescence on the molecular center-of-mass state seems to be still unexplored, which makes the interferometric examination of fluorescence interesting. Here, one expects a reduction of the molecular spatial coherence, as known from atom interferometry [50].

In **Chapter 5**, I discuss collisions between a polar molecule and environmental gas atoms, and their effect on the molecular center-of-mass state (*collisional decoherence*). Such scattering is expected to lead to more pronounced decoherence than fluorescence because the transfered momentum can be larger by orders of magnitude. Because of polarity, the interaction potential is anisotropic, which complicates the theoretical description. Based on the assumption of a large molecular mass and a slow rotation compared to the collision time, I present an analytical expression for results of the master equation describing the molecular center-of-mass motion through a gaseous

environment. Here, I make use of the *monitoring approach* for the derivation of the master equation [41, 51]. The results in this chapter are published in Ref. [43].

As an application of the results in previous chapters, I consider far-field and near-field interferometers in **Chapter 6**. Beside the well known far-field interferometer [19, 52], two interferometers based on the Talbot-Lau scheme are treated: the *Kapitza-Dirac-Talbot-Lau interferometer (KDTLI)* [23, 31] and the *optical time-domain matter-wave (OTIMA)* interferometer [24, 32]. These near-field interferometers are optimized for the interference of large particles and play a central role in high-mass matter-wave interferometry. With the help of these interferometers, I discuss the effect of photon absorption, molecular excitation, fluorescence and collisional decoherence.

Finally, I conclude this thesis and give a short outlook in **Chapter 7**.

2

PHASE-SPACE DESCRIPTION OF THE MOLECULAR CENTER-OF-MASS MOTION

An important ingredient of the present thesis is the description of a particle's motional state in a matter-wave interferometer, which includes the free propagation and the interaction with interferometer components and with various environments. In this chapter, the Wigner representation of quantum mechanics in phase space is reviewed, which is an important tool to describe a quantum motional state [28, 29, 46]. This phase-space representation implicates some essential advantages. First, a quantum motional state is represented by a real-valued distribution function in phase space, instead of the rather abstract density operator in Hilbert space quantum mechanics [53]. This distribution function provides us with an intuitive picture of quantum mechanical phenomena. Second, in this representation it is possible to compare classical and quantum mechanical predictions directly in terms of the phase-space distribution. This fact is especially important in a near-field interferometer, where interference patterns must be distinguished from a possible classical shadow effect (moiré pattern) [28, 31, 54]. Finally, as discussed in Part II of this thesis, the effect of decoherence can be included intuitively and elegantly in the Wigner representation.

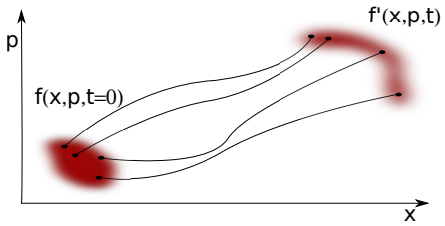

Figure 2: Schematic illustration of the classical phase-space dynamics of the center-of-mass motion in one dimension. An initial phase space distribution $f_0(x,p)$ evolves to the state $f_t(x,p)$ obeying the Liouville equation.

From the classical point of view, a point particle is characterized by its momentum **P** and its center-of-mass position **R**, which correspond to a point in phase space, and its motion is represented by a trajectory, as depicted for the one dimensional case in Fig. 2. The motion of a statistical ensemble of classical particles is governed by the Liouville equation, which describes shifts and deformations of an initial phase-space distribution $f_0(x,p)$ [55]. Quantum mechanics, however, is a statistical theory even for a single particle and a motional state can no longer be described by a point in phase space because of Heisenberg's uncertainty principle. Thus, the concept of the classical trajectory loses its meaning. On the other hand, the mean position and momentum fol-

low the classical equations of motion, $\langle\dot{\mathbf{R}}\rangle = \langle\mathbf{P}\rangle/m$ and $\langle\dot{\mathbf{P}}\rangle = -\nabla_{\mathbf{R}} V(\langle\mathbf{R}\rangle)$, provided the potential $V(\mathbf{R})$ contains only terms up to second order in position $\mathbf{R}$ [56]. This fact indicates a possibility to formulate quantum mechanics in terms of a distribution function in phase space analogous to classical mechanics.

The first phase-space representation of quantum mechanics was discovered by Wigner [57] and generalized by Moyal [58]. Here, a quantum motional state is characterized by a real-valued distribution function, the Wigner function $W(\mathbf{R}, \mathbf{P})$. Since then, a number of different phase-space representations were discovered, for instance the Glauber-P-function [59], the Husimi-Kano Q-funciton [60] and full counting statistics (FCS) [61]. However, these representations are optimized for the quantized electromagnetic field [46] or for quantum transport [62]. The Wigner representation is still most appropriate to describe a mechanical state.

Phase-space dynamics of the Wigner function in interferometers are already discussed in various papers in detail [28, 29, 31, 47]. The aim in this chapter is to give an overview of the Wigner formalism and discuss the interference effect both in the far- and near-field regime. I begin in Sect. 2.1 with the preparation of a coherent matter-wave beam, which is a requisite for all matter-wave experiments. In Sect. 2.2 and 2.3, I shortly review the Wigner function and its dynamics in phase space. The characteristic function associated to the Wigner function is introduced in Sect. 2.4, which will be useful in further calculations. In Sect. 2.5, I consider the interaction between particles and different interferometric components: a material collimator, a material grating, and an optical pure phase grating. Finally in Sect. 2.6, the particle's density distribution is calculated for both a far-field interferometer and a near-field Talbot-Lau interferometer.

2.1 PREPARATION OF A COHERENT MATTER-WAVE BEAM

A matter-wave interferometer consists of a beam source, interferometric components (collimators and gratings) and a detector, see Fig. 3. First of all, the initially incoherent beam must be prepared so that the interference at a diffraction grating is possible. This involves the transversal (x-axis, the grating direction) delocalization of a interfering particle in front of the diffraction grating, which is illustrated as a superposition of two center-of-mas position of a molecule in Fig. 3. The length scale of the delocalization is referred to as the *transversal coherence length* and is connected directly with an interference condition: For interference to occur, at least two neighboring openings of a grating must be illuminated coherently, that is, the coherence length must be at least as large as the grating period d. The coherence length may be defined by means of the non-diagonal elements of the density operator $\rho(-s/2, s/2)$ as discussed in Sect. 2.5.3. A beam of particles is created often by a thermal source (e.g. laser evaporation, thermal sublimation or supersonic expansion of a gas into vacuum [63]) and thus, their transversal coherence is initially on the order of the thermal de Broglie wavelength λ_{th} [64]. Assuming the Maxwell-Boltzmann distribution for a temperature of $T = 1000$ K

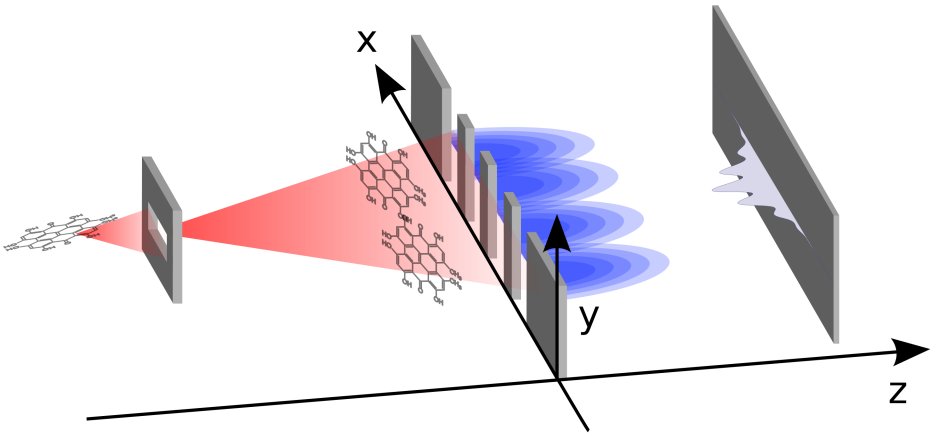

Figure 3: A typical setup for matter-wave interference. For the preparation of a coherent beam, molecules are collimated in both x- and y- direction. Interference occurs if the coherence length of the molecular beam is larger than the distance of two neighboring slits of a diffraction grating. As an example of a interfering particle, the Hypericin ($C_{30}H_{16}O_8$) is depicted in this figure.

and molecular mass of $m = 1000$ amu, this wavelength is $\lambda_{\text{th}} = h/\sqrt{2\pi m k_B T} \approx 1.7$ pm. Thus, the thermal beam is initially too incoherent for interference experiments.

A possible way to prepare the transverse coherence is to collimate a beam e.g. by a material slit of width D_c in x-direction. The collimation and the subsequent free propagation over a distance L in z-direction create a transverse coherence of about $W_c = L\lambda_{\text{dB}}/D_c$, see Sect. 2.5.3. The interference condition is then given by $L\lambda_{\text{dB}}/D_c \gtrsim 2d$. For typical values $d = 100$ nm, $D_c = 5$ μm and $\lambda_{\text{dB}} = 2$ pm, the collimation condition is $L \gtrsim 0.6$ m. In practice, all particles experience the same grating potent irrespective of their y-positon because of an additional collimation in y-direction and the velocity selection.

The spread of the longitudinal momentum of particles Δp_z plays also an important role in the interferometer, because it leads to the smearing of the velocity-dependent interferogram. Defining the *longitudinal coherence length* $L_c = \lambda_{\text{dB}} p_z/\Delta p_z$, which is a measure of the spectral purity of a beam source [65], the condition for a far-field interferometers is $L_c \gtrsim 2\lambda_{\text{dB}}$, as discussed in Sect. 2.6.1. In general, for N-th order interference a longitudinal coherence length of $N\lambda_{\text{dB}}$ is required [47]. For the preparation of longitudinal coherence velocity selectors are used, which serve to decrease the momentum spread Δp_z.

A good collimation of a matter-wave beam, which is a requisite for all matter-wave experiments, admits an important simplification of the Schrödinger equation for the free propagation. It reads

$$E\psi(\mathbf{R}) = -\frac{\hbar^2}{2M}\left(\frac{\partial^2}{\partial x^2} + \frac{\partial^2}{\partial y^2} + \frac{\partial^2}{\partial z^2}\right)\psi(\mathbf{R}) \tag{2.1}$$

with the particle's mass M, kinetic energy E and center-of-mass position $\mathbf{R} = (x, y, z)$. A solution of this differential equation is

$$\psi(\mathbf{R}) = \psi_0 \frac{\exp\left[\mathrm{i}|\mathbf{P}||\mathbf{R}|/\hbar\right]}{|\mathbf{R}|}, \tag{2.2}$$

which correspond to the wave emitted by a point source at the coordinate origin with the momentum $\mathbf{P}$. If a matter-wave beam is well collimated both in x- and y-direction, this solution may be expanded to leading order in terms of $x/z \ll 1$ and $y/z \ll 1$,

$$\begin{aligned} \psi(\mathbf{R}) &= \psi_0 \frac{\mathrm{e}^{\mathrm{i}p_z z/\hbar}}{z} \exp\left[\mathrm{i}\frac{p_z\left(x^2+y^2\right)}{2\hbar z}\right] + \mathcal{O}\left(\frac{x^2+y^2}{z^2}\right) \\ &= \varphi(x,y,z)\mathrm{e}^{\mathrm{i}p_z z/\hbar} + \mathcal{O}\left(\frac{x^2+y^2}{z^2}\right). \end{aligned} \tag{2.3}$$

This approximation is referred to as the *paraxial approximation*. Inserting this approximated solution into (2.1) and neglecting the term $\partial^2\varphi/\partial z^2$, which is of the order of $\mathcal{O}([x^2+y^2]/z^2)$, the Schrödinger equation takes the form

$$\mathrm{i}\hbar v_z \frac{\partial\varphi(x,y,z)}{\partial z} = -\frac{\hbar^2}{2M}\left(\frac{\partial^2}{\partial x^2} + \frac{\partial^2}{\partial y^2}\right)\varphi(x,y,z). \tag{2.4}$$

That is, the 3D stationary Schrödinger equation (2.1) in this limit corresponds to the dynamical 2D Schrödinger equation with the time $t = z/v_z$. In addition, a typical matter-wave experiment is configured so that all particles experience the same grating potential irrespective of their y-positions. Because of this translation invariance the particle's motion may be treated effectively in one dimension.

The motion of a pure quantum state is described by Eq. (2.4) in terms of the wave function. However, in order to incorporate dynamics of a statistical mixture of quantum states, one must apply the density operator $\rho = \sum_j p_j \left|\psi_j\right\rangle\left\langle\psi_j\right|$, where the ensemble is in a state $\left|\psi_j\right\rangle$ with a probability p_j. In the position representation, the non-diagonal elements of the density operator $\left\langle x_1\right|\rho\left|x_2\right\rangle \equiv \rho(x_1, x_2)$ with $x_1 \neq x_2$ represents a measure of correlation between two different positions, i.e. coherence of the state. The diagonal elements $\rho(x, x)$ in contrast gives the spatial distribution of particles. The temporal evolution of the density matrix is given by the von Neumann equation $\partial_t\rho = [\mathsf{H}, \rho]/\mathrm{i}\hbar$ with the Hamilton operator H [56].

Due to some advantages, however, I make use of the phase space description of quantum mechanics, where a state is represented by the Wigner function. In the following section, I give a short review on the Wigner function for the one-dimensional transversal motion of particles.

2.2 WIGNER FUNCTION

In order to formulate quantum mechanics in phase space, one must find an one-to-one map of the density operator ρ to a distribution function $W(x, p)$. For simplicity, I consider the two-dimensional phase space spanned by the position x and the momentum

p. However, the generalization to higher dimensions is straightforward. The distribution function $W(x,p)$ is supposed to fulfill the following axioms for a *quasi-probability distribution function* [46]

$$\int_{\mathbb{R}} \mathrm{d}x\, W(x,p) = w(p), \tag{2.5}$$

$$\int_{\mathbb{R}} \mathrm{d}p\, W(x,p) = w(x), \tag{2.6}$$

$$\int_{\mathbb{R}}\int_{\mathbb{R}} \mathrm{d}x\mathrm{d}p\, W(x,p) = 1. \tag{2.7}$$

Here $w(x) = \langle x\,|\,\rho\,|\,x\rangle$ and $w(p) = \langle p\,|\,\rho\,|\,p\rangle$ are the position and momentum distribution of the quantum state, respectively. Note that a classical distribution function $f(x,p)$ fulfills beside the conditions (2.5)-(2.7) also the positivity condition $f(x,p) \geq 0$. As we will see later in this section, $W(x,p)$ can take negative values, which turns out to highlight the nonclassical features of the state. The conditions (2.5) and (2.6) define the connection between ρ and the sought-after density distribution $W(x,p)$ in terms of position representation. The momentum distribution reads

$$\begin{aligned} w(p) &= \langle p\,|\,\rho\,|\,p\rangle \\ &= \frac{1}{2\pi\hbar}\int_{\mathbb{R}}\int_{\mathbb{R}} \mathrm{d}x\mathrm{d}x'\, \mathrm{e}^{-\mathrm{i}p(x-x')/\hbar}\,\langle x\,|\,\rho\,|\,x'\rangle\,. \end{aligned} \tag{2.8}$$

By means of the transformation $x \to x - s/2$ and $x' \to x + s/2$, Eq. (2.8) is converted to a form

$$w(p) = \frac{1}{2\pi\hbar}\int_{\mathbb{R}} \mathrm{d}x \int_{\mathbb{R}} \mathrm{d}s\, \mathrm{e}^{\mathrm{i}ps/\hbar}\left\langle x - \frac{s}{2}\,\middle|\,\rho\,\middle|\, x + \frac{s}{2}\right\rangle. \tag{2.9}$$

From this expression and Eq. (2.5), one finds a definition of the density distribution

$$W(x,p) = \frac{1}{2\pi\hbar}\int_{\mathbb{R}} \mathrm{d}s\, \mathrm{e}^{\mathrm{i}ps/\hbar}\left\langle x - \frac{s}{2}\,\middle|\,\rho\,\middle|\, x + \frac{s}{2}\right\rangle. \tag{2.10}$$

This expression gives the definition of the *Wigner function* in terms of the density operator in the position representation, which is first introduced by Eugene Wigner in 1934 [57]. Inserting $\mathbb{I} = \int_{\mathbb{R}} \mathrm{d}p_{1,2}\,|p_{1,2}\rangle\,\langle p_{1,2}|$ into (2.10), one obtains

$$W(x,p) = \frac{1}{(2\pi\hbar)^2}\int_{\mathbb{R}} \mathrm{d}p_1 \int_{\mathbb{R}} \mathrm{d}p_2\, \mathrm{e}^{\mathrm{i}x(p_1-p_2)/\hbar}\,\langle p_1\,|\,\rho\,|\,p_2\rangle \int_{\mathbb{R}} \mathrm{d}s\, \mathrm{e}^{\mathrm{i}s(p-p_1/2-p_2/2)/\hbar}.$$

By means of the transformation $p_1 \to p - q/2$ and $p_2 \to p + q/2$, one finds an equivalent expression for the Wigner function, which is defined in terms of the density operator in the momentum representation

$$W(x,p) = \frac{1}{2\pi\hbar}\int_{\mathbb{R}} \mathrm{d}q\, \mathrm{e}^{-\mathrm{i}xq/\hbar}\left\langle p - \frac{q}{2}\,\middle|\,\rho\,\middle|\, p + \frac{q}{2}\right\rangle. \tag{2.11}$$

Because of the hermiticity of the density operator, the Wigner function is always real valued. For the illustration of important properties of the Wigner function, let us

examine a superposition of two plane waves $|\psi\rangle = (|p_1\rangle + |p_2\rangle)/\sqrt{2}$. Inserting the density matrix $\rho = |\psi\rangle\langle\psi|$ in Eq. (2.11), one gets

$$W(x,p) = \frac{1}{2\pi\hbar}\left[\frac{1}{2}\delta(p-p_1) + \frac{1}{2}\delta(p-p_2) + \delta\left(p - \frac{p_1+p_2}{2}\right)\cos\left(\frac{x}{\hbar}(p_1-p_2)\right)\right]. \tag{2.12}$$

The Wigner function consists of two localized distributions at $p = p_1$ and p_2, whose width in the x-direction is infinite reflecting the uncertainty principle. The third term in Eq. (2.12) would be absent in a mixture $\rho = 1/2\,|p_1\rangle\langle p_1| + 1/2\,|p_2\rangle\langle p_2|$ and therefore describes the coherence between the two momentum states. It shows an oscillating behavior and takes also negative values. As become clear in this simple example, negative parts of the Wigner function indicate the presence of quantum coherence.

Moreover, the phase-space area occupied by the Wigner function can not be arbitrary small to accommodate the uncertainty principle. A measure of the occupied phase-space area A can be defined in terms of the phase-space integral over the square of the Wigner function [46],

$$A = \left[\int_{\mathbb{R}}\int_{\mathbb{R}} \mathrm{d}x\mathrm{d}p\, W^2(x,p)\right]^{-1}. \tag{2.13}$$

After some calculations, the phase-space integral can be expressed by a trace over the square of the density operator,

$$\begin{aligned}
\int_{\mathbb{R}}\int_{\mathbb{R}} \mathrm{d}x\mathrm{d}p\, W^2(x,p) &= \frac{1}{(2\pi\hbar)^2}\int_{\mathbb{R}}\mathrm{d}x\int_{\mathbb{R}}\mathrm{d}s_1\left\langle x-\frac{s_1}{2}\middle|\rho\middle|x+\frac{s_1}{2}\right\rangle \\
&\quad\times\int_{\mathbb{R}}\mathrm{d}s_2\left\langle x-\frac{s_2}{2}\middle|\rho\middle|x+\frac{s_2}{2}\right\rangle\int_{\mathbb{R}}\mathrm{d}p\,\mathrm{e}^{\mathrm{i}p(s_1+s_2)/\hbar} \\
&= \frac{1}{2\pi\hbar}\int_{\mathbb{R}}\int_{\mathbb{R}}\mathrm{d}x\mathrm{d}s_1\left\langle x-\frac{s_1}{2}\middle|\rho\middle|x+\frac{s_1}{2}\right\rangle\left\langle x+\frac{s_1}{2}\middle|\rho\middle|x-\frac{s_1}{2}\right\rangle \\
&= \frac{1}{2\pi\hbar}\mathrm{Tr}\left[\rho^2\right].
\end{aligned} \tag{2.14}$$

In the first line of this calculation I make use of the delta function $\delta(x) = \int \mathrm{d}p\ \mathrm{e}^{\mathrm{i}xp}/2\pi$. Because the right side of the Eq. (2.14) is bounded by $\mathrm{Tr}\left[\rho^2\right] \leq 1$ [56], where $\mathrm{Tr}\left[\rho^2\right] = 1$ applies only for a pure state, the phase-pace area is limited by

$$A \geq 2\pi\hbar. \tag{2.15}$$

That is, the phase-space area occupied by a Wigner function takes the minimal value of $2\pi\hbar$ for a pure state.

2.3 FREE PROPAGATION AND GRATING TRANSFORMATION OF THE WIGNER FUNCTION

The coherent dynamics of the density operator ρ is described by the von Neumann equation

$$\partial_t\rho = \frac{1}{\mathrm{i}\hbar}\left[\frac{\mathrm{p}^2}{2m} + \mathrm{V}(\mathrm{x};t), \rho\right], \tag{2.16}$$

where p is the momentum operator, m is the mass of a particle and $\mathsf{V}(\mathsf{x};t)$ is the potential that is diagonal in position and depends explicitly on time t. Evaluating the matrix elements $\langle x - s/2 \,|\, \partial_t \rho \,|\, x + s/2 \rangle$, the corresponding dynamic equation for the Wigner function can be derived [46]

$$\left(\frac{\partial}{\partial t} + \frac{p}{m}\frac{\partial}{\partial x} - \frac{\partial V(x;t)}{\partial x}\frac{\partial}{\partial p} \right) W_t(x,p) = \sum_{\ell=1}^{\infty} \frac{(-1)^\ell (\hbar/2)^{2\ell}}{(2\ell+1)!} \frac{\partial^{2\ell+1} V(x;t)}{\partial x^{2\ell+1}} \frac{\partial^{2\ell+1}}{\partial p^{2\ell+1}} W_t(x,p), \tag{2.17}$$

where I write the time dependence of the Wigner function in the subscript in order to shorten the notation. This Equation (2.17) is referred to as the *quantum Liouville equation*, where the right side of the equation represents the quantum modification of the classical Liouville equation. In the formal classical limit $\hbar \to 0$, assuming that the Wigner function does not depend on $\hbar$ in this limit, the quantum correction vanishes and the classical Liouville equation is recovered. Interestingly, this correction vanishes also for finite $\hbar$ if $\partial_x^{2\ell+1} V(x;t) = 0$ for $\ell \geq 1$. That is, classical and quantum mechanics yield the same dynamics of a phase-space density if the potential depends at most harmonically on x.

For the free propagation $V(x;t) = 0$, the solution of Eq. (2.17) is therefore given in terms of the shearing transformation analogous to classical mechanics [55],

$$W_t(x,p) = W_0(x - pt/m, p). \tag{2.18}$$

For the description of matter-wave interferometers, it is essential to examine the interaction between particles and components of an interferometer such as collimators and gratings. In the presence of a potential $V(x;t) \neq 0$, however, the general solution of the quantum Liouville equation is much more complicated. Fortunately, in a typical matter-wave experiment, the interaction time Δt is very short. If both the shift due to the free propagation $p\Delta t/m \ll a$ and the deflection due to the potential $\sqrt{2|V|/m}\Delta t \ll a$ is small compared to the characteristic length scale of the potential a, the position derivative of the Wigner function in Eq. (2.17) becomes redundant and may be neglected,

$$\frac{\partial}{\partial t} W_t(x,p) = \sum_{\ell=0}^{\infty} \frac{(-1)^\ell (\hbar/2)^{2\ell}}{(2\ell+1)!} \frac{\partial^{2\ell+1} V(x;t)}{\partial x^{2\ell+1}} \frac{\partial^{2\ell+1}}{\partial p^{2\ell+1}} W_t(x,p).$$

This procedure is referred to as the *eikonal approximation* [29].

This equation can be solved by means of the Fourier transform, which allows replacing the momentum derivative ∂_p by $\mathrm{i}s/\hbar$,

$$\begin{aligned} &\frac{\partial}{\partial t} \int_{\mathbb{R}} \mathrm{d}p \, \mathrm{e}^{-\mathrm{i}ps/\hbar} W_t(x,p) \\ &\quad = \sum_{\ell=0}^{\infty} \frac{(-1)^\ell (\hbar/2)^{2\ell}}{(2\ell+1)!} \frac{\partial^{2\ell+1} V(x,t)}{\partial x^{2\ell+1}} \left(\mathrm{i}\frac{s}{\hbar}\right)^{2\ell+1} \int_{\mathbb{R}} \mathrm{d}p \, \mathrm{e}^{-\mathrm{i}ps/\hbar} W_t(x,p) \\ &\quad = \frac{\mathrm{i}}{\hbar} \left[V\left(x + \frac{s}{2}; t\right) - V\left(x - \frac{s}{2}; t\right) \right] \int_{\mathbb{R}} \mathrm{d}p \, \mathrm{e}^{-\mathrm{i}ps/\hbar} W_t(x,p). \end{aligned} \tag{2.19}$$

In the second line of the calculation, I identified the sum as the Taylor expansion of $V(x+s/2;t) - V(x-s/2;t)$. The solution of (2.19) can be expressed in terms of a convolution

$$W_{t_0+\Delta t}(x,p) = \int_{\mathbb{R}} \mathrm{d}p_0 W_{t_0}(x,p_0) T_{\mathrm{W}}(x,p-p_0), \tag{2.20}$$

where t_0 is the starting time of the interaction. The convolution kernel is given by [28]

$$T_{\mathrm{W}}(x,p) = \frac{1}{2\pi\hbar}\int_{\mathbb{R}} \mathrm{d}s\, \exp\left[\mathrm{i}\frac{ps}{\hbar} + \mathrm{i}\phi\left(x-\frac{s}{2}\right) - \mathrm{i}\phi\left(x+\frac{s}{2}\right)\right], \tag{2.21}$$

with the *eikonal phase* $\phi(x)$ defined by the time integral over the potential

$$\phi(x) = -\frac{1}{\hbar}\int_{t_0}^{t_0+\Delta t} \mathrm{d}t\, V(x;t). \tag{2.22}$$

This result corresponds to a transformation of the density matrix $\rho \to \mathsf{U}\rho\mathsf{U}^\dagger$ with the unitary operator $\mathsf{U} = \exp(\mathrm{i}\phi(\mathsf{x}))$.

If the potential is periodic in position with the period d, as is the case for a grating potential, the convolution kernel (2.21) can be expanded as a Fourier series,

$$T_{\mathrm{W}}(x,p) = \frac{1}{2\pi\hbar}\sum_{n\in\mathbb{Z}} \exp\left(\mathrm{i}\frac{2\pi x}{d}n\right)\int_{\mathbb{R}} \mathrm{d}s\, \mathrm{e}^{\mathrm{i}ps/\hbar} B_n\left(\frac{s}{d}\right) \tag{2.23}$$

with the Fourier coefficients

$$B_n(\xi) = \frac{1}{d}\int_{-d/2}^{d/2} \mathrm{d}x\, \exp\left[-\mathrm{i}\frac{2\pi x}{d}n + \mathrm{i}\phi\left(x-d\frac{\xi}{2}\right) - \mathrm{i}\phi\left(x+d\frac{\xi}{2}\right)\right]. \tag{2.24}$$

These coefficients are referred to as the *Talbot coefficients*, which play a central role in matter-wave interferometry. Because of the periodic potential, the Talbot coefficients $B_n(\xi)$ are again periodic in the argument ξ with the period 2.

As shown in Eq. (2.20), the diffraction of a matter wave by a potential can be described in the eikonal approximation by a convolution. It turns out that the calculation is more simple and elegant in the Fourier space, where the convolution turns into a simple multiplication according to the convolution theorem. The Fourier transform of the Wigner function, the *characteristic function*, is treated in the next section.

2.4 CHARACTERISTIC FUNCTION REPRESENTATION

Analogous to the case of classical probability theory, the characteristic function of the Wigner function is defined as the two-dimensional Fourier transform

$$\chi_t(s,q) = \int_{\mathbb{R}}\int_{\mathbb{R}} \mathrm{d}x\mathrm{d}p\, \mathrm{e}^{\mathrm{i}(qx-ps)/\hbar} W_t(x,p). \tag{2.25}$$

The position and the momentum distribution are given in terms of the characteristic function by

$$w(x) = \frac{1}{2\pi\hbar}\int_{\mathbb{R}} \mathrm{d}q\, \mathrm{e}^{-\mathrm{i}qx/\hbar}\chi_t(0,q), \tag{2.26}$$

$$w(p) = \frac{1}{2\pi\hbar}\int_{\mathbb{R}} \mathrm{d}s\, \mathrm{e}^{\mathrm{i}ps/\hbar}\chi_t(s,0). \tag{2.27}$$

Normalization of the Wigner function (2.7) leads to a corresponding condition for the characteristic function

$$\chi_t(0,0) = 1. \tag{2.28}$$

In the characteristic representation, s and q have the dimension of position and momentum, respectively. The free propagation is represented by a shearing transformation analogous to the Wigner function,

$$\chi_t(s,q) = \int_{\mathbb{R}}\int_{\mathbb{R}} \mathrm{d}x\mathrm{d}p\, \mathrm{e}^{\mathrm{i}(qx-ps)/\hbar}W_0(x-pt/m,p) = \chi_0(s-qt/m,q).$$

The eikonal solution in the presence of an interaction potential (2.20) reads

$$\chi_{t_0+\Delta t}(s,q) = \int_{\mathbb{R}} \mathrm{d}q_0\, \chi_{t_0}(s,q_0)T_\chi(s,q-q_0), \tag{2.29}$$

where the convolution kernel is given by

$$T_\chi(s,q) = \frac{1}{2\pi\hbar}\int_{\mathbb{R}} \mathrm{d}x\ \exp\left[\mathrm{i}\frac{qx}{\hbar} + \mathrm{i}\phi\left(x-\frac{s}{2}\right) - \mathrm{i}\phi\left(x+\frac{s}{2}\right)\right]. \tag{2.30}$$

The characteristic function provides some conveniences for describing quantum phase-space dynamics in an interferometer. First, the transformation due to a periodic grating has a simple and intuitive form. By means of the Talbot coefficients $B_n(s/d)$ (2.24), the grating transformation reads

$$\chi_{t_0+\Delta t}(s,q) = \sum_{n\in\mathbb{Z}} B_n\left(\frac{s}{d}\right)\chi_t\left(s, q+\frac{2\pi\hbar}{d}n\right). \tag{2.31}$$

The effect of the grating transformation becomes apparent in this representation: it describes transfers of the grating momentum $2\pi\hbar/d$. The n-th Talbot coefficient $B_n(s/d)$ is then closely related to the probability for the transfer of the n-fold grating momentum. For example, a momentum state $|p\rangle$ turns into a superposition of "kicked" states $|p+2\pi\hbar n/d\rangle$ after the interaction with a pure phase grating, as illustrated in Fig. 4. Second, including the effect of decoherence is much simpler in this representation, as discussed in Part II of this thesis. Because of these advantages, the characteristic function representation is used throughout this thesis.

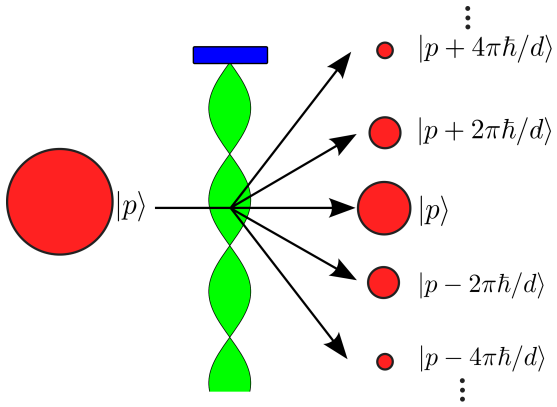

Figure 4: Schematic illustration of transfers of grating momenta in a pure phase grating. The initial momentum eigenstate $|p\rangle$ turns into superposition of different momentum states $|p + 2\pi\hbar n/d\rangle$ after the interaction.

2.5 CALCULATION OF THE CONVOLUTION KERNEL AND THE TALBOT COEFFICIENTS

As shown in the previous section, the calculation of the Talbot coefficients is the central task in describing a matter-wave interferometer. In this section, I consider three elements of a typical matter-wave interferometer: an optical pure phase grating, a material grating and a collimator. The convolution kernel for the collimator and the Talbot coefficients for the gratings are calculated explicitly.

2.5.1 *Optical pure phase grating*

In this section, an idealized optical grating is treated, where the possibility of photon absorptions is neglected. A detailed analysis of the interaction incorporating photon absorptions is given in Chapter 3. Results in this section will be used for the discussion of interference effects in Sect. 2.6.

For an optical pure phase grating, the eikonal phase is given by $\phi(x) = \phi_0 \cos^2(\pi x/d)$, see Chapter 3. Evaluating Eq. (2.24) with this eikonal phase yields the Talbot coefficients

$$B_n\left(\frac{s}{d}\right) = J_n\left[\phi_0 \sin\left(\frac{\pi s}{d}\right)\right], \tag{2.32}$$

where J_n is the Bessel function of the first kind. As discussed in Sect. 2.4, the n-th Talbot coefficient $B_n(s/d)$ is closely related to the probability for the transfer of the n-fold grating momentum $2\pi\hbar n/d$. The Bessel function vanishes rapidly $J_n(\phi_0) \sim (e\phi_0/2n)^n/\sqrt{2\pi n}$ as $n \to \infty$ [66]. That is, one can estimate the maximal number of the transfered momentum N_f to

$$N_f \sim \frac{e}{2}\phi_0. \tag{2.33}$$

For the typical value of $\phi_0 = \pi$, an optical grating transfers no more than 4 grating momenta to the particles according to this estimate.

2.5.2 *Material grating*

For the description of a realistic material grating two effects must be included: the projection of a particle's density distribution and the dispersive interaction between particles and grating walls. Assuming that particles are absorbed and thus removed from the beam if they collide against the grating walls, the grating transformation of the density operator is given by

$$\rho \to t_{\mathrm{g}}(\mathrm{x})\mathrm{e}^{\mathrm{i}\phi(\mathrm{x})}\rho t_{\mathrm{g}}(\mathrm{x})\mathrm{e}^{-\mathrm{i}\phi(\mathrm{x})}, \tag{2.34}$$

where $t_{\mathrm{g}}(x) = \sum_{n\in\mathbb{Z}} \Theta(D_{\mathrm{g}}/2 - |x + nd|)$ is the transmission function with the Heaviside function Θ, slit width D_{g} and grating period d. For the zeroth slit, $n = 0$, the transmission function is $t_{\mathrm{g}} = 1$ for $x \in [-D_{\mathrm{g}}/2, D_{\mathrm{g}}/2]$ and $t_{\mathrm{g}} = 0$ otherwise. Note that this grating transformation is no longer unitary. The eikonal phase ϕ includes the dispersive interactions between the grating walls and a particle. The corresponding Talbot coefficients then read

$$\begin{aligned} B_n(\xi) &= \frac{1}{d}\int_{-d/2}^{d/2} \mathrm{d}x\, t_{\mathrm{g}}\left(x - d\frac{\xi}{2}\right) t_{\mathrm{g}}\left(x + d\frac{\xi}{2}\right) \\ &\quad \times \exp\left[-\mathrm{i}\frac{2\pi x}{d}n + \mathrm{i}\phi\left(x - d\frac{\xi}{2}\right) - \mathrm{i}\phi\left(x + d\frac{\xi}{2}\right)\right]. \end{aligned} \tag{2.35}$$

For $\xi = 0$ the terms with the eikonal phase ϕ vanish and this integral can be evaluated analytically to

$$B_n(0) = f\mathrm{sinc}(f\pi n), \tag{2.36}$$

where $f = D_{\mathrm{g}}/d$ is the opening fraction of the grating.

A realistic model for the interaction potential between a particle and a grating wall involves the Casimir-Polder interaction [28, 67]. Effects of dispersive interactions are discussed in several articles for the near-field [21, 22, 28, 29] and also for far-field interferometry [52]. It turns out that a grating with dispersive interactions can be effectively approximated in a far-field interferometer by an interaction-free grating with a smaller slit width [52, 68].

For the present thesis, which deals only with optical diffraction gratings, the precise form of the interaction potential plays no role.

2.5.3 *Collimator*

A collimator is utilized in an interferometer for a preparation of a coherent matter-wave beam. Here, one may neglect the dispersive forces between particles and collimator walls because the width of a collimator is typically much larger than the range

of dispersive forces. For the calculation of the convolution kernel (2.29), the term $\exp[\mathrm{i}\phi(x)]$ is replaced by the transmission function $t_\mathrm{c}(x) = \Theta(D_\mathrm{c}/2 - |x|)$ with the collimator width D_c. It yields

$$\begin{aligned} T_\mathrm{coll}(s,q) &= \frac{1}{2\pi\hbar}\int_\mathbb{R} \mathrm{d}x\, \mathrm{e}^{\mathrm{i}qx/\hbar} t_\mathrm{c}\left(x - \frac{s}{2}\right) t_\mathrm{c}\left(x + \frac{s}{2}\right) \\ &= \Theta(D_\mathrm{c} - |s|)\frac{D_\mathrm{c} - |s|}{2\pi\hbar}\mathrm{sinc}\left[\frac{(D_\mathrm{c} - |s|)\, q}{2\hbar}\right]. \end{aligned} \tag{2.37}$$

In order to illustrate the effect of a collimator, let us consider the collimation of a fully incoherent state $\chi_0(s,q) \propto \delta(s)\delta(q)$, which corresponds to a constant Wigner function[1]. After the collimation and a free propagation for the time interval $t = L/v_z$, the characteristic function reads

$$\chi_t(s,q) = \frac{2\pi\hbar}{D_\mathrm{c}} T_\mathrm{coll}(s - qt/m, q). \tag{2.38}$$

As a measure for the spatial coherence of two points separated by the distance s, let us consider the non-diagonal elements of the density operator

$$\left\langle -\frac{s}{2}\middle|\,\rho\,\middle|\frac{s}{2}\right\rangle = \frac{1}{2\pi\hbar}\int_\mathbb{R} \mathrm{d}q\, \chi_t(s,q) = \frac{1}{D_\mathrm{c}}\mathrm{sinc}\left(\frac{\pi s}{W_\mathrm{c}}\right). \tag{2.39}$$

This function corresponds to the two-point correlation function for positions separated by a distance s. In Eq. (2.39) the *coherence length* is introduced as the characteristic length

$$W_\mathrm{c} = \frac{2\pi\hbar L}{D_\mathrm{c} p_z} = \frac{L\lambda_\mathrm{dB}}{D_\mathrm{c}}, \tag{2.40}$$

where $\lambda_\mathrm{dB} = 2\pi\hbar/p_z$ is the de Broglie wavelength of a particle (assuming the transversal momentum is much smaller than the longitudinal one $p/p_z \ll 1$). That means the collimation and subsequent free propagation over a distance L create a spatial coherence of about W_c. For the interference at the grating with period d, at least two neighboring grating slits must be illuminated coherently, $W_\mathrm{c} = L\lambda_\mathrm{dB}/D_\mathrm{c} \gtrsim 2d$. The required period of the diffraction grating scales linearly with the de Broglie wavelength and thus this collimation condition amounts to a critical limit for high-mass interferometry in this scheme.

2.6 MOLECULAR DENSITY DISTRIBUTION IN INTERFEROMETRY

Having introduced the Wigner function to describe a quantum state in phase space, I am now in position to consider matter-wave dynamics in concrete interferometer

1 As discussed in Sect. 2.2, the phase-space area A occupied by the Wigner function is limited by $A \geq 2\pi\hbar\left(\mathrm{Tr}\left[\rho^2\right]\right)^{-1}$. A completely incoherent quantum state with $\mathrm{Tr}\left[\rho^2\right] = 0$ thus corresponds to a constant Wigner function.

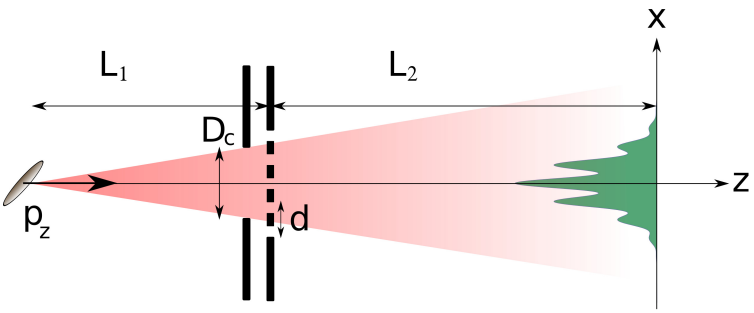

Figure 5: Schematic set up of a far-field interferometer

setups. As discussed in Sect. 2.1, we may treat transversal and longitudinal motional state separately for well collimated beams. Thus, one may calculate in the transverse x-direction $W_{t=mz/p_z}(x,p)$ with a constant longitudinal momentum p_z for the matter-wave dynamics in interferometers. At the end, the results must be averaged over p_z weighted by the momentum distribution $\mu(p_z)$.

In general, a grating interaction changes both the transversal and longitudinal momentum $p \to p + \Delta p$ and $p_z \to p_z + \Delta p_z$. As discussed in Sect. 2.4, the change of the transversal momentum is given in terms of the grating momentum $\Delta p \sim 2\pi\hbar/d$ with the grating period d. Due to the energy conservation

$$(p_z + \Delta p_z)^2 + (p + \Delta p)^2 = p^2 + p_z^2$$

the modification of the longitudinal momentum yields for a collimated beam

$$|\Delta p_z| \approx \frac{|p|}{p_z}\Delta p \ll \langle p_z \rangle .$$

Thus the longitudinal motion may be treated as unmodified throughout the interferometer.

2.6.1 *Far-field scheme*

Figure 5 shows a typical setup for far-field interference. Particles are emitted from a point-like source, interact with a collimator with width D_c after the free propagation over the distance L_1. After a subsequent interaction with a diffraction grating of period d and another free propagation over the distance L_2, they finally reach the detection screen. A more realistic, spatially extended beam source can be described by an incoherent sum of point sources, which leads to a smearing of the interference pattern, as we will see later in this section.

The characteristic function immediately after the point-like source is proportional to $\delta(s)$. The shearing transformation $s \to s - pL_1/p_z$ and subsequent collimator and grating transformation (2.31) result in

$$\chi_{L_1}(s,q) = \frac{2\pi\hbar}{D_c}\sum_{n\in\mathbb{Z}} B_n\left(\frac{s}{d}\right) T_{\text{coll}}\left(s, q - \frac{p_z s}{L_1} + \frac{2\pi\hbar}{d}n\right). \tag{2.41}$$

Note that I assumed that the collimator and diffraction grating are at the same place in order to simplify the problem. Here, $T_{\mathrm{coll}}(s,q)$ is the convolution kernel of a collimator (2.37) and $B_n(s/d)$ is the n-th Talbot coefficient (2.24). The normalization factor $2\pi\hbar/D_\mathrm{c}$ guarantees $\chi_{L_1}(0,0)=1$. The density distribution in the detection screen is calculated from the characteristic function $\chi_{L_1+L_2}(s,q)=\chi_{L_1}(s-pL_2/p_z,q)$ using Eq. (2.26),

$$\begin{aligned} w(x) &= \frac{1}{2\pi\hbar}\int_{\mathbb{R}} \mathrm{d}q\, \mathrm{e}^{-\mathrm{i}qx/\hbar}\chi_{L_1}(-pL_2/p_z,q) \\ &= \frac{1}{D_\mathrm{c}}\sum_{n\in\mathbb{Z}}\int_{\mathbb{R}} \mathrm{d}q\, \mathrm{e}^{-\mathrm{i}xq/\hbar} B_n\left(-\frac{qL_2}{p_z d}\right) \\ &\quad \times T_{\mathrm{coll}}\left[-\frac{q}{p_z}L_2, \left(1+\frac{L_2}{L_1}\right)q+\frac{2\pi\hbar}{d}n\right]. \end{aligned} \tag{2.42}$$

Inserting the convolution kernel of a collimator (2.37), the density distribution reads

$$\begin{aligned} w(x) &= \frac{L_T}{D_\mathrm{c}L_2}\sum_{n\in\mathbb{Z}}\int_{-D_\mathrm{c}/d}^{D_\mathrm{c}/d}\mathrm{d}q_0\, \exp\left(\mathrm{i}\frac{2\pi x}{d}\frac{L_\mathrm{T}}{L_2}q_0\right)(D_\mathrm{c}/d-|q_0|)B_n(q_0) \\ &\quad \times \mathrm{sinc}\left\{\pi(D_\mathrm{c}/d-|q_0|)\left[L_T\left(\frac{1}{L_2}+\frac{1}{L_1}\right)q_0-n\right]\right\}. \end{aligned} \tag{2.43}$$

Here, the Talbot time and Talbot length are introduced,

$$t_\mathrm{T}=\frac{md^2}{2\pi\hbar} \text{ and } L_\mathrm{T}=v_z t_\mathrm{L}=\frac{d^2}{\lambda_\mathrm{dB}}, \tag{2.44}$$

which define the typical time and length scale of near field interference.

NEAR-FIELD INTERFERENCE So far, no far-field approximation is utilized, thus Eq. (2.43) is valid also in the near field. For a better illustration of near-field interference, I consider a large distance $L_1/L_\mathrm{T}\gg 1$ and the limit of a large collimator opening $D_\mathrm{c}\gg d$. In this limit, the curvature of the spherical wave created by the point-like source (see Fig. 5) can be neglected at the diffraction grating, which corresponds to the illumination of the diffraction grating with a plane wave. Using a representation of the δ-function $\lim_{a\to\infty} a\,\mathrm{sinc}(\pi a x)=\delta(x)$, the density distribution (2.43) simplifies in this case to

$$w(x)=\sum_{n\in\mathbb{Z}} B_n\left(\frac{L_2}{L_T}n\right)\exp\left(\mathrm{i}\frac{2\pi x}{d}n\right). \tag{2.45}$$

As discussed in Sect. 2.3, the Talbot coefficients $B_n(s/d)$ are periodic in s with period $2d$. That is, if the ratio L_2/L_T is an even number $2N$ with $N\in\mathbb{N}$, the density distribution corresponds to $|t(x)|^2$, the transmission function of the grating,

$$w(x)\overset{L_2/L_T=2N}{=}\sum_{n\in\mathbb{Z}} B_n(0)\exp\left(\mathrm{i}\frac{2\pi x}{d}n\right)=|t(x)|^2.$$

This periodic self-imaging of the transmission function is the *Talbot effect*, which was first observed with light in 1836 by Henry Fox Talbot [69].

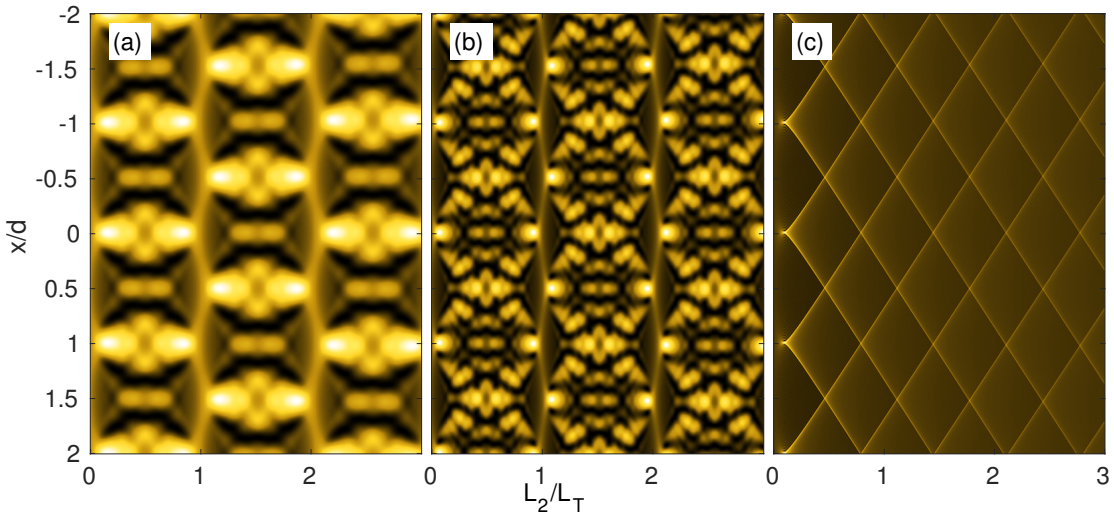

Figure 6: Near-field interference pattern depending on transversal x/d and longitudinal position L_2/L_T. An optical pure phase diffraction grating (2.32) with the maximal phase of (a) $\phi_0 = \pi$ and (b) $\phi_0 = 2\pi$ are considered. Panel (c) shows the density distribution predicted by classical mechanics, which is calculated by means of the classical Talbot coefficients (2.67) with the maximal phase $\phi_0 = \pi$. For this figure, the collimator opening and the distance between the beam source and the diffraction grating are assumed to be very large, $D_c/d \gg 1$ and $L_1 \gg L_T$. In Panel (a) and (b), the period of the interference pattern in the longitudinal direction is given by twice the Talbot length $L_2 = 2L_T$. As illustrated in panel (b), a high phase shift creates finer structures in the interference pattern because the number of contributing Fourier components increases linearly with the eikonal phase, see Eq. (2.33).

In the same way, the density distribution can be calculated for an odd ratio, $L_2/L_T = 2N+1$

$$w(x) \overset{L_2/L_T=2N+1}{=} \sum_{n\in\mathbb{Z}} B_n(1) \exp\left(\mathrm{i}\frac{2\pi x}{d} n\right) = \left| t\left(x + \frac{d}{2}\right)\right|^2 .$$

The result is a shifted transmission function, because the Talbot coefficients fulfill $B_n(1) = \exp(\mathrm{i}\pi n) B_n(0)$. Figure 6 shows the near-field density distribution (2.45) for an optical pure phase grating. The interferogram is also referred to as the *Talbot carpet*; it depends on the lateral x/d and the longitudinal position L_2/L_T. The density distribution is periodic both in x- and z-direction with the period d and $2L_T$, respectively. The Talbot effect emerges at $L_2/L_T = 1, 2, 3, \ldots$, where the transmission function of the optical grating $|t(x)|^2 = 1$ is reconstructed. The high contrast in the density distribution between two Talbot length $L_2/L_T \in (N, N+1)$ is the result of quantum interference, which is absent in the classical prediction shown in Fig. 6 (c). This interference pattern is highly non-sinusoidal in the x-direction because many Fourier components contribute to the interferogram in the near-field regime. The estimated number of the contributing Fourier components for an optical pure phase grating is $N_f = e\phi_0/2$, see Section. 2.5.1. For a typical value of $\phi_0 = \pi$, this number is $N_f \sim 4$.

FAR-FIELD INTERFERENCE In order to discuss the far-field interference effect, I transform the density distribution (2.43) into a more appropriate form. Summarizing the collimator and grating transformation into a single mappring $\rho \to \mathsf{t}(\mathsf{x})\rho\mathsf{t}^\dagger(\mathsf{x})$ with the grating function $t(x)$, the total convolution kernel for the characteristic funciton reads

$$T_{\mathrm{tot}}(s,q) = \sum_{n\in\mathbb{Z}} B_n\left(\frac{s}{d}\right) T_{\mathrm{coll}}\left(s, q+\frac{2\pi\hbar}{d}n\right) = \frac{1}{2\pi\hbar}\int_{\mathbb{R}} \mathrm{d}x\, \mathrm{e}^{\mathrm{i}xq/\hbar} t\left(x-\frac{s}{2}\right) t^*\left(x+\frac{s}{2}\right). \tag{2.46}$$

Inserting this kernel in Eq. (2.42), the density distribution yields

$$\begin{aligned} w(x) &= \frac{1}{2\pi\hbar D_{\mathrm{c}}}\int_{\mathbb{R}} \mathrm{d}q\mathrm{d}x'\, \exp\left(\frac{\mathrm{i}}{\hbar}q\left[x - x'\left(1+\frac{L_2}{L_1}\right)\right]\right) \\ &\quad \times t\left(x' - \frac{q}{2p_z}L_2\right) t^*\left(x' + \frac{q}{2p_z}L_2\right). \end{aligned} \tag{2.47}$$

Defining two shifted variables $x_1 = x' - qL_2/2p_z$ and $x_2 = x' + qL_2/2p_z$, this expression finally reduces to

$$\begin{aligned} w\left(\frac{x}{\Delta x}\right) &= \frac{L_T}{d^2 L_2 D_{\mathrm{c}}}\int_{\mathbb{R}} \mathrm{d}x_1\mathrm{d}x_2\, \exp\left(\mathrm{i}\frac{2\pi L_T}{L_2}\right. \\ &\quad \left.\times\left[(x_1-x_2)x - \frac{(x_1^2-x_2^2)}{2}\left(1+\frac{L_2}{L_1}\right)\right]\right) t(x_1)t^*(x_2) \\ &= \frac{L_T}{L_2 D_{\mathrm{c}}}\left|\int_{\mathbb{R}} \mathrm{d}x_0\, \exp\left[\mathrm{i}\frac{2\pi x}{d\Delta x}x_0 - \mathrm{i}\frac{\pi d}{d\Delta x}x_0^2\left(1+\frac{L_2}{L_1}\right)\right] t(x_0)\right|^2, \end{aligned} \tag{2.48}$$

where $\Delta x = dL_2/L_T$ is a new length scale, which corresponds to the separation of two neighboring diffraction peaks in a far-field interferogram. As expected, Eq. (2.48) reproduces the well known result of the Kirchhoff integral with the Fresnel approximation [65]. The paraxial approximation, which is used to separate the longitudinal and transversal motion (see Sect. 2.1), corresponds to the Fresnel approximation in Electrodynamics. In the Fraunhofer limit $L_2/L_T \gg (D_{\mathrm{c}}/d)^2$, the term with x_0^2 is neglected and the density distribution is determined by the squared modulus of the Fourier transform of the grating function $t(x)$.

Figure 7 shows the density distribution (2.48) for an optical pure phase grating. In the near-field regime, $L_2/L_T \lesssim D_{\mathrm{c}}/2d$, the Talbot interference pattern is still visible and behind this regime, separated diffraction peaks begin to emerge. The separation of the diffraction peaks Δx grows linearly with the longitudinal distance, $\Delta x = dL_2/L_T$, and they are already well separated for $L_2/L_T \gtrsim 2D_{\mathrm{c}}/d$. The Talbot length for a molecule is typically in the range of $\sim$ 1cm ($v_z = 60$ m/s, $m = 1000$ amu), implying that the Fraunhofer limit $L_2 \gg (D_{\mathrm{c}}/d)^2 L_T \approx 1$m (for $D_{\mathrm{c}}/d = 10$) is often not reached in a experiment.

Finally, I consider a more realistic, spatially extended beam source with an arbitrary source distribution $w_0(x)$ and with the longitudinal momentum distribution $\mu(p_z)$. Be-

cause an extended source can be described by an incoherent sum of point-like sources, a simple geometrical consideration leads to the averaged interference pattern

$$\overline{w}(x) = \int_{\mathbb{R}} \mathrm{d}p_z\, \mu(p_z) \int_{\mathbb{R}} \mathrm{d}x_0\, w_0(x_0) w\left[\frac{x}{\Delta x(p_z)} - \frac{L_2}{L_1} x_0\right]. \tag{2.49}$$

That is, in order to avoid a complete blurring of the interference pattern, the width of the beam source Δw_0

$$\Delta w_0 \quad \lesssim \quad L_1 \Delta x / 2L_2 = \lambda_{\mathrm{dB}} \frac{L_1}{2d}, \tag{2.50}$$

The longitudinal momentum distribution Δp_z must fulfill the conditions $\Delta x(p_z) - \Delta x(p_z + \Delta x) \lesssim \Delta x(p_z)$, which can be simplified to

$$\frac{\Delta p_z}{p_z} \quad \lesssim \quad \frac{1}{2}. \tag{2.51}$$

Note that I assumed $\Delta p_z \ll p_z$ for this estimation.

The condition (2.50) sets a strong limit for high-mass matter-wave interference in a far-field scheme. The required grating period scales linearly with the de Broglie wavelength of a particle, $d \lesssim \lambda_{\mathrm{dB}} L_1 / 2\Delta w_0$ and thus it reaches quickly a unfabricably low value of $d \leq 100$ nm [47]. In principle, one can increase the factor $L_1/\Delta w_0$ and so the required period by better collimation but the inevitable loss of particles prevents this procedure.

In contrast, the near-field Talbot-Lau scheme, which is the subject in the next section, is more suitable for a high-mass interference. A interferometer in this scheme does not require collimation (at least in principle) and, more importantly, the required period of the diffraction grating merely scales as the square root of the de Broglie wavelength, see Eq. (2.57).

2.6.2 *Near-field Talbot-Lau scheme*

A Talbot-Lau type interferometer requires three aligned gratings. The first and second grating have longitudinal separation of L_1, the third grating is shifted in the lateral direction by x_s relative to the other gratings and is placed at the distant L_2 behind the second grating, see Fig. 8. I consider here the most relevant case for experiments that all three grating have the same period d. The general case of non-equal grating period is analyzed in [28, 29]. In contrast to the far-field calculation in Sect. 2.6.1, I consider here a relaxed collimation condition. That is, the width of the transversal the momentum distribution $\sigma_p = \sqrt{\langle p^2 \rangle + \langle p \rangle^2}$ shall be much larger than the grating momentum $2\pi\hbar/d$ and the beam size is much larger than the grating period. However, the eikonal approximation for the grating transformation must be still valid, i.e. $p_{\max} \Delta t / M \ll d$, where $p_{\max}$ is the maximal transversal momentum of particles, Δt the interaction time for the grating transformation and M the particle's mass. As we will see later in this

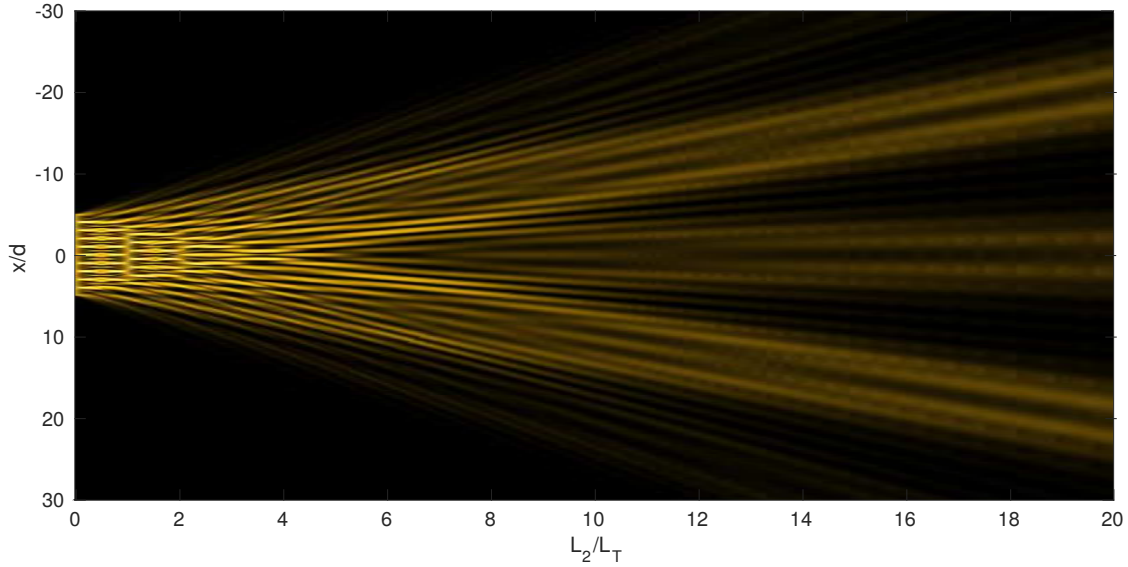

Figure 7: Density distribution after the collimator of the width $D_c/d = 10$ and after an optical pure phase grating with the maximal phase shift $\phi_0 = \pi$. The distance between the beam source and the diffraction grating is chosen to be large $L_1/L_T = 100$. In the near-field regime $L_2/L_T \lesssim 5$, the Talbot effect is still visible, see for comparison Fig. 6. Diffraction peaks emerge if the distance L_2 is sufficiently large.

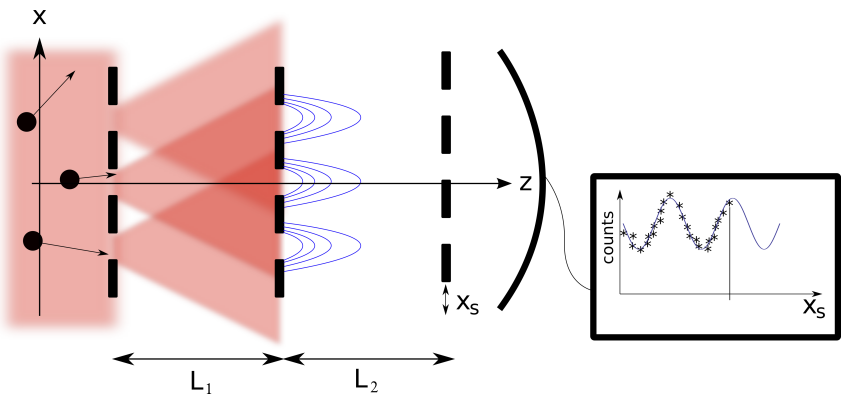

Figure 8: Schematic illustration of a Talbot-Lau interferometer. An incoherent and broad molecular beam propagating in z-direction passes three gratings with the same period d, which are separated with the distances L_1 and L_2. The detector measures the total count of molecules depending on the lateral position of the third grating x_s. In order to measure interference fringes with a high contrast, the distances between the grating must fulfill the resonance condition $L_1/L_2 \in \mathbb{N}$.

section, interference in the Talbot-Lau scheme is still possible even for this relaxed condition.

In the course of this thesis, I consider two kinds of interferometers in the Talbot-Lau scheme: the KDTLI (Kapitza-Dirac-Talbot-Lau interferometer) [31, 44, 70], and the OTIMA (optical time-domain ionizing matter-wave) interferometer [24, 32]. KDTLI operates with two material masks (first and third grating) and with an optical grating in the center. In OTIMA, all three gratings are formed by standing laser light with sufficient photon energy to ionize the particles. The details of these interferometers are treated in Chap. 3. The interference pattern in the KDTLI is discussed later in this section, where photon absorptions in an optical grating are neglected.

In the following, the density distribution of the interfering particles in a Talbot-Lau interferometer is examined. For that I consider the dynamics of the characteristic function $\chi_t(s,q)$ in three different sections of the interferometer: the section between the first and second grating, between the second and third grating and finally between the third grating and detector.

FIRST GRATING $\rightarrow$ SECOND GRATING Assuming that the beam width of particles is wide compared to the grating period, and their momentum distribution is given by a Gaussian of width σ_p, the initial Wigner function reads $W_0(x,p) \propto \exp(-(p/\sigma_p)^2/2)$. Inserting this into Eq. (2.25), I get the corresponding initial characteristic function

$$\chi_0(s,q) \propto \delta(q) \exp\left[-\frac{1}{2}\left(\frac{\sigma_p s}{\hbar}\right)^2\right]. \tag{2.52}$$

Note that the state is not normalized. Here, I chose a gaussian momentum distribution for the convenience of the calculation. However, the exact form of the distribution does not influence the contrast of the interference pattern, as we will see later in this section. According to the grating transformation Eq. (2.31), the characteristic function immediately after the grating reads

$$\chi_0'(s,q) = \sum_{n\in\mathbb{Z}} B_n\left(\frac{s}{d}\right) \exp\left[-\frac{1}{2}\left(\frac{\sigma_p s}{\hbar}\right)^2\right] \delta\left(q + \frac{2\pi\hbar}{d}n\right). \tag{2.53}$$

Because I consider here a large momentum spread of the momentum distribution, $\sigma_p \gg 2\pi\hbar/d$, the characteristic function (2.53) is only nonzero for $s/d \ll 1$. That is, for the first grating transformation, the approximation $B_n^{(1)}(s/d) \approx B_n^{(1)}(0)$ may be used. After the first grating transformation and the free propagation over the distance L_1, the characteristic function reads

$$\chi_{L_1}(s,q) = \frac{2\pi\hbar}{d} \sum_{n\in\mathbb{Z}} B_n^{(1)}(0) \exp\left[-\frac{1}{2}\left(\frac{\sigma_p}{\hbar}\right)^2 \left(s - \frac{q}{p_z}L_1\right)^2\right] \delta\left(q + \frac{2\pi\hbar}{d}n\right). \tag{2.54}$$

The purpose of the first grating is to create the spatial coherence for the interference at the second grating. For the discussion of the created coherence, let us consider for example a material grating with the opening fraction f, see Sect. 2.5.2. The coherence

of the density operator $\langle -s/2 \,|\, \rho \,|\, s/2 \rangle$, which is a measure of the spatial coherence, is given by

$$\begin{aligned}\langle -s/2 \,|\, \rho \,|\, s/2 \rangle &= \frac{1}{2\pi\hbar} \int_{\mathbb{R}} \mathrm{d}q \, \chi_{L_1}(s,q) \\ &= f \sum_{n\in\mathbb{Z}} \operatorname{sinc}(\pi f n) \exp\left[-\frac{1}{2} \left(\frac{\sigma_p d}{\hbar} \right)^2 \left(\frac{s}{d} - \frac{L_1}{L_T} n \right)^2 \right] \\ &\approx f \operatorname{sinc}\left(\frac{L_T \pi f}{L_1 d} s \right) \sum_{n\in\mathbb{Z}} \exp\left[-\frac{1}{2} \left(\frac{\sigma_p d}{\hbar} \right)^2 \left(\frac{s}{d} - \frac{L_1}{L_T} n \right)^2 \right]. \end{aligned} \tag{2.55}$$

In the last line, the approximation $\sigma_p d/\hbar \gg 1$ is used again. The coherence length W_c, defined by the width of the function $\langle -s \,|\, \rho \,|\, s \rangle$, is determined by the envelop function $\operatorname{sinc}(\pi s/W_\mathrm{c})$ and given by

$$W_\mathrm{c} = d \frac{L_1}{L_T f}. \tag{2.56}$$

At least two neighboring grating slits must be illuminated coherently for interference. This gives the condition for the distance between first and the second grating $L_1 \gtrsim 2 f L_T$. This inequality leads to the condition for the required period of the grating in the Talbot-Lau scheme

$$d \lesssim \sqrt{\frac{L_1 \lambda_\mathrm{dB}}{2f}}. \tag{2.57}$$

In contrast to the far-field scheme, the required grating period scales merely as the square root of the de Broglie wavelength, which makes this setup suitable for high-mass matter-wave experiments.

SECOND GRATING → THIRD GRATING After the passage through the second grating and the free propagation over the distance L_2, the characteristic function reads

$$\chi_{L_1+L_2}(s,q) = \sum_{n\in\mathbb{Z}} B_n^{(2)} \left(\frac{s}{d} - \frac{q}{d\,p_z} L_2 \right) \chi_{L_1} \left(s - \frac{q}{p_z} L_2 \right). \tag{2.58}$$

The density distribution in front of the third grating is then given by

$$\begin{aligned} w(x) &= \frac{1}{2\pi\hbar} \int_{\mathbb{R}} \mathrm{d}q \, \mathrm{e}^{-\mathrm{i}qx/\hbar} \chi_{L_1+L_2}(0,q) \\ &= \sum_{\ell\in\mathbb{Z}} \mathrm{e}^{\mathrm{i}2\pi x \ell/d} \sum_{n\in\mathbb{Z}} B_n^{(1)}(0) B_{\ell-n}^{(2)} \left(\ell \frac{L_2}{L_T} \right) \\ &\quad \times \exp\left[-\frac{1}{2} \left(\frac{\sigma_p d L_2}{\hbar L_T} \right)^2 \left(\ell + \frac{L_1}{L_2} n \right)^2 \right]. \end{aligned} \tag{2.59}$$

Because of the exponential suppression, only those Talbot coefficients contribute appreciably in the sum (2.59), which fulfill the *resonance condition*

$$\ell + \frac{L_1}{L_2} n = 0. \tag{2.60}$$

To illustrate the emergence of the Talbot-Lau interference pattern, I exemplary consider the KDTLI, i.e. a material and an optical grating for the first and second grating, respectively. Figure 9 shows the evolution of the particle's density distribution in this interferometer. Directly after the first grating a classical shadow effect is present, which disappears quickly for $L/L_T > 0$. Behind the optical grating, structures in the density distribution emerge for some longitudinal positions L_2. Note that the pattern immediately after the second grating $L_2/L_T \approx 0$ is indistinguishable from the classical deflection effect. As discussed in Sect. 2.7, classical mechanics predicts a focusing of the beam directly behind an optical grating because particles experience a force toward the intensity maximum of the optical grating for attractive potentials.

The other structures in the density distribution are a consequence of quantum interference. The contrast of the interference pattern is maximal at positions $L_1/L_2 \in \mathbb{N}$ that fulfill the resonance condition (2.60). This phenomenon is referred to as the *Talbot-Lau effect*. The period of the interference patterns in the case of $L_1/L_2 = j$, $j \in \mathbb{N}$ exhibit the period jd as shown in Fig. 9. The most relevant interference pattern for matter-wave experiments is at $L_2 = L_1$, where the interferogram has the grating period d.

THIRD GRATING $\rightarrow$ DETECTOR The detector measures the number of transmitted particles through the third grating depending on its relative displacement x_s to the other gratings. The signal S is given by the integral of the transmission function of the third grating $|t_g(x - x_s)|^2$ and the density distribution (2.59),

$$S(x_s) \propto \int_{\mathbb{R}} \mathrm{d}x \, |t_g(x - x_s)|^2 w(x).$$

Here, I consider the most relevant resonance case $L_2 = L_1 = L$. Inserting the Fourier series of the transmission function $|t_g(x)|^2 = \sum_{n\in\mathbb{Z}} B_n^{(3)}(0) \exp(\mathrm{i}2\pi x n/d)$, the signal reads [28, 31]

$$\begin{aligned} S(x_s) &\propto \sum_{j\in\mathbb{Z}} B_j^{(3)}(0) \int_{\mathbb{R}} \mathrm{d}x \, w(x) \exp\left(\mathrm{i}\frac{2\pi(x - x_s)}{d} j\right) \\ &= \bar{S}\left[1 + \sum_{j=1}^{\infty} \mathcal{V}_j\left(\frac{L}{L_T}\right) \cos\left(\frac{2\pi x_s}{d} j\right)\right] \end{aligned} \tag{2.61}$$

with the position mean of the signal $\bar{S} = \int dx_s S(x_s)$ and the Fourier coefficients

$$\mathcal{V}_j(\xi) = 2\frac{B_{-j}^{(1)}(0) B_{2j}^{(2)}(j\xi) B_{-j}^{(3)}(0)}{B_0^{(1)}(0) B_0^{(2)}(0) B_0^{(3)}(0)}. \tag{2.62}$$

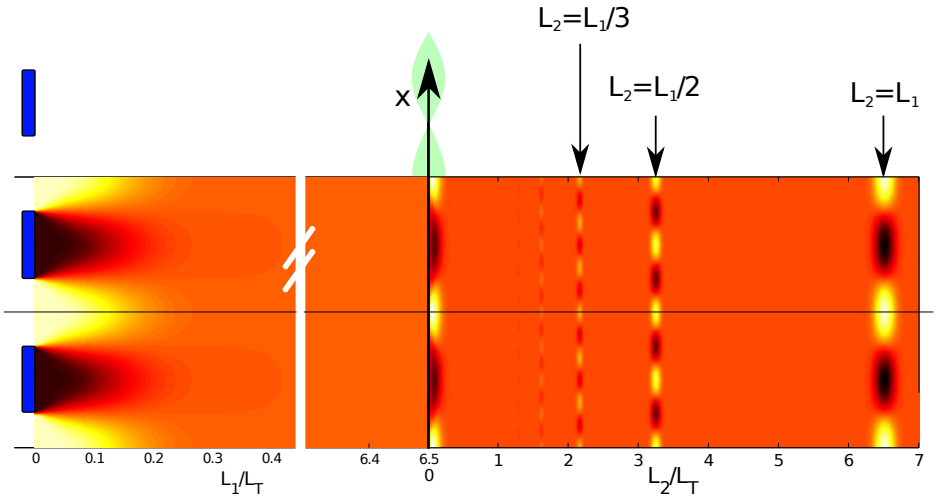

Figure 9: The density distribution in the KDTLI with a material grating (at $L_1 = 0$) and an optical pure phase grating (at $L_1/L_T = 6.5$). A maximal phase modulation of the optical grating $\phi_0 = \pi$ is chosen and the width of the momentum distribution is given by $\sigma_p/\hbar = 10d$. Directly after the first grating, the classical shadow effect is visible, which disappears beyond $L_1/L_T \gtrsim 0.1$. The density distribution is constant in front of the second grating. The interference fringes emerge behind the second grating for longitudinal distances that fulfill the resonance condition $L_1/L_2 \in \mathbb{N}$. The density contrast immediately behind the second grating is the result of the classical focusing effect.

Because this coefficients decrease quickly for large Fourier order j, the signal S can be well approximated by a sinusoidal curve in practice. For example for a KDTLI with the realistic values (opening fraction $f = 0.42$, phase modulation $\phi_0 = \pi$ and grating separation $L/L_T = 1.5$), the ratio between the first and second Fourier coefficients is $|\mathcal{V}_2/\mathcal{V}_1| \approx 0.02$. In this case, the signal is characterized solely by the mean counts $\bar{S}$ and the sinusoidal visibility $\mathcal{V}_{\text{sin}} \equiv \mathcal{V}_1$

$$S(x_s) \approx \bar{S}\left[1 + \mathcal{V}_{\text{sin}} \cos\left(\frac{2\pi x_s}{d}\right)\right], \tag{2.63}$$

where

$$\mathcal{V}_{\text{sin}} = 2\frac{B_{-1}^{(1)}(0)B_2^{(2)}(L/L_T)\,B_{-1}^{(3)}(0)}{B_0^{(1)}(0)B_0^{(2)}(0)\,B_0^{(3)}(0)}. \tag{2.64}$$

If the grating separation corresponds to a multiple of the Talbot-length, $L/L_T = N$ with $N \in \mathbb{N}$, the Talbot-coefficients in Eq. (2.64) fulfill $B_n(N) = \exp(i\pi n)B_n(0)$, as discussed in Sect. 2.6.1. Thus, $B_n(N)$ corresponds to the n-th Fourier coefficient of the grating transmission $|t(x)|^2$,

$$B_n(N) = \frac{1}{d}\int_{-d/2}^{d/2} \mathrm{d}x\, \exp\left(-i\frac{2\pi x}{d}n\right)|t(x)|^2.$$

As a consequence, the phase effect of the grating does not show up for these grating separations. For a pure phase grating, $|t(x)|^2 = 1$, one expects a zero visibility for $L/L_T = N$. A more detailed examination of the effects of phase and amplitude modulation is presented in Chapter 6.

2.7 CLASSICAL GRATING TRANSFORMATION

It is important, especially for near-field matter-wave experiments probing the wave nature of quantum particles, to distinguish quantum interference from the classical moiré effect. In this section, I consider the dynamics of a classical phase-space density distribution $f_t(x,p)$ in an interferometer. It turns out that one can obtain the classical results by replacing the Talbot coefficients $B_n(s/d)$ with the classical ones $C_n(s/d)$ (2.67).

As discussed in Section 2.3, the free propagation is described by a shearing transformation $f_t(x,p) = f_0(x - pt/m, p)$ both in quantum and classical mechanics. In the presence of an interaction potential, the classical Liouville equation is given by the limit $\hbar \to 0$ of Eq. (2.17). Using the eikonal approximation $\partial_x f_t(x,p) = 0$, it reads

$$\left[\frac{\partial}{\partial t} - \frac{\partial V(x;t)}{\partial x}\frac{\partial}{\partial p}\right] f_t(x,p) = 0. \tag{2.65}$$

Analogous to the quantum case, this differential equation can be solved by means of a Fourier transform. The solution is given by the convolution [28, 47]

$$f_{t_0+\Delta t}(x,p) = \int_{\mathbb{R}} \mathrm{d}p_0\, f_{t_0}(x, p-p_0) T_{\mathrm{cl}}(x,p_0)$$

with the convolution kernel

$$T_{\mathrm{cl}}(x,p) = \delta(p - \hbar\partial_x\phi(x)) = \frac{1}{2\pi\hbar}\sum_{n\in\mathbb{Z}} \exp\left(\mathrm{i}\frac{2\pi x}{d}n\right)\int_{\mathbb{R}} \mathrm{d}s\, \mathrm{e}^{\mathrm{i}ps/\hbar} C_n\left(\frac{s}{d}\right). \tag{2.66}$$

Here, $\phi(x)$ is the eikonal phase (2.22) and the classical Talbot coefficients are defined by

$$C_n(\xi) = \frac{1}{d}\int_{-d/2}^{d/2} \mathrm{d}x\, \exp\left[-\mathrm{i}\frac{2\pi x}{d}n - \mathrm{i}\xi d\partial_x\phi(x)\right]. \tag{2.67}$$

Note that $\hbar\partial_x\phi(x)$ represents the time integration of the force acting on a particle in a potential.

A significant difference compared to the quantum Talbot coefficients (2.24) is that the coefficients (2.67) are not periodic in the argument s/d. However, in the limit of $s/d \ll 1$, the eikonal phase in Eq. (2.24) can be approximated by $\phi(x + s/2) - \phi(x - s/2) = s\partial_x\phi(x) + \mathcal{O}[(s/d)^2]$. In this case, the classical and quantum mechanical Talbot coefficients are the same

$$B_n(s/d) \overset{s/d\ll 1}{=} C_n(s/d). \tag{2.68}$$

That is, the repeating structure of the Talbot-Lau interference pattern (see Fig. 9), which originates from the periodicity of the Talbot-coefficients $B_n(L_2/L_\mathrm{T})$, is classically inexplicable. However, classical and quantum mechanics predict the same density distribution directly behind the diffraction grating $L_2/L_T \approx 0$.

3

INTERACTION BETWEEN MOLECULES AND GRATINGS OF LIGHT

Optical gratings are essential tools in matter-wave experiments. Although material gratings are successfully utilized in several high-mass interference experiments [21, 52], a strong velocity-dependent phase modulation of the matter-wave, which originates from the van der Waals interaction between molecules and grating walls, can lead to a blurring of the interferogram [47]. A laser grating does not have this problem and because of its perfectly defined period, high transmission and tunable interaction potential, it is more suitable for a high-mass interferometry [24, 25, 70]. The aim of this chapter is to introduce a model that describes the interaction between a standing-wave laser grating and a delocalized complex molecule. Because light-matter interactions depend strongly on the size and internal structure of the interacting particle, let us consider sequentially the case of an electron, an atom and a molecule.

Already in 1933, Kapitza and Dirac discussed the diffraction of an electron in a standing-wave of light [71]. They described the interaction in terms of *stimulated Compton scattering*: an electron absorbs and subsequently re-emits a photon, the latter being stimulated by a counter-propagating photon, see Fig. 10(a). Because the emitted photon has the same frequency and propagation direction as the stimulating photon, the electron experiences a total momentum transfer of twice a photon momentum $2\hbar k_{\mathrm{L}}$, which corresponds to the grating momentum $2\pi\hbar/d$ with the grating period $d = \lambda_{\mathrm{L}}/2 = \pi/k_{\mathrm{L}}$. This phenomenon is known as the *Kapitza-Dirac effect* [72].

In contrast to an electron, which has no internal structure, an atom exhibits discrete internal energy levels, which lead to resonance phenomena in the light interaction. If the laser frequency ω_{L} is near the resonance frequency $\omega_{\mathrm{L}} \approx \omega_0 = (E_2 - E_1)/\hbar$ between two electronic states with energy E_1 and E_2, an oscillation of the electronic population between these two levels is induced, as is illustrated in Fig. 10(b). This is the *Rabi oscillation*, which plays a central role in atomic interferometry [73]. However, if a laser is far-off detuned, i.e. $|\omega_{\mathrm{L}} - \omega_0| \gg \omega_0$, the Rabi oscillation is suppressed and the laser-atom interaction can be approximately described in terms of the dipole interaction [74]. The details are discussed in Sect. 3.2.

Internal states of a molecule are more complicated compared to an atom as illustrated schematically in Fig. 10(c). A molecule additionally possesses numerous internal rotational and vibrational (rovibrational) states, whose lifetimes are on the order of a few picoseconds [36]. Because of the extremely short lifetimes, the Rabi oscillation between two rovibrational states can not complete a cycle. We will see in this case that the molecule-laser interaction can be effectively described in terms of the photon ab-

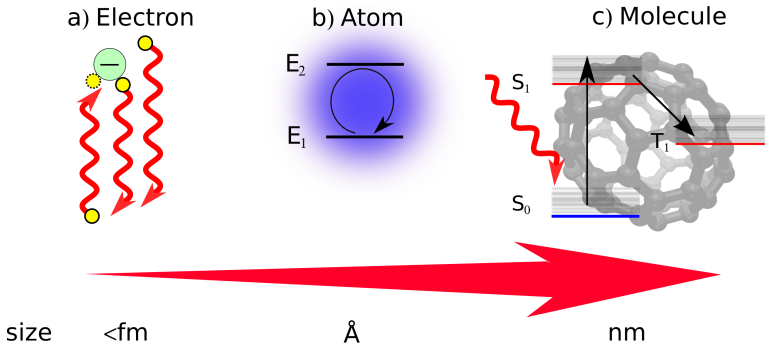

Figure 10: A schematic illustration of the interaction between a standing-wave laser and a particle of different sizes. (a) An electron experiences a force due to stimulated Compton scattering (Kapitza-Dirac-effect), which corresponds to an absorption and a stimulated emission of a photon. In this process twice a photon momentum $2\hbar k_{\mathrm{L}}$ is transfered to the electron. (b) In the case of atom-light interaction, the electronic states of an atom (in this figure with the energy E_1 and E_2) must be taken into account. An essential consequence is the oscillation of the electronic population between different states, known as the Rabi oscillation. (c) In contrast to an atom, a molecule exhibits numerous internal rovibrational states, whose lifetime is on the order of picoseconds. One expects no Rabi oscillations between different rovibrational states because of the extremely short lifetime. Molecular internal states can be categorized into singlet and triplet states, which is depicted by $|\mathrm{S}_0\rangle$, $|\mathrm{S}_1\rangle$ and $|\mathrm{T}_1\rangle$ in this figure, depending on the spin of electrons [35]. Here, the subscript 0 and 1 stand for the ground state and first excited state, respectively. Molecular photophysical processes can be explained effectively by the excitation and deactivation of electrons between these internal levels.

sorption and the dipole interaction just like in the case of an atom in a far-off detuned laser. Furthermore, absorption of photons can lead to the population of the molecular triplet state, which can exhibit different optical properties compared to the ground state.

A challenge in describing the interaction between a delocalized molecular matter wave and an optical grating is to consider both the center-of-mass motion and numerous internal molecular processes like fluorescence. I begin reviewing some relevant molecular photophysical processes in Sect. 3.1. In order to find a connection between atomic and molecular interferometry, I consider in Sect. 3.2 Rabi oscillations between a ground and an excited state with a fast relaxation time. It is shown that the Rabi model is not realistic for a complex molecule due to fast decay channels. In Sect. 3.3 I introduce the *ladder model*, which describes molecular diffraction at an optical grating in the presence of the excitation of molecules to the triplet state. Note that I neglect in this chapter the effect of fluorescence, which is examined in detail in Chapter 4. Finally in Sect. 3.4, I present the calculation of the Talbot-coefficients, which play a central role in the theoretical description of matter-wave interferometry.

spectral region	wavelength	photon energy [eV]	photophysical process
γ-rays	20 pm	$6.2 \cdot 10^4$	nuclear effects
UV	50 nm	24	ionization
visible	500 nm	2.5	electronic transition
infrared	10 µm	$1.2 \cdot 10^{-1}$	vibrational transitions
microwave	1 mm	$1.2 \cdot 10^{-3}$	rotational transitions

Table 1: Photophysical processes occurring in a molecule for different photon energies.

3.1 PHOTOPHYSICAL PROCESSES OF MOLECULES

Molecular photophysical processes are conveniently visualized by the *Jablonski diagram*, which is introduced in Sect. 3.1.1. A number of molecular internal processes (internal conversion, internal system crossing, vibrational relaxation, fluorescence and phosphorescence) are discussed with the help of this diagram. In Sect. 3.1.2, the deactivation processes of the excited states are examined, where I introduce the *quantum yield*, which plays an important role in molecular spectroscopy. The spatial distribution of the laser intensity is decisive for photophysical processes, which is examined in Sect. 3.1.3.

3.1.1 *The Jablonski diagram*

The mechanism of interaction between light and a molecule depends strongly on the photon energy. Table 1 shows different molecular photophysical processes and associated spectral regions of the electromagnetic field. A typical energy separation of two rovibrational states is between 10^{-3} and 10^{-1} eV, which corresponds to the infrared and to the microwave domain. The ionization energy of most molecules is in the range of 7 to 15 eV [75], that is, the relevant photophysical processes occurring for an ultraviolet light is ionization. For an optical grating in matter-wave experiments, visible laser light is usually used, which leads to electronic transitions of molecules.

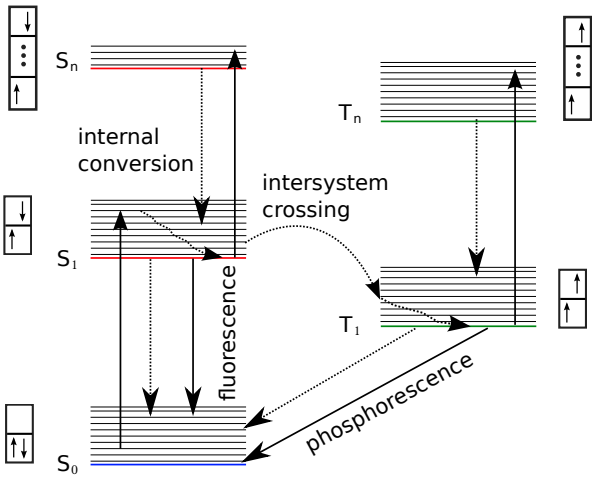

Figure 11: A Jablonski diagram of a typical molecule. The solid and dashed lines denote radiationless and radiative transitions, respectively.

Analogously to atomic spectroscopy, electronic transitions in molecules can be

visualized by a energy level diagram, which is referred to as the *Jablonski diagram* in molecule spectroscopy [36, 76]. As shown in Fig. 11, molecular internal levels can be divided into *singlet* and *triplet states* depending on the electron spins. If all valence electrons of a molecule appear in a spin-up-down pair as denoted with two antiparallel arrows in Fig. 11, the molecular state is singlet S_n. Here, the subscript n stands for the rank of the excitation. If at least one electron-pair appears in a spin-up-up or spin-down-down configuration as denoted with two parallel arrows in Fig. 11, the molecule is in a triplet state T_n. It is known that most of molecules have a singlet ground state S_0 [1].

Absorption of a photon promotes an electron to the excited singlet state $S_0^* \rightarrow S_1^*$, where the superscript $*$ denotes the vibrational excitation. Note that a direct transition from a singlet to triplet state is forbidden because of the different symmetries: singlet and triplet wave functions are symmetric and antisymmetric under the permutation of two electrons, respectively. According to the selection rule [35, 77], optical dipole transitions are allowed only between states with the same permutation symmetry. The transition between a singlet and a triplet state is thus said to be *spin forbidden.*

In most cases, a molecule is vibrationally excited after absorption of a photon. The vibrational excitation relaxes to the equilibrium state $S_1^* \rightarrow S_1$ after a very short time of picoseconds [76]. In this process, the excess photon energy is redistributed between the numerous internal degrees of freedom, which is also referred to as *intramolecular vibrational randomization* [78, 79]. Further photon absorptions promotes the electron further to the higher excited states $S_1 \rightarrow S_n$, which has an extremely short lifetime of $10^{-14} - 10^{-12}$ sec [36, 76]. Because of this short lifetime, the decay $S_n \rightarrow S_1$ takes place radiationless, which is denoted as the *internal conversion.* Again, the excess photon energy is redistributed into the many molecular rovibrational degrees of freedom.

Once a molecule reaches the vibrational equilibrium of the excited state S_1, there are three possibilities for further deactivations. First, the radiationless internal conversion to the ground state $S_1 \rightarrow S_0^*$. Second, a radiative decay to the ground state $S_1 \rightarrow S_0^* + \gamma$, which is known as *fluorescence*. And finally, a radiationless decay to the triplet state $S_1 \rightarrow T_1^*$, the *intersystem crossing*. The intersystem crossing is a spin-changing transition and becomes possible with the help of the spin-orbit coupling [36]. Because the direct transition between a singlet and a triplet state is spin forbidden, the lowest triplet state T_1 has a comparably long lifetime of $10^{-4} - 100$ sec. A triplet state can decay either radiatively (*phosphorescence*, $T_1 \rightarrow S_0^* + \gamma$) or radiationless via internal conversion ($T_1 \rightarrow S_0^*$). Table 2 summarizes the typical time scales of the different photophysical processes.

The interaction time between a laser and a traversing molecule is given by $t_L = \sqrt{\pi/2} w_z / v_z$ with the gaussian waist of the laser w_z and the longitudinal velocity of a molecule v_z. It is typically in the order of about 0.5 µs, see Sect. 3.1.3. That is, in the context of matter-wave interferometry, the internal conversion of highly excited state, $S_n \rightarrow S_1$ and $T_n \rightarrow T_1$, and the vibrational relaxation may be treated as instantaneous. In addition, the decay of the triplet state $T_1 \rightarrow S_0$ may be neglected because of its long

1 Molecular oxygen is a rare example of of a triplet ground electronic state.

Process	transition	time scale in sec
Light absorption	$S_0 \to S_n$	$< 10^{-15}$ (instantanous)
Internal conversion	$S_n \to S_1$, $T_n \to T_1$	$10^{-14} - 10^{-12}$
	$S_1 \to S_0$	$> 10^{-8}$
	$T_1 \to S_0$	$10^{-4} - 10$
Intersystem crossing	$S_1 \to T_1$	$10^{-11} - 10^{-7}$
Vibrational relaxation	$S_n^* \to S_n$, $T_n^* \to T_n$	$10^{-14} - 10^{-10}$
Fluorescence	$S_1 \to S_0 + \gamma$	$10^{-9} - 10^{-6}$
Phosphorescence	$T_1 \to S_0 + \gamma$	$10^{-4} - 100$

Table 2: Photophysical processes of a molecule and their typical time scales. The values of time scale are taken from [36] except for the vibrational relaxation [80].

lifetime. Thus, in the given time scale of the interaction, the molecular internal state may be approximated by the three level system consisting of the ground state S_0, the lowest singlet S_1, and the lowest triplet state T_1.

3.1.2 *Decay of the first singlet excited state* S_1

As discussed in the previous section, the first singlet excited state S_1 has three channels for further decay; fluorescence, internal conversion and intersystem crossing. For a systematic analysis of decay processes, it is essential to consider the probability P_A that a molecule undergoes the specific process A after absorption of a photon. For this sake, I consider the situation that molecules are illuminated by a short light pulse with the duration t_L. After this interaction time, the probability that a molecule is still in the ground state is given by $P_0 = \exp(-\gamma t_L)$, where γ is the rate for photon absorption. Now for the examination of the decay processes, I consider the following rate equations involving the population of the excited state P_1, and the probabilities P_F, P_{IC} and P_{ISC} relating to the fluorescence, internal conversion and intersystem crossing, respectively. They read

$$\partial_t P_1 = -\gamma_{tot} P_1, \quad \partial_t P_F = \gamma_F P_1 \tag{3.1}$$

$$\partial_t P_{IC} = \gamma_{IC} P_1, \quad \partial_t P_{ISC} = \gamma_{ISC} P_1, \tag{3.2}$$

where γ_A is the rate for the decay process A given by the inverse of the lifetime $\gamma_A = 1/\tau_A$ and $\gamma_{tot} = \gamma_F + \gamma_{IC} + \gamma_{ISC}$ denotes the total decay rate. For the initial values $P_1(0) = 1 - P_0$ and $P_A(0) = 0$, the solutions of these differential equation system read $P_1(t) = (1 - P_0)\exp(-\gamma_{tot} t)$ and $P_A(t) = \gamma_A(1 - P_0)[1 - \exp(-\gamma_{tot} t)]/\gamma_{tot}$. Thus the probability P_A in the limit of a long decay time is given by $\lim_{t\to\infty} P_A(t) =$

molecule	Φ_T	Φ_F	$\Phi_{IC} = 1 - \Phi_T - \Phi_F$	τ_{tot} in ns
C_{60} (in toluene)	0.96 [85]	$2.2 \cdot 10^{-4}$ [86]	0.04	1.3 [85]
C_{70} (in toluene)	0.9 [87]	$8.5 \cdot 10^{-4}$[87]	0.1	0.7[85]
TPP (in toluene)	0.73 [88]	0.1 [88]	0.17	16 [89]
Hypericin (in ethanol)	0.52 [90]	0.48 [91]	0	5.5 [91]
Anthracene (in ethanol) [83]	0.72	0.27	0	5.1

Table 3: Quantum yields for different decay channels and the lifetime of the singlet excited state.

$\gamma_A(1 - P_0)/\gamma_{tot}$. The ratio of this probability $P_A(\infty)$ to the probability for the light absorption $(1 - P_0)$

$$\Phi_A = \frac{\gamma_A}{\gamma_F + \gamma_{IC} + \gamma_{ISC}} \tag{3.3}$$

is the *quantum yield* of a decay process A, which plays an important role in molecular spectroscopy [36].

Table 3 shows quantum yields and lifetimes of the singlet excited state S_1 for several molecules, which are already used as the interfering particles in matter-wave experiments [19, 22, 44, 81]. The lifetimes shown in Tab. 3 are much smaller than the typical time for a molecule transversing an optical grating $t_L \sim 0.5\,\mu s$, see Sect. 3.1.3. C_{60} and C_{70} prefer to decay via intersystem crossing with the quantum yield greater than 0.9 and the fluorescence rate is practically zero. Hypericin ($C_{30}H_{16}O_8$), TPP (tetraphenylporphyrin, $C_{44}H_{30}N_4$) and Anthracene ($C_{14}H_{10}$) can decay both over fluorescence and radiationless internal conversion to the ground state. Note that the values in Table 3 are measured in solvation and that they can differ from the molecular vacuum properties. However, the deviation is expected be small for large molecules because they predominantly deactivate the excitation by internal processes [82]. In addition, the quantum yield of the intersystem crossing can depend on the internal temperature of molecules [82–84]. Hot molecules are expected to have a larger quantum yield Φ_{ISC} for inter-system crossing than the values in Table 3, which are properties of room temparature molecules.

3.1.3 *Gaussian laser*

The spatial light intensity distribution plays a major role for the description of laser-molecule interaction. In this section I consider an optical grating made by a gaussian laser mode, which is often applied in matter-wave experiments. First of all, in order to create a thin optical grating, the incoming laser is focused in the z-direction (molecular beam direction) by means of a cylinder lens, see Fig. 12. Note that the laser is unfocused in y-direction so that molecules experience the same laser intensity irrespective

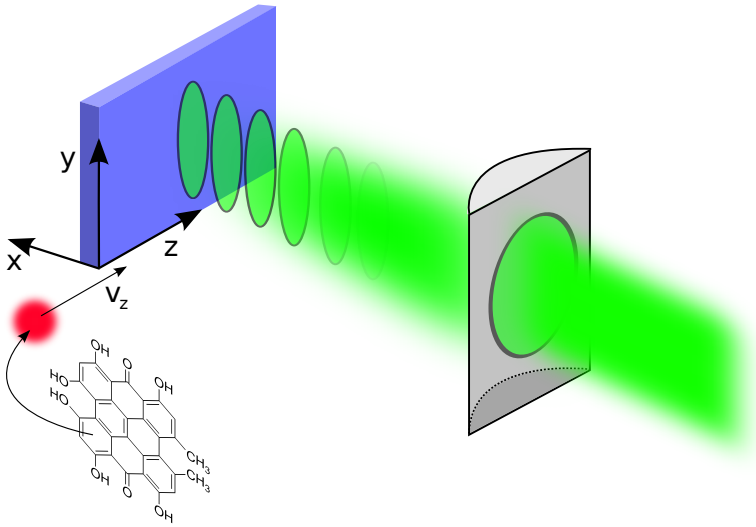

Figure 12: Schematic illustration of a typical standing-wave laser grating. A laser is focused in the direction of the molecular propagation (z-axis) by means of a cylinder lens. A standing wave in x-direction is created by placing a mirror near the focus of the lens.

to their y-coodinates. If the initial laser waist is w_y (assumed to be symmetric in y- and z-direction), the waist in z-direction at the focus is given by [92]

$$w_z = \frac{\lambda_L f}{\pi w_y}, \tag{3.4}$$

where λ_L is the laser wavelength and f is the focus length of a cylinder lens. For typical values $\lambda_L = 532$ nm, $f = 100$ mm and $w_y = 425$ µm, the focused waist is $w_z \approx 40$ µm. Placing a mirror at the focus, a standing wave is created, whose intensity profile is given by

$$I(x,y,z) = \frac{8P_L}{\pi w_y w_z} \exp\left(-\frac{2y^2}{w_y^2} - \frac{2z^2}{w_z^2}\right) \cos^2(k_L x), \tag{3.5}$$

where P_L is the running wave laser power. The prefactor $8P_L/\pi w_y w_z$ in Eq. (3.5) is determined from the condition that the surface integral of the intensity in the yz-plane corresponds to the laser power, $\int_{\mathbb{R}} dy dz\, I(x,y,z) = 4P_L \cos^2(k_L x)$. Note that the peak intensity of a standing-wave is increased by the factor 4 compared to a running wave. In practice, the molecular beam is collimated around $y = 0$, where the intensity has its maximum. Because the molecular beam width is much smaller than the laser width w_y, one may set $y = 0$ for all molecules passing through the grating. Thus, I assume $y = 0$ for further calculations.

In most of calculations carried out in this thesis, analytical solutions are unfortunately not available with this exact gaussian intensity profile Eq. (3.5). However, the interaction processes depend mainly on the maximum of the intensity and on the inter-

action time in the case of a thin grating [93]. Thus the gaussian intensity distribution may be approximated by a rectangular function

$$I_c(x,z) = I_{\max}\Theta\left(\sqrt{\frac{\pi}{2}}w_z - 2|z|\right)\cos^2(k_L x), \tag{3.6}$$

where $\Theta(z)$ is the Heavyside theta function and $I_{\max} = 8P_L/\pi w_y w_z$ is the maximum of the laser intensity. The width of this function $w_z\sqrt{\pi/2}$ is determined from the condition that the total laser power $4P_L\cos^2(k_L x)$ remains constant. Equation (3.6) implies the interaction time

$$t_L = \sqrt{\frac{\pi}{2}}\frac{w_z}{v_z}, \tag{3.7}$$

where v_z is the molecular velocity in z-direction. For the typical values $w_z = 40\,\mu m$ and $v_z = 100\,m/s$, the interaction time is $t_L = \sqrt{\pi/2}w_z/v_z \approx 0.5\,\mu s$, which is much larger than the time scales for many photophysical processes of a molecule, see Tab. 2.

3.2 RABI MODEL WITH A FAST DECAY CHANNEL

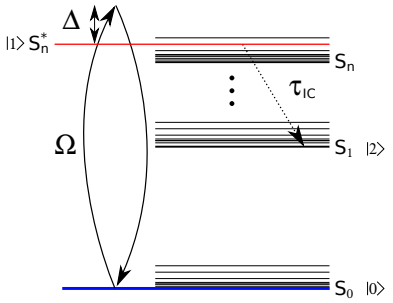

Figure 13: Schematic illustration of the Rabi oscillation between the ground state S_0 and the excited state S_n^*. The excited state is assumed to decay to S_1 with the rate $1/\tau_{IC}$.

So far, I treated internal molecular processes. In this section I consider a delocalized molecular state passing through an optical grating. For this sake, the molecular internal dynamics must be incorporated into the description of the center-of-mass motion. It is in general quite a challenging task due to the numerous internal states of a complex molecule. Here, I consider the internal dynamics between a ground state S_0 and an excited state S_n^*, which relaxes to the lowest singlet excited state S_1 via internal conversion, see Fig. 13. As discussed in Sect. 3.1.1, the lifetime τ_{IC} is much smaller than the laser-molecule interaction time t_L. We will see that the interaction can be described in terms of photon absorptions and the dipole interaction due to the small decay time τ_{IC}. For convenience, I denote the states $|0\rangle \mathrel{\hat{=}} |S_0\rangle$, $|1\rangle \mathrel{\hat{=}} |S_n^*\rangle$ and $|2\rangle \mathrel{\hat{=}} |S_1\rangle$.

The laser shall drive the transition between $|0\rangle$ and $|1\rangle$ with a detuning $\Delta = \omega_L - \omega_0$, where ω_0 is the resonance frequency of the transition and ω_L is the laser frequency. The laser-molecule interaction is then characterized by a position-dependent Rabi frequency in the rotating wave approximation [73],

$$\Omega(x) = -\frac{d_z E_0}{\hbar}\cos(k_L x) =: \Omega_0\cos(k_L x), \tag{3.8}$$

where $d_z = \langle 0 \,|\, ez \,|\, 1 \rangle$ is the transition dipole moment assuming that the laser is linearly polarized in z-direction [56]. Note that Eq. (3.8) does not depend on the z-coordinate (molecular beam direction) because I assume a constant intensity profile of the laser, see Sect. 3.1.3. In terms of the Rabi frequency the interaction Hamiltonian reads as $\mathsf{H} = \frac{\hbar}{2} \left[\Omega(x) \,|1\rangle \langle 0| - \Delta \,|1\rangle \langle 1| \right] + \text{h.c}$ [73]. The relaxation of the excited state is, however, an incoherent process and thus cannot be described by the Hamilton operator. A spontaneous decay can be incorporated with the help of the *master equation*

$$\partial_t \rho = \frac{1}{\mathrm{i}\hbar} [\mathsf{H}, \rho] + \mathsf{L}\rho\mathsf{L}^\dagger - \frac{1}{2}\{\mathsf{L}^\dagger\mathsf{L}, \rho\} \tag{3.9}$$

with the Lindblad operator $\mathsf{L} = |2\rangle \langle 1| / \sqrt{\tau_{\mathrm{IC}}}$ describing the relaxation $|1\rangle \to |2\rangle$ [94]. The braces $\{A, B\} = AB + BA$ in Eq. (3.9) denote the anticommutator. Decomposing the density operator into the matrix elements $\rho_{nn'}(x, x'; t) := \langle x, n| \, \rho \, |x', n'\rangle$, the master equation corresponds to nine partially coupled differential equations. Four coupled differential equations contain the ground state density matrix $\rho_{00}(x, x'; t)$,

$$\frac{\partial}{\partial t}\rho_{00} = -\frac{\mathrm{i}}{2} \left[\rho_{10}\Omega(x) - \rho_{01}\Omega(x') \right] \tag{3.10}$$

$$\left(\frac{\partial}{\partial t} + \frac{1}{\tau_{\mathrm{IC}}} \right) \rho_{11} = \frac{\mathrm{i}}{2} \left[\rho_{10}\Omega(x') - \rho_{01}\Omega(x) \right] \tag{3.11}$$

$$\left(\frac{\partial}{\partial t} + \frac{1}{2\tau_{\mathrm{IC}}} \right) \rho_{01} = -\frac{\mathrm{i}}{2} \left[\rho_{11}\Omega(x) - \rho_{00}\Omega(x') + 2\Delta\rho_{01} \right] \tag{3.12}$$

$$\left(\frac{\partial}{\partial t} + \frac{1}{2\tau_{\mathrm{IC}}} \right) \rho_{10} = \frac{\mathrm{i}}{2} \left[\rho_{11}\Omega(x') - \rho_{00}\Omega(x) + 2\Delta\rho_{10} \right], \tag{3.13}$$

where the argument $(x, x'; t)$ of the density operator is omitted for simplicity. This differential equation system can be solved exactly, but instead of lengthy general solutions let us focus on the relevant solution in the limiting cases.

In the limit of an infinitely long lifetime, $\tau_{\mathrm{IC}} \to \infty$, one obtains the well-known Rabi oscillation between the ground and the excited state with the position-dependent frequency $\sqrt{\Delta^2 + \Omega^2(x)}$ [73]. If the lifetime is finite, the coherences ρ_{01} and ρ_{10} are exponentially suppressed, which leads to a damping of the Rabi oscillation and to a population transfer to the state S_1. In the limit of a short lifetime $\tau_{\mathrm{IC}}/t_{\mathrm{L}} \ll 1$, Eqs. (3.12) and (3.13) may be solved in the quasi-stationary approximation, where the time derivatives are neglected. In addition, due to the short lifetime, the state $|1\rangle$ is scarcely populated, $|\rho_{11}| \ll |\rho_{00}|$. In this approximation the stationary solutions of the coherences are given by [95]

$$\rho_{01} \approx \frac{2\Delta\tau_{\mathrm{IC}}^2 - \mathrm{i}\tau_{\mathrm{IC}}}{1 + 4\Delta^2\tau_{\mathrm{IC}}^2}\Omega(x')\rho_{00}, \quad \rho_{10} \approx -\frac{2\Delta\tau_{\mathrm{IC}}^2 - \mathrm{i}\tau_{\mathrm{IC}}}{1 + 4\Delta^2\tau_{\mathrm{IC}}^2}\Omega(x)\rho_{00}. \tag{3.14}$$

Inserting these solutions into (3.10), one gets the differential equation for the ground state, which can be integrated analytically for an arbitrary initial condition $\rho(x,x';0) = \widetilde{\rho}(x,x')$,

$$\begin{aligned}\rho_{00}(x,x';t_L) &= \widetilde{\rho}(x,x')\exp\left(i\phi_0\left[\cos^2(k_L x)-\cos^2\left(k_L x'\right)\right]\right)\\ &\quad\times\exp\left(-\frac{n_0}{2}\left[\cos^2(k_L x)+\cos^2\left(k_L x'\right)\right]\right).\end{aligned} \tag{3.15}$$

Thus, the ground state dynamics can be described in terms of two constants

$$\phi_0 = \frac{t_L\Delta\tau_{IC}^2\Omega_0^2}{1+4\Delta^2\tau_{IC}^2}, \quad n_0 = \frac{t_L\tau_{IC}\Omega_0^2}{1+4\Delta^2\tau_{IC}^2}. \tag{3.16}$$

To illustrate the meaning of the constant n_0, let us consider the population of the ground state density operator $\rho_{00}(x,x) = \exp\left[-n_0\cos^2(k_L x)\right]$, which corresponds to the transmission of molecules on the ground state. This expression is the position dependent Poisson probability $e^{-n(x)}$ for absorbing no photons within the interaction time, where $n(x) = n_0\cos^2(k_L x)$ is the mean absorbed photon number. That is, the constant n_0 stands for the mean absorbed photon number at the anti-nodes of the standing light field. The other constant ϕ_0 describes a unitary transformation of the density operator $\rho \to U\rho U^\dagger$ with $U = \exp(i\phi_0\cos^2[k_L x])$. The associated interaction potential can be obtained from Eq. (2.22),

$$V(x) = -\frac{\hbar}{t_L}\phi_0\cos^2(k_L x) = -\frac{\alpha}{4}E_0^2\cos^2(k_L x), \tag{3.17}$$

where $\alpha = 4d_z^2\Delta\tau_{IC}^2/(1+4\Delta^2\tau_{IC}^2)$. This potential is proportional to the laser intensity and thus the constant α can be interpreted as the effective polarizability of the molecule [74]. Equation (3.17) can be expressed as the time averaged interaction potential between laser and polarized molecule, see Sect. 3.3.1,

$$V(x) = -\frac{1}{2}\langle\alpha E^2(x,t)\rangle_t. \tag{3.18}$$

That means, because of the fast relaxation of the vibrational states, the laser-molecule interaction can be effectively described in terms of the polarization and the photon absorption cross section of the molecule. Based on these results, I introduce in the next section a model of the laser-molecule interaction in a more realistic scenario, where molecular triplet excited states are also taken into account.

3.3 LADDER MODEL FOR ABSORBING MOLECULES

As discussed in the previous section, the molecule-light interaction can be described by the dipole interaction and the photon absorption process due to fast vibrational decays. However, for a more realistic description one must also include also the intersystem crossing $S_1 \to T_1$, internal conversion $S_1 \to S_0$ and fluorescence $S_1 \to S_0 + \gamma$, as

discussed in Sect. 3.1. Furthermore, a molecule in the triplet state T_1 can exhibit an enhanced polarizability and absorption cross section compared to the ground state [36], which makes the theoretical description more involved.

For the examination of the effect of molecular triplet state, I consider in this section that the singlet lifetime of a molecule is much shorter than the interaction time $\tau_{\mathrm{tot}}/t_{\mathrm{L}} \ll 1$ and that the quantum yield for the intersystem crossing is $\Phi_{\mathrm{ISC}} = 1$. That is, any photon absorption is assumed to transfer a molecule to the triplet state instantaneously. In this case, the internal molecular states may be approximated by two energy levels: a ground state S_0 and a triplet state T_1. This approximation is well justified some molecules e.g. for C_{60} and C_{70}, however it likely to fail for TPP, Hypericin or Anthracene, whose quantum yields for the decay to the ground state are not negligible, see Table 3 in Sect. 3.1.2. The general case, incorporating the singlet excited state dynamics, is treated in Chapter 4, where also the effect of fluorescence is discussed.

In Sect. 3.3.1, I consider the dipole interaction of a molecule in a standing-wave laser beam, which depends on the polarizability of the ground state $\alpha(\omega_{\mathrm{L}})$ and of the triplet state $\alpha_{\mathrm{T}}(\omega_{\mathrm{L}})$. Note that the polarizability is a function of the laser frequency ω_{L}. In contrast to the previous Rabi model, the change of the polarizability $\alpha \to \alpha_{\mathrm{T}}$ after the absorption of a photon must be taken into account. The probability of photon absorption is described in terms of the ground state and triplet state absorption cross section $\sigma(\omega_{\mathrm{L}})$ and $\sigma_{\mathrm{T}}(\omega_{\mathrm{L}})$. As discussed in Sect. (3.3.2), each absorption event implies the *coherent* transfer of a photon momentum $\pm\hbar k_{\mathrm{L}}$. In Sect. 3.3.3, I introduce a master equation including both the dipole-interaction and photon absorptions. The master equation is solved for the case $\alpha = \alpha_{\mathrm{T}}$, $\sigma = \sigma_{\mathrm{T}}$ in Sect. 3.3.3 and also for the general case $\alpha \neq \alpha_{\mathrm{T}}$, $\sigma \neq \sigma_{\mathrm{T}}$ in Sect. 3.3.4. Finally in Sect. 3.3.5, an interpretation of the solutions of the master equation is discussed.

3.3.1 *Dipole interaction between molecule and light*

The interaction potential of a polarizable molecule with permanent dipole moment $\mathbf{d}$ and polarizability α in a electric field $\mathbf{E}(\mathbf{r};t)$ is given by [2, 35]

$$V(\mathbf{r};t) = -\mathbf{d}\cdot\mathbf{E}(\mathbf{r};t) - \frac{1}{2}\alpha|\mathbf{E}(\mathbf{r};t)|^2. \tag{3.19}$$

The electric field of a standing-wave laser beam reads $\mathbf{E}(\mathbf{r};t) = \Re\left[E_0(x,y,z)\mathbf{e}_z \mathrm{e}^{-\mathrm{i}\omega_{\mathrm{L}}t}\right]$, where I assume a linear polarization of the laser in z-direction. Because of the fast oscillation of the electric field with the frequency ω_{L}, the time averaged interaction potential $\overline{V}$ is relevant on the time scale of the interaction t_{L},

$$\begin{aligned}\overline{V}(x,z) := \langle V(x,0,z;t)\rangle_t &= -\mathbf{d}\cdot\langle\mathbf{E}(x,0,z;t)\rangle_t - \frac{1}{2}\alpha\langle|\mathbf{E}(x,0,z;t)|^2\rangle_t \\ &= -\frac{1}{4}\alpha E_0^2(x,0,z).\end{aligned} \tag{3.20}$$

Here, I assume that the molecular beam is collimated around $y = 0$, see also Sect. 3.1.3. Note that the interaction due to the permanent dipole moment $\mathbf{d}$ vanishes after the

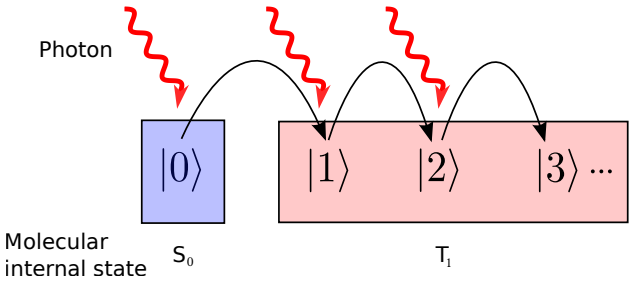

Figure 14: Schematic illustration of the ladder model. Absorption of a photon changes the internal state $|\ell\rangle \rightarrow |\ell+1\rangle$. Once molecule is excited to the triplet state, further photon absorptions lead only to the stepwise heating of the molecule.

time averaging and the interaction potential is given solely by the polarizability α and the time independent electric field amplitude $E_0(\mathbf{r})$. Using the relation between intensity and electric field, $I = \varepsilon_0 c|E|^2/2$, the interaction potential for a gaussian laser is given by

$$\overline{V}(x,z) = -\frac{4P}{\pi w_y w_z}\frac{\alpha}{\varepsilon_0 c}\exp\left(-\frac{2z^2}{w_z^2}\right)\cos^2(k_L x)\,. \tag{3.21}$$

Inserting this potential into Eq. (2.22), the associated position dependent eikonal phase is calculated to [31]

$$\begin{aligned}\phi(x) &= -\frac{1}{\hbar}\int_{-\infty}^{\infty} dt\, \overline{V}(x,0,v_z t)\\ &= \phi_0 \cos^2(k_L x) \quad \text{with} \quad \phi_0 = \sqrt{\frac{8}{\pi}}\frac{\alpha}{\hbar\varepsilon_0 c}\frac{P_L}{w_y v_z}.\end{aligned} \tag{3.22}$$

3.3.2 *Photon absorption*

For the description of photon absorptions I assume that the excess photon energy $\hbar\omega_L$ after the absorption is redistributed immediately among the molecular internal degrees of freedom. This assumption is well justified for a sufficiently large molecule whose internal degrees of freedom act as its own heat sink [82]. As a consequence, absorption of photons leads to the stepwise increase of the internal microcanonical temperature by $\Delta T = \hbar\omega_L/C$, where C is the heat capacity of the molecule. I introduce the ladder model in order to incorporate this stepwise heating: Starting from a molecule in its electronic ground state $|0\rangle$, every subsequent photon absorption shall excite the internal state to distinct orthogonal states $|1\rangle \rightarrow |2\rangle \rightarrow |3\rangle \rightarrow \ldots$. The internal temperature of the state $|\ell\rangle$ is then given by $T_\ell = T_0 + \ell\Delta T$.

In addition, a photon absorption effects the transfer of the momentum $\hbar k_L$. Because a standing-wave is a superposition of two counter propagating plane waves, one expects that an absorption splits a momentum eigenstate $|p\rangle$ into a superposition

$$|p\rangle \rightarrow \frac{1}{\sqrt{2}}(|p+\hbar k_L\rangle + |p-\hbar k_L\rangle) = \sqrt{2}\cos(k_L x)\,|p\rangle\,. \tag{3.23}$$

As shown in Eq. (3.23), this coherent momentum splitting can be described by the operator $\sqrt{2}\cos(k_L x)$. This transformation holds for an arbitrary state

$$|\psi\rangle \to \sqrt{2}\cos(k_L x)\,|\psi\rangle\,. \tag{3.24}$$

For a dynamical description of the absorption processes, the position dependent rates of photon absorption $\gamma(x)$ of the ground state and $\gamma_T(x)$ of the triplet state must be taken into account. The rate is given by the absorption cross section σ multiplied by the photon flux,

$$\gamma(x;t) = \frac{\sigma}{\hbar\omega_L} I(x,0,v_z t). \tag{3.25}$$

Integration over the time yields the absorption number in the laser

$$\begin{aligned} n(x) &= \int_{-\infty}^{\infty} \mathrm{d}t\, \gamma(x;t) \\ &= n_0 \cos^2(k_L x) \quad \text{with} \quad n_0 = \frac{8}{\sqrt{2\pi}} \frac{\sigma}{\hbar\omega_L} \frac{P_L}{w_y v_z}. \end{aligned} \tag{3.26}$$

3.3.3 *Master equation for the ladder model*

Having reviewed the dipole interaction and photon absorption separately in the last two sections, I am finally in a position to combine these effects. In order to describe the interaction between a delocalized matter-wave of a molecule and light, I make use of a master equation, which includes both the dipole interaction and photon absorptions.

The Hamiltonian of a molecule in an optical grating is given in terms of the dipole potential

$$\mathsf{H} = V(x, v_z t)|0\rangle\langle 0| + \sum_{\ell=1}^{\infty} V_T(x, v_z t)|\ell\rangle\langle\ell|. \tag{3.27}$$

The dipole potentials for the singlet and triplet state are denoted by V and V_T, respectively. Because the polarizability and absorption cross section are largely independent of the molecular internal temperature [96], I assume that the triplet state potential V_T is the same for all $|\ell \geq 1\rangle$. The kinetic term in Eq. (3.27) is neglected because we are dealing with a well collimated molecular beam and the eikonal approximation may be applied, see Sect. 2.3. Photon absorption can be described as a jump process in terms of a Lindblad-type master equation [97, 98]. Motivated from Eq. (3.24), the Lindblad operator describing the photon absorptions is given by

$$\mathsf{L} = \sqrt{\gamma(t)}\cos(k_L x)\,|1\rangle\langle 0| + \sqrt{\gamma_T(t)} \sum_{\ell=1}^{\infty} \cos(k_L x)\,|\ell+1\rangle\langle\ell|\,. \tag{3.28}$$

Note that the factors $\sqrt{\gamma(t)}$ and $\sqrt{\gamma_T(t)}$ in Eq. (3.28) are chosen so that the master equation incorporates the correct Poissonian probability for absorptions in the case of $\gamma = \gamma_T$. The Lindblad operator (3.28) describes two effects of photon absorption: The stepwise change of state $|\ell\rangle \to |\ell+1\rangle$ (stepwise heating) and the coherent transfer of a photon momentum $\pm\hbar k_L$, as discussed in Sect. 3.3.2.

The evolution of the density operator follows the master equation $\partial_t \rho = [\mathsf{H}, \rho]/\mathrm{i}\hbar + \mathsf{L}\rho\mathsf{L}^\dagger - \{\mathsf{L}^\dagger\mathsf{L}, \rho\}/2$. In the basis of internal states and center-of-mass position $\rho_{\ell\ell'}(x, x'; t) = \langle \ell, x \,|\, \rho \,|\, \ell', x' \rangle$, the master equation corresponds to a sequence of coupled ordinary differential equations. Because all molecules are initially in the ground state, all non-diagonal elements $\rho_{\ell\ell'}(\ell \neq \ell')$ vanish. The remaining differential equations for the internally diagonal terms $\rho_{\ell\ell}(x, x'; t)$ read

$$\begin{aligned}
\partial_t \rho_{00} &= \left[\frac{V(x, v_z t) - V(x', v_z t)}{\mathrm{i}\hbar} - \gamma(t) \frac{\cos^2(k_\mathrm{L} x) + \cos^2(k_\mathrm{L} x')}{2} \right] \rho_{00}, && (3.29) \\
\partial_t \rho_{11} &= \left[\frac{V_\mathrm{T}(x, v_z t) - V_\mathrm{T}(x', v_z t)}{\mathrm{i}\hbar} - \gamma_\mathrm{T}(t) \frac{\cos^2(k_\mathrm{L} x) + \cos^2(k_\mathrm{L} x')}{2} \right] \rho_{11} \\
&\quad + \gamma(t) \cos(k_\mathrm{L} x) \cos(k_\mathrm{L} x') \rho_{00}. && (3.30) \\
\partial_t \rho_{\ell\ell} &= \left[\frac{V_\mathrm{T}(x, v_z t) - V_\mathrm{T}(x', v_z t)}{\mathrm{i}\hbar} - \gamma_\mathrm{T}(t) \frac{\cos^2(k_\mathrm{L} x) + \cos^2(k_\mathrm{L} x')}{2} \right] \rho_{\ell\ell} \\
&\quad + \gamma_\mathrm{T}(t) \cos(k_\mathrm{L} x) \cos(k_\mathrm{L} x') \rho_{\ell-1\ell-1} \quad (\text{for } \ell > 1). && (3.31)
\end{aligned}$$

The imaginary terms in Eqs. (3.29)-(3.31) describe the dipole interaction, while the other terms represent absorption of photons with the rates $\gamma(t)$ and $\gamma_\mathrm{T}(t)$.

Let us first consider the simplified case that the ground state and triplet state have the same optical properties, i.e. $V_\mathrm{T} = V$ and $\gamma_\mathrm{T} = \gamma$. The general case is considered in the next section. In this simplified case, the equation system (3.29)-(3.31) can be solved sequentially beginning with the ground state equation. For the initial condition of a incoming molecule $\rho_{00}(x, x'; -\infty) = \widetilde{\rho}(x, x')$, the solution of the ground state reads

$$\begin{aligned}
\rho_{00}(x, x'; t) &= \widetilde{\rho}(x, x') \exp\left[\int_{-\infty}^{t} \mathrm{d}\tau \, \frac{V_0(x, v_z\tau) - V_0(x', v_z\tau)}{\mathrm{i}\hbar} \right] \\
&\quad \times \exp\left[-\frac{\cos^2(k_\mathrm{L} x) + \cos^2(k_\mathrm{L} x')}{2} \int_{-\infty}^{t} \mathrm{d}\tau \, \gamma(\tau) \right]. && (3.32)
\end{aligned}$$

Note that I do not use the approximation of the laser intensity Eq. (3.6) in this calculation. Based on this result, solutions for all higher states can be calculated. The outgoing density operator for $t \to \infty$ is given by

$$\rho_{\ell\ell}(x, x', \infty) = U(x) U^*(x') K_\ell(x) K_\ell(x') \widetilde{\rho}(x, x'). \tag{3.33}$$

The dipole interaction leads to the unitary transformation of the density operator $\rho \to \mathsf{U}\rho\mathsf{U}^\dagger$ with the operator $\mathsf{U} = \exp(\mathrm{i}\phi(\mathsf{x}))$. The effect of photon absorptions is represented by the non-unitary operator

$$\mathsf{K}_\ell(\mathsf{x}) = \sqrt{\frac{n_0^\ell}{\ell!}} \cos^\ell(k_\mathrm{L}\mathsf{x}) \exp\left[-\frac{n_0}{2} \cos^2(k_\mathrm{L}\mathsf{x}) \right], \tag{3.34}$$

For the diagonal elements of the solution (3.33), which corresponds to the spatial distribution of molecules, the effect of the dipole interaction vanishes and the solution

corresponds to the position dependent Poisson probability for absorbing ℓ-photons, $\rho_{\ell\ell}(x,x;\infty) = n^{\ell}(x)\exp(-n(x))/\ell!$. If a detector in an experiment is insensitive to internal molecular states, the unconditional solution ρ_{un} is relevant, which is defined by the sum

$$\begin{aligned}\rho_{\mathrm{un}}(x,x') &:= \sum_{\ell=0}^{\infty}\rho_{\ell\ell} = \widetilde{\rho}(x,x')U(x)U^{*}(x')\sum_{\ell=0}^{\infty}K_{\ell}(x)K_{\ell}(x') \\ &= \widetilde{\rho}(x,x')\exp\left[\mathrm{i}\phi(x)-\mathrm{i}\phi(x')\right] \\ &\quad\times\exp\left(-\frac{n_0}{2}\left[\cos\left(k_{\mathrm{L}}x\right)-\cos\left(k_{\mathrm{L}}x'\right)\right]^2\right). \end{aligned} \tag{3.35}$$

3.3.4 *Incorporating excited state polarizability and absorption cross section*

In the previous section, the master equation of the ladder model is solved under the assumption that the polarizability and the absorption cross section are independent of the molecular internal states. This assumption is valid if the absorbed photon number is small, that is, the triplet state is sparsely populated. However, if the population of the triplet state can no longer be neglected, this assumption may no longer be justified. Therefore, I present the solution of the master equation (3.29)-(3.31) incorporating the triplet state polarizability and absorption cross section.

First of all, I introduce two dimensionless parameters $\eta_{\mathrm{p}}^{(\mathrm{T})}$ and $\eta_{\mathrm{a}}^{(\mathrm{T})}$, which describe the change of the triplet state dipole potential $V_{\mathrm{T}} = \eta_{\mathrm{p}}^{(\mathrm{T})}V$ and the absorption rate $\gamma_{\mathrm{T}} = \eta_{\mathrm{a}}^{(\mathrm{T})}\gamma$. In order to obtain an analytical solution of the master equation, I approximate the Gaussian laser envelope by a rectangular shape with the effective interaction time $t_{\mathrm{L}} = \sqrt{\pi/2}w_z/v_z$. This assumption, which leaves the time-integrated parameters ϕ_0 and n_0 unchanged, is well justified in the *Raman-Nath regime*, i.e. for a short interaction time [93], see also Sect. 3.1.3. For notational simplicity, I introduce four abbreviations

$$D(x,x') = \mathrm{i}\left[\phi(x)-\phi(x')\right]-\frac{1}{2}\left[n(x)+n(x')\right] \tag{3.36}$$

$$D_{\mathrm{T}}(x,x') = \mathrm{i}\eta_{\mathrm{p}}^{(\mathrm{T})}\left[\phi(x)-\phi(x')\right]-\frac{\eta_{\mathrm{a}}^{(\mathrm{T})}}{2}\left[n(x)+n(x')\right] \tag{3.37}$$

$$N(x,x') = n_0\cos(k_{\mathrm{L}}x)\cos(k_{\mathrm{L}}x') \tag{3.38}$$

$$N_{\mathrm{T}}(x,x') = n_0\eta_{\mathrm{a}}^{(\mathrm{T})}\cos(k_{\mathrm{L}}x)\cos(k_{\mathrm{L}}x') \tag{3.39}$$

With these abbreviations, the master equation reads

$$\partial_t\rho_{00} = \frac{D(x,x')}{t_{\mathrm{L}}}\rho_{00} \tag{3.40}$$

$$\partial_t\rho_{11} = \frac{D_{\mathrm{T}}(x,x')}{t_{\mathrm{L}}}\rho_{11}+\frac{N(x,x')}{t_{\mathrm{L}}}\rho_{00} \tag{3.41}$$

$$\partial_t\rho_{\ell\ell} = \frac{D_{\mathrm{T}}(x,x')}{t_{\mathrm{L}}}\rho_{\ell\ell}+\frac{N_{\mathrm{T}}(x,x')}{t_{\mathrm{L}}}\rho_{\ell-1\ell-1}\quad(\text{for }\ell\geq 2). \tag{3.42}$$

These equations can be evaluated iteratively beginning with the ground state solution $\rho_{00}(x,x';t) = \widetilde{\rho}(x,x')\exp(D(x,x')t/t_{\mathrm{L}})$, where $\widetilde{\rho}(x,x')$ is the spatial part of the initial density operator, i.e. $\rho_{\ell\ell}(x,x';0) = \widetilde{\rho}(x,x')\delta_{\ell 0}$. Equation (3.41) can be solved by means of the ansatz $\rho_{11} = C(t)\exp(D_{\mathrm{T}}t/t_{\mathrm{L}})$. Inserting this into Eq. (3.41), the unknown function $C(t)$ can be determined,

$$\begin{aligned} \partial_t C(t) &= \frac{N\widetilde{\rho}}{t_{\mathrm{L}}}\mathrm{e}^{(D-D_{\mathrm{T}})t/t_{\mathrm{L}}}, \\ \Rightarrow C(t) &= \frac{N\widetilde{\rho}}{t_{\mathrm{L}}}\int_0^t \mathrm{d}\tau\, \mathrm{e}^{(D-D_{\mathrm{T}})\tau/t_{\mathrm{L}}} = \frac{N\widetilde{\rho}}{D-D_{\mathrm{T}}}\left(\mathrm{e}^{(D-D_{\mathrm{T}})t/t_{\mathrm{L}}}-1\right). \end{aligned} \tag{3.43}$$

Here and from now on, I drop the arguments (x,x') of the functions D, D_{T} N, N_{T} and $\widetilde{\rho}$, in oder to simplify the expressions. In the same way, the solutions for all higher states can be calculated,

$$\rho_{\ell\ell}(x,x';t_{\mathrm{L}}) = \widetilde{\rho}\frac{NN_{\mathrm{T}}^{\ell-1}}{(D-D_{\mathrm{T}})^{\ell}}\left(\mathrm{e}^{D}-\mathrm{e}^{D_{\mathrm{T}}}\sum_{j=0}^{\ell-1}\frac{[D-D_{\mathrm{T}}]^j}{j!}\right). \tag{3.44}$$

This solution can be expressed in a compact form by means of the confluent hypergeometric function ${}_1F_1$ [66],

$$\rho_{\ell\ell}(x,x';t_{\mathrm{L}}) = \widetilde{\rho}\frac{NN_{\mathrm{T}}^{\ell-1}}{\ell!}\mathrm{e}^{D}{}_1F_1(\ell;\ell+1;-[D-D_{\mathrm{T}}]). \tag{3.45}$$

If $\eta_{\mathrm{a}}^{(\mathrm{T})} = \eta_{\mathrm{p}}^{(\mathrm{T})} = 1$, the confluent hypergeometric function is ${}_1F_1(\ell;\ell+1;0) = 1$ and the solution Eq. (3.45) reduces to Eq. (3.33).

Again, the unconditional solution can be calculated as the sum $\rho_{\mathrm{un}}(x,x') = \sum_{\ell=0}^{\infty}\rho_{\ell\ell}(x,x';t_{\mathrm{L}})$. This sum can be evaluated analytically using the integral representation of the hypergeometric function ${}_1F_1(\ell;\ell+1;z) = \ell\int_0^1 \mathrm{d}\theta\, \mathrm{e}^{z(1-\theta)}(1-\theta)^{\ell-1}$ [66]. Using this, the unconditional density operator is given by

$$\begin{aligned} \rho_{\mathrm{un}}(x,x';t_{\mathrm{L}}) &= \widetilde{\rho}\left\{\mathrm{e}^{D} + N\int_0^1 \mathrm{d}\theta\, \exp\left[D\theta + D_{\mathrm{T}}(1-\theta)\right]\sum_{\ell=1}^{\infty}\frac{\left[N_T(1-\theta)\right]^{\ell-1}}{(\ell-1)!}\right\} \\ &= \widetilde{\rho}\left\{\mathrm{e}^{D} + \frac{N\left[\exp\left(D_{\mathrm{T}}+N_{\mathrm{T}}\right) - \exp(D)\right]}{D_{\mathrm{T}}+N_{\mathrm{T}}-D}\right\}. \end{aligned} \tag{3.46}$$

It can be readily checked that the diagonal elements of this unconditional density operator are unchanged, $\rho_{\mathrm{un}}(x,x;t_{\mathrm{L}}) = \widetilde{\rho}(x,x)$, i.e. an optical grating does not affect the molecular spatial distribution immediately after the interaction.

3.3.5 *Optical grating transformation as a generalized measurement*

Having presented the solutions of the master equation in the previous sections, I am now in a position to discuss their interpretation. The dipole interaction leads to the unitary transformation of the density operator $\rho \to \exp(\mathrm{i}\phi(\mathrm{x}))\rho\exp(-\mathrm{i}\phi(\mathrm{x}))$ with the

position dependent eikonal phase $\phi(x)$, see Sect. 3.3.3. However, the absorption of photons is an incoherent process because of the dissipation of the photon energy and thus the state transformation cannot be represented by a unitary operator. Such incoherent transformations of a quantum state can be formulated within the framework of *operational quantum theory* [99]. In this theory, photon absorptions can be described as a *generalized measurement transformation* with a set of operators $\{\mathsf{M}_\ell\}$, which fulfill the normalization condition $\sum_{\ell=0}^{\infty}\mathsf{M}_\ell^\dagger\mathsf{M}_\ell = \mathbb{I}$ [100, 101]. Here ℓ is the number of absorbed photons, which can in principle post-detected by a detector sensitive to the internal molecular temperature. Given a measurement result ℓ, the conditional transformation of the reduced molecular state ρ reads

$$\rho \to \rho^{(\ell)} := \frac{\mathsf{M}_\ell\rho\mathsf{M}_\ell^\dagger}{\mathrm{Tr}\left[\mathsf{M}_\ell^\dagger\mathsf{M}_\ell\rho\right]}. \tag{3.47}$$

Note that the solution of the master equation $\rho_{\ell\ell}(x,x')$ and the conditional density operator $\rho^{(\ell)}$ are normalized differently: While the $\rho_{\ell\ell}(x,x')$ fulfill the condition $\sum_{\ell=0}^{\infty}\rho_{\ell\ell}(x,x) = 1$, the conditional density operator $\rho^{(\ell)}$ is normalized with respect to the trace $\mathrm{Tr}\left[\rho^{(\ell)}\right] = 1$.

First of all, let us consider the simplified case, where $\eta_{\mathrm{p}}^{(\mathrm{T})} = \eta_{\mathrm{a}}^{(\mathrm{T})} = 1$, that is, the polarizability and absorption cross section are independent of the molecular internal states. In this case, the measurement operator M_ℓ can be readily identified from the solution of the master equation (3.33) as

$$\begin{aligned}\mathsf{M}_\ell &= \mathsf{U}(\mathsf{x})\mathsf{K}_\ell(\mathsf{x}) \\ &= \sqrt{\frac{n_0^\ell}{\ell!}}\cos^\ell(k_{\mathrm{L}}\mathsf{x})\exp\left[\mathrm{i}\left(\phi_0 - \frac{n_0}{2}\right)\cos^2(k_{\mathrm{L}}x)\right].\end{aligned} \tag{3.48}$$

In order to illustrate the influence of absorptions on matter-wave diffraction, let us examine how the measurement operators M_ℓ act on a momentum eigenstate $|p\rangle$, i.e. when a perfectly collimated plane matter wave hits the grating. For this sake, it is convenient to expand the operators in a Fourier series

$$\mathsf{U}(\mathsf{x}) = \sum_{\nu\in\mathbb{Z}} u_\nu \exp\left(\mathrm{i}\frac{2\pi\mathsf{x}}{d}\nu\right), \quad \mathsf{K}_\ell = \sum_{\nu\in\mathbb{Z}} \kappa_{\ell,\nu}\exp\left(\mathrm{i}\frac{2\pi\mathsf{x}}{d}\nu\right). \tag{3.49}$$

The Fourier coefficients of the unitary operator are given by

$$\begin{aligned}u_\nu &= \frac{1}{2\pi}\int_{-\pi}^{\pi}\mathrm{d}x'\,\exp\left[-\mathrm{i}\nu x' + \mathrm{i}\phi_0\cos^2\left(\frac{x'}{2}\right)\right] \\ &= \mathrm{e}^{\mathrm{i}\phi_0/2}I_\nu\left(\mathrm{i}\frac{\phi_0}{2}\right).\end{aligned} \tag{3.50}$$

Here I_ν is the modified Bessel function of the first kind [66]. Analogously, the coefficients $\kappa_{\ell,\nu}$ can be determined to be

$$\begin{aligned}\kappa_{\nu,\ell} &= \sqrt{\frac{n_0^\ell}{\ell!}}\frac{1}{2\pi}\int_{-\pi}^{\pi}\mathrm{d}x'\,\cos^\ell(k_\mathrm{L}x')\exp\left[-\mathrm{i}\nu x'-\frac{n_0}{2}\cos^2\left(\frac{x'}{2}\right)\right]\\ &= \sqrt{\frac{n_0^\ell}{\ell!}}\frac{\mathrm{e}^{-n_0/4}}{2^\ell}\sum_{n=0}^{\ell}\binom{\ell}{n}\frac{1}{2\pi}\int_{-\pi}^{\pi}\mathrm{d}x'\,\exp\left[-\mathrm{i}\,(\nu+n-\ell/2)\,x'-\frac{n_0}{4}\cos\left(\frac{x'}{2}\right)\right]\\ &= \sqrt{\frac{n_0^\ell}{\ell!}}\frac{\mathrm{e}^{-n_0/4}}{2^\ell}\sum_{n=0}^{\ell}\binom{\ell}{n}I_{\nu+n-\ell/2}\left(-\frac{n_0}{4}\right). \qquad (3.51)\end{aligned}$$

In the first line of this calculation, I make use of the binomial expansion of $\cos^\ell(k_\mathrm{L}x)$.

It follows from the Fourier decomposition (3.50) that the dipole interaction leads to the transfer of the grating momentum $2\hbar k_\mathrm{L}$ [31, 44, 102],

$$\mathsf{U}(x)|p\rangle = \mathrm{e}^{\mathrm{i}\phi_0/2}\sum_{\nu=-\infty}^{\infty}I_\nu\left(\mathrm{i}\frac{\phi_0}{2}\right)|p+2\nu\hbar k_\mathrm{L}\rangle\,. \qquad (3.52)$$

The Fourier coefficients u_ν relate closely to the probability for a transfer of a ν-fold grating momentum, which is given by $|\,\langle p+2\nu\hbar k_\mathrm{L}\,|\,\mathsf{U}(x)\,|\,p\rangle\,|^2 = J_\nu^2(\phi_0/2)$ [102]. The transformation (3.52) describes the ideal phase-grating effect for non-absorbing particles. If a molecule absorbs no photon, the incoherent part of the measurement operator transforms the momentum eigenstate to

$$\mathsf{K}_0(x)|p\rangle = \mathrm{e}^{-n_0/4}\sum_{\nu=-\infty}^{\infty}I_\nu\left(-\frac{n_0}{4}\right)|p+2\nu\hbar k_\mathrm{L}\rangle\,. \qquad (3.53)$$

Remarkably, a diffraction effect is present because the matter-wave *amplitude* is modulated by this conditional transformation: The spatial density of the post-measurement state is redistributed closer to the standing-wave nodes where absorption events rarely take place. Note that this conditional transformation (3.53) is also used to describe the diffraction at optical ionization gratings [32, 33], where only those particles arrive at the detector that have not absorbed any photon, see also Sect. 6.2.

In the case of ℓ subsequent absorption processes, the conditional transformation is given by [44]

$$\begin{aligned}\mathsf{K}_\ell(x)|p\rangle &= \frac{\mathrm{e}^{-n_0/4}}{2^\ell}\sqrt{\frac{n_0^\ell}{\ell!}}\sum_{\nu=-\infty}^{\infty}I_\nu\left(-\frac{n_0}{4}\right)\sum_{n=0}^{\ell}\binom{\ell}{n}\\ &\quad\times|p+2\hbar k_\mathrm{L}\nu+(\ell-2n)\hbar k_\mathrm{L}\rangle\,. \qquad (3.54)\end{aligned}$$

Apart from the conditional diffraction by amplitude modulation, this transformation consists of a coherent transfer of ℓ photon recoils in units of $\pm\hbar k_\mathrm{L}$: Each absorption event splits the momentum state into two branches shifted by $\pm\hbar k_\mathrm{L}$, which can be seen as the quantum analogue of a Galton board.

The situation is more complicated if the modified triplet state polarizability $\alpha_\mathrm{T} = \eta_\mathrm{p}^{(\mathrm{T})}\alpha$ and absorption cross section $\sigma_\mathrm{T} = \eta_\mathrm{a}^{(\mathrm{T})}\sigma$ are taken into account. It turns out that the corresponding measurement operator can be obtained from the solution of the master equation (3.45) using the integral representation of the hypergeometric function, ${}_1F_1(\ell;\ell+1;z) = \ell\int_0^1 \mathrm{d}\theta\, \mathrm{e}^{z(1-\theta)}(1-\theta)^{\ell-1}$ [66]. In this integral representation, the solution reads

$$\rho_{\ell\ell} = \frac{\widetilde{\rho}}{t_\mathrm{L}}\int_0^{t_\mathrm{L}} \mathrm{d}t_1\, \frac{NN_\mathrm{T}^{\ell-1}}{(\ell-1)!}\left(1-\frac{t_1}{t_\mathrm{L}}\right)^{\ell-1} \mathrm{e}^{Dt_1/t_\mathrm{L}+D_\mathrm{T}(1-t_1/t_\mathrm{L})} \tag{3.55}$$

$$= \frac{1}{t_\mathrm{L}}\int_0^{t_\mathrm{L}} \mathrm{d}t_1\, \widetilde{\mathsf{M}}_\ell(x;t_1/t_\mathrm{L})\widetilde{\rho}(x,x')\widetilde{\mathsf{M}}_\ell^*(x';t_1/t_\mathrm{L}). \tag{3.56}$$

From this solution the measurement operator for $\ell > 0$ can be determined as

$$\widetilde{\mathsf{M}}_\ell(\mathsf{x};\theta) = \sqrt{\frac{n_0^\ell\left[\eta_\mathrm{a}(1-\theta)\right]^{\ell-1}}{(\ell-1)!}}\cos^\ell(k_\mathrm{L}\mathsf{x}) \times \exp\left[\mathrm{i}\left(\theta+\eta_\mathrm{p}^{(\mathrm{T})}(1-\theta)\right)\phi(\mathsf{x}) - \left(\theta+\eta_\mathrm{a}^{(\mathrm{T})}(1-\theta)\right)n(\mathsf{x})/2\right]. \tag{3.57}$$

For the case of $\ell = 0$, the transformation operator is given by $\widetilde{\mathsf{M}}_0(\mathsf{x};t_1) = \mathsf{M}_0(\mathsf{x})$ from Eq. (3.48).

The measurement operator (3.57) depends on a new parameter $t_1 \in [0, t_\mathrm{L}]$, which can be interpreted as the time of the first photon absorption. With this time, the state transformation can be divided into three regimes: ① For $0 \le t < t_1$, the quantum state transforms in terms of the measurement operator M_0 with the ground state properties ϕ_0 and n_0. ② At $t = t_1$, an absorption event transforms the state with the jump operator $\sqrt{n_0}\cos(k_\mathrm{L}\mathsf{x})$, see Eq. (3.28). ③ For the remaining time $t_1 < t \le t_\mathrm{L}$, the state transformation is given by the measurement operator $\mathsf{M}_{\ell-1}$ with the excited-state properties $\eta_\mathrm{p}^{(\mathrm{T})}\phi_0$ and $\eta_\mathrm{a}^{(\mathrm{T})}n_0$. Thus the measurement operator $\widetilde{\mathsf{M}}_\ell(\mathsf{x};t_1)$ can be equivalently expressed as

$$\widetilde{\mathsf{M}}_\ell(\mathsf{x};\theta) = \underbrace{\mathsf{M}_0\left(\phi_0\theta, n_0\theta\right)}_{①}\underbrace{\sqrt{n_0}\cos(k_\mathrm{L}\mathsf{x})}_{②}\underbrace{\mathsf{M}_{\ell-1}\left(\eta_\mathrm{p}^{(\mathrm{T})}\phi_0\left[1-\theta\right], \eta_\mathrm{a}^{(\mathrm{T})}n_0\left[1-\theta\right]\right)}_{③}. \tag{3.58}$$

3.4 CALCULATION OF THE TALBOT COEFFICIENTS FOR THE LADDER MODEL

For calculating the molecular density distribution in matter-wave interferometers Talbot coefficients are needed, as discussed in Chapter 2. In this section, I present the calculation of the Talbot-coefficients based on the results of the ladder model introduced in Sect. 3.3. If the polarizability and absorption cross section are independent of the molecular internal state, i.e. $\eta_\mathrm{p}^{(\mathrm{T})} = \eta_\mathrm{a}^{(\mathrm{T})} = 1$, the Talbot coefficients can be evaluated analytically, as we will see later in this section.

3.4.1 *Unconditional Talbot coefficients*

Let us first consider the simpler case of unconditional Talbot coefficients, which are required if a detector is insensitive to the internal molecular temperature. They are given by the Fourier integral of the unconditional solution of the master equation (3.35),

$$\begin{aligned} B_n(\xi) &= \frac{1}{d}\int_{-d/2}^{d/2} \mathrm{d}x\, \exp\left(-\mathrm{i}\frac{2\pi x}{d}n\right) \sum_{\ell=0}^{\infty} M_\ell(x-\xi d/2) M_\ell^*(x+\xi d/2) \\ &= \frac{\mathrm{e}^{-\zeta'_{\mathrm{abs}}(\xi)}}{2\pi}\int_{-\pi}^{\pi} \mathrm{d}x'\, \exp\left(-\mathrm{i}nx' + \zeta_{\mathrm{coh}}(\xi)\sin(x') - \zeta'_{\mathrm{abs}}(\xi)\cos(x')\right). \end{aligned} \tag{3.59}$$

Here, the functions

$$\zeta_{\mathrm{coh}}(\xi) := \phi_0 \sin(\pi\xi), \quad \zeta'_{\mathrm{abs}}(\xi) := n_0 \sin^2\left(\frac{\pi\xi}{2}\right) \tag{3.60}$$

represent the dipole interaction and photon absorptions, respectively [31, 33]. The prime sign for ζ'_{abs} is used in order to distinguish it from ζ_{abs}, which appears in the calculation of the conditional Talbot coefficients in the next section. The integral (3.59) can be evaluated by means of the convolution theorem. The Talbot coefficients are then given by a discrete convolution of two Bessel functions

$$B_n(\xi) = \mathrm{e}^{-\zeta'_{\mathrm{abs}}} \sum_{j\in\mathbb{Z}} J_j\left(\zeta_{\mathrm{coh}}\right) I_{n-j}\left(\zeta'_{\mathrm{abs}}\right), \tag{3.61}$$

where $J_j(x)$ is the Bessel function of the first kind [66]. By means of a special case of Graf's addition theorem [66], this convolution can be evaluated analytically [31, 33],

$$\sum_{j\in\mathbb{Z}} J_j(u)\, I_{j+n}(v) = \left(\frac{u-v}{u+v}\right)^{n/2} J_{-n}\left(\mathrm{sgn}(u+v)\sqrt{u^2+v^2}\right) \tag{3.62}$$

$$\Leftrightarrow \sum_{j\in\mathbb{Z}} J_j(u)\, I_{n-j}(v) = \left(\frac{u+v}{u-v}\right)^{n/2} J_n\left(\mathrm{sgn}(u-v)\sqrt{u^2+v^2}\right). \tag{3.63}$$

For the second line of this calculation, I make use of $I_{-\nu}(x) = I_\nu(x)$, $J_n(-x) = (-1)^n J_n(x)$ [66] and

$$\left(\frac{u-v}{u+v}\right)^{-n/2} \mathrm{sgn}(u+v)^n = \left(\frac{u+v}{u-v}\right)^{n/2} \mathrm{sgn}(u-v)^n \quad \forall u, v \in \mathbb{R}. \tag{3.64}$$

The unconditional Talbot coefficients then read [33]

$$B_n(\xi) = \mathrm{e}^{-\zeta'_{\mathrm{abs}}} \left(\frac{\zeta_{\mathrm{coh}} + \zeta'_{\mathrm{abs}}}{\zeta_{\mathrm{coh}} - \zeta'_{\mathrm{abs}}}\right)^{n/2} J_n\left[\mathrm{sgn}\left(\zeta_{\mathrm{coh}} - \zeta'_{\mathrm{abs}}\right)\sqrt{\zeta_{\mathrm{coh}}^2 - \left(\zeta'_{\mathrm{abs}}\right)^2}\right]. \tag{3.65}$$

Note that the earlier model predict different Talbot coefficients, where photon absorption was treated as a classical random walk in phase space [31], disregarding the

coherent transfer of photon momenta in a standing wave. Curiously, the difference are given by merely the sign flip $\zeta_{\mathrm{coh}} \to -\zeta_{\mathrm{coh}}$ in 3.65, which is equivalent to replacing $B_n(\xi)$ by $B_n(-\xi) = B_{-n}(\xi)$ using the relation (3.64). That is the difference vanish for both pure phase and pure absorptive gratings.

3.4.2 *Conditional Talbot coefficients*

The conditional Talbot coefficients can be calculated from the solution of the ladder master equation (3.45),

$$B_n(\xi;\ell) \;=\; \frac{1}{d}\int_{-d/2}^{d/2} \mathrm{d}x\, \exp\left(-\mathrm{i}\frac{2\pi x}{d}n\right) M_\ell(x-\xi d/2)M_\ell^*(x+\xi d/2). \quad (3.66)$$

Using again the convolution theorem, the Talbot coefficients may be represented by a discrete convolution

$$B_n(\xi;\ell) = \sum_{j\in\mathbb{Z}} J_j\left(\zeta_{\mathrm{coh}}\right) B^{\mathrm{abs}}_{n-j}(\xi;\ell). \quad (3.67)$$

Here, the coefficients $B_n^{\mathrm{abs}}(\xi)$ relate to the absorption part of the interaction and are given by the Fourier integral

$$\begin{aligned} B_n^{\mathrm{abs}}(\xi;\ell) \;&=\; \frac{1}{d}\int_{-d/2}^{d/2} \mathrm{d}x\, \exp\left(-\mathrm{i}\frac{2\pi x}{d}n\right) K_\ell(x-\xi d/2)K_\ell(x+\xi d/2) \\ &=\; \frac{\mathrm{e}^{-n_0/2}}{\ell!}\frac{1}{2\pi}\int_{-\pi}^{\pi}\mathrm{d}x'\,\mathrm{e}^{-\mathrm{i}x'n}\left(\frac{n_0}{2}\cos(x')+\zeta_{\mathrm{abs}}(\xi)\right)^{\ell}\mathrm{e}^{-\zeta_{\mathrm{abs}}(\xi)\cos x'}. \quad (3.68) \end{aligned}$$

The function ζ_{abs} represents the effect of photon absorption and is defined by

$$\zeta_{\mathrm{abs}}(\xi) := \frac{n_0}{2}\cos(\pi\xi) = \frac{n_0}{2} - \zeta'_{\mathrm{abs}}(\xi). \quad (3.69)$$

Note that this definition differs from ζ'_{abs} in the unconditional case, see Eq. (5.40). Using the binomial expansion, the Fourier integral can be evaluated to

$$\begin{aligned} B_n^{\mathrm{abs}}(\xi;\ell) \;&=\; \frac{\mathrm{e}^{-n_0/2}}{\ell!}\sum_{k=0}^{\ell}\binom{\ell}{k}\zeta_{\mathrm{abs}}^{\ell-k}\left(\frac{n_0}{2}\right)^k\frac{1}{2\pi}\int_{-\pi}^{\pi}\mathrm{d}x'\,\cos^k(x')\mathrm{e}^{-\zeta_{\mathrm{abs}}\cos(x')} \\ &=\; \frac{\mathrm{e}^{-n_0/2}}{\ell!}\sum_{k=0}^{\ell}\binom{\ell}{k}\zeta_{\mathrm{abs}}^{\ell-k}\left(\frac{n_0}{2}\right)^k(-1)^k\frac{\partial^k}{\partial\zeta_{\mathrm{abs}}^k}I_n\left(-\zeta_{\mathrm{abs}}\right) \\ &=\; \frac{\mathrm{e}^{-n_0/2}}{\ell!}\sum_{k=0}^{\ell}\sum_{m=0}^{k}\left(\frac{n_0}{4}\right)^k\frac{(\ell-m)!\zeta_{\mathrm{abs}}^{\ell-k}}{(\ell-k)!(k-m)!}I_{n-k+2m}\left(-\zeta_{\mathrm{abs}}\right). \quad (3.70) \end{aligned}$$

For the third line of this calculation, I make use of the derivative relation of the Bessel function $[\partial_z]^k I_n(z) = 2^{-k}\sum_{m=0}^{k}\binom{k}{m}I_{n-k+2m}$ [66]. Using again a special case (3.63) of Graf's addition theorem, I finally obtain an analytic result for the conditional Talbot coefficients. The coefficients for $\ell = 0$ read

$$B_n(\xi;0) = \mathrm{e}^{-n_0/2}\left(\frac{\zeta_{\mathrm{coh}}-\zeta_{\mathrm{abs}}}{\zeta_{\mathrm{coh}}+\zeta_{\mathrm{abs}}}\right)^{n/2} J_n\left[\mathrm{sgn}\left(\zeta_{\mathrm{coh}}+\zeta_{\mathrm{abs}}\right)\sqrt{\zeta_{\mathrm{coh}}^2-\zeta_{\mathrm{abs}}^2}\right]. \tag{3.71}$$

This coincides with the Talbot coefficients for a single-photon ionization grating [32, 33]. For $\ell > 0$ the Talbot coefficients read

$$B_n(\xi;\ell) = \sum_{k=0}^{\ell}\sum_{m=0}^{k}\left(\frac{n_0}{4}\right)^k \frac{(\ell-m)!\zeta_{\mathrm{abs}}^{\ell-k}}{\ell!(\ell-k)!(k-m)!} B_{n-k+2m}(\xi;0). \tag{3.72}$$

The Eqs. (3.65) and (3.72) are used for the numerical calculation of interferograms in several matter-wave interferometers in Chapter 6.

In this Chapter, I examined how the triplet excited state affects the diffraction of molecules by an optical grating. I introduced the ladder model to describe the interplay of the molecular center-of-mass motion and the internal dynamics, where I assumed that the quantum yields of fluorescence $S_1 \to S_0 + \gamma$ and internal conversion $S_1 \to S_0$ are small, $\Phi_{\mathrm{IC}},\ \Phi_{\mathrm{F}} \ll 1$. In the next chapter, I discuss the more general case including fluorescence and internal conversion, which are expected to have an large impact on the molecular motional state.

4

INCORPORATING FLUORESCENCE

In the previous chapter, I introduced the ladder model of a delocalized molecular matter-wave with a standing light field. It delivers reliable results if the singlet lifetime is short compared to the interaction time and if the intersystem crossing dominates the relaxation process. While it is a good approximation e.g. for C_{60} or C_{70} [44], this model is likely to fail for a molecule which has a large fluorescence yield e.g. Hypericine, TPP and Anthracene. In this chapter, I present a master equation, which includes also the effect of fluorescence.

One of the most striking effect of fluorescence in a matter-wave interferometer is *decoherence*, the reduction of the molecular center-of-mass coherence, as already observed in atom interferometry [103]. In principle, one could obtain information on the whereabouts of a molecule by measuring a fluorescence photon implying that fluorescence leads to decoherence. As we will see in Chapter 6, the effect of fluorescence can no longer be neglected if the mean absorbed photon number of the molecule exceeds $n_0 \gtrsim 2$.

In Sect. 4.1 I consider the molecular dynamics consisting of three internal states: a ground S_0, a singlet excited S_1 and a triplet excited state T_1. Because the lifetime of the singlet excited state is usually much shorter than the interaction time, it is reasonable to consider the effect of fluorescence in the limit of $\tau_{\mathrm{tot}}/t_{\mathrm{L}} \ll 1$ treated in Sect. 4.2.

4.1 FLUORESCENCE MASTER EQUATION

The ladder master equation introduced in the previous chapter describes the effect of photon absorptions by considering the conditional state $\rho_{\ell\ell}$ associated to the number of absorbed photons ℓ. The aim of this chapter is to examine the effect of fluorescence, and because the fluorescence lifetime is largely independent of the molecular internal temperature [84], I consider the unconditional density operator $\rho = \sum_{\ell=0}^{\infty} \rho_{\ell\ell}$, where the absorbed photon number is traced out. After reviewing general characteristics of fluorescence in Sect. 4.1.1, a fluorescence master equation is introduced and solved in Sect. 4.1.2.

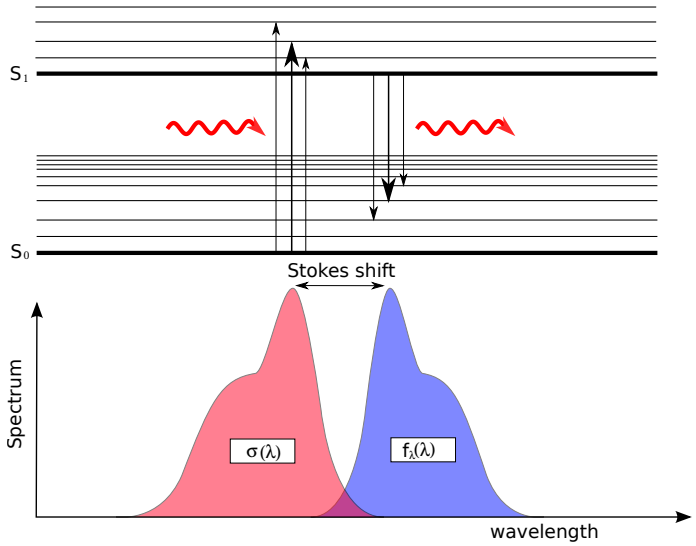

Figure 15: This figure illustrates schematically the photoexcitation of a molecule $S_0 \rightarrow S_1^*$ as well as fluorescence $S_1 \rightarrow S_0 + \gamma$ and the associated absorption and fluorescence spectra $\sigma(\lambda)$ and $f_\lambda(\lambda)$. Note that the molecule is excited both in the electronic and vibrational states S_1^* after the absorption of photons. The maximum of the fluorescence spectrum $f_\lambda(\lambda)$ is red shifted compared to the absorption spectrum $\sigma(\lambda)$, which is known as *Stokes Shift*.

4.1.1 *General characteristics of fluorescence*

Fluorescence originates from the vibrational ground state of the first excited state, $S_1 \rightarrow S_0^* + \gamma$. Note that the decay to the vibrational ground state $S_1 \rightarrow S_0 + \gamma$ is not preferred according to the *Franck-Condon principle* [35]. This principle states that an electronic transition between the two vibrational states is more likely if the overlap of two vibrational wave functions is large. For most molecules, however, the wavefunction overlap between the vibrational ground states of S_1 and S_0 is small [35].

In contrast to an atomic photon emission, fluorescence exhibits a quasi-continuous spectrum $f_\lambda(\lambda)$ because numerous vibrational states are involved, see Fig. 15. The decay of a higher singlet state to the next lower singlet state $S_n \rightarrow S_{n-1}$ occurs predominantly radiationless over internal conversion because of its extremely short lifetime. In addition, fluorescence originates usually from the vibronic ground state S_1, and thus a fluorescence spectrum $f_\lambda(\lambda)$ is generally independent of the excitation wavelength, which is known as the *Kasha's rule* [76, 83].

Often the fluorescence spectrum corresponds to a mirror image of the absorption spectrum as depicted in Fig. 15. This phenomenon is known as the *mirror-image rule* and results from the fact that the vibrational level spacings in the ground S_0 and excited state S_1 are similar. Relating to the mirror-image rule, the maximum of a fluorescence spectrum is red shifted comparing to the absorption spectrum. This displacement is referred to as the *Stokes shift*, which was already observed in 1845 by G. G.

Stokes [76]. This phenomenon can be led back to the fact that the excess energy of the absorbed photon dissipates due to radiationless relaxations, see also Sect. 3.1.

An emission of a fluorescence photon also effects the molecular center-of-mass state: A molecule experience a momentum recoil $-\hbar\mathbf{k}_F$ with the wavevector of a fluorescence photon $\mathbf{k}_F$. Because it is possible, in principle, to gain "which-way" information on the molecular position from an emitted photon, fluorescence leads to the reduction of the molecular coherence. The precision of a position measurement increases with the frequency of the emitted photon according to the *Abbe diffraction limit* [65]. That means, the higher the fluorescence frequency is, the greater is the effect of decoherence.

4.1.2 *Formulation of a master equation*

Having reviewed the general properties of fluorescence, I present in this section a master equation, which describes the molecule-light interaction including the effect of fluorescence. As discussed in Sect. 3.1, internal molecular states can be approximated effectively by the three level system consisting of a singlet ground state $|0\rangle$, an excited singlet state $|1\rangle$ and the lowest triplet state $|2\rangle$. In contrast to the ladder model introduced in Sect. 3.3, where only the ground and triplet state play a major role, I consider the more general case, where also the singlet excited state is taken into account. The singlet excited state has three decay channels: decay over intersystem crossing to the triplet state, decay over internal conversion and fluorescence to the ground state. The rate of each process shall be denoted by γ_{ISC}, γ_{IC} and γ_F, respectively.

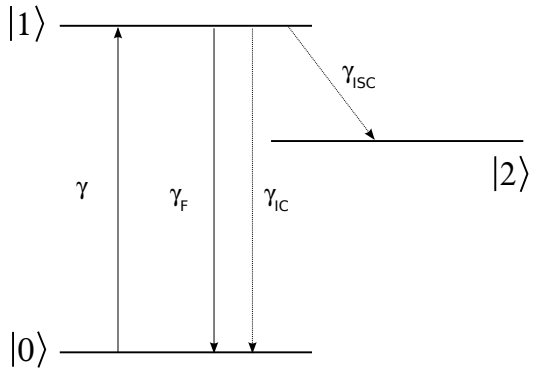

Figure 16: Schematic illustration of the three level model. Solid and dashed lines represent radiative and radiationless process, respectively.

Using the approximated laser intensity (3.6), the dipole interaction can be described by the Hamiltonian

$$H = \frac{\phi_0}{t_L}\cos^2(k_L x)\left[|0\rangle\langle 0| + \eta_p^{(S)}|1\rangle\langle 1| + \eta_p^{(T)}|2\rangle\langle 2|\right], \tag{4.1}$$

where $\eta_p^{(S)}$ and $\eta_p^{(T)}$ are the enhancement factors of the molecular polarizability for the singlet and triplet excited state, respectively. In order to incorporate the effect of photon absorptions and decays, I introduce six Lindblad operators

$$\mathsf{L}_0 = \sqrt{\gamma}\cos(k_{\mathrm{L}}\mathsf{x})\,|1\rangle\langle 0|\,, \qquad \mathsf{L}_1 = \sqrt{\gamma\eta_{\mathrm{a}}^{(\mathrm{S})}}\cos(k_{\mathrm{L}}\mathsf{x})\,|1\rangle\langle 1|\,, \tag{4.2}$$

$$\mathsf{L}_2 = \sqrt{\gamma\eta_{\mathrm{a}}^{(\mathrm{T})}}\cos(k_{\mathrm{L}}\mathsf{x})\,|2\rangle\langle 2|\,, \quad \mathsf{L}_3 = \sqrt{\gamma_{\mathrm{ISC}}}\,|2\rangle\langle 1|\,, \tag{4.3}$$

$$\mathsf{L}_4 = \sqrt{\gamma_{\mathrm{IC}}}\,|0\rangle\langle 1|\,, \qquad \mathsf{L}_5 = \sqrt{\gamma_{\mathrm{F}}}\exp\left(-\mathrm{i}\mathbf{k}\cdot\mathbf{e}_x\mathsf{x}\right)|0\rangle\langle 1|\,. \tag{4.4}$$

The operators L_0, L_1 and L_2 represent the effect of a photon absorption in the levels 0, 1, 2, respectively ,where the operator $\cos(k_{\mathrm{L}}\mathsf{x})$ describes the coherent transfer of the photon momentum, see Eq. (3.28). Note that the operators L_1 and L_2 do not change the internal electronic level because of the fast internal conversion of the excitation energy. The other operators L_3, L_4 and L_5 stand for the decay processes of the singlet excited state. The operator L_5 for fluorescence contains $\exp(-\mathrm{i}\mathbf{k}\cdot\mathbf{e}_x\mathsf{x})$, which represents a momentum kick $\hbar\mathbf{k}$ projected on the x-axis (laser direction). Note that only molecular motion in x-direction is relevant, as discussed in Chapter 2.

Assuming an isotropic emission of the fluorescence photons, the master equation reads

$$\partial_t\rho = \frac{1}{\mathrm{i}\hbar}[\mathsf{H},\rho] + \sum_{j=0}^{4}\mathsf{L}_j\rho\mathsf{L}_j^\dagger - \frac{1}{2}\{\mathsf{L}_j^\dagger\mathsf{L}_j,\rho\} + \int\frac{\mathrm{d}^3k}{4\pi k^2}f_k(k)\left[\mathsf{L}_5\rho\mathsf{L}_5^\dagger - \frac{1}{2}\{\mathsf{L}_5^\dagger\mathsf{L}_5,\rho\}\right]. \tag{4.5}$$

Here, the fluorescence part is averaged over the wavevector $\mathbf{k}$ weighted by the normalized isotropic spectrum $f_k(k)/4\pi k^2$. For the matrix elements $\rho_{jj}(x,x') = \langle j,x\,|\,\rho\,|\,j,x'\rangle$, the master equation (4.6) results three coupled differential equations

$$\partial_t\rho_{00} = \frac{D(x,x')}{t_{\mathrm{L}}}\rho_{00} + \left[\gamma_{\mathrm{IC}} + \gamma_{\mathrm{F}}F(x-x')\right]\rho_{11} \tag{4.6}$$

$$\partial_t\rho_{11} = \left[D_{\mathrm{S}}(x,x') + N_{\mathrm{S}}(x,x') - \gamma_{\mathrm{tot}}t_{\mathrm{L}}\right]\frac{\rho_{11}}{t_{\mathrm{L}}} + \frac{N(x,x')}{t_{\mathrm{L}}}\rho_{00} \tag{4.7}$$

$$\partial_t\rho_{22} = \left[D_{\mathrm{T}}(x,x') + N_{\mathrm{T}}(x,x')\right]\frac{\rho_{22}}{t_{\mathrm{L}}} + \gamma_{\mathrm{ISC}}\rho_{11}, \tag{4.8}$$

where the following abbreviations are introduced,

$$\begin{aligned} D_{\mathrm{S}}(x,x') &= \mathrm{i}\eta_{\mathrm{P}}^{(\mathrm{S})}\left[\phi(x) - \phi(x')\right] - \frac{\eta_{\mathrm{a}}^{(\mathrm{S})}}{2}\left[n(x) + n(x')\right] \\ N_{\mathrm{S}}(x,x') &= n_0\eta_{\mathrm{a}}^{(\mathrm{S})}\cos(k_{\mathrm{L}}x)\cos(k_{\mathrm{L}}x'). \end{aligned}$$

Note that the internally non-diagonal elements vanish for the initial condition $\rho_{jj'}(x,x';t=0) = \widetilde{\rho}(x,x')\delta_{j0}\delta_{j'0}$. Here, the total decay rate of the singlet state is denoted by $\gamma_{\mathrm{tot}} = \gamma_{\mathrm{ISC}} + \gamma_{\mathrm{IC}} + \gamma_{\mathrm{F}}$ and the effect of fluorescence contains the function

$$\begin{aligned} F(x-x') &= \int_0^\infty \mathrm{d}k\, f_k(k)\int\frac{d\Omega}{4\pi}\mathrm{e}^{-\mathrm{i}\mathbf{k}\cdot\mathbf{e}_x(x-x')} \\ &= \int_0^\infty \mathrm{d}k\, f_k(k)\mathrm{sinc}\left[k(x-x')\right]. \end{aligned} \tag{4.9}$$

It can be shown by means of the triangle inequality for the integral that this function is bounded by $|F(x-x')| \leq 1$ with the equality only for $x - x' = 0$. That is, this function represents the reduction of the spatial coherence i.e. decoherence due to fluorescence.

At first, the differential equations (4.6) and (4.7) are solved using the general solution of the 2×2 coupled differential equations presented in Appendix A. For the initial condition $\rho_{jj}(x,x';0) = \widetilde{\rho}(x,x')\delta_{j0}$, the solution reads

$$\begin{aligned}\rho_{00}(x,x';t_{\mathrm{L}}) &= \frac{\widetilde{\rho}}{\lambda_+ - \lambda_-}\Bigg\{\lambda_+ \mathrm{e}^{\lambda_+ t_{\mathrm{L}}} - \lambda_- \mathrm{e}^{\lambda_- t_{\mathrm{L}}} \\ &\quad -\frac{1}{t_{\mathrm{L}}}\left(D_{\mathrm{S}} + N_{\mathrm{S}} - \gamma_{\mathrm{tot}} t_{\mathrm{L}}\right)\left(\mathrm{e}^{\lambda_+ t_{\mathrm{L}}} - \mathrm{e}^{\lambda_- t_{\mathrm{L}}}\right)\Bigg\} \qquad (4.10)\\ \rho_{11}(x,x';t_{\mathrm{L}}) &= \frac{N\widetilde{\rho}}{\lambda_+ - \lambda_-}\left(\mathrm{e}^{\lambda_+ t_{\mathrm{L}}} - \mathrm{e}^{\lambda_- t_{\mathrm{L}}}\right), \qquad (4.11)\end{aligned}$$

where $\lambda_\pm$ are the eigenvalues given by

$$\begin{aligned}\lambda_\pm(x,x') &= \frac{1}{2t_{\mathrm{L}}}\Big[D + D_{\mathrm{S}} + N_{\mathrm{S}} - \gamma_{\mathrm{tot}} t_{\mathrm{L}} \\ &\quad \pm\sqrt{(D - D_{\mathrm{S}} - N_{\mathrm{S}} + \gamma_{\mathrm{tot}} t_{\mathrm{L}})^2 + 4N t_{\mathrm{L}}(\gamma_{\mathrm{IC}} + \gamma_{\mathrm{F}} F(x-x'))}\Big]. \qquad (4.12)\end{aligned}$$

The solution for the triplet state can be obtained by means of the ansatz $\rho_{22} = C(x,x';t)$ $\exp[(D_T + N_T)t/t_{\mathrm{L}}]$. Inserting this into the differential equation (4.8), the unknown function $C(x,x';t)$ can be determined to

$$\begin{aligned}C(x,x';t) &= \gamma_{\mathrm{ISC}}\int_0^t \mathrm{d}\tau\, \rho_{11}\mathrm{e}^{-(D_T+N_T)\tau/t_{\mathrm{L}}} \\ &= \widetilde{\rho}\frac{\gamma_{\mathrm{ISC}} N}{\lambda_+ - \lambda_-}\Bigg\{\frac{\exp\left[(\lambda_+ t_{\mathrm{L}} - D_T - N_T)\, t/t_{\mathrm{L}}\right] - 1}{\lambda_+ t_{\mathrm{L}} - D_T - N_T} \\ &\quad -\frac{\exp\left[(\lambda_- t_{\mathrm{L}} - D_T - N_T)\, t/t_{\mathrm{L}}\right] - 1}{\lambda_- t_{\mathrm{L}} - D_T - N_T}\Bigg\}. \qquad (4.13)\end{aligned}$$

The solution of the triplet state then reads

$$\begin{aligned}\rho_{22}(x,x';t_{\mathrm{L}}) &= \widetilde{\rho}\frac{\gamma_{\mathrm{ISC}} N}{\lambda_+ - \lambda_-}\Bigg\{\frac{\exp\left(\lambda_+ t_{\mathrm{L}}\right) - \exp\left(D_T + N_T\right)}{\lambda_+ t_{\mathrm{L}} - D_T - N_T} \\ &\quad -\frac{\exp\left(\lambda_- t_{\mathrm{L}}\right) - \exp\left(D_T + N_T\right)}{\lambda_- t_{\mathrm{L}} - D_T - N_T}\Bigg\}. \qquad (4.14)\end{aligned}$$

As an application of this result, I examine interference pattern of fluorescing molecules in several interferometers in Chapter 6.

For a graphical examination of the solutions (4.10), (4.11) and (4.14), it is convenient to look at the reduction of spatial coherence $\rho(-s/2, s/2)$ associated with the

separation length s and molecular transmission $\rho(x, x)$. Figure 17(a) shows the coherence $\rho(-s/2, s/2)$ for three different internal molecular states. At the separations $|s/d| = (2n+1)$, where $n \in \mathbb{N}$, the coherence of the ground state reaches its maximum $\rho_{00} = 1$, while the singlet and triplet coherence vanishes. These separations correspond to the distance between two nodes of the laser intensity, as depicted in Fig. 17(c), and thus the grating does not affect this superposition state. As expected, the spatial coherence of a molecule is suppressed with increasing separation due to fluorescence decoherence. However, the triplet state seems to be more robust against decoherence compared to the ground and singlet exited state. This is due to the fact that a significant amount of the triplet population experiences no fluorescence. As we will see in Sect. 4.2.2, about 32% of triplet molecules undergo no fluorescence for the parameters in Fig. 17. As expected, the transmission of the ground state becomes maximal at the laser anti-nodes and minimal at the laser nodes, see Fig. 17(b). Because the intersystem-crossing quantum yield is chosen to be small $\Phi_{\mathrm{ISC}} = 0.05$, the mean triplet population is only $\sim 13\%$ after the interaction.

4.2 FLUORESCENCE IN THE LIMIT OF SHORT SINGLET LIFETIME

Because a typical singlet lifetime $\tau_{\mathrm{tot}} \sim 10$ ns is much shorter than the typical laser-molecule interaction time $t_{\mathrm{L}} \sim 0.5$ µs, the singlet excited state is expected to play a minor role in the interaction process. In this section, I consider the limit of a short singlet lifetime $\tau_{\mathrm{tot}}/t_{\mathrm{L}} \to 0$, which leads to a considerable simplification of the general solution of the fluorescence master equation. For detailed analysis of the fluorescence effect, it turns out to be useful to distinguish the molecules in terms of the number of fluorescence events ℓ_{F}. It is natural to expect that the more fluorescence events take place, the stronger gets the effect of decoherence. In Sect. 4.2.2, I introduce the master equation, which depends also on the number of fluorescence photon ℓ_{F} and present its analytical solution.

4.2.1 *Unconditional solution of the master equation*

Let us consider the solution of the master equation (4.10), (4.11) and (4.14) in the limit of short singlet lifetime. First of all, a Taylor expansion of the exponential terms yields

$$\mathrm{e}^{\lambda_+ t_{\mathrm{L}}} = \exp\left(D + N\left[\Phi_{\mathrm{IC}} + \Phi_{\mathrm{F}} F\right]\right) + \mathcal{O}\left(\frac{\tau_{\mathrm{tot}}}{t_{\mathrm{L}}}\right), \tag{4.15}$$

$$\mathrm{e}^{\lambda_- t_{\mathrm{L}}} = \mathrm{e}^{-t_{\mathrm{L}}/\tau_{\mathrm{tot}}}\left\{\exp\left(D_{\mathrm{S}} + N_{\mathrm{S}} - N\left[\Phi_{\mathrm{IC}} + \Phi_{\mathrm{F}} F\right]\right) + \mathcal{O}\left(\frac{\tau_{\mathrm{tot}}}{t_{\mathrm{L}}}\right)\right\}, \tag{4.16}$$

where Φ_{IC} and Φ_{F} are the quantum yields for the internal conversion and fluorescence, see Sect. 3.1.2. In this expansion, the role of the eigenvalues $\lambda_\pm$ becomes clear: λ_+ and λ_- are relevant for the dynamics of the ground and singlet excited state, respectively.

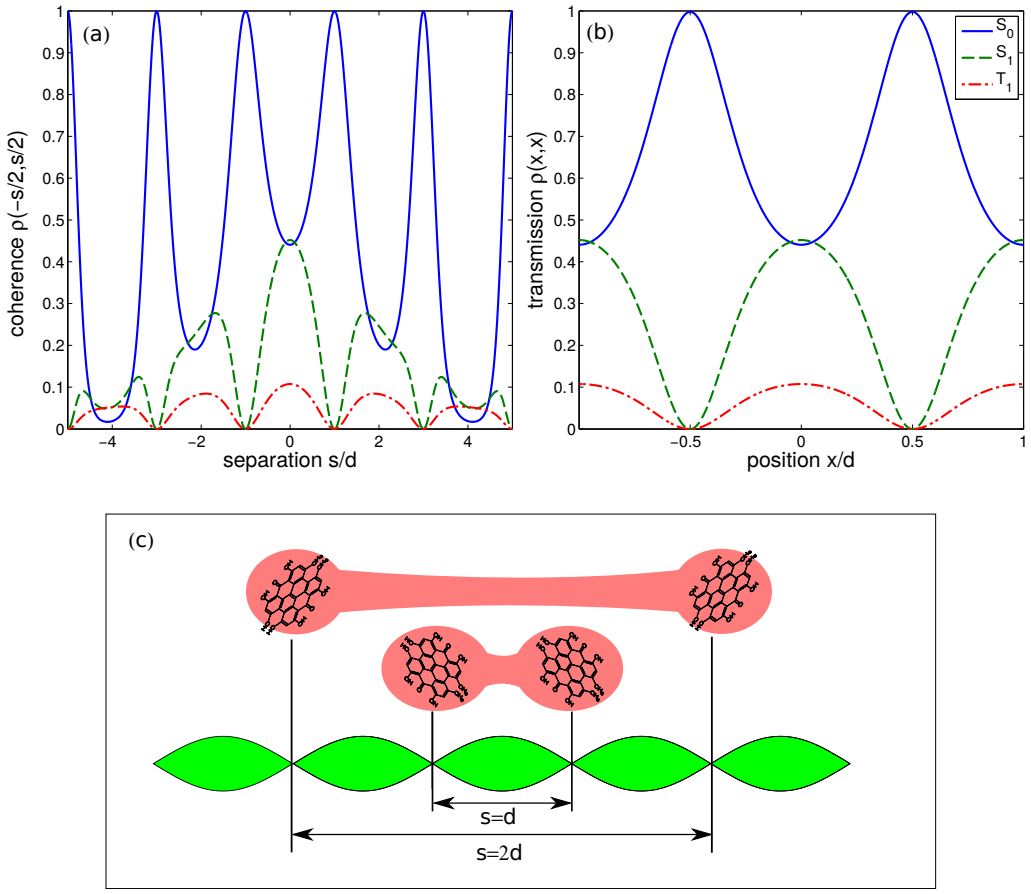

Figure 17: Panel (a) shows the spatial molecular coherence $\rho(-s/2, s/2)$ after the interaction with an optical grating. The solid, dashed and dash-dotted lines stand for the ground state S_0, excited singlet state S_1 and the triplet state T_1, respectively. For a better illustration, I assume the incident molecule to be a plane wave, i.e. a constant initial coherence and density distribution $\widetilde{\rho}(-s/2, s/2) = \widetilde{\rho}(x, x) = 1$. The spatial coherence of a molecule is reduced for a large separation $|s|$ due to the effect of fluorescence decoherence. The separation $|s/d| = (2n+1)$, $n \in \mathbb{N}$, corresponds to the distance between adjacent intensity nodes, and thus there is no interaction between laser light and the molecule in this state. Hence, the coherence of the ground state remains maximal $\rho_{00} = 1$, while the coherences of S_1 and T_1 vanish. This phenomenon is illustrated in Panel (c). Panel (b) shows the molecular transmission $\rho(x, x)$ after an optical grating. The transmission of the ground state (solid line) is maximal and minimal at nodes and anti-nodes of the laser intensity, respectively. In order to demonstrate the fluorescence effect, I assumed a large fluorescence quantum yield $\Phi_F = 0.95$, a short singlet lifetime with $\gamma_{tot} t_L = 5$ and a high absorption number $n_0 = 5$. The quantum yields and the enhancement factors are set to $\Phi_{ISC} = 0.05$, $\Phi_{IC} = 0$ and , $\eta_a^{(S)} = \eta_a^{(T)} = 1$. For simplicity, I consider here a delta-like spectral density of fluorescence $f_k(k) = \delta(k - k_L)$, where the fluorescence wavevector is chosen to $k_F = 0.7 k_L$. Note that both the spatial coherence $\rho(-s/2, s/2)$ and the transmission $\rho(x, x)$ do not depend on the strength of the dipole interaction and are real functions.

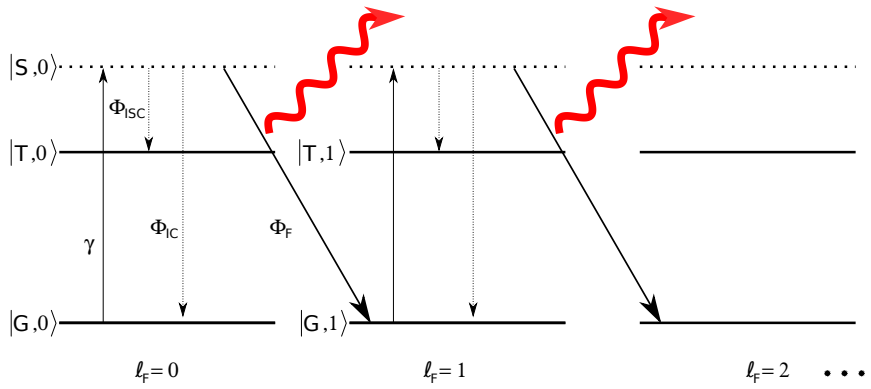

Figure 18: In order to construct a master equation which also depends on the number of fluorescence events ℓ_F, I label the molecular state additionally with ℓ_F, i.e. $|G, \ell_F\rangle$, $|S, \ell_F\rangle$ and $|T, \ell_F\rangle$ for ground, singlet, and triplet excited state, respectively. Absorption of a photon excites a molecule to the singlet state, $|G, \ell_F\rangle \to |S, \ell_F\rangle$, whose lifetime is assumed to be short, $\tau_{tot} \ll t_L$. The singlet excited state decays either over intersystem crossing, internal conversion or fluorescence with the corresponding quantum yield Φ_{ISC}, Φ_{IC} and Φ_F. In addition, fluorescence causes the stepwise increase of the number ℓ_F, $|S, \ell_F\rangle \to |G, \ell_F + 1\rangle$. Because the triplet lifetime is much larger than the interaction time, the decay of the triplet to the singlet state $T_1 \to S_0$ is neglected, see also Sect. 3.1.

Equation (4.16) shows that the terms with $\exp(\lambda_- t_L)$ are suppressed by the factor $\exp(-t_L/\tau_{tot})$ and can be neglected. In other words, the dynamics of the singlet excited state becomes redundant in this limit. The leading order contribution of the solutions of the master equation is then given by

$$\rho_{00}(x, x'; t_L) = \widetilde{\rho} \exp\left[D + N\left(\Phi_{IC} + \Phi_F F\right)\right] + \mathcal{O}\left(\frac{\tau_{tot}}{t_L}\right) \tag{4.17}$$

$$\rho_{11}(x, x'; t_L) = \mathcal{O}\left(\frac{\tau_{tot}}{t_L}\right)$$

$$\rho_{22}(x, x'; t_L) = \frac{\Phi_{ISC} N\left[\widetilde{\rho} \exp\left(D_T + N_T\right) - \rho_{00}\right]}{D_T + N_T - D - N\left(\Phi_{IC} + \Phi_F F\right)} + \mathcal{O}\left(\frac{\tau_{tot}}{t_L}\right), \tag{4.18}$$

where Φ_{ISC} is the quantum yield for the intersystem crossing, see Sect. 3.1.2. Note that the functions D, D_T, N, N_T and F in Eqs. (4.17) and (4.18) depend on positions x and x', as defined by Eqs. (3.36)-(3.39) and Eq. (4.9). It can be readily shown that the transmission of the molecule is normalized: $\rho_{00}(x, x) + \rho_{22}(x, x) = 1$. As expected, the total quantum state $\rho_{00}(x, x') + \rho_{22}(x, x')$ in the limit of $\Phi_{ISC} = 1$ and $\Phi_{IC} = \Phi_F = 0$ reduces to the unconditional results of the ladder model, see Eq. (3.35).

4.2.2 *Conditional master equation in terms of the number of fluorescence events*

In order to provide a more detailed analysis of the fluorescence effect, I introduce in this section the number ℓ_F that counts the fluorescence events. The greater the number

ℓ_F, the greater a decoherence effect we expect. Of course, if a molecule does not emit a fluorescence photon ($\ell_F = 0$), there is no decoherence. The singlet ground, singlet and triplet excited state are denoted by $|G, \ell_F\rangle$, $|S, \ell_F\rangle$ and $|T, \ell_F\rangle$, respectively. An absorption event, which promotes a molecule to the singlet excited state, $|G, \ell_F\rangle \to |S, \ell_F\rangle$, occurs with the rate γ. In the limit $\tau_{tot}/t_L \to 0$, this state decays immediately either over intersystem crossing, internal conversion or fluorescence with the quantum yields Φ_{ISC}, Φ_{IC} and Φ_F. In the case of fluorescence, the number ℓ_F is increased by 1, $|S, \ell_F\rangle \to |G, \ell_F + 1\rangle$.

These photophysical processes can be described by four Lindblad operators,

$$L_1 = \sqrt{\gamma \eta_a^{(T)}} \cos(k_L x) \sum_{\ell_F=0}^{\infty} |T, \ell_F\rangle \langle T, \ell_F| \tag{4.19}$$

$$L_2 = \sqrt{\gamma \Phi_{ISC}} \cos(k_L x) \sum_{\ell_F=0}^{\infty} |T, \ell_F\rangle \langle G, \ell_F| \tag{4.20}$$

$$L_3 = \sqrt{\gamma \Phi_{IC}} \cos(k_L x) \sum_{\ell_F=0}^{\infty} |G, \ell_F\rangle \langle G, \ell_F| \tag{4.21}$$

$$L_4 = \sqrt{\gamma \Phi_F} e^{-i\mathbf{k}\cdot\mathbf{e}_x x} \cos(k_L x) \sum_{\ell_F=0}^{\infty} |G, \ell_F + 1\rangle \langle G, \ell_F| . \tag{4.22}$$

The first Lindblad operator L_1 describes photon absorption of a molecule in the triplet state. The other operators $L_2 - L_4$ stand for the three decay processes of the singlet excited state. Note that the operators (4.19)-(4.22) do not contain the singlet excited state $|S, \ell_F\rangle$ because of the assumption $\tau_{tot}/t_L \to 0$. Together with the Hamilton operator H that describes the dipole interaction

$$H = \frac{\phi_0}{t_L} \cos^2(k_L x) \sum_{\ell_F=0}^{\infty} \left[|G, \ell_F\rangle \langle |G, \ell_F| + \eta_p^{(T)} |T, \ell_F\rangle \langle |T, \ell_F| \right], \tag{4.23}$$

the master equation reads

$$\partial_t \rho = \frac{1}{i\hbar}[H, \rho] + \sum_{n=1}^{3} L_n \rho L_n^\dagger - \frac{1}{2}\{L_n^\dagger L_n, \rho\} + \int \frac{d^3k}{4\pi k^2} f_k(k) \left[L_4 \rho L_4^\dagger - \frac{1}{2}\{L_4^\dagger L_4, \rho\} \right]. \tag{4.24}$$

For the matrix elements $\rho_{G,\ell_F} = \langle G, \ell_F | \rho | G, \ell_F \rangle$ and $\rho_{T,\ell_F} = \langle T, \ell_F | \rho | T, \ell_F \rangle$, the master equation corresponds to an infinite set of coupled differential equations,

$$t_L \partial_t \rho_{G,0} = (D + \Phi_{IC} N) \rho_{G,0} \tag{4.25}$$

$$t_L \partial_t \rho_{G,\ell_F} = (D + \Phi_{IC} N) \rho_{G,\ell_F} + \Phi_F N F \rho_{G,\ell_F - 1} \quad (\ell_F \geq 1) \tag{4.26}$$

$$t_L \partial_t \rho_{T,\ell_F} = (D_T + N_T) \rho_{T,\ell_F} + \Phi_{ISC} N \rho_{G,\ell_F}. \tag{4.27}$$

Here, the functions $N(x, x')$, $N_T(x, x')$, $D(x, x')$ and $D_T(x, x')$ are defined by Eqs. (3.36)-(3.39).

For the initial condition $\rho_{\mathrm{G},\ell_\mathrm{F}} = \widetilde{\rho}(x,x')\delta_{\ell_\mathrm{F}0}$, the ground state differential equations (4.26) can be solved iteratively starting with $\rho_{\mathrm{G},0} = \exp(D + \Phi_\mathrm{IC}F(x-x'))$. The solution reads

$$\rho_{\mathrm{G},\ell_\mathrm{F}}(x,x';t_\mathrm{L}) = \widetilde{\rho}\frac{\left[\Phi_\mathrm{F}N(x,x')F(x-x')\right]^{\ell_\mathrm{F}}}{\ell_\mathrm{F}!}\exp\left[D(x,x') + \Phi_\mathrm{IC}N(x,x')\right]. \tag{4.28}$$

The spatial coherence of the molecule gets reduced with the factor $|F(x-x')|^{\ell_\mathrm{F}} \leq 1$ and thus, as expected, the larger the number of emitted photons ℓ_F is, the greater gets the effect of decoherence. Based on the ground state solution (4.28), the triplet state solution can be calculated with the ansatz $\rho_{\mathrm{T},\ell_\mathrm{F}} = C(x,x';t)\mathrm{e}^{(D_\mathrm{T}+N_\mathrm{T})t/t_\mathrm{L}}$. Inserting this ansatz in Eq. (4.27), the unknown function $C(x,x';t)$ is determined to

$$\begin{aligned} C(x,x';t) &= \int_0^t \mathrm{d}t'\,\rho_{\mathrm{G},\ell_\mathrm{F}}\exp\left[-\left(D_\mathrm{T}+N_\mathrm{T}\right)t'/t_\mathrm{L}\right] \\ &= \frac{\Phi_\mathrm{ISC}N\left[\Phi_\mathrm{F}NF(x-x')\right]^{\ell_\mathrm{F}}}{\ell_\mathrm{F}!}\int_0^t \mathrm{d}\tau\,\tau^{\ell_\mathrm{F}}\mathrm{e}^{(D+\Phi_\mathrm{IC}N-D_\mathrm{T}-N_\mathrm{T})\tau/t_\mathrm{L}}. \end{aligned}$$

This integral can be evaluated analytically and the solution for the triplet state reads

$$\begin{aligned} \rho_{\mathrm{T},\ell_\mathrm{F}}(x,x';t_\mathrm{L}) &= \widetilde{\rho}\;\frac{\Phi_\mathrm{ISC}N\left[\Phi_\mathrm{F}NF\right]^{\ell_\mathrm{F}}}{\left[D_\mathrm{T}+N_\mathrm{T}-D-\Phi_\mathrm{IC}N\right]^{\ell_\mathrm{F}+1}}\Bigg[\exp\left(D_\mathrm{T}+N_\mathrm{T}\right) \\ &\qquad -\exp\left(D+\Phi_\mathrm{IC}N\right)\sum_{k=0}^{\ell_\mathrm{F}}\frac{\left[D_\mathrm{T}+N_\mathrm{T}-D-\Phi_\mathrm{IC}N\right]^k}{k!}\Bigg] \qquad (4.29) \\ &= \widetilde{\rho}\frac{\Phi_\mathrm{ISC}N\left[\Phi_\mathrm{F}NF\right]^{\ell_\mathrm{F}}\exp\left(D_\mathrm{T}+N_\mathrm{T}\right)}{(\ell_\mathrm{F}+1)!} \\ &\qquad \times{}_1F_1\left(\ell_\mathrm{F}+1;\ell_\mathrm{F}+2;-\left[D_\mathrm{T}+N_\mathrm{T}-D-\Phi_\mathrm{IC}N\right]\right). \qquad (4.30) \end{aligned}$$

Here, ${}_1F_1(a;b;x)$ is the confluent hypergeometric function [66].

Let us discuss these solutions graphically in Fig. 19, which shows plots of the coherence of the ground state $\rho_{\mathrm{G},\ell_\mathrm{F}}(-s/2,s/2)$ in Panel (a) and of the triplet state $\rho_{\mathrm{T},\ell_\mathrm{F}}(-s/2,s/2)$ in Panel (c). Both the ground state and triplet state coherences are reduced due to fluorescence, except for $\ell_\mathrm{F} = 0$, of course. In addition, Fig. 19(a) and (c) confirm a large decoherence effect for molecules with a high fluorescence number ℓ_F. The transmission of the ground state $\rho_{\mathrm{G},\ell_\mathrm{F}}(x,x)$ and triplet state $\rho_{\mathrm{T},\ell_\mathrm{F}}(x,x)$ are shown in Fig. 19(b) and (d), respectively. Because the quantum yield for the intersystem crossing is chosen to be small, $\Phi_\mathrm{ISC} = 0.05$, the triplet state transmission is much smaller compared to the ground state. Near the intensity nodes of the laser, $x/d = n + 1/2$ with $n \in \mathbb{N}$, molecules without fluorescence ($\ell_\mathrm{F} = 0$) dominate the transmission. For the given parameters, only about 13% of the molecules are in the triplet state after the interaction and about 32% of them experience no fluorescence.

As discussed in this chapter, fluorescence reduces the spatial coherence of molecules. If a molecule emits in total ℓ_F fluorescence photons, its spatial coherence is reduced by

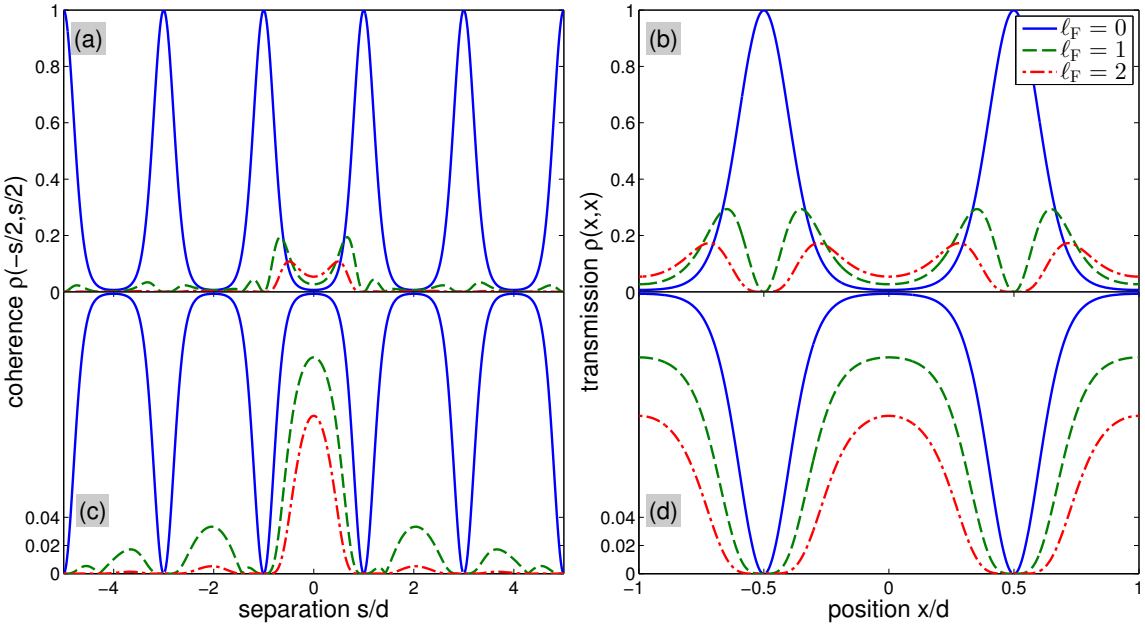

Figure 19: Panel (a) and (c) show the spatial coherence of ground state $\rho_{G,\ell_F}(-s/2, s/2)$ and triplet state molecules $\rho_{T,\ell_F}(-s/2, s/2)$, respectively. The solid lines stand for $\ell_F = 0$, dashed lines for $\ell_F = 1$ and the dash-dotted lines for $\ell_F = 2$. While the solid line indicates no effect of fluorescence, the spatial coherences are reduced for $\ell_F > 0$ due to fluorescence decoherence. The decoherence effect is stronger for $\ell_F = 2$ compared to $\ell_F = 1$. Panel (b) and (d) illustrate the position-dependent transmission for the ground $\rho_{G,\ell_F}(x, x)$ and triplet state $\rho_{T,\ell_F}(x, x)$, respectively. Because of the small intersystem crossing quantum yield $\Phi_{ISC} = 0.05$, the triplet state is much less populated than the ground state. The mean transmission of triplet state is merely about 13%. In addition, the triplet state population consists to a significant amount of molecules that undergo no fluorescence event. For the given parameter, about 32% of triplet molecules are not affected by fluorescence. For these plots I used the same parameters as in Fig. 17.

$\rho'(x, x') \to |F(x - x')|^{\ell_F} \rho(x, x')$, where $F(x - x')$ is the decoherence function defined by Eq. (4.9). I presented the analytical solution for both the conditional and unconditional master equations. Based on the results in this chapter, the effect of the fluorescence on matter-wave interference is examined in detail in Chapter 6.

5

COLLISIONAL DECOHERENCE IN PRESENCE OF A NON-SPHERICAL INTERACTION

So far, I considered the quantum description of the free propagation and the interaction between an optical grating and a molecule. However, in reality no particle is perfectly isolated and thus also the coupling to the environment must be taken into account. For example, a particle can be disturbed by its own emission of thermal photons [37], or by the scattering with environmental photons [50] and gas particles [39]. A coupling to an environment of sufficient size is known to cause the reduction of coherence of in the particle state, which is also referred to as *decoherence* [9–11]. Thus the understanding of these decoherence processes is indispensable in a high-precision matter-wave interferometer [27]. In practice, the main source of decoherence is the scattering with environmental particles, i.e. *collisional decoherence*. While the effect of thermal radiation is only relevant for very hot molecules [39], collisions are omnipresent, independent of molecular internal temperature. In the present thesis I therefore concentrate on collisional decoherence.

The effect of collisions on a center-of-mass (c.m.) quantum state is well understood if the interaction potential between the scatterers is spherical, e.g. for the van der Waals interaction. In this case, the *Quantum linear Boltzmann equation* gives a Markovian, non-perturbative, microscopic description of the particle's motion through a thermal environment [41, 42]. However, large molecules such as biomolecules are predominantly polar, and thus, the scattering potential is non-spherical. In this chapter I examine how the polarity of a molecule affects its collisional decoherence. The results of this chapter are published in [43].

For the formulation of collisional decoherence in the presence of non-spherical interactions, both the molecule's c.m. and its orientational degrees of freedom must be taken into account. In a scattering process, energy exchange can occur between the c.m. and rotation state, that is, for the description one deals with the inelastic scattering, which is captured by the *multi-channel scattering theory* of quantum theory [104–106]. The master equation for the molecular c.m. motion thus depends on the multichannel scattering amplitude [107], which is in general difficult to access. However, the rotational period of a large molecule is typically much larger than the collision time, as examined in Sect. 5.1.3. In this case a molecule may be considered as non-rotating during the interaction and a scattering event becomes effectively elastic [108, 109]. We will see in Sect. 5.1.2 that the master equation for the molecular c.m. depends in this ap-

proximation on the orientation-averaged total and differential cross section. Note that I focus on the c.m. decoherence of non-spherical molecules, rather than orientational [110–112] or configurational decoherence [113].

This chapter is structured as follows: In Sect. 5.1 I shortly review the derivation of the c.m. master equation for a non-spherical molecule in a mono-atomic gas. The scattering between a polar molecule and an atom is examined in detail in Sect. 5.2, where the orientation averaged total and differential cross sections are derived. The solution of the master equation in the limit of large molecular mass is presented in Sect. 5.3.

5.1 MASTER EQUATION FOR THE CENTER-OF-MASS MOTION

It is natural to expect that the molecular c.m. coherence is reduced due to the scattering with environmental particles. In Sect. 5.1.1, I consider a single collision between a molecule and an atom in the limit of large molecular mass, where this intuitive picture is confirmed. The dynamic description of scattering processes on the center-of-mass motion is treated in Sect. 5.1.2, where a master equation is derived by means of the *monitoring approach* [41]. The results in the present section are based on the approximation that a molecule is non-rotating during the scattering process. In Sect. 5.1.3, I examine the validity of this approximation.

5.1.1 *State transformation due to a single collision*

For the description of a single collision, I assume that the molecule and the gas atom are initially uncorrelated. That is, the total density operator is given by the product $\rho_{\mathrm{tot}} = \rho_{\mathrm{M}} \otimes \rho_{\mathrm{g}}$, where ρ_{M} and ρ_{g} are density operator describing a molecule and an atom. Because the interaction potential for the collision depends on the molecular orientation, the molecular density operator ρ_{M} contains both the c.m. (center-of-mass) state ρ and the orientation state ρ_Ω. In order to make the theoretical treatment more general, I consider the case, where $\rho_{\mathrm{M}} \neq \rho \otimes \rho_\Omega$, although the molecular internal states and c.m. state are most likely uncorrelated in practice.

It is known from scattering theory that a collision transforms the density operator ρ_{tot} of an asymptotically incoming state into $\rho'_{\mathrm{tot}} = \mathsf{S}\rho_{\mathrm{tot}}\mathsf{S}^\dagger$, where S is the scattering operator and ρ'_{tot} is the asymptotic outgoing state [40, 104]. The asymptotic molecular c.m. state is obtained by tracing out the molecular orientation and the environmental gas state, $\rho' = \mathrm{Tr}_\Omega\left[\mathrm{Tr}_{\mathrm{gas}}\left[\rho'_{\mathrm{tot}}\right]\right]$. For the examination of the decoherence effect, let us at first consider the spatial coherences

$$\left\langle \mathbf{R}_1 \middle| \rho' \middle| \mathbf{R}_2 \right\rangle = \mathrm{Tr}_\Omega\left[\mathrm{Tr}_{\mathrm{gas}}\left[\left\langle \mathbf{R}_1 \middle| \mathsf{S}\left(\rho_{\mathrm{M}} \otimes \rho_{\mathrm{g}}\right)\mathsf{S}^\dagger \middle| \mathbf{R}_2 \right\rangle\right]\right], \tag{5.1}$$

where $\mathbf{R}_{1/2}$ is the molecular c.m. position. I proceed to evaluate the rotational trace in Eq. (5.1) under the assumption that the molecule is non-rotating during the interaction, i.e. in the *sudden approximation* [108]. As examined in Sect. 5.1.3, this assumption is

well justified for a large molecule interacting with a gas at a room temperature. In this approximation, the scattering operator S is diagonal in the orientation basis with the diagonal element $\mathsf{S}(\Omega)$, where Ω denotes the molecular orientation. The diagonal elements of the total molecular state ρ_{M} in the orientation basis are $\langle \Omega \,|\, \rho_{\mathrm{M}} \,|\, \Omega \rangle = \rho/8\pi^2$. Here, the factor $8\pi^2$ corresponds to the area of the three dimensional configuration space of the orientational degrees of freedom $S = S_2 \times S_1$, represented e.g. by the three Euler angles $\alpha \in [0, 2\pi]$, $\beta \in [0, \pi]$ and $\gamma \in [0, 2\pi]$ [114, 115]. The expression (5.1) then simplifies to

$$\left\langle \mathbf{R}_1 \,\middle|\, \rho' \,\middle|\, \mathbf{R}_2 \right\rangle = \left\langle \mathrm{Tr}_{\mathrm{gas}} \left[\left\langle \mathbf{R}_1 \,\middle|\, \mathsf{S}(\Omega) \left(\rho \otimes \rho_{\mathrm{g}}\right) \mathsf{S}^{\dagger}(\Omega) \,\middle|\, \mathbf{R}_2 \right\rangle \right] \right\rangle_{\Omega}, \tag{5.2}$$

where the orientation average $\langle \cdot \rangle_{\Omega}$ is defined by

$$\langle K \rangle_{\Omega} = \int_S \frac{\mathrm{d}^3\Omega}{8\pi^2} K(\Omega). \tag{5.3}$$

The trace over the gas state in Eq. (5.2) can be calculated conveniently in the position representation of the gas particle $\mathbf{r}$,

$$\left\langle \mathbf{R}_1 \,\middle|\, \rho' \,\middle|\, \mathbf{R}_2 \right\rangle = \left\langle \int \mathrm{d}^3 r \; \langle \mathbf{r}| \langle \mathbf{R}_1| \, \mathsf{S}(\Omega) \left(\rho \otimes \rho_{\mathrm{g}}\right) \mathsf{S}^{\dagger}(\Omega) \, |\mathbf{R}_2\rangle \, |\mathbf{r}\rangle \right\rangle_{\Omega}. \tag{5.4}$$

For the further evaluation, I insert four identity operators in the representation of the gas-particle position ($\tilde{\mathbf{r}}_1$, $\tilde{\mathbf{r}}_2$) and the molecule position ($\tilde{\mathbf{R}}_1$, $\tilde{\mathbf{R}}_2$),

$$\begin{aligned} \left\langle \mathbf{R}_1 \,\middle|\, \rho' \,\middle|\, \mathbf{R}_2 \right\rangle = \Big\langle \int \mathrm{d}^3 r \int \mathrm{d}^3\tilde{r}_1 \mathrm{d}^3\tilde{r}_2 \mathrm{d}^3\tilde{R}_1 \mathrm{d}^3\tilde{R}_2 \; \langle \mathbf{r}| \langle \mathbf{R}_1| \, \mathsf{S}(\Omega) \, |\tilde{\mathbf{R}}_1\rangle \, |\tilde{\mathbf{r}}_1\rangle \left\langle \tilde{\mathbf{R}}_1 \,\middle|\, \rho \,\middle|\, \tilde{\mathbf{R}}_2 \right\rangle \\ \times \left\langle \tilde{\mathbf{r}}_1 \,\middle|\, \rho_{\mathrm{g}} \,\middle|\, \tilde{\mathbf{r}}_2 \right\rangle \langle \tilde{\mathbf{r}}_2| \left\langle \tilde{\mathbf{R}}_2 \right| \mathsf{S}^{\dagger}(\Omega) \, |\mathbf{R}_2\rangle \, |\mathbf{r}\rangle \Big\rangle_{\Omega}. \end{aligned} \tag{5.5}$$

Because the scattering operator affects only the relative position of the scatterers, $\mathsf{S}(\Omega) = \mathbb{I}_{\mathrm{c.m.}} \otimes [\mathsf{S}_0(\Omega)]_{\mathrm{rel}}$, the matrix element $\langle \mathbf{r}'| \langle \mathbf{R}'| \, \mathsf{S}(\Omega) \, |\mathbf{R}\rangle \, |\mathbf{r}\rangle$ simplifies in the c.m. and in the relative coordinate. In the limit $m/M \to 0$ with molecular mass M and atomic mass m, the matrix element is given by [104]

$$\begin{aligned} \langle \mathbf{r}'| \langle \mathbf{R}'| \, \mathsf{S}(\Omega) \, |\mathbf{R}\rangle \, |\mathbf{r}\rangle &= \delta^{(3)}(\mathbf{R}' - \mathbf{R}) \left\langle \mathbf{r}' - \mathbf{R} \,\middle|\, \mathsf{S}_0(\Omega) \,\middle|\, \mathbf{r} - \mathbf{R} \right\rangle & (5.6) \\ &= \delta^{(3)}(\mathbf{R}' - \mathbf{R}) \left\langle \mathbf{r}' \,\middle|\, \mathrm{e}^{-\mathrm{i}\mathfrak{p}\cdot\mathbf{R}/\hbar} \mathsf{S}_0(\Omega) \mathrm{e}^{\mathrm{i}\mathfrak{p}\cdot\mathbf{R}/\hbar} \,\middle|\, \mathbf{r} \right\rangle. & (5.7) \end{aligned}$$

For the second line of this calculation, I make use of the translation operator $\mathrm{e}^{-\mathrm{i}\mathfrak{p}\cdot\mathbf{R}/\hbar} \, |\mathbf{r}\rangle = |\mathbf{r} + \mathbf{R}\rangle$, where $\mathfrak{p}$ is the momentum operator acting on the state of the gas particle [53]. Inserting this result in Eq. (5.5) and evaluating the δ-functions, I end up with [40]

$$\begin{aligned} \left\langle \mathbf{R}_1 \,\middle|\, \rho' \,\middle|\, \mathbf{R}_2 \right\rangle &= \langle \mathbf{R}_1 \,|\, \rho \,|\, \mathbf{R}_2 \rangle \left\langle \int \mathrm{d}\mathbf{r} \int \mathrm{d}\tilde{\mathbf{r}}_1 \mathrm{d}\tilde{\mathbf{r}}_2 \, \langle \mathbf{r}| \, \mathrm{e}^{-\mathrm{i}\mathfrak{p}\cdot\mathbf{R}_1/\hbar} \mathsf{S}_0(\Omega) \mathrm{e}^{\mathrm{i}\mathfrak{p}\cdot\mathbf{R}_1/\hbar} \, |\tilde{\mathbf{r}}_1\rangle \right. \\ &\quad \left. \times \left\langle \tilde{\mathbf{r}}_1 \,\middle|\, \rho_{\mathrm{g}} \,\middle|\, \tilde{\mathbf{r}}_2 \right\rangle \langle \tilde{\mathbf{r}}_2| \, \mathrm{e}^{-\mathrm{i}\mathfrak{p}\cdot\mathbf{R}_2/\hbar} \mathsf{S}_0^{\dagger}(\Omega) \mathrm{e}^{\mathrm{i}\mathfrak{p}\cdot\mathbf{R}_2/\hbar} \, |\mathbf{r}\rangle \right\rangle_{\Omega} & (5.8) \\ &= \langle \mathbf{R}_1 \,|\, \rho \,|\, \mathbf{R}_2 \rangle \left\langle \mathrm{Tr}_{\mathrm{gas}} \left[\mathcal{S}_{R_2}^{\dagger}(\Omega) \mathcal{S}_{R_1}(\Omega) \rho_{\mathrm{g}} \right] \right\rangle_{\Omega}, & (5.9) \end{aligned}$$

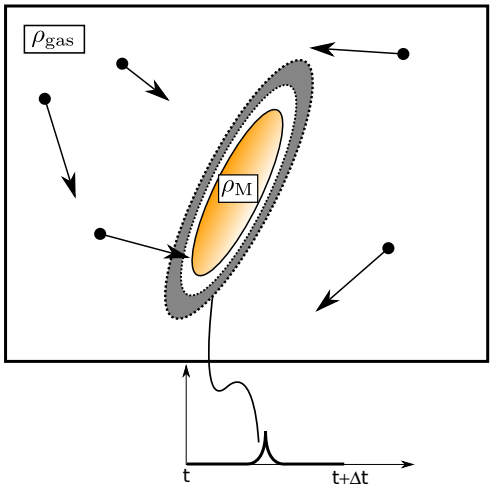

Figure 20: For a monitoring approach of a master equation, one considers a molecule interacting with environmental gas atoms. Here the multi-body scatterings are excluded. In accordance with the Markov assumption, the collision induced correlation between a molecule and a gas particle disperses quickly. That is, the total quantum state prior to each scattering process is given by the product $\rho_{\mathrm{tot}} = \rho_{\mathrm{M}} \otimes \rho_{\mathrm{g}}$. A challenge to derive a master equation is to incorporate the state-dependent scattering rate into the dynamical description. For this sake, an imaginary transit detector is introduced, which monitors the molecule continuously and detects a gas particle before each scattering event with the temporal resolution Δt.

where the abbreviation $\mathcal{S}_{R_j}(\Omega) = \mathrm{e}^{-\mathrm{i}\mathbf{p}\cdot\mathbf{R}_j/\hbar}\mathsf{S}_0(\Omega)\mathrm{e}^{\mathrm{i}\mathbf{p}\cdot\mathbf{R}_j/\hbar}$ is introduced in order to simplify the expression. It can be readily shown from the unitarity of the scattering operator $\mathsf{S}_0^\dagger\mathsf{S}_0 = \mathbb{I}$ that the diagonal elements $\langle\mathbf{R}\,|\,\rho'\,|\,\mathbf{R}\rangle$ in Eq. (5.9) are unchanged by the scattering. In contrast, the coherences are modified by the factor $\left\langle \mathrm{Tr}_{\mathrm{gas}}\left[\mathcal{S}_{R_2}^\dagger(\Omega)\mathcal{S}_{R_1}(\Omega)\rho_g\right]\right\rangle_\Omega$. By means of the Cauchy inequality, it can be shown that the absolute value of this factor is smaller than unity,

$$\begin{aligned}\left|\mathrm{Tr}_{\mathrm{gas}}\left[\mathcal{S}_2^\dagger(\Omega)\mathcal{S}_1(\Omega)\rho_{\mathrm{g}}\right]\right| &\leq \sqrt{\mathrm{Tr}_{\mathrm{gas}}\left[\mathcal{S}_{R_2}^\dagger(\Omega)\mathcal{S}_{R_2}(\Omega)\right]}\sqrt{\mathrm{Tr}_{\mathrm{gas}}\left[\mathcal{S}_{R_1}(\Omega)\rho_{\mathrm{g}}^2\mathcal{S}_{R_1}^\dagger(\Omega)\right]} \\ &= \sqrt{\mathrm{Tr}_{\mathrm{gas}}\left[\rho_{\mathrm{g}}^2\right]} \leq 1. \end{aligned} \tag{5.10}$$

Thus, as expected, collision reduces the molecular spatial coherence.

5.1.2 *Monitoring approach for the master equation*

As shown in the previous section, a single collision with an environmental particle leads to the reduction of the molecular spatial coherence, which is described by the scattering operator $\mathsf{S}(\Omega)$. In order to describe the dynamics of the motional molecular state through a gaseous environment, one requires additionally the collision probability, which depends on both the molecular state ρ_{M} and the gas state ρ_{g}. The *monitoring*

approach incorporates this state-dependent probability into the scattering description in a consistent way [41]. What follows is a brief summary of the derivation of the master equation with this approach.

First of all, for the description of the collision probability, a rate operator Γ is introduced, which is completely positive operator and acts in a two particle Hilbert space. In the limit of a slowly rotating molecule, this operator is diagonal in the molecular orientation with the diagonal elements $\Gamma(\Omega)$. Furthermore, just like the scattering operator $S(\Omega)$, it acts solely on the relative state, $\Gamma = \mathbb{I}_{\text{c.m.}} \otimes [\Gamma_0(\Omega)]_{\text{rel}}$. The probability for the collision to occur in a small time interval Δt is given in terms of the rate operator by [41]

$$\text{Prob}\left(C_{\Delta t}|\rho\right) = \Delta t \text{Tr}\left[\Gamma \rho_{\text{tot}}\right]. \tag{5.11}$$

In the monitoring approach for the master equation, scattering processes are thought to be "monitored" by an imaginary transit detector with the temporal resolution Δt, see Fig. 20. This imaginary detector tells us whether a gas atom is about to scatter off the molecule, or not. Note that this monitoring changes the quantum state according to the theory of generalized measurements as $\rho_{\text{tot}} \to \rho'_{\text{tot}} = \mathcal{M}(\rho_{\text{tot}}|C_{\Delta t})$, where $\mathcal{M}(\cdot|C_{\Delta t})$ is a completely positive map and satisfies $\text{Tr}[\mathcal{M}(\rho_{\text{tot}}|C_{\Delta t})] = \Delta t \text{Tr}[\Gamma \rho_{\text{tot}}]$ [100, 101]. In order to specify this measurement transformation $\mathcal{M}(\cdot|C_{\Delta t})$, two properties for the imaginary transit detector are proposed:

1. There is no classical uncertainty for the measurement (measurement is *efficient*).
2. There is no measurement induced back-action (measurement is *minimally invasive*).

These two conditions are well justified because the only task of this imaginary detector is to incorporate the collision probability into the scattering description in a consistent way. With these two conditions the measurement transformation can be specified to [41, 42]

$$\mathcal{M}(\rho_{\text{tot}}|C_{\Delta t}) = \frac{\Gamma^{1/2} \rho_{\text{tot}} \Gamma^{1/2}}{\text{Tr}[\Gamma \rho_{\text{tot}}]} \Delta t. \tag{5.12}$$

Because the rate operator Γ and the scattering operator S depend only parametrically on the molecular orientation in my calculation, the master equation can be derived following the same steps as for a spherical particle [41, 42]. Combining the measurement transformation (5.12) and the scattering transformation $\rho_{\text{tot}} \to \rho'_{\text{tot}} = S \rho_{\text{tot}} S^\dagger$, the molecular c.m. master equation is obtained in the limit of the continuous monitoring $\Delta t \to 0$ [51, 116],

$$\frac{\partial}{\partial t}\rho = \frac{1}{i\hbar}[H, \rho] + \mathcal{R}\rho + \mathcal{L}\rho. \tag{5.13}$$

The first term with the free Hamiltonian $H = P^2/2M$ describes the free propagation. The first superoperator

$$\mathcal{R}\rho = i \left\langle \text{Tr}_{\text{gas}} \left(\left[\Gamma^{1/2} \text{Re}\left(T\right) \Gamma^{1/2}, \rho \otimes \rho_g \right] \right) \right\rangle_\Omega \tag{5.14}$$

describes the renormalization of the system energy due to the coupling to the environment, where $\mathsf{T} = \mathsf{T}(\Omega)$ is the non-trivial part of the scattering operator $\mathsf{S}(\Omega) = 1 + i\mathsf{T}(\Omega)$. Note that the orientation dependence of the operators in Eq. (5.14) are dropped for convenience. The bracket $\langle\cdot\rangle_\Omega$ denotes the orientation average, see Eq. (5.3). The second superoperator

$$\mathcal{L}\rho = \left\langle \mathrm{Tr}_{\mathrm{gas}}\left(\mathsf{T}\Gamma^{1/2}\rho\otimes\rho_{\mathrm{g}}\Gamma^{1/2}\mathsf{T}^\dagger - \frac{1}{2}\left\{\rho\otimes\rho_{\mathrm{g}}, \Gamma^{1/2}\mathsf{T}^\dagger\mathsf{T}\Gamma^{1/2}\right\}\right)\right\rangle_\Omega \tag{5.15}$$

stands for an incoherent evolution of ρ due to scatterings. Note that the Markov assumption is made for the derivation of (5.13), that is, the collision induced molecule-gas correlation disperses completely before a new scattering.

Assuming that the environmental gas state is in thermal equilibrium for all times, the trace over the gas state can be evaluated explicitly. Instead of the complicated general expression of the quantum linear Boltzmann equation [51], let us consider the relevant limit of high molecular mass $m/M \to 0$, which results in considerable simplifications. In this limit, Eq. (5.14) yields a constant energy shift, which can be dropped [42]. The second term in Eq. (5.14) describes decoherence in the position representation [51],

$$\lim_{m/M\to 0}\langle \mathbf{R}_1 \,|\, \mathcal{L}\rho \,|\, \mathbf{R}_2\rangle = -\gamma\left[1-\eta(\mathbf{R}_1-\mathbf{R}_2)\right]\langle \mathbf{R}_1 \,|\, \rho \,|\, \mathbf{R}_2\rangle\,. \tag{5.16}$$

Here, γ is the scattering rate and can be given as

$$\gamma = \frac{n_{\mathrm{g}}}{m}\int \mathrm{d}^3p\; p\mu(|\mathbf{p}+m\mathbf{v}_{\mathrm{M}}|)\,\langle\sigma_{\mathrm{tot}}(p)\rangle_\Omega\,, \tag{5.17}$$

where $p = |\mathbf{p}|$ is the norm the momentum vector, n_{g} is the density of the gas, $\mu(|\mathbf{p}|)\mathrm{d}^3p$ is the momentum distribution of a gas and $\langle\sigma_{\mathrm{tot}}(p)\rangle_\Omega$ is the orientation averaged total scattering cross section. Note that the thermal gas distribution $\mu(|\mathbf{p}+m\mathbf{v}_{\mathrm{M}}|)$ is shifted by $m\mathbf{v}_{\mathrm{M}}$ due to the molecule's velocity $\mathbf{v}_{\mathrm{M}}$. Since the most probable momentum p_{g} of gas particles (given by $\sqrt{2mk_{\mathrm{B}}T}$ for the Maxwell-Boltzmann distribution) of gas particles is usually much higher than the momentum mv_{M}, the scattering rate can be expanded in orders of $mv_{\mathrm{M}}/p_{\mathrm{g}}$. This yields

$$\gamma = \frac{4\pi n_{\mathrm{g}}}{m}\int_0^\infty \mathrm{d}p\; p^3\mu(p)\,\langle\sigma_{\mathrm{tot}}(p)\rangle_\Omega\left[1+\mathcal{O}\left(\frac{m^2v_{\mathrm{M}}^2}{p_{\mathrm{g}}^2}\right)\right]. \tag{5.18}$$

The effective strength of the decoherence due to a single scattering is described by the *decoherence function*

$$\begin{aligned}\eta(\mathbf{R}) &= \frac{1}{N}\int_0^\infty \mathrm{d}p\; p^3\int \mathrm{d}^2n\int \mathrm{d}^2n'\mu(|\mathbf{p}+m\mathbf{v}_{\mathrm{M}}|)\\ &\quad\times\left\langle|f(p,\mathbf{n}\cdot\mathbf{n}')|^2\right\rangle_\Omega \exp\left(\frac{ip}{\hbar}(\mathbf{n}-\mathbf{n}')\cdot\mathbf{R}\right),\end{aligned} \tag{5.19}$$

where $\mathbf{n}$ and $\mathbf{n}'$ are the incoming and outgoing directions of the scattered gas atom, respectively. This function is given in terms of the orientation averaged differential

cross section $\left\langle |f(p, \mathbf{n}\cdot\mathbf{n}')|^2 \right\rangle_\Omega$. The normalization constant N ensures $\eta(0) = 1$, so that the diagonal elements of ρ remain unchanged. Because of the orientation average, the differential scattering cross section $\langle |f(p, \mathbf{n}\cdot\mathbf{n}')|^2\rangle_\Omega$ depends on the angle between incoming and outgoing momentum rather than on the individual directions. Again, this result can be expanded in orders of $mv_\mathrm{M}/p_\mathrm{g}$ to

$$\begin{aligned}\eta(\mathbf{R}) &= \frac{8\pi^2}{N}\int_0^\infty \mathrm{d}p\, p^3\mu(p)\int_0^\pi \mathrm{d}\theta\, \sin\theta\langle |f(p,\cos\theta)|^2\rangle_\Omega \\ &\quad\times \mathrm{sinc}\left[\sin\left(\frac{\theta}{2}\right)\frac{2p|\mathbf{R}|}{\hbar}\right]\left[1+\mathcal{O}\left(\frac{m^2v_\mathrm{M}^2}{p_\mathrm{g}^2}\right)\right] \end{aligned} \tag{5.20}$$

with $\cos\theta = \mathbf{n}\cdot\mathbf{n}'$. It is demonstrated in Appendix B.1 that the linear order in Eq. (5.20) vanishes. The normalization constant N is then determined to

$$N = \frac{1}{4\pi}\int_0^\infty \mathrm{d}p\, p^3\mu(p)\langle\sigma_\mathrm{tot}(p)\rangle_\Omega, \tag{5.21}$$

where I used the relation $2\pi\int_0^\pi \mathrm{d}\theta\ \sin\theta\left\langle |f(p,\cos\theta)|^2\right\rangle_\Omega = \langle\sigma_\mathrm{tot}(p)\rangle_\Omega$.

The main approximation made in the course of this section is that molecules are considered to be non-rotating during the scattering processes. In the next section the validity of this approximation is examined by comparing the rotational period τ_rot and the collision time τ_c.

5.1.3 *Validity of non-rotating approximation*

For the examination of a non-rotating molecule, I first consider the collision time τ_c. The most relevant long-range interaction potentials between a molecule and an atom are of the form $V(r) = -C/r^s$ with an interaction constant C and the relative distance between the scatterers r. The interaction potential between a polar molecule and an atom contains an anisotropic part, which induces small correction in the total and differential cross section, as discussed in Sect. 5.2. For an estimation of the interaction time I ignore this anisotropy in this section. From the total scattering cross section $\sigma_0(p)$ [117], one estimates the effective interaction range

$$R_\mathrm{w} = 2\sqrt{\frac{\sigma_0(p)}{\pi}} = 2\sqrt{2\sin\left(\frac{\pi}{2}\frac{s-3}{s-1}\right)\Gamma\left(\frac{s-3}{s-1}\right)}\left[\frac{\sqrt{\pi}C}{\hbar v}\frac{\Gamma\left(\frac{s-1}{2}\right)}{\Gamma(s/2)}\right]^{1/(s-1)},$$

where v is the relative velocity of scatterers. The collision time can be then estimated to $\tau_\mathrm{c} = R_\mathrm{w}/v_\mathrm{g}$, where v_g is the most probable velocity of gas atoms. Assuming the Maxwell-Boltzmann distribution with the temperature T, the most probable velocity is given by $v_\mathrm{g} = \sqrt{2k_\mathrm{B}T/m}$. For the dipole-induced dipole interaction, the interaction constant is given by $C = \alpha_0 d_0^2/32\pi^2\varepsilon_0^2$, where α_0 is the polarizability of a gas atom and d_0 is the dipole moment of a molecule, see Sect. 5.2.1. Considering the collision between a molecule with the dipole moment 5 Debye and a helium atom with $m =$ 4 amu, $\alpha_0/4\pi\varepsilon_0 = 0.2\,\text{Å}^3$ and $T = 300$ K, the interaction time is estimated to $\tau_\mathrm{c} \simeq$ 0.8 ps.

molecule	mass in amu	size in Å	estimated rotation period in ps
(a)$C_{30}H_{12}F_{30}N_2O_4$	1034	$b = 3$, $b_z = 16$	25
(b)C_{60}	720	$b = 4$, $b_z = 4$	15
(c)TPP	614	$b = 5$, $b_z = 1$	14

Table 4: Estimation of the rotation period for some molecules approximated by a spheroid with an internal molecular temperature $T_M = 1000$ K. Note that the length of semi-axes are estimated by a visual judgment. Some of these molecules are already applied in matter-wave experiments: (a) perfluoroalkyl-functionalized diazobenzene [23] (b) C_{60} fullerene [19, 44, 81] (c) TPP.

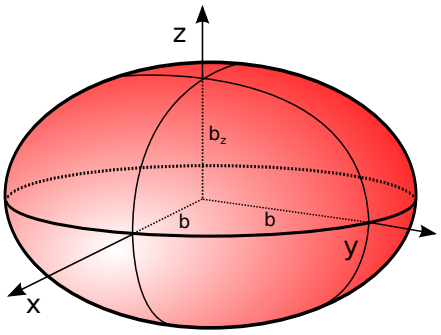

Figure 21: Spheroid with z as the symmetry axis

For an estimation of the molecular rotational period, I approximate molecules as a spheroid with the semi-axes b (along the x- and y-axis) and b_z (along the z-axis), see Fig. 21. Its moments of inertia relating to the rotation about the principal axes are given by $I_z = 2Mb/5$ (about the z-axis) and $I = M(b^2 + b_z^2)/5$ (about the x- and y-axes). Assuming that internal molecular states are in thermodynamical equilibrium with the temperature T_M, each rotational degrees of freedom possesses the energy $k_B T_M/2$. Thus the frequency of the molecular rotation may be estimated to

$$\omega_z = \sqrt{\frac{k_B T_M}{I_z}}, \quad \omega = \sqrt{\frac{k_B T_M}{I}}.$$

In order to simplify the discussion, I consider the mean rotational period $\overline{\omega} = (2\omega + \omega_z)/3$. Table 4 shows the estimated periods $2\pi/\overline{\omega}$ for some organic molecules, applied as interfering particles in matter-wave experiments. The internal temperature of the molecules is assumed to be larger than room temperature (in Tab. 4 I assumed $T_M = 1000$ K) because they are often emitted by an oven in practice. For the high mass molecules considered in Tab. 4, the values of the rotational periods are about 20 times larger than the collision time. Thus the approximation of a non-rotating molecule is well justified, which was applied in order to derive the master equation in Sect. 5.1.2.

5.2 COLLISIONAL DECOHERENCE

Collisional decoherence is chracterized by the scattering rate γ and the decoherence function $\eta(\mathbf{R})$, as discussed in Sect. 5.1. In this section, I present an approximated analytical expression of these functions for the scattering between a polar molecule

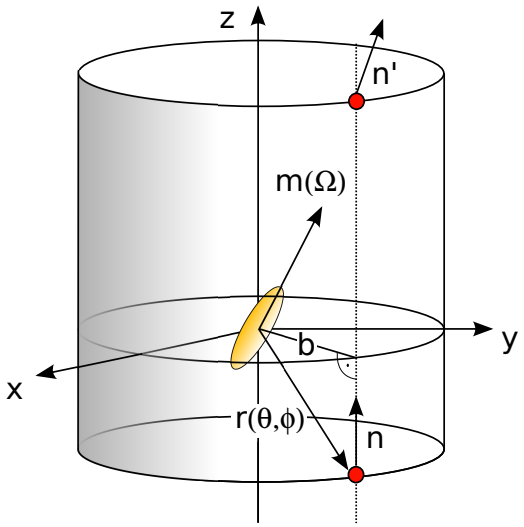

Figure 22: Definition of a coordinate for a molecule-atom scattering. A molecule is arranged at the origin, whose orientation is given by the unit vector $\mathbf{m}(\Omega)$. The gas atom is propagating initially in $\mathbf{n}$-direction with the impact parameter b, which is scattered asymptotically for $t \to \infty$ into $\mathbf{n}'$-direction.

and non-polar gas atoms. In the final section, I will also give an analytical expression for the Fourier transform of the decoherence function $\widetilde{\eta}(\mathbf{Q})$, which corresponds to the distribution of the transfered momentum $\mathbf{Q}$ due to collisions. As the first step, I calculate the total and the differential scattering cross section in Sect. 5.2.1 and 5.2.2.

5.2.1 *Total scattering cross section*

I begin the calculation of the cross sections with the definition of the interaction potential between a polar molecule and an atom. In terms of the multipole expansion of a electrostatic interaction potential, the leading order contribution is the dipole-induced dipole interaction [118]. In order to make the interaction slightly more general, I consider potentials of the form

$$V\left(r, \cos\Theta\right) = -\frac{C}{r^s}\left(1 + a\cos^2\Theta\right) \tag{5.22}$$

with $s \geq 3$, which also includes the anisotropic van der Waals interaction of a linear molecule [119]. The polar and van der Waals interaction are always attractive, i.e. $C > 0$. However, the present calculation can also be applied to a repulsive potential. The potential is homogeneous of degree s relating to the relative distance $|\mathbf{r}| = r$ and depends on the angle Θ between the molecular orientation represented by the unit vector $\mathbf{m}(\Omega)$ and the relative position $\mathbf{r}$, i.e. $\cos\Theta = \mathbf{m}\cdot\mathbf{r}/r$. The strength of the interaction and the anisotropy is quantified by the constants C and a, respectively. In the case of the dipole-induced dipole interaction, the parameters correspond to $s = 6$, $C = \alpha_0 d_0^2/32\pi^2\varepsilon_0^2$ and

$a = 3$, where α_0 is the atomic polarizability and d_0 is the molecular dipole moment [119].

For the calculation of the cross sections for a fixed molecular orientation, I make use of *Schiff's approximation*, which corresponds to the eikonal approximation for an anisotropic scattering potential [120]. This approximation is valid if the kinetic energy of the scatterer fairly exceeds the magnitude of the potential energy, $E \gg |V|$, and if the interaction range of the potential is much larger than the de Broglie wavelength of the scattering atom λ, i.e. $a \ll \lambda/2\pi$ [117, 120]. For a room-temperature gas, this approximation is well justified and shows a good agreement with the numerical result, see Fig. 23 and 24. In this case, the scattering particle is only slightly deflected by the interaction and the motion may be treated effectively one-dimensional. Thus the phase difference between an incident and outgoing wave, the *scattering phase*, is appropriately given by the integral of the interaction potential $V(r, \Theta)$ along the straight trajectory [121]

$$\chi(\mathbf{b}; \mathbf{m}) = -\frac{m}{\hbar p} \int_{-\infty}^{\infty} \mathrm{d}z \, V\left(\sqrt{b^2 + z^2}, (\mathbf{b} + z\mathbf{e}_z) \cdot \mathbf{m}/r\right), \tag{5.23}$$

where the initial relative momentum is chosen to be along the z-axis, $\mathbf{p} = p\mathbf{e}_z$ and $\mathbf{b} = \mathbf{r} - z\mathbf{e}_z$ is the impact vector (see Fig. 22). This integral can be evaluated analytically using cylinder coordinate

$$\chi(\mathbf{b}; \mathbf{m}) = -\frac{mC\sqrt{\pi}\Gamma[(s-1)/2]}{\hbar p \Gamma(s/2)} \frac{G^{2/(s-1)}(\mathbf{m})}{b^{s-1}}. \tag{5.24}$$

Here the angle dependent term is defined by

$$G(\mathbf{m}) = \left[1 + \frac{a}{s}(\mathbf{m} \cdot \mathbf{e}_z)^2 + \frac{a(s-1)}{s}(\mathbf{m} \cdot \mathbf{e}_x)^2\right]^{(s-1)/2}. \tag{5.25}$$

With the scattering phase (5.24) the scattering amplitude in Schiff's approximation can be given by [120]

$$f(p, \mathbf{n}'; \mathbf{m}) = -\mathrm{i}\frac{p}{2\pi\hbar} \int \mathrm{d}^2 b \, e^{-\mathrm{i}p\mathbf{n}'_\perp \cdot \mathbf{b}/\hbar} \left(\exp\left[\mathrm{i}\chi(\mathbf{b}; \mathbf{m})\right] - 1\right), \tag{5.26}$$

where $\mathbf{n}'_\perp$ is the xy-components of the projection of the out-going gas particle $\mathbf{n}'$. This approximation provides reliable results for small angle scattering [108], which will show to be most important for the decoherence function, see Sect. 5.2.4.

According to the optical theorem [53], the total scattering cross section can be obtained from the scattering amplitude (5.26) evaluated at $\mathbf{n}' = \mathbf{n} = \mathbf{e}_z$. The orientation averaged total cross section is then given by [108]

$$\langle \sigma_{\mathrm{tot}}(p) \rangle_\Omega \quad = \quad \sigma_0(p) \, \langle G(\mathbf{m}) \rangle_\Omega, \tag{5.27}$$

where

$$\sigma_0(p) = 2\pi \sin\left(\frac{\pi}{2}\frac{s-3}{s-1}\right) \Gamma\left(\frac{s-3}{s-1}\right) \left(\frac{\sqrt{\pi}mC}{\hbar p} \frac{\Gamma[(s-1)/2]}{\Gamma(s/2)}\right)^{2/(s-1)}, \tag{5.28}$$

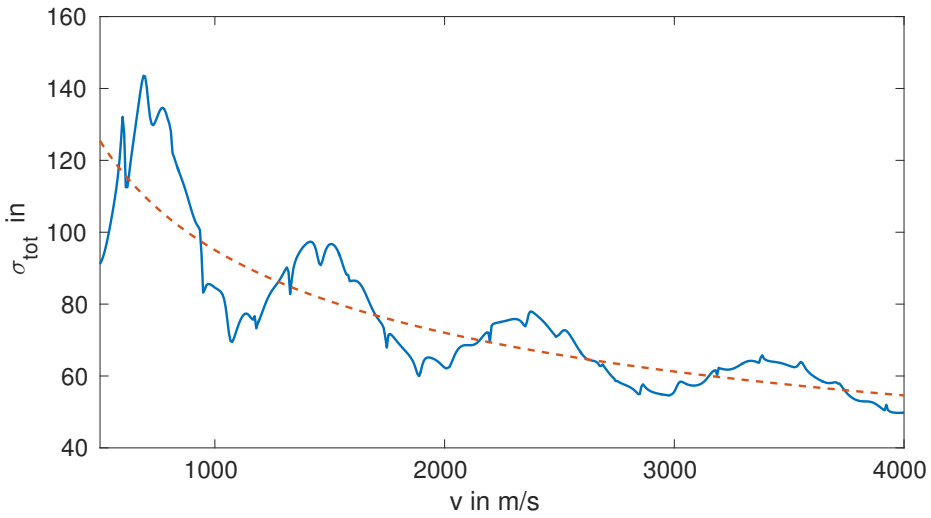

Figure 23: The total scattering cross section depending on the relative collision velocity v. The solid and dashed lines correspond to the numerical and approximate analytical results (Eq. (5.29)), respectively. For the numerical calculation the Log-derivative method is applied [122, 123] to a spheric interaction potential $V(r) = -C(1 + a/3)/r^6$. The numerical data exhibits numerous resonances and an oscillating behavior, which correspond to orbiting resonances and the glory diffraction [124]. For this plot, parameters are set to $d_0 = 5$ Debye, $\alpha_0/4\pi\varepsilon_0 = 0.2\,\text{Å}^3$ and $m = 4$ amu, which corresponds to the scattering with a helium atom.

is the total cross section resulting from the isotropic part of the interaction potential, i.e. for $a = 0$ [117]. The orientation averaged function $\langle G(\mathbf{m})\rangle$ in Eq. (5.27) can be well approximated by $(1 + a/3)^{2/(s-1)}$, see Appendix B.2. The differential cross section is then given by a compact expression

$$\langle \sigma_{\text{tot}}(p)\rangle_\Omega \approx \sigma_0(p)\left(1 + \frac{a}{3}\right)^{2/(s-1)}. \tag{5.29}$$

Thus the anisotropy of the potential (5.22) enhances the total cross section by a constant factor, $C \to (1 + a/3)C$.

Figure 23 compares the approximate analytically result Eq. (5.29) with a numerical calculation. The numerical data is the result of implementing Johnson's log derivative method [122, 123] for the spherical potential with the enhanced interaction constant $C(1 + a/3)$. The numerous resonances in the numerical cross section are due to the instable orbiting of the gas atom around the molecule, known as *orbiting resonances* [124]. The oscillating behavior of the numerical total scattering cross section at long velocity scales can be led back to the *glory diffraction* [124]. The approximate analytical curve in Fig. 23 does not contain these oscillations and resonances. However, these deviations turn out to play a minor role in the calculation of the decoherence function in Sect. 5.2 because their influences average out in the evaluation, see also Sect. 5.2.4.

5.2.2 *Differential cross section*

Let us now turn our attention to the differential scattering cross section. In general, the scattering amplitude (5.26) cannot be evaluated in closed form. For a systematic approximation of the scattering amplitude, I first consider the small angle expansion. As presented in Appendix B.2, the differential cross section can be expanded as

$$\langle |f(p,\cos\theta)|^2\rangle_\Omega = A(p)\left[1-\left(\frac{\theta}{\theta_*(p)}\right)^2+\mathcal{O}(\theta^4)\right], \tag{5.30}$$

where the amplitude $A(p)$ and the angle $\theta_*(p)$ are given by

$$A(p) = \left(\frac{p\langle\sigma_{\rm tot}(p)\rangle_\Omega}{4\pi\hbar\cos[\pi/(s-1)]}\right)^2, \tag{5.31}$$

$$\theta_*(p) = \frac{\hbar}{p}\sqrt{\frac{8\pi}{\langle\sigma_{\rm tot}(p)\rangle_\Omega}}\Gamma\left(\frac{s-3}{s-1}\right)\Gamma^{-1/2}\left(\frac{s-5}{s-1}\right). \tag{5.32}$$

In accordance with the result for the total scattering cross section, the anisotropy of the interaction effectively enhances the interaction constant by $C \to (1+a/3)C$.

Thus the differential cross section decays quadratically with the angle θ in the small angle regime. For the calculation of the decoherence function (5.19), however, one requires the differential cross section for all angles $\theta \in [0,\pi]$. One possibility to overcome this problem is to approximate the cross section by a Gaussian curve with amplitude $A(p)$ and width $\theta_*(p)$

$$\langle |f(p,\cos\theta)|^2\rangle_\Omega \approx A(p)\exp\left[-\left(\frac{\theta}{\theta_*(p)}\right)^2\right]. \tag{5.33}$$

It was demonstrated in [109] that this approximation gives reliable results for $\theta \ll 1$, which I will refer from now on as the *soft scattering region*. However, a crucial shortcoming of this approximation is that Eq. (5.33) does not contain the correct asymptotic behavior for $\theta \sim 1$ [125, 126],

$$\langle |f(p,\cos\theta)|^2\rangle_\Omega \xrightarrow{\theta\sim 1} I_{\rm cl}(p)\theta^{-2(s+1)/s}, \tag{5.34}$$

where

$$I_{\rm cl}(p) = \frac{1}{s}\left(\frac{(s-1)\sqrt{\pi}mC(1+a/3)}{p^2}\frac{\Gamma[(s-1)/2]}{\Gamma(s/2)}\right)^{2/s}. \tag{5.35}$$

This is the known result from classical scattering theory [117]. I will refer to this regime, where classical scattering theory can be applied, as the *hard scattering region*. The emergence of the classical behavior for a large scattering angle is due to the fact that the transfered momentum fairly exceeds the uncertainty in the momentum, $Q \gg \Delta p$ and thus quantum effects may be neglected [127]. The approximated small angle result

Eq. (5.33) is compared with a numerical calculation in Fig. 24(a), which confirms a good agreement for $\theta \lesssim 0.1$. In the hard scattering region $\theta \gtrsim 0.1$, however, there is a clear deviation from the numerical result. The numerical data indicates that the classical differential cross section provides a good approximation in this region.

To achieve a better approximation for all angles, I consider the following ansatz for the differential cross section

$$\left\langle |f(p,\cos\theta)|^2 \right\rangle_\Omega \approx A(p) \exp\left[-\left(\frac{\theta}{\theta_*(p)} \right)^2 \right] + \left[1 - \exp\left(-\left[\frac{\theta}{\theta_{\rm cl}(p)} \right]^\nu \right) \right] I_{\rm cl}(p) \theta^{-2(s+1)/s}. \tag{5.36}$$

Here, the task of the function $[1-\exp(-[\theta/\theta_{\rm cl}]^\nu)]$ is to connect the soft and the hard collision region smoothly. The function $\theta_{\rm cl}(p)$ denotes the angle, where the classical scattering becomes noticeable. Because the small angle behavior $|f(p,\cos\theta)|^2 \propto \theta^2$ must not be disturbed by the additional term $(1-\exp[-(\theta/\theta_{\rm cl})^\nu]) I_{\rm cl}\theta^{-2(s+1)/s}$, the power ν must fulfill the condition $\nu > 4 + 2/s$. Furthermore, the power ν is chosen to be as small as possible in order to guarantee a smooth connection between the soft and hard collision region. From these conditions, the optimal value of the power ν can be determined to

$$\nu \;=\; \left\lceil 4 + \frac{2}{s} \right\rceil = 5. \tag{5.37}$$

Here, $\lceil x \rceil = \min(k \in \mathbb{Z} | k \geq x)$ denotes the ceiling function.

The remaining unknown angle $\theta_{\rm cl}(p)$ is determined from the condition that the angular integral over the differential cross section (5.36) must result in the total scattering cross section (5.29), i.e. $2\pi \int {\rm d}\theta \, \sin\theta \left\langle |f(p,\cos\theta)|^2 \right\rangle_\Omega = \langle \sigma_{\rm tot}(p) \rangle_\Omega$. Let us consider at first the soft collision part of the angular integral. The integral can be evaluated in the small angle approximation, where $\sin\theta$ is replaced by θ and the integration boundary is extended to infinity. It yields

$$\begin{aligned} 2\pi \int_0^\infty {\rm d}\theta \, \theta A(p) \exp\left[-\left(\frac{\theta}{\theta_*(p)} \right)^2 \right] &= \pi A(p) \theta_*^2(p) \\ &= h(s) \, \langle \sigma_{\rm tot}(p) \rangle_\Omega \, . \end{aligned} \tag{5.38}$$

The calculated value differs form the total scattering cross section by the factor

$$h(s) = \Gamma^2\left(\frac{s-3}{s-1} \right) \Big/ 2\Gamma\left(\frac{s-5}{s-1} \right) \cos^2\left(\frac{\pi}{s-1} \right). \tag{5.39}$$

Note that the result Eq. (5.38) is only meaningful for $s \geq 6$, where this factor takes values $0 < h(s) < 1$. For the most relevant case of $s = 6$, this factor is $F(6) \approx 0.36$, that is, about 64% of the total scattering cross section originates from hard scatterings. As shown in Fig. 25, this factor converges for large s to $1/2$.

Assuming that the remaining fraction of the total scattering cross section $[1-h(s)]$ $\langle\sigma_{\mathrm{tot}}(p)\rangle_\Omega$ comes from the hard scattering part of the differential cross section (5.36), the unknown function $\theta_{\mathrm{cl}}(p)$ can be determined,

$$\begin{aligned} 2\pi\int_0^\infty \mathrm{d}\theta\ \left[1-\exp(-(\theta/\theta_{\mathrm{cl}})^5\right] I_{\mathrm{cl}}(p)\theta^{-(s+2)/s} &\stackrel{!}{=} (1-h(s))\,\langle\sigma_{\mathrm{tot}}(p)\rangle_\Omega \\ \Leftrightarrow \theta_{\mathrm{cl}}(p) &= \left[\frac{s\pi\Gamma(1-2/5s)I_{\mathrm{cl}}(p)}{(1-h(s))\,\langle\sigma_{\mathrm{tot}}(p)\rangle_\Omega}\right]^{s/2} \end{aligned} \tag{5.40}$$

As a result, the differential cross section (5.36) includes both the correct small angle behavior (Eq. (5.30)) and the asymptotic behavior for a hard scattering (Eq. (5.34)). It agrees very well with the numerical results, as shown in Fig. 24(b). The oscillating structures in the numerical data originate from the glory effect [128]. This effect, however, average out in the evaluation of the decoherence function (5.19) and can therefore be ignored in our case.

Having presented the analytical expression for the total and differential cross section, I am now finally in the position to compute the scattering rate γ and the decoherence function $\eta(\mathbf{R})$ in the following sections.

5.2.3 *Scattering rate*

In order to calculate the scattering rate, I insert the total scattering cross section (5.29) into Eq. (5.17). Assuming the Boltzmann distribution for the gas momentum $\mu(p)\mathrm{d}^3p = \exp[-(p/p_{\mathrm{g}})^2]/(\sqrt{\pi}p_{\mathrm{g}})^3\mathrm{d}^3p$, the rate is

$$\begin{aligned} \gamma &= \frac{2n_{\mathrm{g}}p_{\mathrm{g}}\,\langle\sigma_{\mathrm{tot}}(p_{\mathrm{g}})\rangle_\Omega}{m\sqrt{\pi}}\mathrm{e}^{-(mv_{\mathrm{M}}/p_{\mathrm{g}})^2}\int_0^\infty \mathrm{d}x\, x^{(3s-5)/(s-1)}\mathrm{e}^{-x^2} \\ &\quad\times\int_0^\pi \mathrm{d}\theta\ \sin\theta\exp\left[-2\left(\frac{mv_{\mathrm{M}}}{p_{\mathrm{g}}}\right)x\cos\theta\right], \end{aligned} \tag{5.41}$$

where $x = p/p_{\mathrm{g}}$ is the dimensionless integration variable, $v_{\mathrm{M}} = |\mathbf{v}_{\mathrm{M}}|$ is the molecular velocity and θ is the angle between $\mathbf{p}$ and $\mathbf{v}_{\mathrm{M}}$, i.e. $\cos\theta = \mathbf{p}\cdot\mathbf{v}_{\mathrm{M}}/pv_{\mathrm{M}}$. These three integrals can be evaluated analytically without any approximations to

$$\begin{aligned} \gamma &= \frac{2n_{\mathrm{g}}p_{\mathrm{g}}\,\langle\sigma_{\mathrm{tot}}(p_{\mathrm{g}})\rangle_\Omega}{m\sqrt{\pi}}\mathrm{e}^{-(mv_{\mathrm{M}}/p_{\mathrm{g}})^2}\Gamma\left(\frac{2s-3}{s-1}\right) \\ &\quad\times{}_1F_1\left[\frac{2s-3}{s-1};\frac{3}{2};-\left(\frac{mv_{\mathrm{M}}}{p_{\mathrm{g}}}\right)^2\right], \end{aligned} \tag{5.42}$$

where ${}_1F_1(a;b;x)$ is the confluent hypergeometric function [66]. Because in practice, the molecular velocity is much smaller than the most probable velocity of the gas particles, it is reasonable to consider the expansion in terms of $mv_{\mathrm{M}}/p_{\mathrm{g}}$ [28],

$$\gamma = \frac{2n_{\mathrm{g}}p_{\mathrm{g}}}{m\sqrt{\pi}}\Gamma\left(\frac{2s-3}{s-1}\right)\langle\sigma_{\mathrm{tot}}(p_{\mathrm{g}})\rangle_\Omega\left(1+\mathcal{O}\left[\left(\frac{mv_{\mathrm{M}}}{p_{\mathrm{g}}}\right)^2\right]\right). \tag{5.43}$$

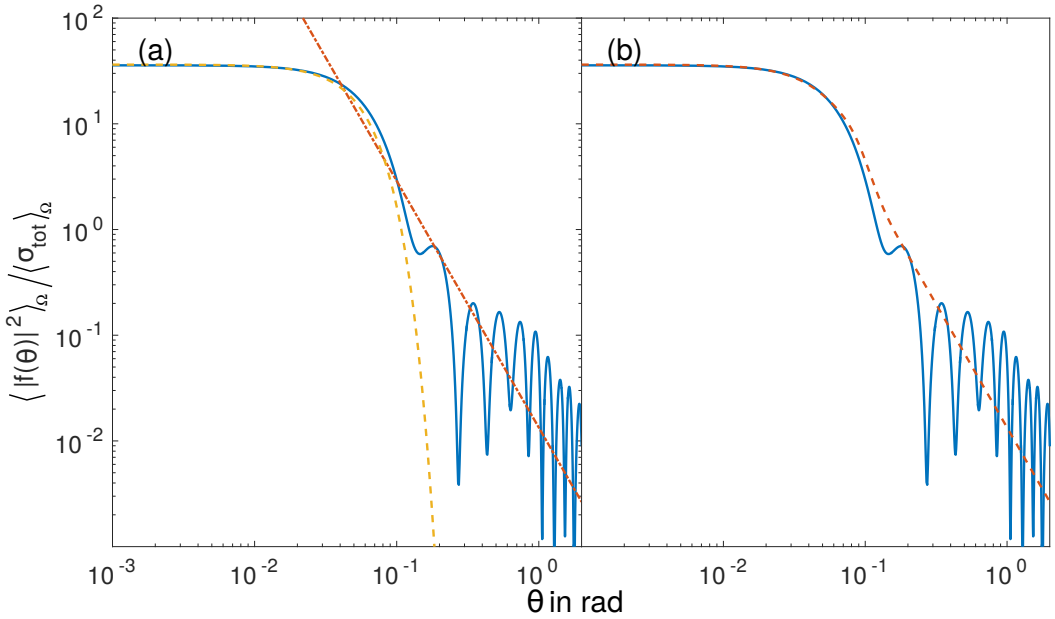

Figure 24: Comparison between the numerically calculated differential cross section (solid line) and the approximate analytical results. (a) The dashed line corresponds to the exponentially approximated small angle result (Eq. (5.33)), which shows a good agreement for the soft collision regime $\theta \lesssim 0.1$. The classical result (Eq. (5.34), dash-dotted line) approximates the hard collision behavior of the differential cross section for $\theta \gtrsim 0.1$. (b) The dashed line shows the improved theoretical result (Eq. (5.36)), which also incorporates the correct classical asymptotic behavior in the hard scattering region. The relative velocity of scatterers is chosen to $v = 1000$ m/s. The same parameters are taken as in Fig. 23.

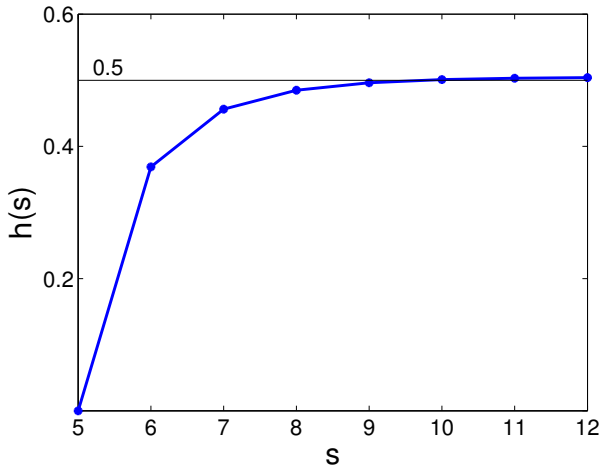

Figure 25: The soft collision contribution of the total scattering cross section $h(s)$. For the most relevant case of $s = 6$, hard scattering contribution is ca. 64%. This factor converges to $1/2$ for $s \to \infty$.

This is a good approximation for $mv_M/p_g \lesssim 0.5$, where the relative error is smaller than 4% for all powers s. For $s = 6$ and a typical value $mv_M/p_g = 0.1$, the relative error of this approximation is merely 0.1%.

The scattering rate is proportional to $n_g p_g \langle \sigma_{tot}(p_g) \rangle_\Omega / m$, which is the effective current of gas atoms passing through the total scattering cross section. For the case of the dipole-induced dipole interaction, the scattering rate reads to leading order in mv_M/p_g as

$$\gamma_{d-id} = \frac{2^{7/5}}{\sqrt{\pi}} \Gamma\left(\frac{9}{5}\right) \frac{n_g p_g \sigma_0(p_g)}{m}. \tag{5.44}$$

In particular, it is proportional to $n_g \alpha_0^{2/5} d_0^{4/5} (T/m)^{3/10}$ and thus depends only weakly on the gas temperature T and the polarizability of the gas atoms. The anisotropy of the interaction potential leads to an additional prefactor $2^{2/5} \simeq 1.3$ compared to the scattering rate of a spherical molecule [28].

5.2.4 *Decoherence function*

First of all, for the calculation of the decoherence function $\eta(\mathbf{R})$ (Eq. (5.20)) its normalization constant N must be determined, see Eq. (5.21). Assuming again the Boltzmann distribution, it reads

$$N = \frac{4p_g}{\sqrt{\pi}} \int_0^\infty dx\, x^3 e^{-x^2} \langle \sigma_{tot}(p_g x) \rangle_\Omega, \tag{5.45}$$

where $x = p/p_g$ is a dimensionless integration variable. With the total scattering cross section, $\langle \sigma_{tot}(p_g x) \rangle_\Omega = x^{-2/(s-1)} \langle \sigma_{tot}(p_g) \rangle_\Omega$, the remaining integral over x can be evaluated and the normalization constant is determined to

$$N = 2\pi^{-1/2} p_g \langle \sigma_{tot}(p_g) \rangle_\Omega \Gamma\left(\frac{2s-3}{s-1}\right). \tag{5.46}$$

The evaluation of the decoherence function for a general case $\mathbf{R} \neq 0$ is more complicated. Because the main contribution of the differential cross section (5.36) is in the small angle region $\theta \lesssim 1$ (see Fig. 24), the integral for the decoherence function can be evaluated in an approximation, where I replace $\sin\theta$ by θ and extend the integration boundary to infinity, i.e. $\int_0^\pi d\theta \to \int_0^\infty d\theta$. The decoherence function (5.20) in the leading order contribution in mv_M/p_g reads

$$\begin{aligned} \eta(\mathbf{R}) \approx\ & \frac{4\pi}{\langle \sigma_{tot}(p_g) \rangle_\Omega \Gamma\left[(2s-3)/(s-1)\right]} \int_0^\infty dx\, x^3 e^{-x^2} \int_0^\infty d\theta\, \theta \\ & \times \langle |f(p_g x, \cos\theta)| \rangle_\Omega \operatorname{sinc}\left(\frac{p_g |\mathbf{R}|}{\hbar} x\theta\right) \left(1 + \mathcal{O}\left[\left(\frac{mv_M}{p_g}\right)^2\right]\right). \end{aligned} \tag{5.47}$$

Let us consider the angle integration in the soft and hard collision region, separately.

In the case of the exponential differential cross section, this angle integral can be evaluated to

$$A(p)\int_0^\infty \mathrm{d}\theta\,\theta\exp\left[-\left(\frac{\theta}{\theta_*(p)}\right)\right]\operatorname{sinc}\left(\frac{p|\mathbf{R}|}{\hbar}\theta\right)$$
$$= h(s)\frac{\langle\sigma_{\mathrm{tot}}(p_\mathrm{g})\rangle_\Omega}{2\pi}x^{-2/(s-1)}D_1\left(\frac{p_\mathrm{g}|\mathbf{R}|\theta_*(p_\mathrm{g})}{2\hbar}x^{1/(s-1)}\right). \tag{5.48}$$

Here, I defined an auxiliary function

$$D_1(x) = \frac{e^{-x^2}}{x}\int_0^x \mathrm{d}\xi\, e^{\xi^2}, \tag{5.49}$$

which is related to the Dawson's integral $F(x)$ by $D_1(x) = F(x)/x$ [66]. The function $D_1(x)$ is symmetric and monotonically decreasing, with its maximum value $D_1(x = 0) = 1$. It decreases for large arguments as $D_1(x) \sim 1/x^2$, see also Fig. 26.

In the case of the hard scattering part of the differential cross section, the angular integral cannot be evaluated in closed form. This integral can be approximately evaluated by replacing the function $[1 - \exp(-[\theta/\theta_{\mathrm{cl}}]^5)]$ by a Heaviside function $\Theta(\theta - \theta'(p))$. The detailed calculation is shown in Appendix B.3. The approximated result is given by

$$I_{\mathrm{cl}}(p)\int_0^\infty \mathrm{d}\theta\,\theta^{-(s+2)/s}\left(1-\exp\left[-\left(\frac{\theta}{\theta_{\mathrm{cl}}(p)}\right)^5\right]\right)\operatorname{sinc}\left(\frac{p|\mathbf{R}|}{\hbar}\theta\right)$$
$$\approx [1-h(s)]\frac{\langle\sigma_{\mathrm{tot}}(p_\mathrm{g})\rangle_\Omega}{2\pi}x^{-2/(s-1)}D_2\left(\frac{p_\mathrm{g}|\mathbf{R}|\theta_{\mathrm{cl}}(p_\mathrm{g})}{2\hbar\Gamma^{s/2}(1-2/5s)}x^{1/(s-1)}\right), \tag{5.50}$$

where I defined another auxiliary function

$$D_2(x) = {}_1F_2\left[-\frac{1}{s};\frac{3}{2},\frac{s-1}{s};-x^2\right] - \frac{2^{(s+2)/s}}{s}\cos\left(\frac{\pi}{s}\right)\Gamma\left(-\frac{s+2}{s}\right)|x|^{2/s}. \tag{5.51}$$

Here, ${}_1F_2(a;b,c;x)$ is a generalized hypergeometric function [129]. This function is confined by $|D_2(x)| \leq 1$, where equality holds only for $x = 0$ and converges to $D_2(x) \to 0$ for large arguments $x \to \infty$.

Using the results for the angular integration Eq. (5.49) and (5.50), the decoherence function reads

$$\eta(\mathbf{R}) = \int_0^\infty \mathrm{d}\xi\,\nu(\xi)\Bigg(h(s)D_1\left[\frac{p_\mathrm{g}|\mathbf{R}|\theta_*(p_\mathrm{g})}{2\hbar}\xi\right]$$
$$+[1-h(s)]D_2\left[\frac{p_\mathrm{g}|\mathbf{R}|\theta_{\mathrm{cl}}(p_\mathrm{g})}{2\hbar\Gamma^{s/2}(1-2/5s)}\xi\right]\Bigg), \tag{5.52}$$

where $\xi = (p/p_\mathrm{g})^{1/(s-1)}$ is a new dimensionless integration variable. Here, $\nu(\xi)$ is a probability distribution defined by

$$\nu(\xi) = \frac{2(s-1)}{\Gamma[(2s-3)/(s-1)]}\xi^{4s-7}\exp\left(-\xi^{2(s-1)}\right), \tag{5.53}$$

which fulfills the normalization condition $\int_0^\infty \mathrm{d}\xi \nu(\xi) = 1$. The function $\nu(\xi)$ is sharply peaked near its mean value

$$\xi_s = \Gamma\left(2 - \frac{1}{2[s-1]}\right) \Big/ \Gamma\left(2 - \frac{1}{s-1}\right) \tag{5.54}$$

so that the function $D_1(x)$ and $D_2(x)$ are approximately linear in this region. This allows us to approximate the integral (5.52) to obtain the decoherence function. The detailed calculation is presented in Appendix B.4. The approximated decoherence function reads

$$\eta(\mathbf{R}) \approx h(s) D_1\left(\frac{|\mathbf{R}|}{w_\eta}\right) + [1 - h(s)] D_2\left(\frac{|\mathbf{R}|}{w_\eta}\mu(s)\right), \tag{5.55}$$

where the characteristic width w_η of the decoherence function and the factor $\mu(s)$ are given by

$$w_\eta = \frac{2\hbar}{\xi_s p_\mathrm{g} \theta_*(p_\mathrm{g})} = \left[\xi_s \Gamma\left(\frac{s-3}{s-1}\right)\right]^{-1} \sqrt{\frac{\langle \sigma_\mathrm{tot}(p_\mathrm{g})\rangle}{2\pi} \Gamma\left(\frac{s-5}{s-1}\right)}. \tag{5.56}$$

$$\begin{aligned} \mu(s) &= \Gamma^{-s/2}\left(1 - \frac{2}{5s}\right) \frac{\theta_\mathrm{cl}(p_\mathrm{g})}{\theta_*(p_\mathrm{g})} \\ &= \frac{(s-1)}{\sqrt{8[1-h(s)]}} \sqrt{\Gamma\left(\frac{s-5}{s-1}\right)} \left[\Gamma\left(\frac{s-3}{s-1}\right)\right]^{-(s+1)/2} \\ &\quad \times \left[2(1-h(s)) \sin\left(\frac{\pi}{2}\frac{s-3}{s-1}\right)\right]^{(1-s)/2}. \end{aligned} \tag{5.57}$$

For the most relevant case $s = 6$, this factor is given by $\mu(6) \simeq 1.2$.

In spite of the some approximations made in the evaluation, the expression Eq. (5.55) agrees very well with the numerical calculation, as shown in Fig. 26(a). This surprisingly good agreement is partially due to the fact that the glory oscillation and orbiting resonances in the cross sections discussed in Sect. 5.2.1 and 5.2.2 average out in the evaluation of the decoherence function. The hard scattering part of the decoherence function becomes noticeable for a small path separation $|\mathbf{R}| \lesssim w_\eta$. Thus the asymptotic behavior for $R \to \infty$ and the width of the decoherence function, which are important properties for its characterization, are mainly determined by soft collisions. A superposition state with a large spatial separation $|\mathbf{R}| \gg w_\eta$ suffers a total decoherence, where the decoherence function (5.19) shows the asymptotic behavior $\eta(\mathbf{R}) \to 0$. The width of the decoherence function Eq. (5.56) decreases with increasing momentum as $\propto p_\mathrm{g}^{-1/(s-1)}$. Thus as expected, the higher the temperature of a gas is, the more pronounced is the decoherence effect. In the case of the dipole-induced dipole interaction, the width of the decoherence function $w_\eta \approx 0.6\sqrt{\langle \sigma_\mathrm{tot}(p_\mathrm{g})\rangle_\Omega}$ is typically in the of range of nanometers. The width is estimated to $w_\eta \simeq 0.5$ nm if a polar molecule with a dipole moment $d_0 = 5$ Debye is propagating in a helium gas with the most probable velocity $p_\mathrm{g}/m = 10^3$ m/s.

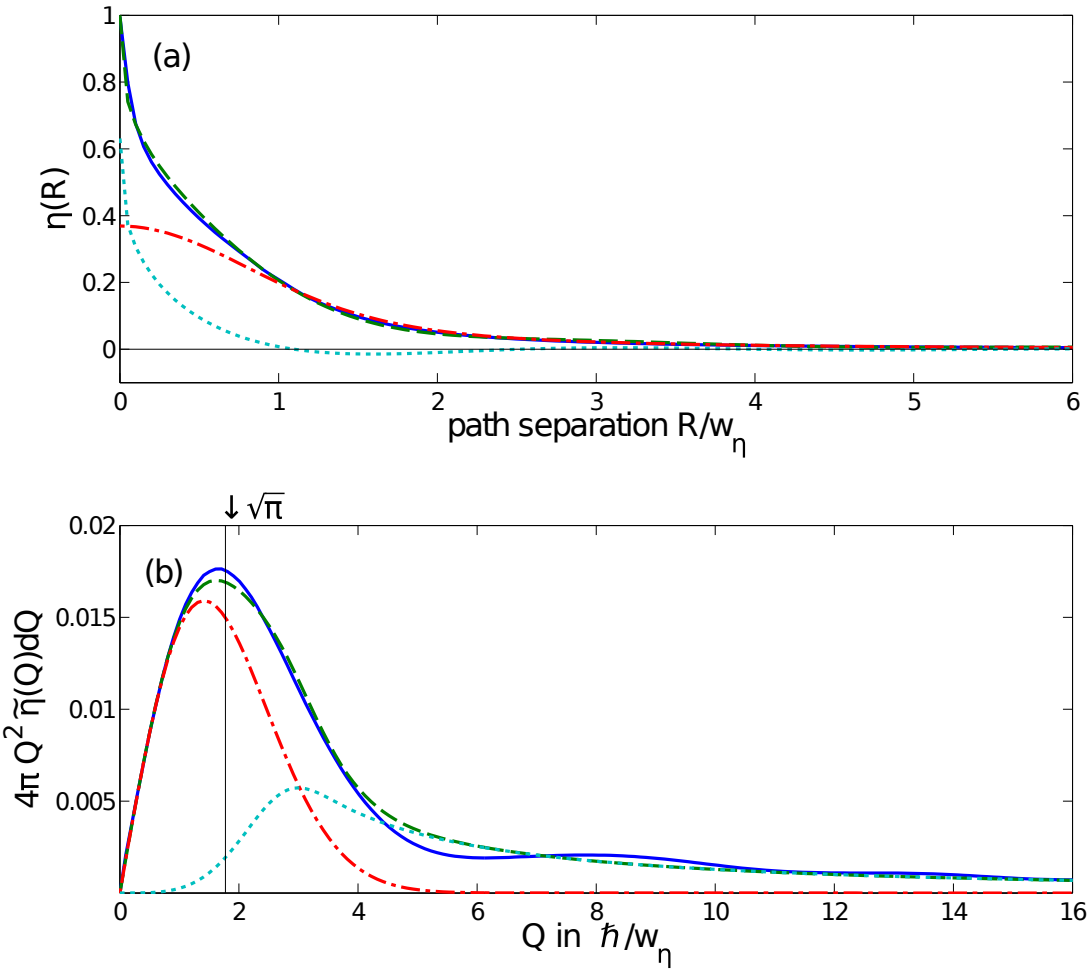

Figure 26: (a) Comparison of the numerical and the approximate analytical decoherence function $\eta(\mathbf{R})$. For the numerical data (solid line), the numerical differential cross section in Fig. 24 is used. The numerical integration of Eq. (5.20) with this differential cross section gives the solid line in Panel (a). The dash-dotted and dotted lines show the theoretical results for the soft, $h(s)D_1(|\mathbf{R}|/w_\eta)$, and hard collision, $(1-h(s))D_2(|\mathbf{R}|\mu(s)/w_\eta)$, respectively. The dashed line stands for the total theoretical decoherence function $\eta(\mathbf{R})$ Eq. (5.55). (b) Comparison between the numerical and theoretical results for the transfered momentum distribution $\widetilde{\eta}(\mathbf{Q})$. The solid curve is the result of the numerical integration of Eq. (5.60) using the differential cross section from Fig. 24. The dash-dotted and dotted lines are theoretical results for the soft scattering ($\widetilde{\eta}_s(\mathbf{Q})$, Eq. (5.64)) and hard scattering contribution ($\widetilde{\eta}_h(\mathbf{Q})$, Eq. (5.66)), respectively. The dashed line shows the total theoretical kick distribution $\widetilde{\eta}(\mathbf{Q}) = \widetilde{\eta}_s(\mathbf{Q}) + \widetilde{\eta}_h(\mathbf{Q})$. For this Figure a gas temperature of $T = 300$ K is assumed. Otherwise the same parameter are used as in Fig. 23 and 24.

5.2.5 *Kick distribution*

The decoherence function treated in the previous section describes the decay of the spatial coherence by a single scattering event. Another useful quantity is the distribution of the transfered momentum $\mathbf{Q}$, which is given by the Fourier transform of the decoherence function [28]

$$\begin{aligned}\widetilde{\eta}(\mathbf{Q}) &= \frac{1}{(2\pi\hbar)^3}\int \mathrm{d}^3R\eta(|\mathbf{R}|)\exp\left(-\mathrm{i}\frac{\mathbf{Q}\cdot\mathbf{R}}{\hbar}\right)\\ &= \frac{1}{2\pi^2\hbar^3}\int_0^\infty \mathrm{d}R\, R^2\eta(R)\mathrm{sinc}\left(\frac{QR}{\hbar}\right),\end{aligned} \tag{5.58}$$

Here, the norm of the vectors $R = |\mathbf{R}|$ and $Q = |\mathbf{Q}|$ are introduced. Instead of using the approximated decoherence function (5.55), I insert the general expression Eq. (5.20) into Eq. (5.58). Using the orthogonality relation of the sinc-function [66]

$$\int_0^\infty \mathrm{d}x\, x^2\mathrm{sinc}(kx)\ \mathrm{sinc}(k'x) = \pi\delta(k-k')/2k^2, \tag{5.59}$$

the kick distribution can be evaluated to

$$\begin{aligned}\widetilde{\eta}(\mathbf{Q}) &= \left[\left\langle\sigma_{\mathrm{tot}}(p_\mathrm{g})\right\rangle_\Omega \Gamma\left(\frac{2s-3}{s-1}\right)Q^2\right]^{-1}\int_0^\infty \mathrm{d}x\, x^3\mathrm{e}^{-x^2}\\ &\quad\times\int_0^\pi \mathrm{d}\theta\ \sin\theta\left\langle\left|f(p_\mathrm{g}x,\cos\theta)\right|^2\right\rangle_\Omega \delta\left(Q-2p_\mathrm{g}x\sin\left(\frac{\theta}{2}\right)\right),\end{aligned} \tag{5.60}$$

where $x = p/p_\mathrm{g}$. The delta function in Eq. (5.60) guarantees the conservation of the total momentum after a scattering event, i.e. $\mathbf{Q} = \mathbf{p} - \mathbf{p}'$, where $\mathbf{p}$ and $\mathbf{p}'$ are the incoming and outgoing momentum of the gas particle. In accordance with the conservation of the energy, the norm of the transfered momentum must fulfill $|\mathbf{Q}| = p\sqrt{2-2\cos\theta} = 2p\sin(\theta/2)$ with the scattering angle θ. Evaluating the delta function in the small angle approximation, where $\sin\theta \approx \theta$, the distribution function reads

$$\widetilde{\eta}(\mathbf{Q}) \approx \left[\left\langle\sigma_{\mathrm{tot}}(p_\mathrm{g})\right\rangle_\Omega \Gamma\left(\frac{2s-3}{s-1}\right)Qp_\mathrm{g}^2\right]^{-1}\int_0^\infty \mathrm{d}x\, x\mathrm{e}^{-x^2}\left\langle\left|f(p_\mathrm{g}x,\cos\theta)\right|^2\right\rangle_\Omega\Bigg|_{\theta=Q/p_\mathrm{g}x} \tag{5.61}$$

$$= \widetilde{\eta}_\mathrm{s}(\mathbf{Q}) + \widetilde{\eta}_\mathrm{h}(\mathbf{Q}). \tag{5.62}$$

In the following, I consider the soft scattering part $\widetilde{\eta}_\mathrm{s}(\mathbf{Q})$ and the hard scattering part $\widetilde{\eta}_\mathrm{h}(\mathbf{Q})$ of the kick distribution separately.

Inserting the soft scattering part of the differential cross section Eq. (5.33) into Eq. (5.61), the distribution reads

$$\widetilde{\eta}_s(\mathbf{Q}) = \frac{A(p_\mathrm{g})}{2Qp_\mathrm{g}^2\left\langle\sigma_{\mathrm{tot}}(p_\mathrm{g})\right\rangle_\Omega}\int_0^\infty \mathrm{d}\xi\,\frac{\nu(\xi)}{\xi^2}\exp\left[-\left(\frac{Q}{p_\mathrm{g}\theta_*(p_\mathrm{g})\xi}\right)^2\right], \tag{5.63}$$

where $\xi = x^{1/(s-1)}$. The probability function $\nu(\xi)$ is defined in Eq. (5.53). This integral can be evaluated in the same approximation applied for the calculation of the decoherence function, see Sect. 5.2.4 and Appendix B.4. The approximated expression of the distribution function is then given by

$$\begin{aligned}\widetilde{\eta}_s(\mathbf{Q}) &\approx \frac{A(p_\mathrm{g})}{2Qp_\mathrm{g}^2\left\langle\sigma_\mathrm{tot}(p_\mathrm{g})\right\rangle_\Omega \xi_s^2}\exp\left[-\left(\frac{Q}{p_\mathrm{g}\theta_*(p_\mathrm{g})\xi_s}\right)^2\right] \\ &= \frac{h(s)}{2\pi Q}\left(\frac{w_\eta}{2\hbar}\right)^2\exp\left[-\left(\frac{Qw_\eta}{2\hbar}\right)^2\right], \qquad (5.64)\end{aligned}$$

which involves the mean transferred momentum $\sqrt{\pi}\hbar/w_\eta$. The same result can be obtained by a direct Fourier transformation of the decoherence function Eq. (5.49). Analogously, the hard scattering part can be evaluated to

$$\begin{aligned}\widetilde{\eta}_h(\mathbf{Q}) &= \frac{1-h(s)}{2s\pi\Gamma(1-2/5s)Q^2}\left(\frac{\theta_\mathrm{cl}(p_\mathrm{g})p_\mathrm{g}}{Q}\right)^{2/s} \\ &\quad\times\int_0^\infty \mathrm{d}\xi\,\nu(\xi)\xi^{2/s}\left(1-\exp\left[-\left(\frac{Q}{p_\mathrm{g}\theta_\mathrm{cl}(p_\mathrm{g})\xi}\right)^5\right]\right) \qquad (5.65) \\ &\approx \frac{1-h(s)}{2s\pi\Gamma(1-2/5s)Q^3}\left(\frac{Qw_\eta}{2\hbar\mu(s)}\right)^{-2/s}\left(1-\exp\left[-\left(\frac{Qw_\eta}{2\hbar\mu(s)}\right)^5\right]\right). \qquad (5.66)\end{aligned}$$

Note that the singularity of $\widetilde{\eta}(\mathbf{P})$ at $\mathbf{P}=0$ reflects the fact that the decoherence function (5.55) is not normalizable, i.e. $\int \mathrm{d}^3R\ \eta(\mathbf{R}) = \infty$. Nevertheless, its Fourier transform (5.62) is normalized $\int \mathrm{d}^3Q\ \widetilde{\eta}(\mathbf{Q}) = 1$ in accordance with $\eta(0) = 1$. Figure 26(b) shows the distribution for the absolute value of the transfered momentum $4\pi Q^2\widetilde{\eta}(|\mathbf{Q}|)$, which confirms a good agreement of the theory with the numerical result. The most probable transfered momentum seems to be well approximated by $\sqrt{\pi}\hbar/w_\eta$ (solid vertical line in Fig. 26(b)). As expected, the hard collision part of the differential cross section describes a high transfered momentum $Q \gtrsim 2\hbar/w_\eta$.

5.3 PHASE-SPACE DYNAMICS IN THE PRESENCE OF COLLISIONAL DECOHERENCE

Having derived an analytical expression for the decoherence function $\eta(\mathbf{R})$, which describes the loss of spatial coherences due to a singe collision, I am now in a position to treat the molecular motional state in a gaseous environment. As demonstrated in Sect. 5.1, the master equation in the limit of high molecular mass $m/M \to \infty$ is given by

$$\partial_t \left\langle \mathbf{R}_1 \right| \rho \left| \mathbf{R}_2 \right\rangle = \frac{1}{\mathrm{i}\hbar}\left\langle \mathbf{R}_1 \right| [\rho, \mathsf{H}] \left| \mathbf{R}_2 \right\rangle - \gamma(t)[1-\eta(\mathbf{R}_1-\mathbf{R}_2)]\left\langle \mathbf{R}_1 \right| \rho \left| \mathbf{R}_2 \right\rangle, \qquad (5.67)$$

where $\gamma(t)$ is the scattering rate and $\eta(\mathbf{R})$ is the decoherence function. Here I consider the one-dimensional dynamics in the x-direction, which is relevant for the application

to the matter wave interferometer in Chap. 6, as discussed in Sect. 2.1. For simplicity I denote the molecular c.m. coordinate and momentum in x-direction as $\mathbf{R} \cdot \mathbf{e}_x = x$ and $\mathbf{P} \cdot \mathbf{e}_x = p$.

The master equation (5.67) can be conveniently solved using the characteristic function of the Wigner function, see Sect. 2.25. Let us first consider the free propagation in absence of collisional decoherence. As discussed in Sect. 2.3, the free evolution of the Wigner function is described by the equation $\partial_t W(x,p) = -p\partial_x W(x,p)/M$. This corresponds in the picture of the characteristic function to

$$\partial_t \chi_t(s,q) \stackrel{\gamma=0}{=} -\int\int \mathrm{d}x\mathrm{d}p\, \mathrm{e}^{\mathrm{i}(qx-ps)/\hbar} \frac{p}{M}\frac{\partial}{\partial x} W_t(x,p) = -\frac{q}{M}\frac{\partial}{\partial s}\chi_t(s,q). \quad (5.68)$$

Its solution is a shearing transformation $\chi_t(s,q) = \chi_0(s - qt/m, q)$ as in the Wigner representation, see Sect. 2.3. Thus the master equation Eq. (5.67) in the characteristic function representation reads

$$\partial_t \chi_t(s,q) = -\frac{q}{M}\partial_s \chi_t(s,q) - \gamma(t)[1-\eta(s)]\chi_t(s,q). \quad (5.69)$$

On the one hand, this partial differential equation has a simple solution $\chi_t(s,0) = \chi_0(s,0)\exp(-\int_0^t \mathrm{d}\tau\, \gamma(\tau)[1-\eta(s)])$ if $q = 0$. On the other hand, the general solution must contain the free propagation solution $\chi_t(s,q) = \chi_0(s - qt/m, q)$ in the limit of $\gamma \to 0$. Combining these two special solutions, one gets the general solution of Eq. (5.69) [130]

$$\chi_t(s,q) = \chi_0\left(s - \frac{qt}{M}, q\right) \exp\left\{\int_0^t \mathrm{d}\tau\, \gamma(\tau)\left[\eta\left(s - \frac{q}{M}(t-\tau)\right) - 1\right]\right\}. \quad (5.70)$$

It can be readily shown that this characteristic function solves the differential equation (5.69). Thus in the characteristic function representation, the effect of decoherence is represented by an exponential factor.

6

APPLICATION TO MATTER-WAVE INTERFEROMETRY

In the previous chapters, I concentrated on the description of the molecule-light interaction including diverse photophysical molecular processes as well as the effect of molecule-atom scattering. As an application, I examine interference of molecules in some prominent interferometers in this chapter: the KDTL (Kapitza-Dirac-Talbot-Lau) interferometer in Sect. 6.1, OTIMA (Optical time-domain ionizing matter-wave) interferometer in Sect. 6.2 and a far-field interferometer in Sect. 6.3. Interferometers show the quantum nature of particles in an illustrative way and can also be applied for a measurement of vacuum properties of particles [47]. In the course of this chapter, I especially highlight three effects with the help of interferometers: photon absorption, fluorescence and collisional decoherence.

Photon absorption results in a transfer of momentum and excites a molecule. The absorption-induced recoil can shift an interferogram, which is well illustrated especially in a far-field interferometer: noticeable additional sub-peaks occur in the interferogram, see Sect. 6.3.1. In addition, an optical excitation of a molecule can enhance its absorption cross section and the polarizability, which is shown to have a significant effect on both the near- and far-field interference. That is, an interferometer with optical gratings can be used for a measurement of excited state properties of molecules, which are otherwise hard to access.

Both fluorescence and collisional decoherence are expected to result in a reduction of interference contrast, which is discussed in Sect. 6.1 and 6.4. Compared to fluorescence, the decoherence due to scattering with an environmental gas is more pronounced because the collision-induced momentum transfer is typically about 100 times larger than the grating momentum $2\pi\hbar/d$, see also Sect. 5.2.5. Due to this large impact of scatterings, one expects also that a lot of the scattered molecules are kicked out of an interferometer, which causes a signal loss. While collisional decoherence leads to an exponential reduction of the visibility in a near-field interferometer, scattered molecules can create a flat underground in a far-field interferogram as examined in 6.4.

6.1 KAPITZA-DIRAC-TALBOT-LAU INTERFEROMETER

As discussed in Subsection. 2.6.2, the KDTLI is a near-field Talbot-Lau interferometer consisting of three gratings. The first material grating imprints periodic patterns into the molecular density distribution in order to create sufficient spatial coherence in

front of the second grating. The quantum diffraction occurs at the second grating, which is formed by a standing-wave laser beam. The third material grating serves to scan the molecular density distribution. I consider here the most relevant symmetric case, that is, the gratings have the same period d and are equally separated by the distance L. In Sect. 6.1.1, the results of the ladder model are discussed, which describes the transformation of the molecular center-of-mass state by an optical grating. Here, also the triplet excited state of a molecule is taken into account, which can enhance the absorption cross section and polarizability of molecules. The ladder model is a good approximation if the Rabi-oscillation between the ground and excited state is negligible, which is guaranteed by the extremely short lifetime of molecular vibronic states, see Sect. 3.2. Nevertheless, it is an interesting question, how Rabi-oscillations affect the KDTLI interference for dipole transitions with long lifetimes as in the case of atomic interferometry. It turns out that the interferogram gets highly nonsinusoidal, as shown in Sect. 6.1.3. Finally, in Sect. 6.1.4, the effect of fluorescence is examined.

6.1.1 *Ladder model*

As discussed in Sect. 2.6.2, the interference pattern of KDTLI has a sinusoidal form, characterized by the visibility $\mathcal{V}_{\sin}$ and the mean molecular count rate $\overline{S}$, see Eq. (2.64). Due to the absorption-induced increase of the internal temperature, molecules are distinguishable in terms of the absorbed photon number ℓ. If a molecule absorbs ℓ photons, the conditional sinusoidal interference pattern reads

$$S_\ell(x_\mathrm{s}) = \overline{S}_\ell \left[1 + \mathcal{V}_{\sin}(\ell) \cos\left(\frac{2\pi x_\mathrm{s}}{d}\right)\right], \tag{6.1}$$

where x_s is the shift of the third grating and $\overline{S}_\ell$ is the mean molecular counts. The interferogram is characterized by the conditional visibility

$$\mathcal{V}_{\sin}(\ell) = 2\mathrm{sinc}^2(\pi f) \frac{B_2\left(L/L_\mathrm{T};\ell\right)}{B_0\left(0;\ell\right)}, \tag{6.2}$$

where $f = D_\mathrm{g}/d$ is the opening fraction of the material gratings and L_T is the Talbot length, see Eq. (2.44). From the solution of the ladder-model master equation $\rho_{\ell\ell}$, Eq. (3.45), the conditional Talbot-coefficients $B_m(\xi;\ell)$ can be calculated in terms of the Fourier integral

$$B_m(\xi;\ell) = \frac{1}{d}\int_{-d/2}^{d/2} \mathrm{d}x\, \exp\left(-\mathrm{i}\frac{2\pi x}{d}m\right) \frac{\rho_{\ell\ell}(x - d\xi/2, x + d\xi/2)}{\widetilde{\rho}(x - d\xi/2, x + d\xi/2)}. \tag{6.3}$$

Here, $\widetilde{\rho}$ is the initial density operator prior to the laser interaction. Note that the unconditional interferogram is given by the sum $S = \sum_{\ell=0}^{\infty} S_\ell$, however, the unconditional visibility does not corresponds to the sum of conditional ones, $\mathcal{V}_{\sin} \neq \sum_{\ell=0}^{\infty} \mathcal{V}_{\sin}(\ell)$. The unconditional visibility is given by the sum

$$\mathcal{V}_{\sin} = \sum_{\ell=0}^{\infty} B_0(0;\ell)\mathcal{V}_{\sin}(\ell) \tag{6.4}$$

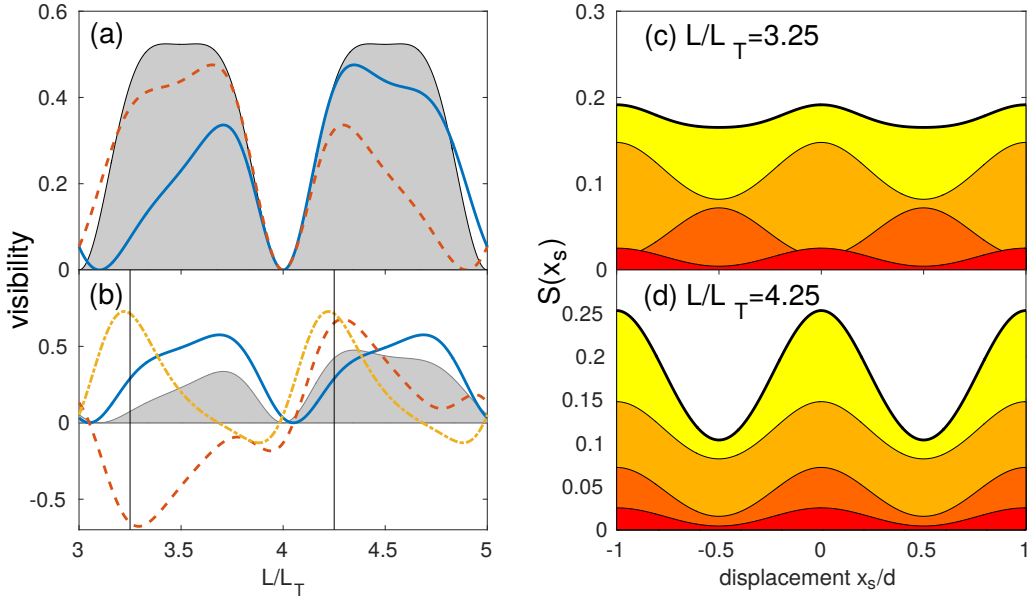

Figure 27: (a) Unconditional sinusoidal visibility based on the ladder model as a function of the Talbot parameter L/L_T. The visibility in the presence of photon absorptions (solid line, $\phi_0 = \pi$, $n_0 = 1$) is compared with the case of a pure phase grating (shadowed area, $\phi_0 = \pi$, $n_0 = 0$). The earlier description of the photon absorption as a classical random-walk [31] (dashed line) does not agree with the correct quantum prediction. (b) The solid, dashed and dash-dotted lines are the conditional visibilities Eq. (6.2) for $\ell = 0,\ 1$, and 2 photon absorptions, respectively. Compared to the unconditional result (shaded area), one expects higher maximal visibilities. Panel (c) and (d) show the KDTLI interferograms for $L/L_T = 3.25$ and 4.25, respectively. These values are indicated in Panel (b) as the vertical lines. The thick top line is the unconditional interferogram and the thin lines correspond to conditional ones for $\ell = 0$, 1 and 2 from the top. For this figure, I set the opening fraction of the first and third grating to $f = 0.42$ and the enhancement factor to $\eta_a^{(T)} = \eta_p^{(T)} = 1$, i.e. a molecule is assumed not to change its properties upon absorption of photons.

weighted by the conditional transmission $B_0(0;\ell)$ with $\sum_{\ell=0}^{\infty} B(0;\ell) = 1$.

In oder to examine the effect of photon absorptions, let us consider the case of $\eta_a^{(T)} = \eta_p^{(T)} = 1$, that the molecular polarizability and the absorption cross section are independent of the internal molecular excitation. In this case the integral in Eq. (6.3) can be evaluated analytically, as presented in Sect. 3.4. Absorption of photons leads to a reduction of the unconditional visibility almost everywhere, as shown in Fig. 27(a), which compares the results in the presence (solid line) and in the absence of absorptions (shadowed area). The reduction is especially pronounced in the range $L/L_T \in [3,\ 4]$, which is due to the fact that some of the conditional interferograms are phase-flipped with respect to the others. Indeed, the conditional interferograms of molecules that absorbed an odd number of photons exhibit a negative visibility in this region,

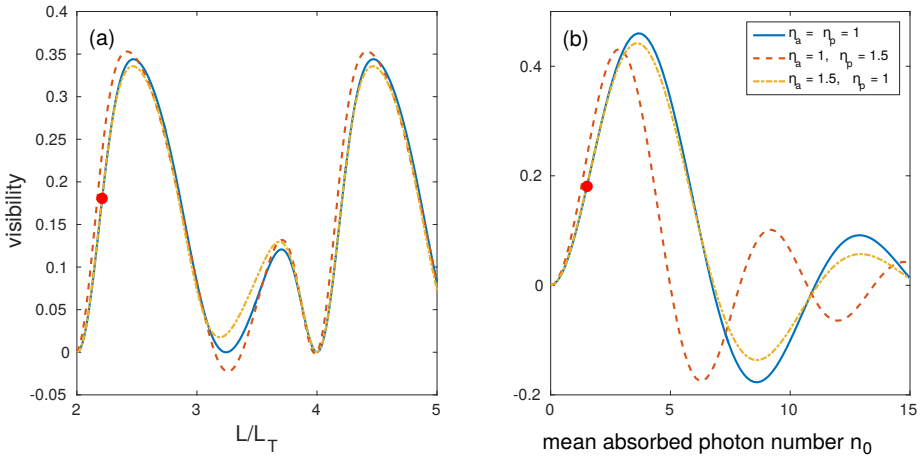

Figure 28: (a) Unconditional visibility as a function of the Talbot parameter L/L_T. The visibility for no triplet enhancement ($\eta_a^{(T)} = \eta_p^{(T)} = 1$, solid line) is compared with the case of an enhanced triplet absorption cross section ($\eta_a^{(T)} = 1.5$ and $\eta_p^{(T)} = 1$, dashed line) and an enhanced triplet polarizability ($\eta_a^{(T)} = 1$ and $\eta_p^{(T)} = 1.5$, dash-dotted line). The mean absorption number $n_0 = 1.5$ and the phase $\phi_0 = 1.25 n_0$ are assumed for this plot. (b) Unconditional visibility as a function of the mean absorbed photon number n_0, which scales linearly with the laser power. For this plot, the Talbot parameter is fixed to $L/L_T = 2.2$. For reference, the red dots denotes the same spot ($L/L_T = 2.2$, $n_0 = 1.5$) in both panels.

as shown in Fig. 27(b). In contrast, in the region $L/L_T \in [4, 5]$, the conditional interferograms are mostly in phase so that the unconditional visibility is comparably high. This phase flip is illustrated in Fig. 27(c) and (b), where the conditional interferograms are plotted for $L/L_T = 3.25$ and 4.25. In general, conditional interferograms exhibit a higher maximal visibility than the unconditional one, which is mainly due to a low conditional transmission probability: only 36% of the molecules absorb at least one photon. While the conditional interferograms reach a maximal visibility of about 0.7, the unconditional visibility is $\mathcal{V}_{\sin} \lesssim 0.5$, see Fig. 27(b).

It is important to remark that the earlier description of photon absorption implemented as classical random-walk in phase space [31] predicts a different visibility compared to the quantum model. Curiously, these two models predict mirror-imaged visibility curves, see Fig. 27(a). This difference, however, was not observed in previous experiments [23, 31] because this subtle effect is only visible if the molecular velocity distribution is sufficiently narrow. A new experiment with an improved velocity selection indicates the correctness of the ladder model [44], which is discussed in the next section.

The results in Fig. 27 are valid for low laser powers, where the ground state population dominates the molecular dynamics. However, for high laser powers, the long-lived molecular triplet state can no longer be neglected. For C_{70} in toluene, the absorption cross section of the triplet state exceeds that of the singlet state by the factor 1.5 (for the

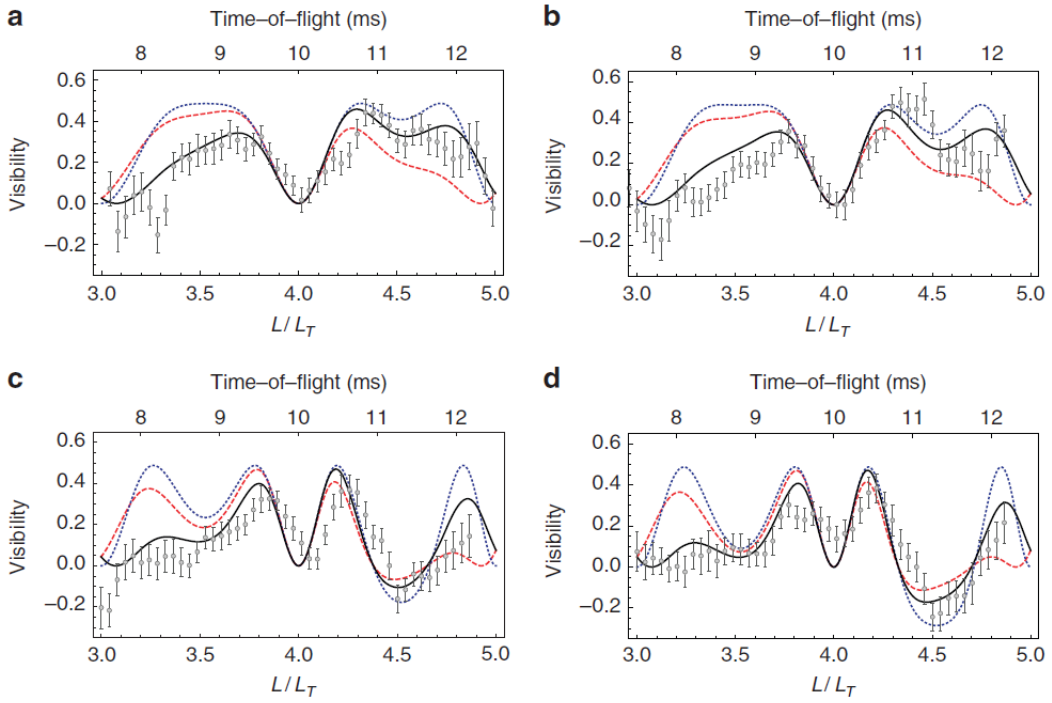

Figure 29: Panels (a)-(d) show experimental data measured in the KDTLI (gray points) and the unconditional visibility as predicted by the ladder model (solid line) for a laser power of (a) $P = 3.5$ W, (b) $P = 3.75$ W, (c) $P = 5.25$ W and (d) $P = 5.75$ W [44]. C_{70} molecules interfere in this experiment, whose polarizability and absorption cross section are given by $\alpha(C_{70}) = 4\pi\varepsilon_0 \times 114$ Å and $\sigma = 1.97 \cdot 10^{-21}$ m^2 for the laser wavelength of $\lambda_L = 532$ nm [81]. The blue dotted curve is the quantum prediction of a pure phase grating. The red dashed curve corresponds to the result of the absorption model, which treats photon absorptions incoherently in terms of the random momentum kicks in phase space [31].

laser wavelength of 523 nm) [131]. As shown in Fig. 28(a), the enhanced triplet-state polarizability and absorption hardly effects the visibility for $n_0 = 1.5$. For higher laser powers, where the mean absorption number exceeds $n_0 \gtrsim 2.5$, the effect of the molecular triplet state becomes visible, see Fig. 28(b). While the visibility is significantly affected by an enhanced polarizability (dashed line), the enhancement of the absorption cross section (dash-dotted line) seems to have a modest effect. That is, KDTLI could provide a non-spectroscopic measurement of the molecular excited-state polarizability, which is in general hard to access. (Because the triplet polarizability for C_{70} cannot be found in the literature, I assumed $\eta_p^{(T)} = \eta_a^{(T)} = 1.5$ for Fig. 28)

6.1.2 *Experimental verification of the ladder model*

Figure 29 shows the comparison between the experimental KDTLI visibilities (gray dots) and the theoretical prediction of the ladder model Eq. (6.4) (solid curve). The experimental data confirm the characteristic reduction of the visibility for the region $L/L_{\mathrm{T}} \in [3,\ 4]$ compared to the case of a pure phase grating (blue dotted line). The previous model, which treats photon absorptions as a classical random walk in phase space [31], cannot explain this reduction. That is, this experimental data provide evidence that the momentum transfer of $\pm\hbar k_{\mathrm{L}}$ due to a photon absorption is a coherent process as described in the ladder model. The negative visibilities in Fig. 29 indicate phase flips of the interferogram, as discussed in the previous section.

The experimental data do not indicate any effect of enhanced triplet-absorption cross section and triplet-polarizability of the C_{70} molecule. The mean absorbed photon number in this experiment is $n_0 \lesssim 1.8$ and thus the laser power is not high enough for the measurement of the enhancement factors $\eta_{\mathrm{a}}^{(\mathrm{T})}$ and $\eta_{\mathrm{p}}^{(\mathrm{T})}$. With increasing laser power, the visibility curve gets more structured, as illustrated by Panels (a)-(d), and the mean visibility becomes smaller [23, 31]. This effect might be a challenge for future KDTLI experiments with greater laser powers.

6.1.3 *Rabi model*

In the present thesis, photon absorptions by molecules are treated incoherently, assuming that Rabi-transitions between two molecular vibronic states are suppressed due to extreme short life times of the excited states. While it is a good approximation for many large molecules, there are also special cases, where a few Rabi cycles are permitted [132, 133]. My aim in this section is to examine the effect of Rabi-oscillations on the KDTLI interferogram.

For the examination of Rabi oscillation effects, I consider the dynamics between the molecular ground state $|\mathrm{S}_0\rangle \mathrel{\hat{=}} |0\rangle$and an excited state $|\mathrm{S}_n^*\rangle \mathrel{\hat{=}} |1\rangle$, which decays with the lifetime τ_{IC} to the lowest singlet excited state $|\mathrm{S}_1\rangle \mathrel{\hat{=}} |2\rangle$, see Sect. 3.2. If the decay time of the excited state is comparable to the interaction time t_{L}, the internal dynamics exhibits damped Rabi oscillations. The Rabi-oscillations due to an optical grating imprint an oscillating structure in the ground state transmission, because the oscillation frequency $\Omega_{\mathrm{R}}(x) = \sqrt{\Omega_0^2 \cos^2(k_{\mathrm{L}} x) + \Delta^2}$ depends on the position of the particle x, where Ω_0 is the on-resonance Rabi frequency and Δ is the detuning. This phenomenon is illustrated in Fig. 30(a), which compares the transmission of the ladder model Eq. (3.33) (shadowed area) to that of the Rabi-model (solid line). The transmission of the Rabi-model in Fig. 30(a) corresponds to the solution $\rho_{00}(x, x; t_{\mathrm{L}})$ of the master equation (3.10)-(3.13). For the Rabi case, there are two minima of zero transmission between a standing-wave node and an antinode, which correspond to an effective π- and 3π-pulse length. At an antinode, the transmission is below 100% due to losses into the dark state.

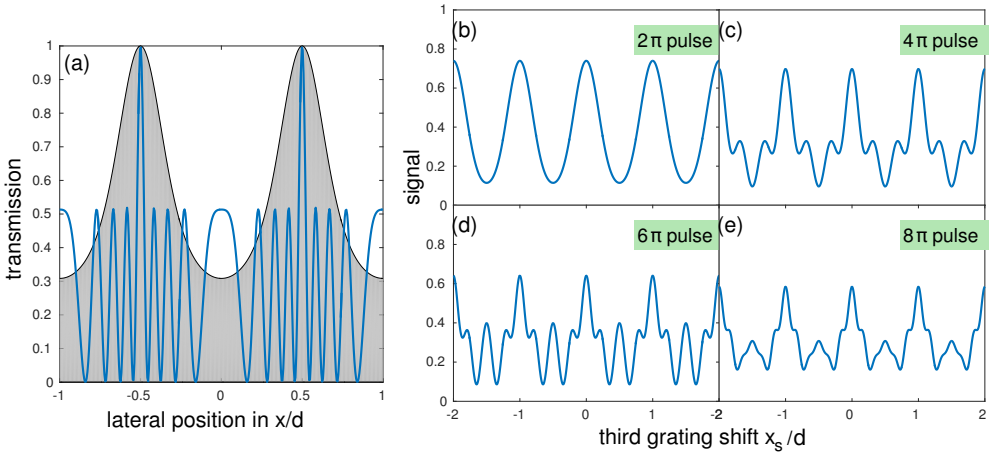

Figure 30: (a) Transmission probability for molecules ending up in the ground state. The solid line corresponds to the analytical solution $\rho_{00}(x, x; t_L)$ of the master equation (3.10)-(3.13). For comparison, a conditional transmission of the ladder model for zero photon absorption ($n_0 = 1.2$, shadowed area) is shown. Here, I assumed the resonant case $\Delta = 0$, a long excited state lifetime $\tau_{IC} = t_L$ and the Rabi frequency $\Omega_0 t_L = 4\pi$, i.e. a 4π-pulse at the laser anti-nodes. (b)-(e) Numerical results for the KDTLI fringe pattern (2.61) in the presence of Rabi oscillations. For better illustration of the Rabi-effect on the interferogram, the detector is assumed to be sensitive only to the ground-state particles. The separation of the KDTLI gratings is $L = 2L_T$ and the opening fraction of the first and the third grating is chosen to be small, $f = 0.1$. The Rabi frequencies are $\Omega_0 t_L = 2\pi$ to 8π in panels (b) to (e), respectively. The interferograms become highly nonsinusoidal because higher-order fringes emerge with each Rabi cycle.

Because of the additional oscillation in the molecular transmission probability, one expects higher-order fringe oscillations also in the KDTLI interferograms. Figure 30(b)-(e) shows the interferograms of ground-state molecules for different Rabi frequencies, which indicates the higher harmonics in the fringe patterns. For these curves the ground-state density operator $\rho_{00}(x, x'; t_\mathrm{L})$, evaluated from the master equation (3.10)-(3.13), is inserted into Eq. (2.61). Note that the opening fraction of the first and third grating is assumed to be small, $f = 0.1$, not to wash out small structures in the fringe pattern.

6.1.4 *Fluorescence*

The ladder model delivers reliable results for molecules, where the intersystem crossing dominates the deactivation processes of the singlet excited state, e.g. for C_{60} or C_{70}. However for molecules with sufficiently high fluorescence yield, e.g. Hypericin or TPP, one expects in addition decoherence due to fluorescence, i.e. reduction of the interference visibility. The calculation of the sinusoidal visibility is analogous to the ladder model in Sect. 6.1.1. The conditional visibility reads

$$\mathcal{V}_\mathrm{sin}(\ell_\mathrm{F}) = 2\mathrm{sinc}^2(\pi f)\frac{B_2\left(L/L_\mathrm{T}; \ell_\mathrm{F}\right)}{B_0\left(0; \ell_\mathrm{F}\right)} \tag{6.5}$$

if a molecule undergoes ℓ_F fluorescence events. The conditional Talbot coefficients $B_m(\xi; \ell_\mathrm{F})$ can be calculated from the solutions of the fluorescence master equation (4.28) and (4.30),

$$\begin{aligned} B_m(\xi; \ell_\mathrm{F}) &= \frac{1}{d}\int_{-d/2}^{d/2} \mathrm{d}x\, \exp\left(-\mathrm{i}\frac{2\pi x}{d}m\right) \\ &\quad \times \frac{\rho_{\mathrm{G},\ell_\mathrm{F}}(x - d\xi/2, x + d\xi/2) + \rho_{\mathrm{T},\ell_\mathrm{F}}(x - d\xi/2, x + d\xi/2)}{\widetilde{\rho}(x - d\xi/2, x + d\xi/2)} \end{aligned} \tag{6.6}$$

Here, the subscripts G and T stand for the ground state and triplet state, respectively. The unconditional visibility is given by the sum over all conditionals $B_m(\xi) = \sum_{\ell_\mathrm{F}=0}^{\infty} B_m(\xi; \ell_\mathrm{F})$.

It turns out that the effect of fluorescence decoherence is small directly behind a diffraction grating, as illustrated in Fig. 31(a). Note that for simplicity I assumed a δ-like fluorescence spectrum $f_k(k) = \delta(k - k_\mathrm{F})$ with the fluorescence wavenumber $k_\mathrm{F} = 0.7k_\mathrm{L}$ in Fig. 31. The mean momentum recoil $\hbar k_\mathrm{F}/2$ of a fluorescence photon leads after free propagation over a distance L to a shift of the molecular position of about

$$\Delta x_\mathrm{F} = \frac{\hbar k_\mathrm{F}}{2M}\frac{L}{v_\mathrm{M}} = \frac{k_\mathrm{F} d}{2k_\mathrm{L}}\frac{L}{L_\mathrm{T}}, \tag{6.7}$$

where M and v_M are the mass and the longitudinal velocity of a molecule. For example, for $L/L_\mathrm{T} \lesssim 0.5$ and $k_\mathrm{F} = k_\mathrm{L}$, the estimated shift of molecules due to the emission of a fluorescence photon is $\Delta x_\mathrm{F} \lesssim 0.15d$. Because this shift is small compared to the period of the interferogram d, fluorescence does not lead to a total destruction of the visibility.

This is demonstrated in Fig. 31(b), where the conditional visibilities are shown for different numbers of fluorescence events $\ell_F = 0,\ 1$ and 2 for the solid, dashed and dash-dotted line, respectively. For $L/L_T \lesssim 0.5$ one expects still high visibilities, while for $L/L_T \gtrsim 0.5$ fluorescence deteriorates the conditional visibilities for $\ell_F \geq 1$ almost completely. Of course, the zeroth conditional visibility (solid line in Fig. 31(b)) is not affected by fluorescence, that is why the unconditional visibility is still nonzero even for $L/L_T \gtrsim 0.5$.

Surprisingly, the unconditional visibility is enhanced due to fluorescence in the range $L/L_T \in [1,\ 2]$, see Fig. 31(a). Recalling the ladder model discussed in Sect. 6.1.1, this is the region where photon absorptions deteriorate the visibility because some conditional interferograms exhibit a negative visibility. Due to fluorescence decoherence, the contribution with negative conditional visibilities vanish, which leads to an improvement of the unconditional visibility.

The effect of fluorescence depends sensitively on the mean absorbed photon number n_0, i.e. on the laser power, as shown in Fig. 27(c), where the unconditional visibility is examined for a fixed Talbot parameter $L/L_T = 2.5$. The maximum of the visibility at $n_0 \approx 2$ reduces about 30% due to fluorescence. Interestingly, the effect of fluorescence is less pronounced for a high absorption number n_0. That is, in order to examine the effect of fluorescence, one does not need a high-power laser. A mean absorption number of $n_0 = 1.5 - 3.5$ is quite sufficient for this sake.

6.2 OTIMA INTERFEROMETER

In any interferometer based on the Talbot-Lau scheme the initially incoherent beam of particles must interact with an absorptive grating, which modulates the particle's transmission periodically. In the case of KDTLI, the first material grating serves as a preparer for a coherent beam, see Sect. 2.6.2. In the OTIMA (optical time domain matter wave) interferometer, an absorptive grating is realized by a standing-wave laser grating, whose wavelength is short enough to ionize particles [32]. OTIMA consists of the three ionizing optical gratings and operates in time-domain, that is, these gratings are switched on for a short time interval. One of the useful features of OTIMA is the fact that the interference pattern is largely independent of the particle's longitudinal coherence and of the dispersive phase shifts, a general characteristic of time-domain interferometers [24].

In Sect. 6.2.1, I discuss the OTIMA interference assuming that a single absorption event leads to an ionization of a particle. A detailed description for this case is presented also in Ref. [32]. In Sect. 6.2.2, I consider a particle, which can store multiple photon energies before it gets ionized.

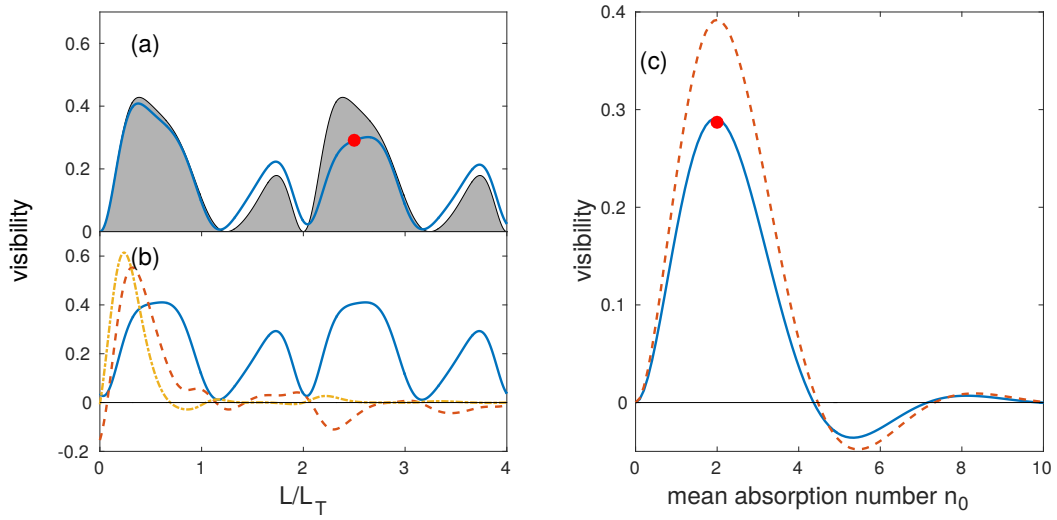

Figure 31: (a) Unconditional KDTLI visibility as a function of the Talbot parameter L/L_{T} in the presence (solid line) and in the absence of fluorescence (shadowed area). The quantum yields are chosen to be $\Phi_{\mathrm{ISC}} = 0.52$, $\Phi_{\mathrm{IC}} = 0$ and $\Phi_{\mathrm{F}} = 0.48$ for the solid line, which corresponds to Hypericin. The shadowed area is a prediction of the ladder model. (b) The conditional visibilities for different numbers of fluorescence events $\ell_{\mathrm{F}} = 0$ (solid line), 1 (dashed line) and 2 (dash-dotted line). For Panels (a) and (b) the mean absorbed photon number and the phase are set to $n_0 = 2$ and $\phi_0 = 1.25 n_0$, respectively. (c) Unconditional visibility as a function of the mean absorption number n_0 for a fixed Talbot parameter $L/L_{\mathrm{T}} = 2.5$. The visibility in the presence of fluorescence (solid line) is compared with the result of the ladder model (dashed line). The visibility reduction is maximal for $n_0 \approx 2$. The red dots denote the same point $(L/L_{\mathrm{T}},\ n_0) = (2.5,\ 2)$ in Panel (a) and (c). The fluorescence spectrum is assumed to be δ-shaped in this figure, i.e. $f_k(k) = \delta(k - k_{\mathrm{F}})$ with the fluorescence wavelength $k_{\mathrm{F}} = 0.7 k_{\mathrm{L}}$.

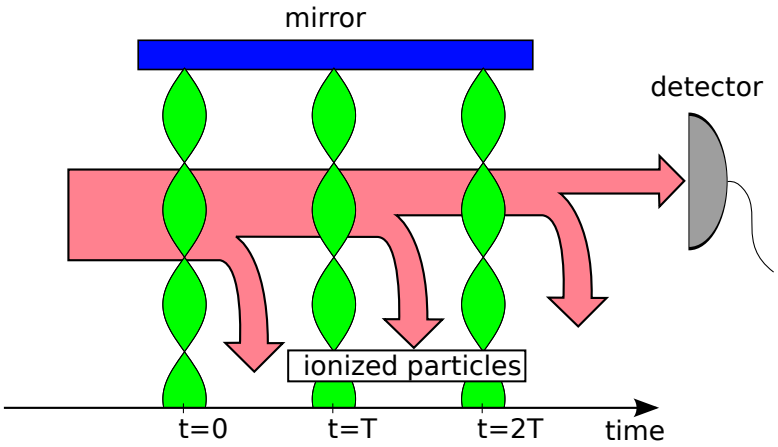

Figure 32: Schematic illustration of the OTIMA setup. A cloud of molecules passes through three pulsed optical ionizing gratings, which illuminate the molecules at times $t = 0$, T and $2T$. The ionized molecules are removed from the interferometer by means of a homogeneous electric field.

6.2.1 *Single-photon ionization grating*

As depicted in Fig. 32, the OTIMA interferometer consists of three optical gratings G_1, G_2 and G_3, which illuminate subsequently a cloud of particles for a short time Δt. The delay time T between two grating pulses serves as a control parameter in OTIMA, while the spatial separation of the gratings are fixed. For realizing an absorptive grating, an UV laser is utilized, whose wavelength is short enough to ionize the particles. These gratings are referred to as a single-photon ionization (SPI) gratings. The ionized particles are then removed from the interferometer by means of a homogeneous electric field. That is, these ionization gratings create a spatial modulation of the non-ionized particles similar to a material grating.

From theoretical point of view, the description of OTIMA and KDTLI is the same: OTIMA can be interpreted as a conditional KDTLI, which detects only such particles that absorb no photons. That is, the OTIMA interferograms are described by means of the conditional Talbot coefficient $B_m(T/t_T; \ell = 0)$, see Eq. (3.71). Note that the interferogram depends on the pulse delay T/t_T, where t_L is the Talbot time, see Eq. (2.44). The sinusoidal visibility is thus given by [32]

$$\begin{aligned} \mathcal{V}_{\text{sin}} &= 2\frac{B_{-1}^{(1)}(0;0)B_2^{(2)}\left(T/t_T;0\right)B_{-1}^{(3)}(0;0)}{B_0^{(1)}(0;0)B_0^{(2)}\left(0;0\right)B_0^{(3)}(0;0)} \\ &= 2\frac{I_1(n_0^{(1)}/2)}{I_0(n_0^{(1)}/2)}\left(\frac{\zeta_{\text{coh}}-\zeta_{\text{abs}}}{\zeta_{\text{coh}}+\zeta_{\text{abs}}}\right)\frac{J_2\left(\sqrt{\zeta_{\text{coh}}^2-\zeta_{\text{abs}}^2}\right)}{I_0(n_0^{(2)}/2)}\frac{I_1(n_0^{(3)}/2)}{I_0(n_0^{(3)}/2)}. \end{aligned} \tag{6.8}$$

Here, the superscript of the absorption number $n_0^{(j)}$ and the Talbot coefficients $B_m^{(j)}(\xi;\ell)$ denotes the j-th grating. This result is examined in detail in [32] and also confirmed experimentally [24, 25].

In the next subsection, I consider the general multi-photon absorption grating, where particles are not ionized until they absorb N photons.

6.2.2 *Multi-photon ionization grating*

If the ionization energy exceeds the photon energy, a particle ends up in an excited but not ionized state after absorption of a photon so that multiple photons are needed for ionization. In OTIMA a particle can absorb photons at three different optical gratings G_1, G_2 and G_3. Assuming that a particle has absorbed ℓ_{tot} photons in total, there are $\sum_{j=0}^{\ell_{\text{tot}}}(j+1) = (\ell_{\text{tot}}+1)(\ell_{\text{tot}}+2)/2$ possibilities to absorb photons at these gratings. For example for $\ell_{\text{tot}} = 1$, an absorption can occur at G_1, G_2 or G_3, i.e. there are three possibilities. For the calculation of the OTIMA visibility with N-photon ionization gratings, all these combinations must be taken into account, i.e. the sinusoidal visibility reads

$$\mathcal{V}_{\text{sin}}^{N} = 2\frac{C_1(T/t_{\text{T}};N)}{C_0(0;N)}. \tag{6.9}$$

Here, $C_j(\xi;N)$ denotes the total Talbot coefficients

$$C_j(\xi;N) = \sum_{\ell_{\text{tot}}=0}^{N}\sum_{\ell_1=0}^{\ell_{\text{tot}}}\sum_{\ell_2=0}^{\ell_{\text{tot}}-\ell_1} B_{-j}^{(1)}(0;\ell_1)B_{2j}^{(2)}(\xi j;\ell_2)B_{-j}^{(3)}(0;\ell_{\text{tot}}-\ell_1-\ell_2), \tag{6.10}$$

where the sum indices $\ell_1$and ℓ_2 stand for the number of absorbed photons at the first and the second grating, respectively. The triple sums in Eq. (6.10) involve all $\sum_{\ell_{\text{tot}}=0}^{N}(\ell_{\text{tot}}+1)(\ell_{\text{tot}}+2)/2 = (N+1)(N+2)(N+3)/6$ possible combinations of the Talbot coefficients. Note that the particle's polarizability and absorption cross section are assumed to be independent of the absorbed photon number ℓ. The effect of the enhancement of the polarizability and absorption cross section is discussed in the next section.

A main consequence of a multi-photon ionization is the reduction of the visibility for a fixed laser power, as shown in Fig. 33(a). The maximal visibility for quadruple-photon ionization gratings (dotted line) is reduced by about 80% compared to the case of SPI gratings. This reduction can be explained by the enhancement of the transmission $C_0(0;N)$, see Fig. 33(b), because the visibility (6.9) is inversely proportional to the transmission.

6.2.3 *Double-photon ionization grating incorporating the excited state*

In a multi-photon ionization grating, one must consider the photo-excitation of particles, which can lead to the enhancement of the polarizability and absorption cross section of the particle. For example, a molecule can be excited to the long-lived triplet

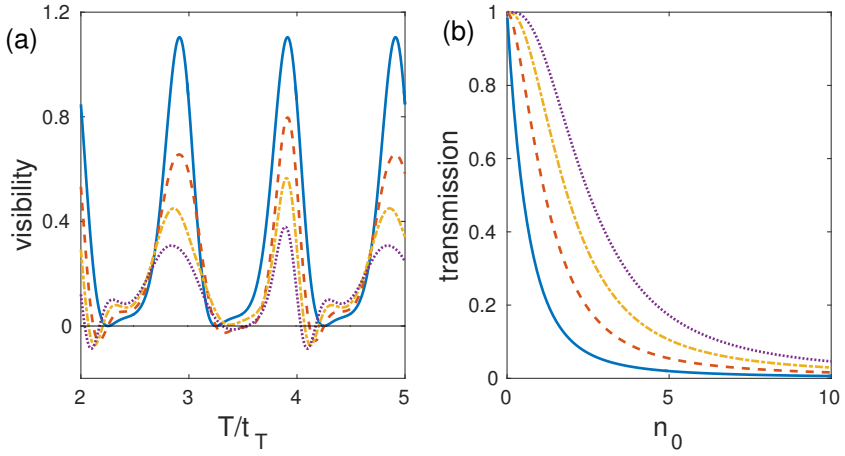

Figure 33: (a) Sinusoidal visibility (6.9) of the OTIMA with multi-photon ionization gratings as a function of the Talbot parameter T/t_{T}. The solid, dashed, dash-dotted and dotted line correspond to the case of single-, double-, triple-, quadruple-photon ionization gratings, respectively. The parameters are set to $n_0 = 2$ and $\phi_0 = 1.25 n_0$(b) Corresponding total transmission through the three optical gratings as a function of the mean absorbed photon number n_0.

state as discussed in Sect. 3.3. For the examination of this effect, I consider in this section the case of a double-photon ionization (DPI) grating.

As discussed in the previous subsection, there are three possibilities for the absorption of a single photon in the case of three DPI gratings. Let us consider at first the case that a particle absorbs a single photon at G_1. Here, the grating transformation of G_1 is given in terms of the conditional Talbot coefficients $B_m^{(1)}(0;\ell = 1)$. Because this particle is excited after G_1, the enhancement of the absorption number $n_0 \to \eta_{\mathrm{a}} n_0$ and phase modulation $\phi_0 \to \eta_{\mathrm{P}} \phi_0$ must be taken into account for the subsequent gratings transformations at G_2 and G_3. The transformation by the gratings G_2 and G_3 are thus represented by the conditional Talbot coefficients $\widetilde{B}_m^{(2)}(\xi;0)$ and $\widetilde{B}_m^{(3)}(0;0)$, respectively. Here, the tilde denotes that the Talbot coefficients refer to an excited particle. Considering all possibilities, the visibility reads

$$\mathcal{V}_{\mathrm{sin}} = 2\frac{C_1(T/t_{\mathrm{T}})}{C_0(0)}, \tag{6.11}$$

where the total Talbot coefficients are given by

$$\begin{aligned} C_j(\xi) \;=\; & B_{-j}^{(1)}(0;0) B_{2j}^{(2)}(\xi j;0) B_{-j}^{(3)}(0;0) + B_{-j}^{(1)}(0;1) \widetilde{B}_{2j}^{(2)}(\xi j;0) \widetilde{B}_{-j}^{(3)}(0;0) \\ & + B_{-j}^{(1)}(0;0) B_{2j}^{(2)}(\xi j;1) \widetilde{B}_{-j}^{(3)}(0;0) + B_{-j}^{(1)}(0;0) B_{2j}^{(2)}(\xi j;0) B_{-j}^{(3)}(0;1). \end{aligned} \tag{6.12}$$

Note that the first term stands for particles that absorbed no photons.

Wile the enhancement of the polarizability η_{p} does not have a major effect (Fig. 34(b)), the enhancement of the absorption cross section leads to a clear increase of the visibility, see Fig. 34(a). It turns out, in the limit of $\eta_{\mathrm{a}} \to \infty$, the DPI visibility (6.11) converges

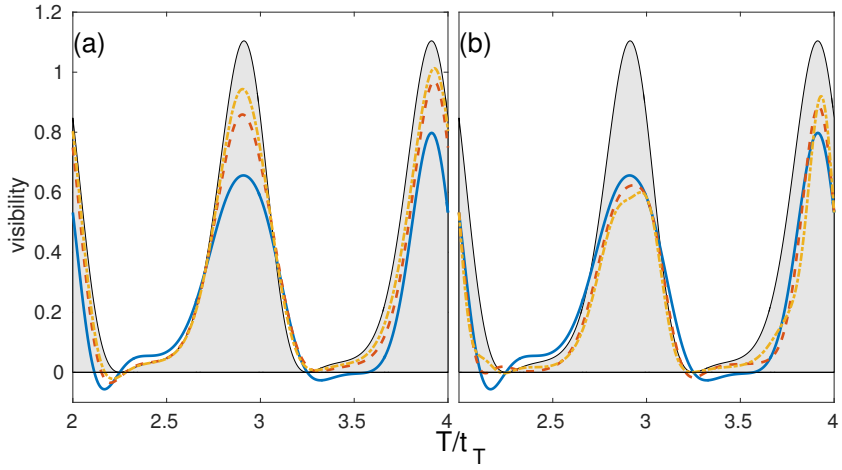

Figure 34: Visibility of OTIMA with DPI gratings as a function of Talbot parameter T/t_T. For the comparison, the shadowed area denotes the visibility in the case of SPI gratings. Panel (a) illustrates the effect of enhancement of the absorption cross section by comparing the visibilities for $\eta_a = 1$ (solid line), $\eta_a = 2$ (dashed line) and $\eta_a = 3$ (dashed-dotted line), while the polarizability is assumed to be unchanged, $\eta_p = 1$. For Panel (b), in contrast, I assumed a constant absorption cross section $\eta_a = 1$ and different excited state polarizability with $\eta_p = 1$ (solid line), $\eta_p = 2$ (dashed line) and $\eta_p = 3$ (dash-dotted line).

to the SPI case (6.8). In this case, the absorption of a single photon implies immediate absorption of an another one, i.e. a DPI grating in this limit is equivalent to a SPI grating. The OTIMA interferometer turns out to be sensitive to the enhancement of the absorption cross section, while the KDTLI is rather suitable for the measurement of the excited state polarizability, see Fig. 28. That is, OTIMA and KDTLI can serve as complementary measurement schemes for excited state properties.

6.3 FAR-FIELD INTERFEROMETER

A far-field interferometer tests the quantum nature of a particle in a very illustrative way since the interference pattern on the detection screen demonstrates clearly the particle-wave duality. Far-field interferometers have been successfully utilized to investigate the quantum properties of electrons [134], atoms [135] and also molecules [19, 52]. In this section I consider a far-field setup with an optical diffraction grating. It turns out that the recoil effect due to photon absorptions is highlighted in a far-field interferogram as additional sub-peaks, see Sect. 6.3.1. The effect of fluorescence is examined in Sect. 6.1.4.

6.3.1 *Ladder model*

A typical far-field interferometer consists of a beam source, a collimator, a diffraction grating, and a detector. The distance between a beam source and a diffraction grating shall be L_1. After the interaction with a diffraction grating, molecules propagate freely over the distance L_2 before they get detected. In this section I assume an optical grating for the diffraction and I present the implications of the ladder model applied to a far-field interferometer. For a detailed description of a far-field set up, see also Fig. 5 in Sect. 2.6.1.

As discussed in Sect. 3.3.5, the solution of the ladder master equation, which describes the transformation of the molecular center-of-mass state by an optical grating, can be given in terms of the generalized measurement operators $\widetilde{M}_\ell(x;\theta)$,

$$\rho_{\ell\ell}(x,x';t_\mathrm{L}) = \int_0^1 \mathrm{d}\theta\, \widetilde{M}_\ell(x;\theta)\widetilde{\rho}(x,x')\widetilde{M}^*_\ell(x';\theta). \tag{6.13}$$

Here, the subscript ℓ denotes the number of absorbed photons and $\widetilde{\rho}(x,x')$ is the initial density operator prior to the grating interaction. The operator $\widetilde{\mathsf{M}}_\ell(\mathsf{x};\theta)$ is diagonal in position x and depends on a dimensionless parameter θ, which corresponds to the time of the first photon absorption $\theta = t_1/t_\mathrm{L}$, see Sect. 3.3.5.

Following the same calculation as in Sect. 2.6.1, the conditional far-field interferogram can be expressed by

$$w_\ell(x/\Delta x) = \frac{d}{\Delta x H}\int_0^1 \mathrm{d}\theta\, \left|\int_{\mathbb{R}} \mathrm{d}x_0\, \exp\left[\mathrm{i}\frac{2\pi x}{d\Delta x}x_0 - \mathrm{i}\frac{\pi d}{d\Delta x}x_0^2\left(1+\frac{L_2}{L_1}\right)\right] t_\ell(x_0;\theta)\right|^2, \tag{6.14}$$

where $t_\ell(x_0;\theta)$ is the grating function describing the molecule-laser interaction,

$$t_\ell(x;\theta) = \Theta(H/2-|x|)\widetilde{M}_\ell(x;\theta). \tag{6.15}$$

Here, the Heaviside function $\Theta(H/2-|x|)$ represents a collimator of width H directly in front of an optical grating. Again, the unconditional interferogram is given by the sum $w(x/\Delta x) = \sum_{\ell_\mathrm{F}=0}^{\infty} w_{\ell_\mathrm{F}}(x/\Delta x)$.

Figure 35 compares the unconditional interferograms in the presence (solid line) and in the absence of photon absorption (shadowed area). The main diffraction peaks appear at $x/\Delta x = n$, $n \in \mathbb{Z}$, where $\Delta x = dL_2/L_\mathrm{T}$ is the separation of two neighboring diffraction peaks. This distance Δx corresponds to the shift, which results from the transfer of one grating momentum $2\pi\hbar/d$ at the diffraction grating. Absorption processes create additional peaks in the interferogram, which are located between the main diffraction peaks, i.e. at $x/\Delta x = 1/2 + n$. An absorption event implies the transfer of half of the grating momentum $\hbar k_\mathrm{L} = \pi\hbar/d$, which leads to the shift of the conditional interferograms in units of $\Delta x/2$. As illustrated in Fig. 35(b), these additional peaks consist of molecules that absorbed an odd number of photons.

I examine the effect of enhancement of the triplet-state polarizability and the absorption cross section with the help of the unconditional interferogram in Fig. 5. The

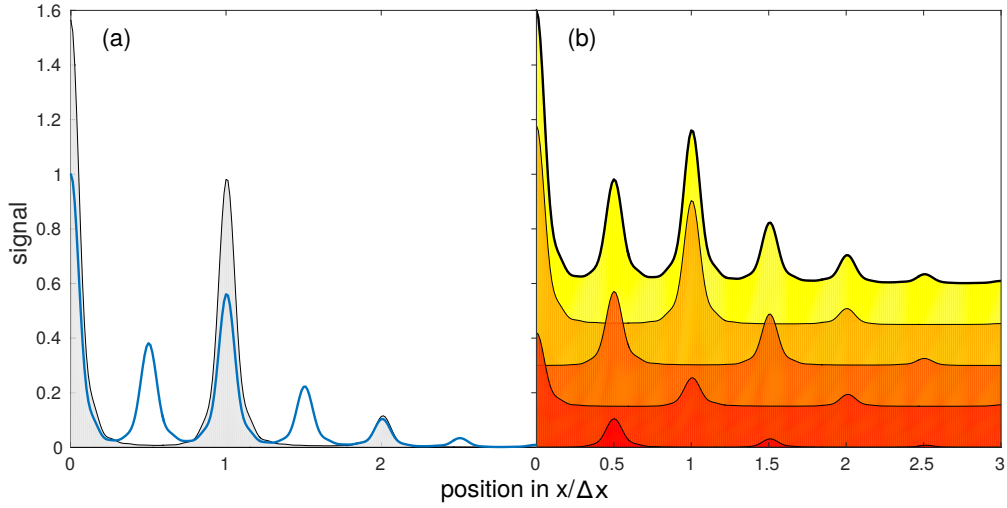

Figure 35: Far-field interferogram as a function of the lateral position $x/\Delta x$, where $\Delta x = dL_2/L_T$ corresponds to the separation of two main diffraction peaks. Panel (a) compares the unconditional interferograms of non-absorbing (shadowed area, $n_0 = 0$, $\phi_0 = 2.5$) and absorbing molecules (solid line, $n_0 = 2$, $\phi_0 = 2.5$). The signal is normalized on the maximum of the solid line. Panel (b) shows the contribution of the conditional interferograms (thin lines) to the unconditional interferogram (top thick line). The thin lines from top to bottom are the conditional interferograms (6.14) for $\ell = 0$, 1 and 2 photon absorptions, respectively. Note that for a better illustration the curves are shifted vertically. For this figure, I assumed $L_1 = L_2$, no enhancement factor for the triplet state, $\eta_a^{(T)} = \eta_p^{(T)} = 1$, the width of the collimator $H/d = 10$, and a finite detector resolution of $D_d/\Delta x = 0.1$.

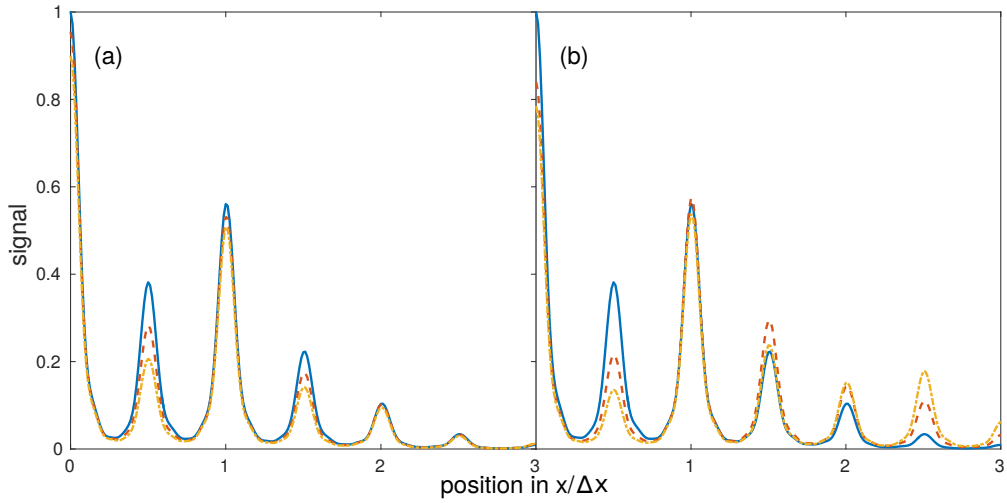

Table 5: Unconditional far-field interferogram as a function of the position $x/\Delta x$. Panel (a) examines the effect of enhanced triplet-state absorption cross section by comparing the interferograms for $\eta_a^{(T)} = 1$ (solid line), $\eta_a^{(T)} = 2$ (dashed line) and $\eta_a^{(T)} = 3$ (dash-dotted line), while the polarizability is assumed to be unchanged, $\eta_p^{(T)} = 1$. The enhancement of the absorption cross section leads to a reduction of the diffraction peaks. The effect is more pronounced for the sub-peaks at $x/\Delta x = 1/2 + n$, $n \in \mathbb{Z}$, compared to the main diffraction peaks at $x/\Delta x = n$. In Panel (b) the interferograms are illustrated for different values of the enhancement factor, $\eta_p^{(T)} = 1$ (solid line), $\eta_p^{(T)} = 2$ (dashed line) and $\eta_p^{(T)} = 3$ (dash-dotted line). Here, the absorption cross section is assumed to be constant $\eta_a^{(T)} = 1$. Otherwise, the same parameters are used as in Fig. 35. A higher triplet state polarizability causes the population of higher diffraction peaks, in contrast to Panel (a).

enhancement factors $\eta_{\mathrm{a}}^{(\mathrm{T})}$ for the absorption cross section and $\eta_{\mathrm{p}}^{(\mathrm{T})}$ for the polarizability are introduced in Sect. 3.3.4. Because the sub-peaks at $x/\Delta x = 1/2 + n$, $n \in \mathbb{Z}$ contain only molecules that absorbed at least one photon, they are more strongly affected by the enhancement compared to the main diffraction peaks. An enhancement of the absorption cross section has its impact on the conditional transmission probability through the grating. The enhancement of the polarizability leads to the population of higher diffraction peaks, see Fig. 5(b).

6.3.2 *Fluorescence*

As discussed in Chapter 4, fluorescence of molecules is expected to have a contrast-reducing effect on a far-field interferogram. In contrast to the ladder model treated in the previous subsection, the solution of the fluorescence master equation (4.27) and (4.28) cannot be represented in the from $\rho = \mathsf{M}\widetilde{\rho}\mathsf{M}^{\dagger}$, where M is a generalized measurement operator. Thus the compact expression (2.48) for the far-field interferogram in terms of a grating function $\mathsf{t}(x)$ cannot be applied. Instead of that, the more general expression Eq. (2.43) of the far-field density distribution is employed,

$$\begin{aligned} w_{\ell_{\mathrm{F}}}(x/\Delta x) &= \frac{D}{\Delta x H}\sum_{n\in\mathbb{Z}}\int_{-D_{\mathrm{c}}/d}^{D_{\mathrm{c}}/d}\mathrm{d}q_0\,\exp\left(\mathrm{i}\frac{2\pi x}{\Delta x}q_0\right)(H/d-|q_0|)B_n(q_0;\ell_{\mathrm{F}}) \\ &\quad\times\mathrm{sinc}\left\{\pi(H/d-|q_0|)\left[L_T\left(\frac{1}{L_2}+\frac{1}{L_1}\right)q_0-n\right]\right\}, \end{aligned} \tag{6.16}$$

which corresponds to a conditional interferogram of a molecule undergoing ℓ_{F} fluorescence events. The n-th Talbot coefficient $B_n(\xi;\ell_{\mathrm{F}})$ is given by the Fourier integral of the solution of the fluorescence master equation,

$$\begin{aligned} B_n(\xi;\ell_{\mathrm{F}}) &= \frac{1}{d}\int_{-d/2}^{d/2}\mathrm{d}x\,\exp\left(-\mathrm{i}\frac{2\pi x}{d}m\right) \\ &\quad\times\frac{\rho_{\mathrm{G},\ell_{\mathrm{F}}}(x-d\xi/2,x+d\xi/2)+\rho_{\mathrm{T},\ell_{\mathrm{F}}}(x-d\xi/2,x+d\xi/2)}{\widetilde{\rho}(x-d\xi/2,x+d\xi/2)} \end{aligned} \tag{6.17}$$

Note that there are two solutions of the fluorescence master equation: the ground state $\rho_{\mathrm{G},\ell_{\mathrm{F}}}$ and the triplet excited state part $\rho_{\mathrm{T},\ell_{\mathrm{F}}}$, see Sect. 4.2.2. If the detection scheme in an experiment is insensitive to the number of fluorescence events ℓ_{F}, the unconditional interferogram is relevant, which is given by the sum $w(x/\Delta x) = \sum_{\ell_{\mathrm{F}}=0}^{\infty} w_{\ell_{\mathrm{F}}}(x/\Delta x)$.

The expected contrast-reducing effect is illustrated in Fig. 36(a) by comparing the interferograms in the presence (solid line) and in the absence of the fluorescence (shadowed area). The reduction is more pronounced for the half-integer sub-peaks at $x/\Delta x = 1/2 + n$, $n \in \mathbb{Z}$, compared to the main diffraction peaks at $x/\Delta x = n$, see discussion in Sect. 6.3.1. For the given quantum yields $\Phi_{\mathrm{ISC}} = 0.42$, $\Phi_{\mathrm{IC}} = 0$ and $\Phi_{\mathrm{F}} = 0.58$, which are properties of hypericin, and the mean absorption number $n_0 = 2$, one still expects a high contrast of the interferogram despite fluorescence decoherence

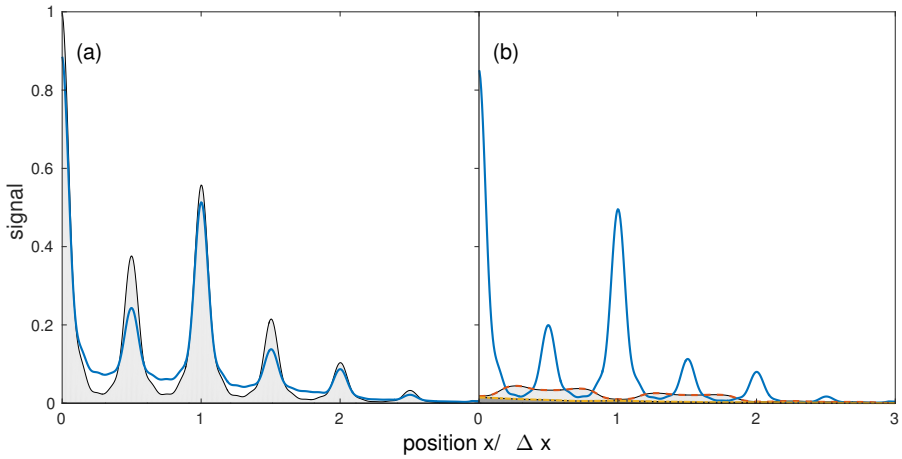

Figure 36: (a) Unconditional interferogram $w(x/\Delta x)$ in the presence (solid line) and in the absence of fluorescence (shaded area), where the quantum yields for the solid line are chosen to $\Phi_{\mathrm{ISC}} = 0.42$, $\Phi_{\mathrm{IC}} = 0$ and $\Phi_{\mathrm{F}} = 0.58$. The shadowed area is the result of the ladder model discussed in Sect. 6.3.1. (b) Conditional interferograms for different number of fluorescence events, $\ell_{\mathrm{F}} = 0$ (solid line), $\ell_{\mathrm{F}} = 1$ (dashed line) and $\ell_{\mathrm{F}} = 2$ (dash-dotted line). The same parameters are used as in Fig. 31.

because 75% of molecules undergo no fluorescence. However, the conditional interferograms for molecules that emit at least one fluorescence photon, exhibit a nearly complete loss of the interference contrast, as depicted in Fig. 36(b).

6.4 COLLISIONAL DECOHERENCE

In this section I consider the effect of collisional decoherence both in a near-field Talbot-Lau and in a far-field interferometer. Because the momentum transfer due to a scattering with an environmental gas atom is about 100 times larger than the grating momentum $2\pi\hbar/d$, one may assume a total loss of spatial coherence of scattered molecules. In this case, one observes an exponential reduction of the visibility in a Talbot-Lau interferometer, $\mathcal{V}_{\mathrm{sin}} \exp(-n_{\mathrm{c}})$, with the mean number of collision events n_{c}, see Sect. 6.4.1. On the other hand, one expects a large loss of molecules because of this large recoil. In order to minimize this loss, I consider a far-field interferometer with a collision chamber placed directly in front of a detector in Sect. 6.4.2.

6.4.1 *Talbot-Lau scheme*

A detailed calculation of the interferogram in an Talbot-Lau interferometer is presented in Sect. 2.6.2. The theoretical description is based on the grating transformation of the characteristic function $\chi_t{}'(s,q) = \sum_{n\in\mathbb{Z}} B_n\,(s/d)\,\chi_t\,(s, q + 2\pi\hbar n/d)$, where $B_n(\xi)$ is the n-th Talbot coefficient, and a free propagation $\chi_t(s,q) = \chi_0(s - qt/M, q)$. In this

section I examine the effect of collisional decoherence on the Talbot-Lau interference visibility.

As discussed in Sect. 5.3, the free propagation of the characteristic function in the presence of decoherence is given by

$$\chi_t(s,q) = \chi_0\left(s - \frac{qt}{M}, q\right) \exp\left\{\int_0^t \mathrm{d}\tau\, \gamma(\tau)\left[\eta\left(s - \frac{q}{M}(t-\tau)\right) - 1\right]\right\}. \tag{6.18}$$

The effect of decoherence is represented by an exponential factor, which contains a decoherence function $\eta(R)$ as well as rate of events $\gamma(t)$. Following the same calculation as in Sect. 2.6.2, the interferogram S is given by

$$S = \overline{S}\left[1 + \sum_{j=1}^{\infty} \mathcal{V}_j\left(\frac{L}{L_\mathrm{T}}\right) D_j\left(\frac{L}{L_\mathrm{T}}\right) \cos\left(\frac{2\pi x_\mathrm{s}}{d} j\right)\right], \tag{6.19}$$

where x_s is the lateral shift of the third grating. The Fourier coefficients $\mathcal{V}_j(\xi)$ (2.62) are modified due to the decoherence represented by an exponential factor

$$\begin{aligned} D_j(\xi) &= \exp\left\{\int_0^1 \mathrm{d}\theta\, \gamma(\xi t_\mathrm{L}\theta)\left[\eta\left(d\xi\theta j\right) - 1\right]\right\}. \\ &\quad \times \exp\left\{\int_0^1 \mathrm{d}\theta\, \gamma(\xi t_\mathrm{L}[\theta+1])\left[\eta\left(d\xi[1-\theta]j\right) - 1\right]\right\} \end{aligned} \tag{6.20}$$

Here, I assumed a symmetric Talbot-Lau setup, i.e. three gratings are equally separated. The first and second exponential function in Eq. (6.20) correspond to decoherence events in the first and second half of the interferometer, respectively. For collisions with environmental gas atoms, the width of the decoherence function $\eta(R)$ is typically on the order of $w_\eta \simeq 0.5$ nm, as discussed in Sect. 5.2.4. Because the grating period in an interferometer is typically $d \simeq 200$ nm and the Talbot parameter is typically $L/L_\mathrm{T} \simeq 2$, the decoherence function in Eq. (6.20) is a very sharply peaked function, which can be approximated by the Kronecker delta, $\eta\left(d\xi\tau j\right) \approx \delta_{j0}$. In this case the modification coefficients (6.20) read

$$D_j(\xi) = \begin{cases} 1 & \text{for } j = 0 \\ \exp(-n_\mathrm{c}) & \text{otherwise} \end{cases}, \tag{6.21}$$

where $n_\mathrm{c} = \int_0^{2\xi t_\mathrm{L}} \mathrm{d}\tau\, \gamma(\tau)$ is the mean number of scattering events. This leads to an exponential decay of the sinusoidal visibility

$$\mathcal{V}_\mathrm{sin} = 2\frac{B_{-1}^{(1)}(0) B_2^{(2)}\left(L/L_T\right) B_{-1}^{(3)}(0)}{B_0^{(1)}(0) B_0^{(2)}\left(0\right) B_0^{(3)}(0)} \exp(-n_\mathrm{c}), \tag{6.22}$$

which is experimentally verified in Ref. [39]. Note that the mean signal $\overline{S}$ is constant in this calculation because I assume an infinitely large detector. However, in a real

experiment, one must also consider the collision-induced signal loss. In this case the 0-th modification coefficient is $D_0 \neq 1$, which represents the reduction of the detected molecular number. The visibility (6.22) must then modified to $\mathcal{V}_{\sin}/D_0$.

Let us estimate the loss of molecules due to scattering with environmental gas atoms. The mean transfered momentum in a scattering event $\sqrt{\pi}\hbar/w_\eta$ (see Eq. (5.64)) leads after a free propagation over a distance z to the lateral shift of a molecule

$$\Delta x_{\mathrm{r}} = \frac{\sqrt{\pi}\hbar}{w_\eta}\frac{z}{v_z} = \frac{1}{2\sqrt{\pi}}\frac{dL}{w_\eta L_{\mathrm{T}}}\frac{z}{L}d, \tag{6.23}$$

where d is the grating period and v_z is the longitudinal velocity of a molecule. If the detectable range is $x/d \in [-f_{\mathrm{d}}/2,\ f_{\mathrm{d}}/2]$, the scattering at a position $z/L \gtrsim \sqrt{\pi} f_{\mathrm{d}} w_\eta L_T/Ld$ results in a loss of the molecule. For typical values of $w_\eta = 0.5$ nm, $d = 200$ nm, $f_{\mathrm{d}} = 3600$, $L/L_{\mathrm{T}} = 2$ and $L = 10$ cm [23], this distance yields $z \gtrsim 80$ cm. That is, the expected signal loss is small owing to the large detection area.

6.4.2 *Far-field scheme*

Unlike in a near-field interferometer, a far-field interferogram is much larger than the grating period. Its width is typically $\simeq 10\,\mu$m, that is, it is about 500 times larger than a grating period. Hence, we expect that collisional decoherence causes the position-dependent modification of far-field interferograms, in contrast to the constant reduction of the visibility in the near field. Nevertheless, a molecule may well get kicked out of the detectable region if a collisions takes place far away from a detector. According to the estimation of the collision-induced shift Eq. (6.23), the collisions that occur at distance $z \gtrsim 3.5$ cm imply signal loss, where I assumed typical values of $f_{\mathrm{d}} = 500$, $L_2/L_{\mathrm{T}} = 100$ and $L_2 = 1$ m. That is, in a simple experiment, where whole interferometer is filled with a gas, one would observe only an exponential decay $\exp(-n_{\mathrm{c}})$ of the interferogram due to the losses of molecules but not the reduction of interference constant [136].

For a more sophisticated examination of the decoherence effect, I consider in this section a collision chamber of width ℓ_{c} filled with a gas, which is placed in front of a detector. The distance between the detector and the right edge of the collision chamber shall be L_{c}. Assuming that a gas is distributed homogeneously within the chamber, the characteristic function at the detection screen $\chi_{t_1+t_2}(s,q)$ is modified by

$$\chi'_{t_1+t_2}(s,q) = \chi_{t_1+t_2}(s,q)\exp\left\{n_{\mathrm{c}}\int_0^1 \mathrm{d}\theta\ \left[\eta\left(s - \frac{q}{Mv_{\mathrm{M}}}(L_{\mathrm{c}} - \ell_{\mathrm{c}}\theta)\right) - 1\right]\right\}, \tag{6.24}$$

where $n_{\mathrm{c}} = \gamma\ell_{\mathrm{c}}/v_{\mathrm{M}}$ is the mean number of scattering events. The dimensionless integration variable θ in Eq. (6.24) corresponds to the relative position in the chamber where a collision takes place. The far-field interferogram $w(x) = \int \mathrm{d}q \mathrm{e}^{-\mathrm{i}qx/\hbar}\chi'_{t_1+t_2}(0,q)$ then reads

$$w(x) = \mathrm{e}^{-n_{\mathrm{c}}}\left[w_0(x) + w_{\mathrm{sc}}(x)\right], \tag{6.25}$$

where the first and second term correspond to the density distribution of non-scattered and scattered molecules, respectively. While the undisturbed interferogram $w_0(x)$ is given by Eq. (2.48), the scattered part is modified by mean of the convolution

$$w_{\mathrm{sc}}(x) = \int \mathrm{d}x' w_0(x') h(x - x') \tag{6.26}$$

with

$$h(x) = \int \frac{\mathrm{d}q}{2\pi\hbar} \mathrm{e}^{-\mathrm{i}qx/\hbar} \left\{ \exp\left[n_{\mathrm{c}} \int_0^1 \mathrm{d}\theta\, \eta\left(\frac{q\left[L_{\mathrm{c}} + \ell_{\mathrm{c}}\theta\right]}{M v_{\mathrm{M}}} \right) \right] - 1 \right\}. \tag{6.27}$$

It can be shown readily that the number of total molecules is unchanged due to scattering, i.e. $\int \mathrm{d}x\; w(x) = \int \mathrm{d}x\; w_0(x)$.

In the case of collisional decoherence, this modification $h(x)$ (solid line in Fig. 37(a)) is a broad function compared to the typical far-field interferogram, which represents a large collision-induced shift of molecules. As discussed in Sect. 5.2.4, the decoherence function $\eta(x)$ due to collisions can be represented by a soft and hard scattering part, see Eq. (5.55). Compared to the soft collision part (dashed line), the hard scattering contribution to the modification $h(x)$ (dash-dotted line) exhibits a flat position dependence. Thus the hard scattering leads merely to a constant redistribution of the scattered molecules on the detection screen.

The scattered molecules form a wide underground in the interferogram as shown in Fig. 37(b). The width of the underground $w_{\mathrm{sc}}(x)$ can be estimated to

$$\frac{\Delta I}{\Delta x} \simeq \frac{d}{2\sqrt{\pi} w_\eta} \frac{L_{\mathrm{c}} + \ell_{\mathrm{c}}/2}{L_2}, \tag{6.28}$$

where I assume that scatterings occur exactly in the middle of the collision chamber. Thus for scattered molecules to be detected, the collision chamber should best be placed directly in front of the detector. As shown in Fig. 37(c), the total interferogram exhibits still a good interference contrast because for the chosen mean number of scatterings, $n_{\mathrm{c}} = 1$, a significant amount of molecules do not experience collisions.

In this chapter I examined effects of internal molecular photophysical processes and collisional decoherence on interferograms of three different types of matter-wave interferometers; the near-field Talbot-Lau interferometers, KDTLI and OTIMA, as well as a far-field interferometer. It was shown that the excitation of a molecule to the triplet state in an optical grating has detectable effects both in near and far field interference if laser powers are sufficiently high. It turns out that the KDTLI is sensitive to the triplet-state polarizability, whereas the effect of the triplet-state absorption cross section is more pronounced in OTIMA. Both the change of polarizability and absorption cross section have a significant effect on the far-field interference. If molecules undergo fluorescence, interference contrasts get reduced both in the near and far field. Interestingly, fluorescence can lead to an enhancement of visibility in the near-field interferograms depending on experimental parameters, as discussed in Sect. 6.1.4. I discussed also multi-photon ionization gratings in OTIMA, which exhibit a significant reduction of the visibility compared to the single ionization case. Finally, I examined

the effect of collisional decoherence. The decoherence effect on near-field interference can be described by an exponential reduction of the visibility. In contrast to the near-field case, collisional decoherence leads to a position dependent modification of the far-field interferogram, see Fig. 37.

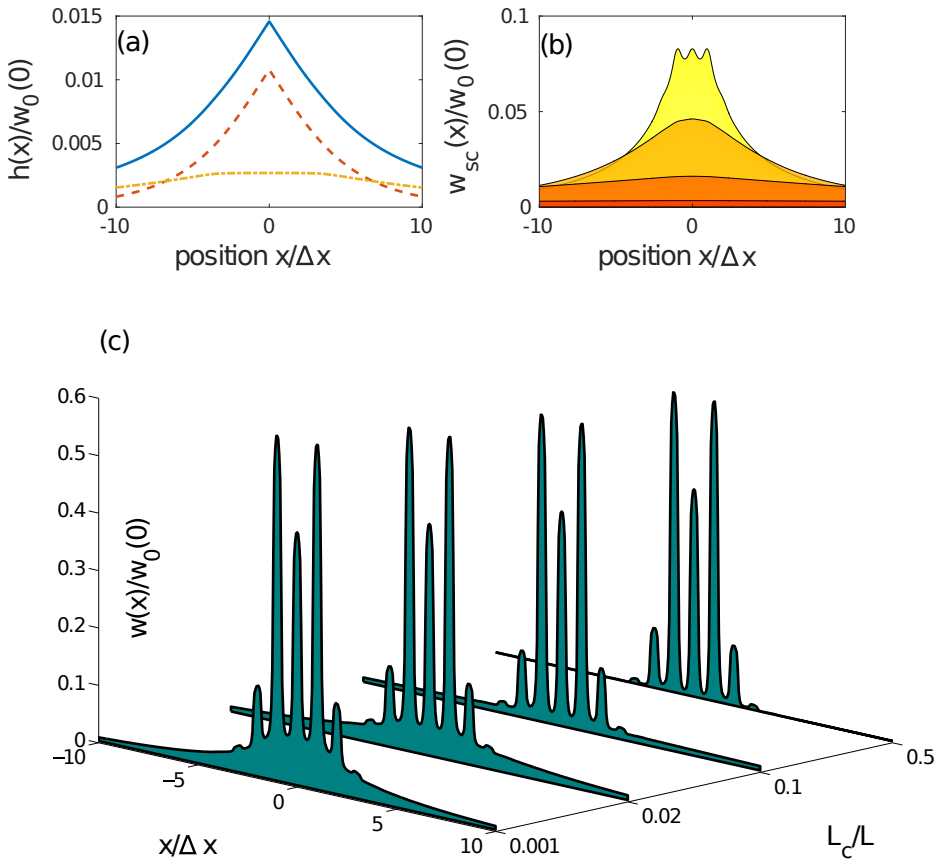

Figure 37: (a)The modification function $h(x)$ as a function of the lateral position $x/\Delta x$. The solid line is the result of the numerical integration of Eq. (6.27) using the collision decoherence function Eq. (5.55). The dashed and dash-dotted line are the results for the soft and hard scattering part of the decoherence function $\eta(\mathbf{R}) = h(s)D_1(|\mathbf{R}|/w_\eta)$ and $\eta(\mathbf{R}) = (1-h(s))D_2(|\mathbf{R}|\mu(s)/w_\eta)$, respectively. For this plot I assume a small width of the collision chamber $\ell_c = 0.05L$ and a small chamber-detector distance $L_c = 0.02L$. (b) The scattered part of the interferogram $w_{sc}(x)$ is shown for different positions of the collision chamber. The lines from top to bottom corresponds to $L_c/L = 0.001$, 0.02, 0.1 and 0.5, respectively. (c) The total far-field interferogram Eq. (6.25) for different positions of the collision chamber L_c. The undisturbed interferogram $w_0(x)$ is the result of Eq. (2.48) assuming a pure phase grating, as described by the total grating function $t(x) = \exp(i\pi\cos^2(x))\Theta(H/2-|x|)$. Here, H is the width of the collimator. The parameters are set to: the mean number of scattering events $n_c = 1$, the width of the collimator $H/d = 10$, the resolution of the detector $D_d/\Delta x = 0.2$ and the distances $L_1 = L_2 = 100L_T$.

7

CONCLUSION AND OUTLOOK

In this thesis, I have treated two main subjects: the interplay of coherent and incoherent processes in the diffraction of the molecular center-of-mass state by an optical grating, and the effect of collisional decoherence due to scattering with environmental gas atoms. After a review of molecular phase-space dynamics in Chapter 2, Chapters 3-5 treated these two main topics. In Chapter 6, I applied and illustrated the results in terms of three interferometric setups; far-field interference, KDTLI and OTIMA interference. These interferometers play a central role in high-mass matter-wave interferometry, which are operated by the Arndt group in the University of Vienna.

Let me summarize some main results of this thesis.

- **Photon absorption** A complex molecule can act as a photon-absorber without subsequent re-emission due to its numerous internal rovibrational states. Each absorption leads to a stepwise increase of molecule's internal temperature. As discussed in Chapter 6, molecules can still interfere after absorption of many photons. If molecules absorb at least one photon, the conditional interferograms can exhibit even higher visibility as the unconditional one in KDTLI, see Fig. 27. The absorption-induced photon-recoil $\hbar k_{\mathrm{L}}$ can shift an interferogram, which is beautifully illustrated in a far-field interferometer: the absorption of photons creates additional sub-peaks in a far-field interferogram beside the main diffraction peaks, see Fig. 35. Because these sub-peaks consist of almost only molecules that absorbed at least one photon, this scheme can be used for separating photo-excited molecules from unexcited ones.

- **Photo-excitation of molecules** Excited molecules can exhibit an enhancement of their polarizability and absorption cross section. This enhancement is shown to have a significant effect both on far-field and near-field interferograms. It turns out that KDTLI and OTIMA are sensitive to the excited-state polarizability and absorption cross section, respectively. Thus, these two Talbot-Lau interferometer can act as complementary measurement schemes for excited-state properties of a molecule. A far-field interferogram is significantly affected by the enhancement of both quantities.

- **Fluorescence** A fluorescent molecule is affected by spatial decoherence because the emitted fluorescence photons can reveal the particle's whereabouts. Indeed, it is shown that if a molecule undergoes at least one fluorescence event, the conditional interferogram is strongly deteriorated, see Fig. 36 and 31. The total unconditional interferogram, in contrast, exhibits still a high interference contrast

because most molecules near the intensity nodes of a laser do not experience photon absorption and are therefore unaffected by fluorescence decoherence.

- **Collisional decoherence of polar molecules** Assuming that the rotation period of a molecule is much larger than the collision time, I derived a master equation by means of the monitoring approach. The master equation for the molecular center-of-mass state can be expressed in terms of the decoherence function and the scattering rate in the limit of large molecular mass. The approximate analytical expressions of these functions are presented in Chapter 5, which agree very well with the numerical results, see Fig. 26. The solution of the master equation is presented in the characteristic function representation in Sec. 5.3. The Fourier transform of the decoherence function corresponds to the distribution of the transfered momentum in scattering events. From the approximated analytical expression of this distribution, Eq. (5.64) and (5.66), one can estimate the most probable transfered momentum, which is about 100 times larger than the grating momentum in typical experimental conditions. That is, a collision destroys the required coherence completely. In a near-field interferometer this leads to the exponential reduction of the visibility with $\exp(-n_c)$, where n_c is the mean number of scattering events. Due to the large momentum transfer, one expects that a large part of the scattered molecules are kicked out of the interferometer, which leads to a signal loss. In order to minimize the signal loss, I considered a far-field interferometer with a collision chamber placed in front of the detector. Depending on the distance between the chamber and the detector, scattered molecules create a broad underground in an interferogram, see Fig. 37.

In this thesis, I treated the interaction between a point-like particle and a light. For future matter-wave experiments with macroscopic objects, however, the size of a considered particle can become larger than the period of an optical grating. In this case, the description of the dipole interaction can no longer be applied and all higher multipole moment must be taken into account. For a spherical dielectric particle, *Mie theory* [137] provides the interaction potential, which is examined in detail in Ref. [33]. The extension of the Mie theory for spheroidal particles [138, 139] is interesting because a large class of molecules can be approximated by a spheroid.

A

GENERAL SOLUTION FOR THE 2 × 2 COUPLED DIFFERENTIAL EQUATIONS

Here, I consider the following coupled differential equations

$$\begin{pmatrix} \partial_t x \\ \partial_t y \end{pmatrix} = \begin{pmatrix} A & B \\ C & D \end{pmatrix} \begin{pmatrix} x \\ y \end{pmatrix}. \tag{A.1}$$

The eigenvalues and corresponding eigenvectors of this system of differential equations are given by

$$\lambda_\pm = \frac{A+D}{2} \pm \frac{\sqrt{(A+D)^2 - 4(AD-BC)}}{2} \tag{A.2}$$

$$v_\pm = \begin{pmatrix} \frac{-D+\lambda_\pm}{C} \\ 1 \end{pmatrix}. \tag{A.3}$$

The general solution then reads

$$\begin{pmatrix} x \\ y \end{pmatrix} = f_+ v_+ \mathrm{e}^{\lambda_+ t} + f_- v_- \mathrm{e}^{\lambda_- t}.$$

The unknown coefficients $f_\pm$ are determined from the initial conditions $x(0) = x_0$ and $y(0) = y_0$ as

$$f_\pm = \pm \frac{1}{(\lambda_+ - \lambda_-)} \left[C x_0 + (D - \lambda_\mp) y_0 \right].$$

Thus, the solution of the initial value problem is given by

$$\begin{aligned} x(t) &= \frac{(\lambda_+ - D)x_0 + B y_0}{\lambda_+ - \lambda_-} \mathrm{e}^{\lambda_+ t} - \frac{(\lambda_- - D)x_0 + B y_0}{\lambda_+ - \lambda_-} \mathrm{e}^{\lambda_- t} \\ y(t) &= \frac{C x_0 - (\lambda_- - D) y_0}{\lambda_+ - \lambda_-} \mathrm{e}^{\lambda_+ t} - \frac{C x_0 + (\lambda_+ - D) y_0}{\lambda_+ - \lambda_-} \mathrm{e}^{\lambda_- t}. \end{aligned}$$

B

SCATTERING RATE AND DECOHERENCE FUNCTION

B.1 INFLUENCE OF THE ANISOTROPY OF THE THERMAL GAS DISTRIBUTION

I consider here the angular integration required to evaluate the decoherence function (5.19), i.e.

$$I = \int \mathrm{d}^2 n \int \mathrm{d}^2 n' \, \mu(|\mathbf{p}+\mathbf{p}_0|)\langle |f(p,\mathbf{n}\cdot\mathbf{n}')|^2\rangle_\Omega \exp\left[\mathrm{i}\zeta \mathbf{u}\cdot(\mathbf{n}-\mathbf{n}')\right], \tag{B.1}$$

where $\mathbf{u} = (\mathbf{R}_2-\mathbf{R}_1)/|\mathbf{R}_2-\mathbf{R}_1|$ and $\zeta = |\mathbf{R}_2-\mathbf{R}_1|p/\hbar$. This function I is expanded in orders of $|\mathbf{p}_0|/p_\mathrm{g}$ assuming that the most probable momentum of the thermal distribution $\mu(|\mathbf{p}|)$ is much larger than the momentum shift $|\mathbf{p}_0| = mv_\mathrm{M}$. In this section, I will show that the linear contribution in this expansion vanishes.

The Taylor expansion of the distribution function up to the linear order gives

$$\mu(|\mathbf{p}+\mathbf{p}_0|) = \mu(p) + (\mathbf{p}_0\cdot\mathbf{n})\partial_p\mu(p)\left[1+\mathcal{O}\left(\frac{mv_\mathrm{M}}{p_\mathrm{g}}\right)\right], \tag{B.2}$$

where $\mathbf{n} = \mathbf{p}/|\mathbf{p}|$. Using this expansion, the zeroth and first order contribution of (B.1) are given by

$$I_0 = 8\pi^2\mu(p)\int_0^\pi \mathrm{d}\theta \, \sin\theta\langle|f(p,\cos\theta)|^2\rangle_\Omega \mathrm{sinc}\left[2\zeta\sin\left(\frac{\theta}{2}\right)\right], \tag{B.3}$$

$$I_1 = [\partial_p\mu(p)]\mathbf{p}_0\cdot\int \mathrm{d}^2 n \int \mathrm{d}^2 n' \, \mathbf{n}\langle|f(p,\mathbf{n}\cdot\mathbf{n}')|^2\rangle_\Omega \exp\left[\mathrm{i}\zeta\mathbf{u}\cdot(\mathbf{n}-\mathbf{n}')\right], \tag{B.4}$$

where $\cos\theta = \mathbf{n}\cdot\mathbf{n}'$. Note that the zeroth order contribution $\mu(p)$ is spherically symmetric, and thus I_0 is independent of the direction $\mathbf{u}$. Because I_1 must invariant under the parity transformation $\mathbf{n}\to-\mathbf{n}$ and $\mathbf{n}'\to-\mathbf{n}'$, its real part must vanish. On the other hand, the imaginary part of I_1 can be expressed as

$$\frac{I_1 - I_1^*}{2\mathrm{i}} \propto \mathbf{p}_0\cdot\nabla_\mathbf{u} I_0. \tag{B.5}$$

That is, the also imaginary part of I_1 vanishes since I_0 is independent of the direction $\mathbf{u}$. Thus the the integral (B.1) are given by

$$I = I_0\left[1+\mathcal{O}\left(\frac{m^2v_\mathrm{M}^2}{p_\mathrm{g}^2}\right)\right] \tag{B.6}$$

B.2 THE SMALL ANGLE DIFFERENTIAL SCATTERING CROSS SECTION

In this section, I consider the small angle expansion of the scattering amplitude Eq. (5.26). For this sake, I use spherical coordinates, where the polar and azimuthal angles (θ, ϕ) and (β, α) denote the outgoing momentum $\mathbf{p}' = p'\mathbf{n}'(\theta, \phi)$ and molecular orientation $\mathbf{m} = \mathbf{m}(\beta, \alpha)$, respectively. In addition, φ is the angle between impact vector $\mathbf{b}$ and the x-axis.

In what follows, I will employ the following two approximations:

$$\frac{1}{2\pi}\int_0^{2\pi} \mathrm{d}\phi (1 + c\cos^2\phi)^\mu \approx \left(1 + \frac{c}{2}\right)^\mu, \tag{B.7}$$

where $0 \leq c \lesssim 3$ and $0 \leq \mu \leq 1$, and

$$\frac{1}{2}\int_0^{\pi} \mathrm{d}\phi \sin\phi (1 + c\cos^2\phi)^\mu \approx \left(1 + \frac{c}{3}\right)^\mu, \tag{B.8}$$

where $|c| < 1$ and $0 \leq \mu \leq 3$. The relative error does not exceed 3% for the parameter range given above.

The integral (5.26) using cylinder coordinate reads

$$\begin{aligned} f(p, \mathbf{n}'; \mathbf{m}) &= -\mathrm{i}\frac{p}{2\pi\hbar}\int_0^{2\pi} \mathrm{d}\varphi \int \mathrm{d}b\, b \mathrm{e}^{-\mathrm{i}pb\sin\theta\sin(\phi-\varphi)/\hbar} \\ &\quad \times \left(\exp\left[-\mathrm{i}B\frac{G^{2/(s-1)}(\beta, \varphi - \alpha)}{b^{s-1}}\right] - 1\right), \end{aligned} \tag{B.9}$$

where $B = mC\sqrt{\pi}\Gamma[(s-1)/2]/\hbar p\Gamma(s/2)$ and the orientation-dependent function is given by

$$G(\beta, \varphi) = \left(1 + \frac{a}{s}\cos^2\beta + \frac{a(s-1)}{s}\cos^2\varphi\sin^2\beta\right)^{2/(s-1)}.$$

The Taylor expansion of Eq. (B.9) yields

$$f(p, \mathbf{n}'; \mathbf{m}) = f_0(p, \mathbf{n}'; \mathbf{m}) + f_2(p, \mathbf{n}'; \mathbf{m})\theta^2 + \mathcal{O}(\theta^4). \tag{B.10}$$

Note that the odd orders do not appear in the expansion (B.10) because they contain the integral $\int_0^{2\pi} \mathrm{d}\varphi \sin^{2k+1}(\phi - \varphi - \alpha)F(\cos^2\varphi)$, which vanishes for all $k \in \mathbb{N}$. The zeroth and second order contribution can be evaluated with the help of following integrals [129]

$$\int_0^\infty \mathrm{d}b\, b^m \sin^2\left(\frac{B}{2b^{s-1}}\right) = \frac{B^{(m+1)/(s-1)}}{2(m+1)}\Gamma\left(\frac{s-m-2}{s-1}\right)\sin\left(\frac{\pi}{2}\frac{s-m-2}{s-1}\right) \tag{B.11}$$

$$\int_0^\infty \mathrm{d}b\, b^m \sin\left(\frac{B}{b^{s-1}}\right) = \frac{B^{(m+1)/(s-1)}}{(m+1)}\Gamma\left(\frac{s-m-2}{s-1}\right)\cos\left(\frac{\pi}{2}\frac{s-m-2}{s-1}\right), \tag{B.12}$$

for $B,\ m \in \mathbb{R}$, and $1 < (m+s)/(s-1) < 3$ as well as $0 < (m+s)/(s-1) < 2$, respectively. Thus, one obtains

$$f_0(p,\mathbf{n}';\mathbf{m}) = \frac{p}{4\pi\hbar}\exp\left(\frac{i\pi}{2}\frac{s-3}{s-1}\right)\Gamma\left(\frac{s-3}{s-1}\right)B^{2/(s-1)}\int_0^{2\pi}\mathrm{d}\varphi\, G(\beta,\varphi), \quad \text{(B.13)}$$

$$f_2(p,\mathbf{n}';\mathbf{m}) = -\frac{p}{16\pi\hbar}\exp\left(\frac{i\pi}{2}\frac{s-5}{s-1}\right)\Gamma\left(\frac{s-5}{s-1}\right)\left(\frac{p\theta}{\hbar}\right)^2 B^{4/(s-1)}$$

$$\times\left[\sin^2(\phi-\alpha)\int_0^{2\pi}\mathrm{d}\varphi\, G^2(\beta,\varphi)+\cos(2\phi-2\alpha)\int_0^{2\pi}\mathrm{d}\varphi\,\cos^2\varphi G^2(\beta,\varphi)\right]. \quad \text{(B.14)}$$

The orientation averaged differential cross section in the small angle expansion then reads

$$\left\langle|f(p,\cos\theta)|^2\right\rangle_\Omega = \left\langle\left|f_0(p,\mathbf{n}';\mathbf{m})\right|^2\right\rangle_\Omega + 2\left\langle\Re\left[f_0(p,\cos\theta)f_2^*(p,\cos\theta)\right]\right\rangle_\Omega\theta^2+\mathcal{O}(\theta^4)$$

$$= A(p)\left[1-\left(\frac{\theta}{\theta_*(p)}\right)^2\right]+\mathcal{O}(\theta^4),$$

where the amplitude $A(p)$ and angle $\theta_*(p)$ are given by

$$A = \left(\frac{p\sigma_0(p)}{4\pi\hbar}\right)^2\left[1+\tan^2\left(\frac{\pi}{s-1}\right)\right]h_1(a), \quad \text{(B.15)}$$

$$\theta_* = \frac{\hbar}{p}\sqrt{\frac{8\pi}{\sigma_0(p)}}\Gamma\left(\frac{s-3}{s-1}\right)\left[\Gamma\left(\frac{s-5}{s-1}\right)h_2(a)\right]^{-1/2}. \quad \text{(B.16)}$$

Here I defined two functions

$$h_1(a) = \frac{1}{8\pi^2}\int_0^\pi\mathrm{d}\beta\,\sin\beta\left[\int_0^{2\pi}\mathrm{d}\varphi G(\beta,\varphi)\right]^2, \quad \text{(B.17)}$$

$$h_2(a) = \frac{1}{4\pi^2 h_1(a)}\int_0^\pi\mathrm{d}\beta\int_0^{2\pi}\mathrm{d}\varphi\mathrm{d}\varphi'\,\sin\beta G(\beta,\varphi)G^2(\beta,\varphi'). \quad \text{(B.18)}$$

With the approximations presented above, the two functions (B.17) and (B.18) can be written as

$$h_1(a) = \left(1+\frac{a}{3}\right)^{4/(s-1)}, \quad \text{(B.19)}$$

$$h_2(a) = \left(1+\frac{a}{3}\right)^{2/(s-1)}, \quad \text{(B.20)}$$

which finally gives Eqs. (5.31) and (5.32), respectively.

B.3 EVALUATION OF THE ANGLE INTEGRAL FOR DECOHERENCE FUNCTION

In this section, I consider an angular integral

$$\mathrm{Int} = I_{\mathrm{cl}}(p)\int_0^\infty\mathrm{d}\theta\,\theta^{-(s+2)/s}\left(1-\exp\left[-\left(\frac{\theta}{\theta_{\mathrm{cl}}(p)}\right)^5\right]\right)\mathrm{sinc}\left(\frac{p|\mathbf{R}|}{\hbar}\theta\right), \quad \text{(B.21)}$$

which appears in the calculation of the hard scattering part of the decoherence function. Because this integration can not be evaluated in closed form, I consider an approximation, where the function $\left(1-\exp\left[-(\theta/\theta_{\mathrm{cl}}(p))^5\right]\right)$ in Eq. (B.21) is replaced by a Heaviside-function $\Theta[\theta-\theta'(p)]$. I determine the unknown angle $\theta'(p)$ so that the integral (B.21) for $|\mathbf{R}|=0$ stays constant in this approximation,

$$\begin{aligned}\int_{\theta'(p)}^{\infty}\mathrm{d}\theta\,\theta^{-(s+2)/s} &\stackrel{!}{=} \int_{0}^{\infty}\mathrm{d}\theta\,\theta^{-(s+2)/s}\left(1-\exp\left[-(\theta/\theta_{\mathrm{cl}})^5\right]\right)\\ \Leftrightarrow\ \theta'(p) &= \frac{\theta_{\mathrm{cl}}(p)}{\Gamma^{s/2}(1-2/5s)}.\end{aligned} \tag{B.22}$$

The angles θ_{cl} and θ' differ by a factor of $\Gamma^{s/2}(1-2/5s)$, which is ≈ 1 for all $s\geq 2$. This approximation allows us an analytical evaluation of (B.21),

$$\begin{aligned}\mathrm{Int} &\approx I_{\mathrm{cl}}(p)\int_{\theta'(p)}^{\infty}\mathrm{d}\theta\,\theta^{-(s+2)/s}\mathrm{sinc}\left(\frac{p|\mathbf{R}|}{\hbar}\theta\right)\\ &= \frac{s}{2}I_{\mathrm{cl}}(p)\theta_{\mathrm{cl}}^{-2/s}(p)\Gamma\left(1-\frac{2}{5s}\right)D_2\left(\frac{2p|\mathbf{R}|}{\hbar\Gamma^{s/2}(1-2/5s)}\theta_{\mathrm{cl}}(p)\right)\\ &= [1-h(s)]\frac{\langle\sigma_{\mathrm{tot}}(p)\rangle_{\Omega}}{2\pi}D_2\left(\frac{2p|\mathbf{R}|}{\hbar\Gamma^{s/2}(1-2/5s)}\theta_{\mathrm{cl}}(p)\right).\end{aligned} \tag{B.23}$$

Here, the function $D_2(x)$ is defined by

$$D_2(x) = {}_1F_2\left[-\frac{1}{s};\frac{3}{2},\frac{s-1}{s};-x^2\right]-\frac{2^{(s+2)/s}}{s}\cos\left(\frac{\pi}{s}\right)\Gamma\left(-\frac{s+2}{s}\right)|x|^{2/s}, \tag{B.24}$$

which corresponds to the hard scattering part of the decoherence function, see Sect. 5.2.4.

B.4 MOMENTUM AVERAGE FOR DECOHERENCE FUNCTION AND KICK DISTRIBUTION

The calculation of the decoherence function $\eta(\mathbf{R})$ in Eq. (5.52) and kick-distribution $\widetilde{\eta}(\mathbf{Q})$ in Eqs. (5.63) and (5.65) involves the evaluation of the following integral

$$\mathrm{Int} = \int_{0}^{\infty}\mathrm{d}\xi\,\nu(\xi)F(\beta\xi), \tag{B.25}$$

where $\nu(\xi)$ is the distribution function defined in Eq. (5.53). In this section, I present an approximated evaluation of this integral, which is based on the fact that the function $\nu(\xi)$ is a sharply peaked function and the function $F(\beta\xi)$ is slowly varying near the maximum of $\nu(\xi)$.

For a systematic approximation of the integral B.25, I expand the function $F(\beta\xi)$ at a point $\xi=\xi_s$ near the maximum of the distribution function,

$$\mathrm{Int} = F(\beta\xi_s)+\sum_{n=0}^{\infty}F^{(n)}(\beta\xi_s)\varepsilon(s,n), \tag{B.26}$$

where $F^{(n)}(\beta\xi_s)$ denotes the n-th derivative of the function $F(\beta\xi)$ evaluated at the point $\xi = \xi_s$. The factor $\varepsilon(s,n)$ contains the integral over ξ, which can be evaluated analytically,

$$\varepsilon(s,n) = \int_0^\infty \mathrm{d}\xi \, \frac{(\xi-\xi_s)^n}{n!} \xi^{4s-7} \exp\left(-\xi^{2(s-1)}\right) \tag{B.27}$$

$$= \frac{1}{2(s-1)} \sum_{k=0}^{n} \Gamma\left[\frac{4s-6+k}{2(s-1)}\right] \frac{(-\xi_s)^{n-k}}{k!(n-k)!}. \tag{B.28}$$

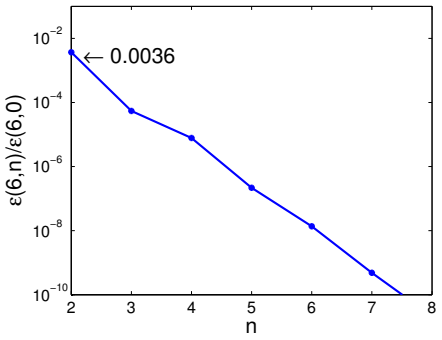

Figure 38: The function $\varepsilon(6,n)$ decays rapidly with n

In order to optimize this approximation, ξ_s is chosen so that the first correction $\varepsilon(s,1)$ vanishes. From this condition I obtain the optimal value for the evaluation point

$$\xi_s = \frac{\Gamma\left(2 - 1/\left[2(s-1)\right]\right)}{\Gamma\left(2 - 1/\left[s-1\right]\right)}, \tag{B.29}$$

which corresponds to the mean value $\int_0^\infty \xi\nu(\xi)\mathrm{d}\xi$. This function $\varepsilon(s,n)$ for the chosen ξ_s (B.29) is a fast decaying function, as shown in Fig. 38. In the case of $s = 6$, the next to leading order contribution $\varepsilon(6,2)/\varepsilon(6,0)$ is merely 0.36%. If the function $F(\beta\xi)$ varies slowly in the vicinity of $\xi \sim \xi_s$, the integral can be approximated by

$$\mathrm{Int} \approx F(\xi_s\beta). \tag{B.30}$$

DANKSAGUNG

Ich danke Klaus Hornberger für seine geduldige, intensive und zielführende Betreuung. Egal wie beschäftigt er war, bei Fragen hat sich er immer Zeit genommen und war immer bereit für ausführliche Diskussionen. Durch die Debatten mit ihm habe ich gelernt, wie man wissenschaftlich systematisch eine Problemlösung erlangt. Dies wird als wertvolle Grundlage meines weiteren Lebens dienen. Ich danke auch den Kollegen von der AG Arndt an der Universität Wien für die fruchtbare Kollaboration und für viele interessante Diskussionen. Es war spannend und begeisterungsreich mit den Experimentatoren aus der hochaktuellen Forschung zu arbeiten. Meine duisburger Kollegen haben immer für gute Laune am Arbeitsplatz gesorgt und ich habe mich stets wohl gefühlt. Stefan und Benjamin haben mich bei der Veröffentlichung der wissenschaftlichen Artikel bereitwillig unterstützt und einen großen Beitrag dazu geleistet. Ohne sie wären meine zwei Veröffentlichungen nicht zustande gekommen und ich danke ihnen für die konstruktive Mitarbeit. Ich möchte ganz besonderes meiner Frau Naeko und meiner ganzen Familie aus Kyoto, Thüringen und Marl danken, ohne deren Unterstützung ich nicht hier wäre.

BIBLIOGRAPHY

[1] M. K. E. L. Planck, *Zur Theorie des Gesetzes der Energieverteilung im Normalspectrum*, Verhandl. Dtsc. Phys. Ges. **2**, 237 (1900). (Cited on page 1.)

[2] J. D. Jackson, *Classical Electrodynamics*, John Wiley & Sons, Inc., New York, 2 edition, 1975. (Cited on pages 1 and 41.)

[3] G. Gabrielse, D. Hanneke, T. Kinoshita, M. Nio, and B. Odom, *New determination of the fine structure constant from the electron g value and QED*, Phys. Rev. Lett. **97**, 030802 (2006). (Cited on page 1.)

[4] T. Kinoshita, *Quantum Electrodynamics*, Advanced series on directions in high energy physics, World Scientific, Singapore, 1990. (Cited on page 1.)

[5] R. P. Crease, *The most beautiful experiment*, Physics World **15**, 19 (2002). (Cited on page 1.)

[6] R. Feynman, R. Leighton, and M. Sands, *The Feynman Lectures on Physics, Volume III*, Basic Books, New York, 2013. (Cited on page 1.)

[7] A. J. Leggett, *Realism and the physical world*, Rep. Prog. Phys. **71**, 022001 (2008). (Cited on page 2.)

[8] E. Schrödinger, *Die gegenwärtige Situation in der Quantenmechanik*, Naturwissenschaften **23**, 823–828 (1935). (Cited on page 2.)

[9] E. Joos, H. D. Zeh, C. Kiefer, D. Giulini, J. Kupsch, and I. O. Stamatescu, *Decoherence and the Appearance of a classical world in quantum theory*, Springer, Berlin, 2002. (Cited on pages 2 and 65.)

[10] M. A. Schlosshauer, *Decoherence and the Quantum-to-Classical Transition*, Springer, Berlin, 2008.

[11] W. H. Zurek, *Decoherence, einselection, and the quantum origins of the classical*, Rev. Mod. Phys. **75**, 715–775 (2003). (Cited on pages 2 and 65.)

[12] R. Ruffini and S. Bonazzola, *Systems of self-gravitating particles in general relativity and the concept of an equation of state*, Phys. Rev. **187**, 1767 (1969). (Cited on page 2.)

[13] L. Diosi, *Gravitation and quantum-mechanical localization of macro-objects*, Phys. Lett. A **105**, 199–202 (1984).

[14] S. Nimmrichter and K. Hornberger, *Stochastic extensions of the regularized Schrödinger-Newton equation*, Phys. Rev. D **91**, 024016 (2015). (Cited on page 2.)

[15] J. R. van Meter, *Schrödinger–Newton 'collapse' of the wavefunction*, Classical Quant. Grav. **28**, 215013 (2011). (Cited on page 2.)

[16] N. Gisin, *Stochastic quantum dynamics and relativity*, Helv. Phys. Acta **62**, 363–371 (1989). (Cited on page 2.)

[17] P. Pearle, *Combining stochastic dynamical state-vector reduction with spontaneous localization*, Phys. Rev. A **39**, 2277 (1989). (Cited on page 2.)

[18] A. Bassi, K. Lochan, S. Satin, T. P. Singh, and H. Ulbricht, *Models of wave-function collapse, underlying theories, and experimental tests*, Rev. Mod. Phys. **85**, 471–527 (2013). (Cited on page 2.)

[19] M. Arndt, O. Nairz, J. Vos-Andreae, C. Keller, G. van der Zouw, and A. Zeilinger, *Wave-particle duality of C_{60} molecules*, Nature **401**, 680–2 (1999). (Cited on pages 2, 3, 5, 36, 72, and 100.)

[20] C. Brand, M. Sclafani, C. Knobloch, Y. Lilach, T. Juffmann, J. Kotakoski, C. Mangler, A. Winter, A. Turchanin, J. Meyer, O. Cheshnovsky, and M. Arndt, *An atomically thin matter-wave beamsplitter*, Nat. Nanotech. **10**, 845–848 (2015). (Cited on page 2.)

[21] B. Brezger, L. Hackermüller, S. Uttenthaler, J. Petschinka, M. Arndt, and A. Zeilinger, *Matter-Wave Interferometer for Large Molecules*, Phys. Rev. Lett. **88**, 100404 (2002). (Cited on pages 2, 3, 17, and 31.)

[22] L. Hackermüller, S. Uttenthaler, K. Hornberger, E. Reiger, B. Brezger, A. Zeilinger, and M. Arndt, *Wave Nature of Biomolecules and Fluorofullerenes*, Phys. Rev. Lett. **91**, 090408 (2003). (Cited on pages 17 and 36.)

[23] S. Gerlich, L. Hackermüller, K. Hornberger, A. Stibor, H. Ulbricht, M. Gring, F. Goldfarb, T. Savas, M. Muri, M. Mayor, and M. Arndt, *A Kapitza-Dirac-Talbot-Lau interferometer for highly polarizable molecules*, Nat. Phys. **3**, 711–715 (2007). (Cited on pages 3, 5, 72, 90, 92, and 107.)

[24] P. Haslinger, N. Dorre, P. Geyer, J. Rodewald, S. Nimmrichter, and M. Arndt, *A universal matter-wave interferometer with optical ionization gratings in the time domain*, Nat. Phys. **9**, 144–148 (2013). (Cited on pages 5, 25, 31, 95, and 98.)

[25] N. Dörre, J. Rodewald, P. Geyer, B. von Issendorff, P. Haslinger, and M. Arndt, *Photofragmentation Beam Splitters for Matter-Wave Interferometry*, Phys. Rev. Lett. **113**, 233001 (2014). (Cited on pages 2, 3, 31, and 98.)

[26] S. Eibenberger, S. Gerlich, M. Arndt, M. Mayor, and J. Tuxen, *Matter-wave interference of particles selected from a molecular library with masses exceeding 10 000 amu*, Phys. Chem. Chem. Phys. **15**, 14696–14700 (2013). (Cited on page 2.)

[27] M. Arndt and K. Hornberger, *Testing the limits of quantum mechanical superpositions*, Nat. Phys. **10**, 271–277 (2014). (Cited on pages 3 and 65.)

[28] K. Hornberger, J. E. Sipe, and M. Arndt, *Theory of decoherence in a matter wave Talbot–Lau interferometer*, Phys. Rev. A **70**, 053608 (2004). (Cited on pages 3, 4, 7, 8, 14, 17, 23, 27, 29, 78, 80, and 84.)

[29] S. Nimmrichter and K. Hornberger, *Theory of near-field matter-wave interference beyond the eikonal approximation*, Phys. Rev. A **78**, 023612 (2008). (Cited on pages 4, 7, 8, 13, 17, and 23.)

[30] S. Y. Buhmann, S. Scheel, S. Å. Ellingsen, K. Hornberger, and A. Jacob, *Casimir-Polder interaction of fullerene molecules with surfaces*, Phys. Rev. A **85**, 042513 (2012).

[31] K. Hornberger, S. Gerlich, H. Ulbricht, L. Hackermüller, S. Nimmrichter, I. V. Goldt, O. Boltalina, and M. Arndt, *Theory and experimental verification of Kapitza–Dirac–Talbot–Lau interferometry*, New J. Phys. **11**, 043032 (2009). (Cited on pages 4, 5, 7, 8, 25, 27, 42, 48, 50, 89, 90, 91, and 92.)

[32] S. Nimmrichter, P. Haslinger, K. Hornberger, and M. Arndt, *Concept of an ionizing time-domain matter-wave interferometer*, New J. Phys. **13**, 075002 (2011). (Cited on pages 3, 5, 25, 48, 52, 95, 97, and 98.)

[33] S. Nimmrichter, *Macroscopic Matter Wave Interferometry*, Springer, Heidelberg, 2014. (Cited on pages 3, 4, 48, 50, 52, and 112.)

[34] O. Nairz, B. Brezger, M. Arndt, and A. Zeilinger, *Diffraction of Complex Molecules by Structures Made of Light*, Phys. Rev. Lett. **87**, 160401 (2001). (Cited on page 3.)

[35] P. W. Atkins and R. S. Friedman, *Molecular Quantum Mechanics*, Oxford University Press, 4 edition, 2005. (Cited on pages 3, 4, 32, 34, 41, and 54.)

[36] M. Klessinger and J. Michl, *Excited states and photochemistry of organic molecules*, VCH, New York, 1995. (Cited on pages 3, 31, 34, 35, 36, and 41.)

[37] L. Hackermuller, K. Hornberger, B. Brezger, A. Zeilinger, and M. Arndt, *Decoherence of matter waves by thermal emission of radiation*, Nature **427**, 711–714 (2004). (Cited on pages 3 and 65.)

[38] K. Hornberger, L. Hackermüller, and M. Arndt, *Influence of molecular temperature on the coherence of fullerenes in a near-field interferometer*, Phys. Rev. A **71**, 023601 (2005). (Cited on page 3.)

[39] K. Hornberger, S. Uttenthaler, B. Brezger, L. Hackermüller, M. Arndt, and A. Zeilinger, *Collisional Decoherence Observed in Matter Wave Interferometry*, Phys. Rev. Lett. **90**, 160401 (2003). (Cited on pages 3, 65, and 106.)

[40] K. Hornberger and J. E. Sipe, *Collisional decoherence reexamined*, Phys. Rev. A **68**, 012105 (2003). (Cited on pages 3, 66, and 67.)

[41] K. Hornberger, *Monitoring approach to open quantum dynamics using scattering theory*, Europhys. Lett. **77**, 50007 (2007). (Cited on pages 3, 5, 65, 66, and 69.)

[42] B. Vacchini and K. Hornberger, *Quantum linear Boltzmann equation*, Phys. Rep. **478**, 71–120 (2009). (Cited on pages 3, 65, 69, and 70.)

[43] K. Walter, B. A. Stickler, and K. Hornberger, *Collisional decoherence of polar molecules*, Phys. Rev. A **93**, 063612 (2016). (Cited on pages 4, 5, and 65.)

[44] J. P. Cotter, S. Eibenberger, L. Mairhofer, X. Cheng, P. Asenbaum, M. Arndt, K. Walter, S. Nimmrichter, and K. Hornberger, *Coherence in the presence of absorption and heating in a molecule interferometer*, Nat. Commun. **6**, 7336 (2015). (Cited on pages 4, 25, 36, 48, 53, 72, 90, and 91.)

[45] K. Walter, S. Nimmrichter, and K. Hornberger, *Multi-photon absorption in optical gratings for matter waves*, arXiv:1608.07135 (accepted by Phys. Rev. A) (2016). (Cited on page 4.)

[46] W. P. Schleich, *Quantum Optics in Phase Space*, Wiley-VCH, Berlin, 1 edition, 2001. (Cited on pages 4, 7, 8, 11, 12, and 13.)

[47] M. Arndt, N. Dörre, S. Eibenberger, P. Haslinger, J. Rodewald, K. Hornberger, S. Nimmrichter, and M. Mayor, *Matter-wave interferometry with composite quantum objects*, Proceedings of the International School of Physics "Enrico Fermi" **188**, 89–141 (2015). (Cited on pages 4, 8, 9, 23, 29, 31, and 87.)

[48] S. W. Hell and J. Wichmann, *Breaking the diffraction resolution limit by stimulated emission: stimulated-emission-depletion fluorescence microscopy*, Opt. Lett. **19**, 780–782 (1994). (Cited on page 4.)

[49] T. Juffmann, A. Milic, M. Müllneritsch, P. Asenbaum, A. Tsukernik, J. Tüxen, M. Mayor, O. Cheshnovsky, and M. Arndt, *Real-time single-molecule imaging of quantum interference*, Nat. Nanotech. **7**, 297–300 (2012). (Cited on page 4.)

[50] M. S. Chapman, T. D. Hammond, A. Lenef, J. Schmiedmayer, R. A. Rubenstein, E. Smith, and D. E. Pritchard, *Photon Scattering from Atoms in an Atom Interferometer: Coherence Lost and Regained*, Phys. Rev. Lett. **75**, 3783–3787 (1995). (Cited on pages 4 and 65.)

[51] K. Hornberger and B. Vacchini, *Monitoring derivation of the quantum linear Boltzmann equation*, Phys. Rev. A **77**, 022112 (2008). (Cited on pages 5, 69, and 70.)

[52] C. Brand, J. Fiedler, T. Juffmann, M. Sclafani, C. Knobloch, S. Scheel, Y. Lilach, O. Cheshnovsky, and M. Arndt, *A Green's function approach to modeling molecular diffraction in the limit of ultra-thin gratings*, Ann. Phys. **527**, 580–591 (2015). (Cited on pages 5, 17, 31, and 100.)

[53] J. J. Sakurai and J. Napolitano, *Modern Quantum Mechanics*, Addison-Wesley, Reading, MA, revised edition, 2011. (Cited on pages 7, 67, and 74.)

[54] I. Amidror, *The Theory of the Moiré Phenomenon: Volume I: Periodic Layers*, Springer London, 2009. (Cited on page 7.)

[55] F. Schwabl, *Statistische Mechanik*, Physica-Verlag, Berlin, 2006. (Cited on pages 7 and 13.)

[56] C. Cohen-Tannoudji, B. Diu, and F. Laloe, *Quantum mechanics. Volume I*, Wiley, New York, 1st edition, 1977. (Cited on pages 8, 10, 12, and 39.)

[57] E. Wigner, *On the Quantum Correction For Thermodynamic Equilibrium*, Phys. Rev. **40**, 749–759 (1932). (Cited on pages 8 and 11.)

[58] J. E. Moyal, *Quantum mechnics as a statistical theory*, Proc. Cambridge Philos. Soc. **45**, 99–124 (1949). (Cited on page 8.)

[59] C. L. Mehta and E. C. G. Sudarshan, *Relation between Quantum and Semiclassical Description of Optical Coherence*, Phys. Rev. **138**, B274–B280 (1965). (Cited on page 8.)

[60] Y. Kano, *A New Phase-Space Distribution Function in the Statistical Theory of the Electromagnetic Field*, J. Math. Phys. **6**, 1913–1915 (1965). (Cited on page 8.)

[61] Nazarov, Yu. V. and Kindermann, M., *Full counting statistics of a general quantum mechanical variable*, Eur. Phys. J. B **35**, 413–420 (2003). (Cited on page 8.)

[62] P. P. Hofer and A. A. Clerk, *Negative Full Counting Statistics Arise from Interference Effects*, Phys. Rev. Lett. **116**, 013603 (2016). (Cited on page 8.)

[63] T. Juffmann, H. Ulbricht, and M. Arndt, *Experimental methods of molecular matter-wave optics*, Rep. Prog. Phys. **76**, 086402 (2013). (Cited on page 8.)

[64] I. Bloch, T. W. Hänsch, and T. Esslinger, *Measurement of the spatial coherence of a trapped Bose gas at the phase transition*, Nature **403**, 166–170 (2000). (Cited on page 8.)

[65] M. Born and E. Wolf, *Principles of Optics: Electromagnetic Theory of Propagation, Interference and Diffraction of Light*, Cambridge University Press, 7th edition, 1999. (Cited on pages 9, 22, and 55.)

[66] M. Abramowitz and I. A. Stegun, editors, *Handbook of Mathematical Functions: with Formulas, Graphs, and Mathematical Tables (Dover Books on Mathematics)*, Dover, New York, 1965. (Cited on pages 16, 46, 48, 49, 50, 51, 62, 78, 81, and 84.)

[67] R. Brühl, P. Fouquet, R. E. Grisenti, J. P. Toennies, G. C. Hegerfeldt, T. Köhler, M. Stoll, and C. Walter, *The van der Waals potential between metastable atoms and solid surfaces: Novel diffraction experiments vs. theory*, Europhys. Lett. **59**, 357 (2002). (Cited on page 17.)

[68] R. E. Grisenti, W. Schöllkopf, J. P. Toennies, G. C. Hegerfeldt, and T. Köhler, *Determination of Atom-Surface van der Waals Potentials from Transmission-Grating Diffraction Intensities*, Phys. Rev. Lett. **83**, 1755–1758 (1999). (Cited on page 17.)

[69] H. F. Talbot, *LXXVI. Facts relating to optical science. No. IV*, Philos. Mag. **9**, 401–407 (1836). (Cited on page 20.)

[70] S. Gerlich, S. Eibenberger, M. Tomandl, S. Nimmrichter, K. Hornberger, P. J. Fagan, J. Tüxen, M. Mayor, and M. Arndt, *Quantum interference of large organic molecules*, Nat. Commun. **2**, 263 (2011). (Cited on pages 25 and 31.)

[71] P. L. Kapitza and P. A. M. Dirac, *The reflection of electrons from standing light waves*, Proc. Cambridge Philos. Soc. **29**, 297–300 (1933). (Cited on page 31.)

[72] D. L. Freimund, K. Aflatooni, and H. Batelaan, *Observation of the Kapitza-Dirac effect*, Nature **413**, 142–143 (2001). (Cited on page 31.)

[73] C. Gerry and P. Knight, *Introductory Quantum Optics*, Cambridge University Press, 2004. (Cited on pages 31, 38, and 39.)

[74] A. P. Kazantsev, G. I. Surdutovich, and V. P. Yakovlev, *Mechanical Action of Light on Atoms*, World Scientific, Singapore, 1990. (Cited on pages 31 and 40.)

[75] J. H. Gross, *Mass Spectrometry: A Textbook*, Springer, Berlin, 2011. (Cited on page 33.)

[76] J. Lakowicz, *Principles of Fluorescence Spectroscopy*, Springer, New York, 3rd edition, 2007. (Cited on pages 34, 54, and 55.)

[77] D. C. Harris and M. D. Bertolucci, *Symmetry and Spectroscopy: An Introduction to Vibrational and Electronic Spectroscopy*, Dover, New York, 1978. (Cited on page 34.)

[78] T. Uzer and W. H. Miller, *Theories of intramolecular vibrational energy transfer*, Phys. Rep. **199**, 73–146 (1991). (Cited on page 34.)

[79] R. Smalley, *Vibrational randomization measurements with supersonic beams*, J. Phys. Chem. **86**, 3504–3512 (1982). (Cited on page 34.)

[80] T. Kulp, R. S. Ruoff, and J. D. McDonald, *Limits on the lifetimes of intramolecular rovibrational relaxation*, J. Chem. Phys. **82**, 2175–2179 (1985). (Cited on page 35.)

[81] S. Eibenberger, X. Cheng, J. P. Cotter, and M. Arndt, *Absolute Absorption Cross Sections from Photon Recoil in a Matter-Wave Interferometer*, Phys. Rev. Lett. **112**, 250402 (2014). (Cited on pages 36, 72, and 91.)

[82] G. W. Robinson, *Intersystem crossing in gaseous molecules*, J. Chem. Phys. **47** (1967). (Cited on pages 36 and 42.)

[83] B. Valeur and M. N. Berberan-Santos, *Molecular Fluorescence: Principles and Applications*, Wiley, Weinheim, 2013. (Cited on pages 36 and 54.)

[84] N. Turro, *Modern Molecular Photochemistry*, University Science Books, Sausalito, CA, 1991. (Cited on pages 36 and 53.)

[85] M. Lee, O.-K. Song, J.-C. Seo, D. Kim, Y. D. Suh, S. M. Jin, and S. K. Kim, *Low-lying electronically excited states of C_{60} and C_{70} and measurement of their picosecond transient absorption in solution*, Chem. Phys. Lett. **196**, 325–329 (1992). (Cited on page 36.)

[86] Y. P. Sun, P. Wang, and N. B. Hamilton, *Fluorescence spectra and quantum yields of buckminsterfullerene (C_{60}) in room-temperature solutions. No excitation wavelength dependence*, J. Am. Chem. Soc. **115**, 6378–6381 (1993). (Cited on page 36.)

[87] J. W. Arbogast and C. S. Foote, *Photophysical properties of C_{70}*, J. Am. Chem. Soc. **113**, 8886–8889 (1991). (Cited on page 36.)

[88] M. Pineiro, A. L. Carvalho, M. M. Pereira, A. D. Gonsalves, L. G. Arnaut, and S. A. J. Formosinho, *Photoacoustic measurements of porphyrin triplet-state quantum yields and singlet-oxygen efficiencies*, J. Chem. Eur. J. **40**, 2299 (1998). (Cited on page 36.)

[89] D. J. Quimby and F. R. Longo, *Luminescence studies on several tetraarylporphins and their zinc derivatives*, J. Am. Chem. Soc. **97**, 5111–5117 (1975). (Cited on page 36.)

[90] A. Michaeli, A. Regev, Y. Mazur, J. Feitelson, and H. Levanon, *Triplet-state reactions of hypericin: time-resolved laser photolysis and electron paramagnetic resonance spectroscopy*, J. Phys. Chem. **97**, 9154–9160 (1993). (Cited on page 36.)

[91] F. Gai, M. J. Fehr, and J. W. Petrich, *Observation of excited-state tautomerization in the antiviral agent hypericin and identification of its fluorescent species*, J. Phys. Chem. **98**, 5784–5795 (1994). (Cited on page 36.)

[92] D. Meschede, *Optics, Light and Lasers: The Practical Approach to Modern Aspects of Photonics and Laser Physics*, Wiley-VCH, Weinheim, 2008. (Cited on page 37.)

[93] C. Keller, J. Schmiedmayer, A. Zeilinger, T. Nonn, S. Dürr, and G. Rempe, *Adiabatic following in standing-wave diffraction of atoms*, Appl. Phys. B **69**, 303–309 (1999). (Cited on pages 38 and 45.)

[94] B. W. Shore and P. L. Knight, *The Jaynes-Cummings Model*, J. Mod. Optic. **40**, 1195–1238 (1993). (Cited on page 39.)

[95] D. O. Chudesnikov and V. P. Yakovlev, *Bragg Scattering on Complex Potential and Formation of Super-Narrow Momentum Distributions of Atoms in Light Fields*, Laser Phys. **1**, 110–119 (1991). (Cited on page 39.)

[96] U. Hohm and K. Kerl, *Temperature dependence of mean molecular polarizability of gas molecules*, Mol. Phys. **58**, 541–550 (1986). (Cited on page 43.)

[97] S. Dyrting and G. J. Milburn, *Quantum scattering of a two-level atom in the limit of large detuning*, Phys. Rev. A **49**, 4180–4188 (1994). (Cited on page 43.)

[98] H. M. Wiseman, *Quantum measurement and control*, Cambridge University Press, 1st edition, 2014. (Cited on page 43.)

[99] P. Busch, M. Grabowski, and P. J. Lahti, *Operational Quantum Physics*, Springer, Berlin, 1997. (Cited on page 47.)

[100] M. A. Nielsen and I. L. Chuang, *Quantum Computation and Quantum Information*, Cambridge University Press, 2011. (Cited on pages 47 and 69.)

[101] A. Peres, *Quantum Theory: Concepts and Methods (Fundamental Theories of Physics)*, Kluwer academic publishers, New York, 1993. (Cited on pages 47 and 69.)

[102] A. D. Cronin, J. Schmiedmayer, and D. E. Pritchard, *Optics and interferometry with atoms and molecules*, Rev. Mod. Phys. **81**, 1051–1129 (2009). (Cited on page 48.)

[103] D. A. Kokorowski, A. D. Cronin, T. D. Roberts, and D. E. Pritchard, *From single- to multiple-photon decoherence in an atom interferometer*, Phys. Rev. Lett. **86**, 2191 (2001). (Cited on page 53.)

[104] J. R. Taylor, *Scattering Theory - The quantum theory of nonrelativistic collisions*, Dover, Mineola, New York, 2000. (Cited on pages 65, 66, and 67.)

[105] M. S. Child, *Molecular Collsion Theory*, Academic Press, London, 1974.

[106] A. M. Arthurs and A. Dalgarno, *The Theory of scattering by a rigid rotor*, Proc. Roy. Soc. (London) **A256**, 540 (1960). (Cited on page 65.)

[107] A. Smirne and B. Vacchini, *Quantum master equation for collisional dynamics of massive particles with internal degrees of freedom*, Phys. Rev. A **82**, 042111 (2010). (Cited on page 65.)

[108] H. G. Bennewitz, K. H. Kramer, W. Paul, and J. P. Toennies, *Messung der Aniotropie des van der Waals-Potentials durch Streuung von Molekülen in definiertem Quantenzustand*, Z. Phys. **177**, 84–110 (1964). (Cited on pages 65, 66, and 74.)

[109] R. Helbing and H. Pauly, *Differentielle Streuquerschnitte bei der Wechselwirkung neutraler Moleküle Messung der Kleinwinkelstreuung*, Z. Phys. **179**, 16 (1964). (Cited on pages 65 and 76.)

[110] A. A. Milner, A. Korobenko, J. W. Hepburn, and V. Milner, *Effects of Ultrafast Molecular Rotation on Collisional Decoherence*, Phys. Rev. Lett. **113**, 043005 (2014). (Cited on page 66.)

[111] B. A. Stickler, B. Papendell, and K. Hornberger, *Spatio-orientational decoherence of nanoparticles*, Phys. Rev. A **94**, 033828 (2016).

[112] C. Zhong and F. Robicheaux, *Decoherence of rotational degrees of freedom*, arXiv:1605.03160 (2016). (Cited on page 66.)

[113] J. Trost and K. Hornberger, *Hund's Paradox and the Collisional Stabilization of Chiral Molecules*, Phys. Rev. Lett. **103**, 023202 (2009). (Cited on page 66.)

[114] D. M. Brink and G. R. Satchler, *Angular Momentum*, Clarendon Press, Oxford, 3rd edition, 1994. (Cited on page 67.)

[115] A. R. Edmonds, *Angular Momentum in Quantum Mechanics*, Princeton University Press, 1996. (Cited on page 67.)

[116] K. Hornberger, *Introduction to Decoherence Theory*, Lect. Notes Phys. **768**, 221–276 (2009). (Cited on page 69.)

[117] L. D. Landau and E. M. Lifshitz, *Course of Theoretical Physics Volume 3: Quantum Mechanics*, Pergamon, Oxford, 3rd edition, 1981. (Cited on pages 71, 74, 75, and 76.)

[118] A. J. Stone and R. J. A. Tough, *Spherical tensor theory of long−range intermolecular forces*, Chem. Phys. Lett. **110**, 123–129 (1984). (Cited on page 73.)

[119] A. J. Stone, *The Theory of Intermolecular Forces*, Oxford University Press, 1997. (Cited on pages 73 and 74.)

[120] L. I. Schiff, *Approximation Method for High-Energy Potential Scattering*, Phys. Rev. **103**, 443–453 (1956). (Cited on page 74.)

[121] F. W. Byron and C. J. Joachain, *Remarkable properties of the eikonal approximation*, Physica **66**, 33–42 (1973). (Cited on page 74.)

[122] B. R. Johnson, *The multichannel log-derivative method for scattering calculations*, J. Comput. Phys. **13**, 445–449 (1973). (Cited on page 75.)

[123] B. R. Johnson, *New numerical methods applied to solving the one-dimensional eigenvalue problem*, J. Chem. Phys. **67**, 4086–4093 (1977). (Cited on page 75.)

[124] G. W. F. Drake, editor, *Springer Handbook of Atomic, Molecular, and Optical Physics*, Springer, New York, 2nd edition, 2005. (Cited on page 75.)

[125] K. E. Mount, *Potential scattering cross sections in the semiclassical limit*, J. Phys. B **6**, 1397 (1973). (Cited on page 76.)

[126] M. V. Berry, *Uniform approximations for glory scattering and diffraction peaks*, J. Phys. B **2**, 381 (1969). (Cited on page 76.)

[127] E. Mason, J. Vanderslice, and C. Raw, *Quantum Effects in Small-Angle Molecular-Beam Scattering*, J. Chem. Phys. **40**, 2153–2164 (1964). (Cited on page 76.)

[128] M. V. Berry and K. E. Mount, *Semiclassical approximations in wave mechanics*, Rep. Prog. Phys. **35**, 315 (1972). (Cited on page 78.)

[129] I. S. Gradshteyn and I. M. Ryzhik, *Table of Integrals, Series, and Products*, Academic Press, Orlando, 7th edition, 2014. (Cited on pages 81 and 116.)

[130] J. Bateman, S. Nimmrichter, K. Hornberger, and H. Ulbricht, *Near-field interferometry of a free-falling nanoparticle from a point-like source*, Nat. Commun. **5**, 4788 (2014). (Cited on page 86.)

[131] H. Gratz and A. Penzkofer, *Triplet–triplet absorption of some organic molecules determined by picosecond laser excitation and time-delayed picosecond light continuum probing*, J. Photoch. Photobio. A **127**, 21–30 (1999). (Cited on page 91.)

[132] A. G. Adam, T. E. Gough, N. R. Isenor, and G. Scoles, *Rabi oscillations and rapid-passage effects in the molecular-beam* CO_2*-laser Stark spectroscopy of* CH_3F, Phys. Rev. A **32**, 1451–1457 (1985). (Cited on page 92.)

[133] K. Shimoda, *High-Resolution Laser Spectroscopy (Topics in Applied Physics)*, Springer, Berlin, 1st edition, 1976. (Cited on page 92.)

[134] C. Jönsson, *Elektroneninterferenzen an mehreren künstlich hergestellten Feinspalten*, Z. Phys. **161**, 454–474 (1961). (Cited on page 100.)

[135] O. Carnal and J. Mlynek, *Young's double-slit experiment with atoms: A simple atom interferometer*, Phys. Rev. Lett. **66**, 2689 (1991). (Cited on page 100.)

[136] C. G. Knobloch, *Diffraction of polarizable and polar molecules at ultrathin material gratings*, Master thesis, University of Vienna, 2014. (Cited on page 107.)

[137] C. F. Bohren and D. R. Huffman, *Absorption and Scattering of Light by Small Particles*, Wiley-VCH, Weinheim, 1983. (Cited on page 112.)

[138] C. Flammer, *Spheroidal Wave Functions*, Stanford University Press, 1st edition, 1957. (Cited on page 112.)

[139] M. I. Mishchenko, J. W. Hovenier, and L. D. Travis, editors, *Light Scattering by Nonspherical Particles: Theory, Measurements, and Applications*, Academic Press, San Diego, 1st edition, 1999. (Cited on page 112.)